



UNIVERSIDAD
DE LA REPUBLICA
URUGUAY



Cohesive sediment dynamics in the Río de la Plata

Estudio de la dinámica de sedimentos cohesivos en el Río
de la Plata

Rodrigo Liber Mosquera Núñez
Cédula de identidad 3.432.313-7

Programa de Posgrado en Ingeniería Mecánica de los Fluidos Aplicada
Facultad de Ingeniería
Universidad de la República

Montevideo – Uruguay
Febrero de 2021



UNIVERSIDAD
DE LA REPUBLICA
URUGUAY



Cohesive sediment dynamics in the Río de la Plata

Estudio de la dinámica de sedimentos cohesivos en el Río
de la Plata

Rodrigo Liber Mosquera Núñez

Tesis de Doctorado presentada al Programa de Posgrado en Ingeniería Mecánica de los Fluidos Aplicada, Facultad de Ingeniería de la Universidad de la República, como parte de los requisitos necesarios para la obtención del título de Doctor en Ingeniería Mecánica de los Fluidos Aplicada.

Director:

Ph.D. Prof. Francisco Pedocchi

Director académico:

Ph.D. Prof. Francisco Pedocchi

Montevideo – Uruguay

Febrero de 2021

Mosquera Núñez, Rodrigo Liber

Cohesive sediment dynamics in the Río de la Plata / Rodrigo Liber Mosquera Núñez. - Montevideo: Universidad de la República, Facultad de Ingeniería, 2021.

207 p.

Director:

Francisco Pedocchi

Director académico:

Francisco Pedocchi

Tesis de Doctorado – Universidad de la República, Programa en Ingeniería Mecánica de los Fluidos Aplicada, 2021.

Referencias bibliográficas: p. 175 – 185.

1. Estuario del Río de la Plata, 2. Hidrodinámica y dinámica de sedimentos, 3. Barro fluido, 4. Autoestratificación, 5. Retrodispersión acústica multifrecuencia. I. Pedocchi, Francisco, . II. Universidad de la República, Programa de Posgrado en Ingeniería Mecánica de los Fluidos Aplicada. III. Título.

INTEGRANTES DEL TRIBUNAL DE DEFENSA DE TESIS

Ph.D. Prof. W. Rockwell Geyer

Ph.D. Prof. J.C. Ismael Piedra-Cueva

Ph.D. Prof. Ricardo N. Szupiany

Ph.D. Prof. Romaric Verney

Ph.D. Prof. Susana B. Vinzón

Montevideo – Uruguay

Febrero de 2021

A mi amor, junto a ella soy una
mejor versión de mi mismo.

Acknowledgements

Thanks to all who generously teach me, supported me and encourage my research in the development of this thesis, allowing me to grow as a research scientist: Rodrigo Alonso; Daniel Barboza; Silvana D’Intino; Marcos Gallo; Matías González; Guillermo Echavarría; Guido Ferrari; Mónica Fossati; Fernanda Maciel; Lucía Ponce de León; Pablo Santoro; Sebastián Solari; Richard Styles; Susana Vinzón; and Ricardo Zouko.

I would also thank to the divers of Techno Dive S.A., and the crew of the multicat Titón and Carlón for their assistance during the mooring works. The Vector ADV used in this study was acquired with funds Fondo María Viñas from the Agencia Nacional de Investigación e Innovación, Uruguay. The field work was performed with the support of the Comisión Sectorial de Investigación Científica of the Universidad de la República, Uruguay.

I finally wish to thank Francisco Pedocchi for being my advisor and mentor as well as my friends and family, especially Vale, for their patient and support.

RESUMEN

En esta tesis se presentan mediciones de campo de sedimento cohesivo cercano al lecho y velocidades del flujo de agua. Estos datos fueron usados para comprender los procesos de transporte de sedimentos en un sitio con fondo de barro cercano a la bahía de Montevideo. El oleaje, las corrientes y las componentes turbulentas del flujo de agua fueron obtenidas usando un velocímetro acústico Doppler (ADV por sus siglas en inglés) ubicado a unos 30 cm encima del lecho. Mediante la utilización de un sensor de retrodispersión acústica multifrecuencia (ABS por sus siglas en inglés) se estimaron también los perfiles de concentración de sedimento de los últimos 40 cm. Se realizaron intensos trabajos de laboratorio con sedimento extraído del sitio de medición, los cuales indicaron que la floculación esperada en el campo no genera sesgos en la estimación de la concentración de sedimentos. De todas maneras, es necesario tomar ciertas precauciones en momentos de gran agitación puesto que la presencia de menos de 5 % de arenas cambian la granulometría del sedimento en movimiento, induciendo mayores estimaciones de concentración de sedimento que las reales. Una nueva técnica de inversión acústica multifrecuencia fue implementada para evitar estos sesgos.

La información recolectada en el campo durante cinco meses y medio muestra que durante oleaje moderado y fuerte, una capa de gran concentración de sedimento cercana al fondo es capaz de mantenerse en movimiento por más de un día. Con espesores cercanos al decímetro y concentraciones mayores a 100 kg/m^3 , el transporte de esta capa debido a las corrientes pudo ser calculada con un modelo analítico que acopla la interacción entre oleaje, corrientes y la autoestratificación debida a sedimentos. La estimación del sedimento transportado mediante este mecanismo permite explicar las tasas de sedimentación reportadas in los canales de acceso del puerto de Montevideo.

Palabras claves:

Estuario del Río de la Plata, Hidrodinámica y dinámica de sedimentos, Barro

fluido, Autoestratificación, Retrodispersión acústica multifrecuencia.

ABSTRACT

Sediment transport processes at the muddy bottom site near Montevideo bay were examined by observing the near seabed cohesive sediment and water velocity. Wave, currents and turbulent components of the water flow were obtained with an acoustic Doppler velocimeter located 30 cm above the seabed, while sediment concentration profiles of the lowest 40 cm were estimated with a multi-frequency acoustic backscatter sensor. Exhaustive laboratory testing of the sediment extracted from the deployment site indicated that flocculation expected in the field did not affect the acoustic estimation of sediment concentration. However, special attention was required during strong agitation since with concentrations of sands under 5 % granulometry of the sediment in motion was modified, leading to unrealistic estimations of higher sediment concentration. A new acoustic multifrequency technique was implemented in order to avoid this bias.

The field data collected during almost six months indicated that a highly concentrated sediment layer near the bottom was kept in motion during moderate and strong waves and would remain for more than one day. Its height was 1 dm and its concentration over 100 kg/m³. Currents caused this layer to travel and this phenomena was calculated with a simplified self-stratified wave-current-sediment coupled analytical model. The associated sediments travel as well and this explains the actual siltation rates in the navigation channels of Montevideo Port.

Keywords:

Río de la Plata estuary, Hydrodynamics and Sediment dynamics, Fluid mud, Self-stratification, Multifrequency acoustic backscatter.

Nomenclature

The following symbols are used in this work:

A_{BA} boric acid sound absorption parameter

A_{MS} magnesium sulfate sound absorption parameter

A_{water} water sound absorption parameter

$C_{\tilde{v}v'}$ coincident spectral density function (co-spectrum) of wave and turbulent velocity components

D fluid region, also transducer directional factor

D_m mean wave direction

E eroded sediment entrainment rate at $z = a$

\bar{F}_{sz} net vertical sediment flux

G_s scatterer shear modulus

H_S significant wave height

\vec{I} instantaneous flux of the total mechanical energy

$|\vec{I}|_{ms}$ mean square intensity amplitude

\vec{I}_i flux of the total mechanical energy of the incident wave

\vec{I}_s flux of the total mechanical energy of the scattered wave

\vec{I} flux of the total mechanical energy

K bulk modulus

K_s scatterer bulk modulus, also suspended particles parameter

K_t transducer parameter

L Monin-Obukov length

$M_{50\%}$ 25th and 75th percentile range of M

$M_{95\%}$ 2.5th and 97.5th percentile range of M

M acoustically determined sediment mass concentration

N number of scatterers

N_s number of samples

P_1 complex fluid pressure
 P characteristic fluid pressure
 Q_{sb} depth integrated sediment transport near the bottom
 Re_δ Reynolds number defined with Stokes viscous boundary layer thickness
 Re_w oscillatory Reynolds number
 Ri_0 bulk Richardson number
 Ri_g gradient Richardson number
 Ri_θ dimensionless reflectivity factor
 R_t electronic transducer receive sensitivity
 S_η wave energy spectrum
 S_p pressure power spectrum
 S_{v_E} East horizontal velocity projection power spectrum
 S_{v_N} North horizontal velocity projection power spectrum
 T_P peak wave period
 T_V voltage transfer function of the system
 U_* shear velocity of the current
 U_E East projection of the currents
 U characteristic velocity
 U_{orb} root mean squared orbital velocity amplitude
 U_t transducer oscillate speed amplitude
 V_{noise} backscattered voltage amplitude noise
 V_{rec} backscattered recorded voltage amplitude
 V_{rms} backscattered voltage amplitude signal
 a vertical height just above the seabed, also sphere radius
 a_g geometric mean sediment radius
 $\langle a_j \rangle$ the j -th moment of n_{pdf}
 a_s sediment radius
 a_t piston-like transducer radius
 $a_{w'}$ Hilbert transform envelope of w'
 c_0 sediment concentration of the seabed
 c_j mass concentration of the j -th sediment class
 c sediment mass concentration
 c_s speed of sound
 \vec{d}_{1s} displacement vector of the scatterer

d water depth
 e_{AP} Ariathurai-Partheniades slope parameter
 \mathbf{e}_r radial direction
 \mathbf{e}_x horizontal Cartesian direction, also stream-wise direction
 \mathbf{e}_y horizontal Cartesian direction
 \mathbf{e}_z vertical Cartesian direction
 $\langle f \rangle$ representative scatterer form factor
 f scatterer form factor, also frequency
 f_s sound frequency
 g acceleration due to Earth gravity
 k_N bottom roughness characteristic dimension
 \mathbf{k} complex wave number
 k wave number
 m_{pdf} mass probability density function
 n_{pdf} size probability density function
 \vec{n} normal outgoing direction
 \mathbf{p} complex pressure field
 p_{eq} equilibrium pressure
 p fluid pressure
 p_{ref} reference pressure amplitude
 p_s pressure of the backscattered wave
 r_0 reference distance from the origin
 r_1 transducer limit between near and far field
 r_R transducer Rayleigh length
 r_f fine fraction mass proportion
 r radial distance of a spherical coordinate system
 s dimensionless excess of shear stress, also water salinity
 t time
 u_{*c} current shear velocity
 u_{*r} combined wave-current shear velocity
 u_A Airy linear wave theory solution
 u_c current velocity field
 u velocity component in the \mathbf{e}_x direction
 u_w wave velocity field

v_E East velocity projection
 v_N North velocity projection
 \vec{v}_s sediment velocity
 \vec{v} velocity field
 v velocity component in the \mathbf{e}_y direction
 w_{si} sediment settling velocity of the i -th class
 w_s terminal sediment fall velocity in quiescent water
 w velocity component in the \mathbf{e}_z direction
 x horizontal Cartesian coordinate
 y horizontal Cartesian coordinate
 z_{0a} apparent bottom roughness
 z_0 hydrodynamic roughness
 z_1 Lundgren's transition layer lower boundary
 z_2 Lundgren's transition layer upper boundary
 z vertical Cartesian coordinate, also height above the bottom
 T transpose
 $_0$ zero order solution
 $_1$ first order solution
 $_j$ j -th sediment class
 $_m$ m -th monochromatic wave direction, also refers to the m -th scatterer particle
 $_n$ n -th monochromatic wave frequency, also refers to the n -th scatterer particle
 p refers to predicted variable
 α_G Madsen and Wikramanayake's dimensionless parameter
 α_s sound attenuation parameter due to sediment
 α sum of the absorption of water and sediment
 α_{wv} sound viscosity absorption for water
 α_w sound attenuation parameter due to water
 β McLean's dimensionless parameter
 γ McLean's dimensionless parameter
 γ_0 Smith and McLean's entrainment formula parameter
 δ_L lutocline height
 δ_S Stokes length, thickness of the laminar boundary layer
 δ_{wc} wave boundary layer height

ϵ sediment volume concentration
 ζ_{n0} vertical dimensionless coordinate at $z = z_0$
 ζ_n vertical dimensionless coordinate
 ζ stratification parameter
 θ_{-3dB} transducer half-beam angle
 θ_c current velocity direction
 θ_{cr} critical Shields value
 θ polar angle of a spherical coordinate system, also water temperature
 θ_w wave velocity direction
 κ von Kármán constant
 λ volume viscosity
 μ dynamic viscosity
 ν_{TN} eddy viscosity in the case without sediment
 ν_{Tm} turbulent sediment diffusivity
 ν_T eddy viscosity
 ν kinematic viscosity
 ξ Rayleigh scale parameter
 Π_s temporal average power of the scattered wave
 ρ_{eq} equilibrium density
 ρ_m water and sediment mixture density
 ρ density
 ρ_s sediment density
 σ_g geometric standard deviation
 σ ratio between ν_T and ν_{Tm}
 τ_b bottom shear stress
 τ_{cr} sediment transport initiation shear stress, also called critical Shields value
 τ_p transducer emitted pulse duration
 τ_s bed shear strength
 τ shear stress
 Φ generic scalar magnitude
 φ azimuthal angle of a spherical coordinate system
 χ^2 chi-squared distribution
 $\langle \chi \rangle$ representative scatterer cross-section
 χ_s scattering cross-section due to scatterer geometry

χ total scattering cross-section
 χ_v scattering cross-section due to viscous dissipation
 Ψ generic scalar magnitude
 ψ near field transducer correction
 ω_{BA} boric acid temperature dependent relaxation frequency
 ω_{MS} magnesium sulfate temperature dependent relaxation frequency
 ω angular frequency
 ω_P peak angular wave frequency
 ω_r representative wave angular frequency
 ∇ . divergence operator
 \mathbf{D} symmetric term of the velocity gradient
 ∇ gradient operator
 H Hilbert transform
 J_n Bessel function of the n -th order
 Δ Laplace operator
 P_n Legendre function of the n -th order
 $\bar{}$ time-average, steady motion component
 \sim wave motion component
 \prime turbulent motion component
cov cross-covariance
 $\frac{\partial}{\partial *}$ partial derivative (with respect to *)
 $\frac{d}{dt}$ total derivative
E expected value
 h_n spherical Hankel function of the n -th order
 j_n spherical Bessel function of the first kind
kei zeroth order Kelvin function
ker zeroth order Kelvin function
MS mean square
RMS root mean square

Contents

Nomenclature	xxii
1 Sediment dynamics in Río de la Plata	1
2 Bottom boundary layer dynamics	9
2.1 Bottom shear stresses over waves and currents	9
2.2 Sediment dynamics	15
2.2.1 Boundary condition.	17
2.3 Hydrodynamics and Sediment dynamics	19
2.3.1 Current and Suspended sediment concentration solution.	22
3 Hydroacoustics applied to sediment transport measurements	25
3.1 Linear theory	25
3.2 Non-linear effects	30
3.3 Absorption in the medium	31
3.4 Radiation from a transducer	31
3.5 Scattering of sound	36
3.6 Incoherent backscatter of suspensions	42
3.7 Acoustic backscatter calibration	45
3.8 Acoustic backscatter inversion	51
4 Field Deployment	57
4.1 Field works	57
4.2 ABS	63
4.3 ADV	63
4.4 CTD	66
4.5 Turbidity meters	67
4.6 ADCP	67

4.7	Complementary data - Gas Sayago buoy	68
5	Laboratory work	71
5.1	Sediment granulometry	71
5.2	ABS calibration and experiments	73
5.2.1	Ballotini glass spheres calibration.	73
5.2.2	Río de la Plata sediment.	76
5.3	Turbidity meters calibration	93
6	General view of collected data	95
6.1	First deployment	96
6.2	Second deployment	99
7	Field data analysis	109
7.1	Lutocline	109
7.2	Currents	111
7.3	Non-stationary motion components	114
7.3.1	Waves.	114
7.3.2	Turbulence.	116
7.3.3	Wave-Turbulence interaction.	119
7.4	Current shear velocity	123
7.5	Mobile sediments	124
8	Results and discussion	129
8.1	Results	129
8.1.1	First event: June 7-8, 2018	130
8.1.2	Second event: June 12-13, 2018	147
8.2	Discussion	158
9	Conclusions and future work	167
9.1	Conclusions - Methodology	167
9.2	Conclusions - Cohesive sediment dynamics in the Río de la Plata	169
9.3	Future work	172
	Bibliography	175
	Appendices	187
	Appendix 1 First deployment.	189

Annexes

201

Anexo 1 Salinity estimation from Acoustic Doppler Velocimeter measurements

203

Chapter 1

Sediment dynamics in Río de la Plata

Cohesive sediment dynamics in estuaries are mainly influenced by currents, tides and waves. Interactions between sediments and flow are complex, and their comprehension is even more complicated in this particular water-bodies due to their physicochemical and biogenic nature (Mehta, 1989). “It is therefore apparent that since physical interactions typically are of first-order significance, a better description of these interactions should lead to improved process modeling and thereby to the development of physical conceptual frameworks essential for understanding chemical and biological effects.” Mehta (1989).

Presently, fine sediment dynamics have been studied for more than six decades, and the current state of the art is extensively summarized by Mehta (2013). In a commonly accepted conceptualization, sediment transport processes are defined by analyzing the vertical structure of averaged concentration profiles in presence of waves and currents. Three main regions may be identified, separated by two significant concentration gradients. In the upper region sediments are in suspension and sediment concentration is relatively low. Flocs settling and turbulent mass diffusion compete to establish a vertical profile with higher concentrations downwards as flocs become larger. Depending on previous suspended sediment concentration or the hydrodynamic boundary layer above the seabed, a highly concentrated sediment layer of mud, often called fluid mud, with a fluid-like behavior may appear.

Fluid mud is considered a high concentration fine sediment mixture near the seabed, with mass concentrations above 10 kg/m^3 and below 400 kg/m^3 .

It can be formed either by settlement of a suspension or erosion of the bed, and has the ability to flow downwards along bottom slopes as a density current, horizontally moved by currents or mixed into the overlying water column depending on the hydrodynamic forces. [McAnally et al. \(2007\)](#) define fluid mud as: “...a high concentration aqueous suspension of fine-grained sediment in which settling is substantially hindered by the proximity of sediment grains and flocs, but which has not formed an interconnected matrix of bonds strong enough to eliminate the potential for mobility... Site-specific definitions, usually 1150–1200 kg/m³ for an upper bulk density limit, have been posed based on navigation and/or dredging management concerns.” Because turbulence mixing is heavily damped in this fluid mud layer, a stable lutocline sometimes appears at top of this layer. Under this layer is the seabed, where mean velocity is zero. Below the seabed, particle-particle contact allows the motionless bed to resist to flow stresses.

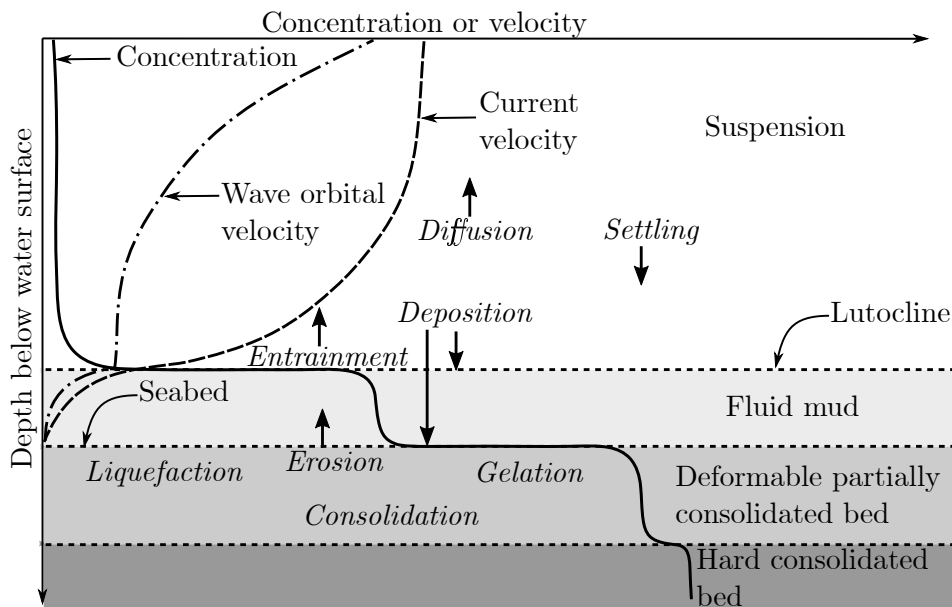


Figure 1.1: Transport processes associated with cohesive sediment dynamics ([Mehta, 2013](#)).

The definitions of the main sediment processes used in this thesis and shown in Fig. 1.1 were adopted from [Mehta \(2013\)](#):

- *Flocculation*: cohesive sediment grains, subjected to gravity, flow and collisions with other particles, present the ability to aggregate in water due to the electrochemical forces forming flocs. Depending on the colli-

sions between particles, ionic concentration and shear stresses imposed by the flow, flocs can manifest different sizes and densities over time.

- *Settling*: depending on their weight, size and shape, flocs and particles fall through the water column due to gravity inducing larger sediment concentration towards the bed. When concentrations are high enough, the sediment can obstruct the upward water flow, resulting in hindered settling.
- *Diffusion*: opposed to settling, the turbulent flow movement mixes the different layers, inducing a net transport of sediment from regions of higher sediment concentration to regions of lower concentration. Turbulent mixing can be diminished because of stratification, when strong vertical density gradients are imposed by changes in sediment concentration or salinity.
- *Deposition*: when settling sediments approach the seabed, they may stay attached to the bed. The process where the material in suspension is incorporated into the fluid mud is also called deposition.
- *Erosion and Entrainment*: depending on the turbulent energy, at boundaries such as the lutocline and the seabed the flow above may pick up sediment from the region below, incorporating the material to its motion. It is called entrainment when the suspension gets sediment from the fluid mud, whereas erosion is when the bed material is captured by the flow above. Due to the fact that fluid mud is not always present, sometimes the term entrainment is used instead of erosion.
- *Gelation and Consolidation*: after certain amount of time, deposited material begins to form a structure by bonding with the other particles, stiffening the bed. Another step in bed formation is consolidation, when the particles reorganize mainly due to gravity, expelling the interstitial water and increasing the bed strength further on.
- *Liquefaction*: when subject to cyclical loading (such as wave motion stresses), rearrangement of particles in the bed may increase the pore water pressure and reduce the interparticle stresses, weakening the bed and eventually initiating its motion.

The Río de la Plata fluvial-estuarine system is located in the east coast of South America, between 34 to 37 °S latitude and 55 to 59 °W longitude. Along the coast of this In this estuary are the largest cities of Argentina and Uruguay

with a population of approximately 40 million. Montevideo, is located halfway along the extension of the Río de la Plata coast, in a region associated to certain complexity in the sediment dynamics since the estuary becomes significantly wider. The reduction in the current velocities added to the salinity intrusion provide natural conditions for the deposit of sediments in this area.

Río de la Plata flows into the Atlantic Ocean and its main tributaries are Paraná and Uruguay rivers. The Río de la Plata is second to Amazon basin in South America. Its water motion is governed mainly by fresh water discharge, astronomical tide, storm surge, winds and its oceanic boundary. It is a microtidal estuary with dominance of 0.5 m amplitude of the M2 tidal constituent, the atmospheric forcing may cause variabilities of the sea level during days to a few weeks in the same order of magnitude as astronomical tides. The main meteorological events are usually developed over the south Argentinean continental shelf and propagated northward along the South American coast, as a coastal trapped wave entering the Río de la Plata, occasionally amplified in the estuary due to strong and persistent southeast local winds as described by [Santoro et al. \(2013\)](#). These events may build up strong currents along the coast of Montevideo with velocities of up to 1 m/s. Local winds generate waves of significant wave height of 2.5 m and periods of 5 seconds, as described by [Mosquera et al. \(2012\)](#). Currents and wave events may produce high shear stresses over the bed due to the small depths (approximately 6 m), causing the erosion and entrainment of the sediment into suspension.

Montevideo bay hosts the main passenger and cargo Uruguayan port, playing an important role in the economy of this country. With siltation rates of approximately 1 m/year (or higher when traffic is reduced), sub-aquatic sedimentation is one of the main issues the port administration has to deal with. Continuous dredging is required to maintain operational depths in the port's navigation channels and dockside areas. In early studies in the port ([INTECOSA, 1987](#)), average suspended sediment concentrations registered were from 40-70 mg/l, and maximum values measured near the bottom were 150 mg/l, indicating that suspended sediment transport is a very significant mechanism in the cohesive sediment dynamics in Montevideo bay. However, siltation rates in the navigation channels could not be explained by this mechanism alone. [Guarga et al. \(1988\)](#) hypothesize that a highly concentrated sediment layer near the bottom can be generated during strong waves outside the bay and transported landward, which explains the sediment dynamics observed

during dredging.

The Institute of Fluids Mechanics and Environmental Engineering (Instituto de Mecánica de los Fluidos e Ingeniería Ambiental - IMFIA in Spanish) has been studying hydrodynamics and sediment dynamics in Río de la Plata and Montevideo bay by field measurements (Guarga et al., 1988; Bellón, 2005), laboratory experiments (Mosquera and Pedocchi, 2012), theoretical analysis (Piedra-Cueva, 1993; Pedocchi et al., 2015) and numerical modeling (Piedra-Cueva and Fossati, 2007; Fossati et al., 2014; Santoro, 2017) over the last 30 years. The early deployments were made near Montevideo in dome-like structures placed at the bottom, with instrumentation facing upwards (Bellón and Piedra-Cueva, 2009). To ensure that the mooring structure would not move with heavy storms during three-month long deployments, it was attached to a concrete block weighing 1 ton. This method presented some technical issues, mainly the burial of the concrete block and dome in the muddy bottom, increasing the cost and difficulty of the extraction maneuver.

With scarce field data in sediment dynamics over the region (Pedocchi et al., 2012; Pedocchi and Mosquera, 2015) and based on channel infill estimations of IMFIA's numerical models in Montevideo bay, Pedocchi et al. (2015) implemented an analytical sediment transport model to predict siltation rates over future dredging procedures required for the installation of an offshore liquefied natural gas terminal. The analytical model was based on the development of a high concentrated sediment layer near the bottom. Using results of currents and waves provided by a numerical model every thirty minutes, the analytical model was calibrated by replicating the annual dredged volumes registered in the navigation channel.

One of the recent efforts in numerical modeling by (Santoro et al., 2017) indicated that the suspended fine-sediment dynamics in the estuary are strongly controlled by sediment exchange between the bed and water column, whereas inside Montevideo bay, the dynamics are controlled mainly by advection of sediment from the nearby coastal area, being the wave-induced bottom shear stress one of the main resuspension forcings. The main characteristics of the fine sediment dynamics in the Río de la Plata were reproduced by evaluating different bed-suspension sediment exchange formulations in a 3D coupled currents, wave and sediment transport numerical model. However, the results on sedimentation in the navigation channels of Montevideo bay and port area are inconsistent with reality, underestimating the observations. Santoro (2017)

concluded that the numerical model used required other transport mechanisms to properly replicate the siltation in the inner port area.

In the last few decades, the ability to measure water motion as well as cohesive and non-cohesive sediment in the field has been substantially enhanced by the development of acoustic instruments and techniques (Fugate and Friedrichs, 2002; Thorne and Hanes, 2002; Hanes, 2012; Vincent and MacDonald, 2015; Wilson and Hay, 2015; Fromant et al., 2017). IMFIA has been using acoustic techniques for a decade. The most recent effort has been a laboratory work in a wave flume (Mosquera and Pedocchi, 2012) to measure waves (Mosquera and Pedocchi, 2013) and study the liquefaction in muddy beds induced by wave action (Mosquera et al., 2014).

The main objective of this work is to acquire a better understanding of the sediment dynamics near Montevideo seabed by determining the governing transport mechanisms as well as deposition and erosion rates of the cohesive sediments. In this sense, a tripod-like structure was applied for deployment of many acoustical and optical instruments in the first meter above the muddy bottom. The deployment site was located 100 meters away from a buoy with oceanographic and meteorological instrumentation that were included to complement the unique data set. As far as the author is concerned, this was the first time that the direct observation of the presence of a highly concentrated sediment layer near Montevideo seabed has been documented, and one of the few times the phenomena has been observed around the globe (Traykovski et al., 2000, 2007; Jaramillo, 2008; Sahin et al., 2013; Safak et al., 2017).

In Chapter 2 appears an overview of the theory of bottom boundary layer dynamics under the presence of currents and waves to justify the computation of bottom shear stresses in this thesis. Entrainment rate formulations are discussed in the context of previous works in Río de la Plata estuary. A coupled Hydrodynamics and Sediment dynamics boundary layer model used to analyze some of the data collected and estimate sediment transport is also presented. Considering the instrumentation used in the field deployment, a brief overview of sound theory restricted to fluids as the propagation media is also included in Chapter 3. Acoustic backscatter inversions and instrument calibration techniques applied in this work are described as well. Chapter 4 includes the field works, deployment site, mooring strategy and instrumentation array used during both deployments. A calibration facility was built at IMFIA's workshop to do laboratory experiments with the instruments deployed. Chapter 5 includes

a series of laboratory work, with samples of sediments of the Río de la Plata estuary extracted from the bottom bed near the deployment site, with the purpose of analyzing the acoustic multi-frequency and optical field measurements. A general view of the complete data set collected during deployments is provided in Chapter 6. Estimations of waves, currents, turbulence, shear velocities and sediment transport are described in Chapter 7. The results and discussions of two of the most intense sediment dynamics events are included in Chapter 8. The conclusions and main contributions of this thesis as well as following steps and future works are summarized in Chapter 9.

Chapter 2

Bottom boundary layer dynamics

2.1 Bottom shear stresses over waves and currents

Bottom boundary layers are relevant due to the characteristics of their dynamics, that cause mass and momentum turbulent mixing. The primary exchange of particles, chemicals and organisms of the water column with the seabed occurs here. [Grant and Madsen \(1986\)](#) reviewed theoretical, field and experimental works in order to comprehend the role played by the most important processes which govern the mean and oscillating flow structure, as well as the continental shelf bottom boundary layer velocity and length scales. Under the motion of waves and currents, two different bottom boundary layer regions develop. The deepest layer thickness, also known as wave boundary layer, is proportional to the wave energy, and it ranges from 2 to 20 cm thick. In this layer, shear stresses and turbulent kinetic energy are governed by waves and currents, whereas above the wave boundary layer the influence of waves decreases.

Following the ideas used to derive the classical Reynolds-averaged Navier–Stokes equations, [Nielsen \(1992\)](#) proposes that for combined wave current flow, the velocity field \vec{v} may be expressed as

$$\begin{aligned} \vec{v} &= u\mathbf{e}_x + v\mathbf{e}_y + w\mathbf{e}_z = \dots \\ &(\bar{u} + \tilde{u} + u')\mathbf{e}_x + (\bar{v} + \tilde{v} + v')\mathbf{e}_y + (\bar{w} + \tilde{w} + w')\mathbf{e}_z, \end{aligned} \tag{2.1}$$

where u , v and w are the velocity field projections over the orthogonal basis \mathbf{e}_x , \mathbf{e}_y and \mathbf{e}_z , and $\bar{\cdot}$, $\tilde{\cdot}$ and \cdot' denote respectively the steady, wave and turbulent motion components. These transformations may be viewed as operations over the different magnitudes, decomposing the flow into three corresponding motions, currents, waves and turbulence. Some properties are required in order to preserve statistical independence between motions when applied to any scalar magnitude Φ (such as the pressure p),

$$\overline{\tilde{\Phi}} = \overline{\Phi'} = \tilde{\Phi} = \tilde{\Phi}' = 0, \quad (2.2)$$

whereas terms obtained from the product of two scalar magnitudes Φ and Ψ ,

$$\overline{\tilde{\Phi}\tilde{\Psi}} = \overline{\tilde{\Phi}\Psi'} = \overline{\tilde{\Phi}\Psi} = \overline{\tilde{\Phi}\tilde{\Psi}} = \overline{\tilde{\Phi}\Psi'} = \overline{\tilde{\Phi}\Psi} = 0. \quad (2.3)$$

Incompressibility is imposed in the mass balance of the flow

$$\nabla \cdot \vec{v} = 0, \quad (2.4)$$

being $\nabla \cdot$ the divergence operator. Applying the properties of decomposition it is possible to see that each motion component is also incompressible. This can be expressed as

$$\begin{aligned} \frac{\partial \bar{u}}{\partial x} + \frac{\partial \bar{v}}{\partial y} + \frac{\partial \bar{w}}{\partial z} &= 0, \\ \frac{\partial \tilde{u}}{\partial x} + \frac{\partial \tilde{v}}{\partial y} + \frac{\partial \tilde{w}}{\partial z} &= 0, \\ \frac{\partial u'}{\partial x} + \frac{\partial v'}{\partial y} + \frac{\partial w'}{\partial z} &= 0, \end{aligned} \quad (2.5)$$

where $\frac{\partial}{\partial x}$, $\frac{\partial}{\partial y}$ and $\frac{\partial}{\partial z}$ are the partial derivatives with respect to the horizontal x , y and vertical z spatial coordinates. Inserting Eq. 2.1 into the Navier-Stokes equation and projecting over the horizontal direction \mathbf{e}_x the following expression is obtained

$$\begin{aligned} \frac{\partial(\bar{u} + \tilde{u} + u')}{\partial t} + \vec{v} \cdot \nabla(\bar{u} + \tilde{u} + u') &= \dots \\ -\frac{1}{\rho} \frac{\partial(\bar{p} + \tilde{p} + p')}{\partial x} + \nu \Delta(\bar{u} + \tilde{u} + u'), \end{aligned} \quad (2.6)$$

where $\frac{\partial}{\partial t}$ is the partial derivative respect to time t , ρ and ν are the density and

kinematic viscosity of the fluid, and ∇ and Δ are the gradient and Laplace operators respectively. From Eq. 2.5, the steady transformation of Eq. 2.6 becomes

$$\begin{aligned} \frac{\partial \bar{u}^2}{\partial x} + \frac{\partial \bar{u}\bar{v}}{\partial y} + \frac{\partial \bar{u}\bar{w}}{\partial z} + \frac{\partial \bar{u}^2}{\partial x} + \frac{\partial \bar{u}\bar{v}}{\partial y} + \frac{\partial \bar{u}\bar{w}}{\partial z} + \frac{\partial \bar{u}^2}{\partial x} + \frac{\partial \bar{u}'v'}{\partial y} + \frac{\partial \bar{u}'w'}{\partial z} \dots \\ = -\frac{1}{\rho} \frac{\partial \bar{p}}{\partial x} + \nu \left(\frac{\partial^2 \bar{u}}{\partial x^2} + \frac{\partial^2 \bar{u}}{\partial y^2} + \frac{\partial^2 \bar{u}}{\partial z^2} \right), \end{aligned} \quad (2.7)$$

whereas for the wave transformation it becomes

$$\begin{aligned} \frac{\partial \tilde{u}}{\partial t} + 2 \frac{\partial \tilde{u}\tilde{u}}{\partial x} + \frac{\partial(\tilde{u}\tilde{v} + \tilde{u}\tilde{v})}{\partial y} + \frac{\partial(\tilde{u}\tilde{w} + \tilde{u}\tilde{w})}{\partial z} + \frac{\partial \tilde{u}^2}{\partial x} + \frac{\partial \tilde{u}\tilde{v}}{\partial y} + \frac{\partial \tilde{u}\tilde{w}}{\partial z} + \dots \\ \frac{\partial \tilde{u}^2}{\partial x} + \frac{\partial \tilde{u}'v'}{\partial y} + \frac{\partial \tilde{u}'w'}{\partial z} = -\frac{1}{\rho} \frac{\partial \tilde{p}}{\partial x} + \nu \left(\frac{\partial^2 \tilde{u}}{\partial x^2} + \frac{\partial^2 \tilde{u}}{\partial y^2} + \frac{\partial^2 \tilde{u}}{\partial z^2} \right). \end{aligned} \quad (2.8)$$

To obtain an analytical solution that provides a qualitative description of the flow, [Grant and Madsen \(1979\)](#) propose a very idealized boundary layer. They assume horizontal homogeneity of the steady motion and simple bottom topography. No-slip boundary conditions at the bottom imposed in the mass balance (Eq. 2.5), imply that $\bar{w} = 0$. Reorganizing the terms that account for the momentum flux in the vertical direction, yields an expression of the shear stress of the steady motion $\overline{\tau_{xz}}$ as

$$\overline{\tau_{xz}} = \rho\nu \frac{\partial \bar{u}}{\partial z} - \overline{\rho\tilde{u}\tilde{w}} - \overline{\rho u'w'}, \quad (2.9)$$

and of the shear stress of the wave motion $\widetilde{\tau_{xz}}$ as

$$\widetilde{\tau_{xz}} = \rho\nu \frac{\partial \tilde{u}}{\partial z} - \rho\tilde{u}\tilde{w} - \rho\tilde{u}\tilde{w} - \rho\tilde{u}'w'. \quad (2.10)$$

The shear stresses in the \mathbf{e}_y direction $\overline{\tau_{yz}}$ and $\widetilde{\tau_{yz}}$ are obtained similarly.

Using a quadratic drag law to scale the instantaneous shear stress in the wave-current boundary layer, [Grant and Madsen \(1979\)](#) identify two regions: inside the wave boundary layer ($z < \delta_{wc}$) where turbulence intensity is governed by both current and waves; and outside the wave boundary layer ($z > \delta_{wc}$) where turbulence production is associated to current only. Therefore [Grant and Madsen \(1979\)](#) propose a two layer eddy viscosity model to close

Eqs. 2.7 and 2.8. The proposed closure for the shear stresses is

$$\overline{\tau_{xz}} = \rho\nu_T \frac{\partial \bar{u}}{\partial z}, \quad \overline{\tau_{yz}} = \rho\nu_T \frac{\partial \bar{v}}{\partial z}, \quad (2.11)$$

$$\widetilde{\tau_{xz}} = \rho\nu_T \frac{\partial \tilde{u}}{\partial z}, \quad \widetilde{\tau_{yz}} = \rho\nu_T \frac{\partial \tilde{v}}{\partial z}, \quad (2.12)$$

where the time-invariant eddy viscosity ν_T is defined in each layer as

$$\nu_T = \begin{cases} \kappa u_{*r} z & \text{for } z < \delta_{wc} \\ \kappa u_{*c} z & \text{for } z > \delta_{wc}, \end{cases} \quad (2.13)$$

κ is von Karman's coefficient ($= 0.41$), u_{*c} and u_{*r} are the current and combined wave-current shear velocities and δ_{wc} is the height of the wave boundary layer. In order to consider irregular waves Madsen (1994) extends this analytical model.

Current motion solution

Madsen (1994) hypothesize that Eq. 2.7 can be rewritten as

$$0 = \frac{\partial \overline{\tau_{xz}}}{\partial z} = \frac{\partial}{\partial z} \left[\rho\nu_T \frac{\partial \bar{u}}{\partial z} \right]. \quad (2.14)$$

Using the law of the wall arguments established in Nezu and Nakagawa (1993) and defining the current velocity field u_c

$$u_c = \bar{u} \mathbf{e}_x + \bar{v} \mathbf{e}_y = |u_c| (\cos \theta_c \mathbf{e}_x + \sin \theta_c \mathbf{e}_y), \quad (2.15)$$

the solution of the velocity profile $|u_c|$ is

$$\begin{aligned} |u_c| &= \frac{u_{*c}^2}{\kappa u_{*r}} \log \frac{z}{z_0} & \text{for } z < \delta_{wc}, \\ |u_c| &= \frac{u_{*c}}{\kappa} \log \frac{z}{z_{0a}} & \text{for } z > \delta_{wc}, \end{aligned} \quad (2.16)$$

where z_0 is the hydrodynamic roughness and z_{0a} is the apparent bottom roughness experienced by the current produced by of the waves

$$\log \frac{\delta_{wc}}{z_{0a}} = \frac{u_{*c}}{u_{*r}} \log \frac{\delta_{wc}}{z_0}. \quad (2.17)$$

This solution assumes a constant steady shear stress $\bar{\tau}$

$$\bar{\tau} = \bar{\tau}_{xz}\mathbf{e}_x + \bar{\tau}_{yz}\mathbf{e}_y = |\bar{\tau}|(\cos\theta_c\mathbf{e}_x + \sin\theta_c\mathbf{e}_y), \quad (2.18)$$

with $|\bar{\tau}| = \rho u_{*c}^2$.

A value of 3 mm for the bottom roughness characteristic dimension k_N in Montevideo bay was proposed by [Fossati \(2013\)](#) and [Santoro \(2017\)](#) and used here as well. For this value the flow becomes hydraulically rough with shear velocities over 2 cm/s (moderate waves and currents), and the expression $z_0 = k_N/30$ may be used to determine the hydrodynamic roughness.

Wave motion solution

Also, Eq. 2.8 can be rewritten as

$$\frac{\partial \tilde{u}}{\partial t} = -\frac{1}{\rho} \frac{\partial \tilde{p}}{\partial x} + \frac{\partial}{\partial z} \left[\rho \nu_T \frac{\partial \tilde{u}}{\partial z} \right], \quad (2.19)$$

and by defining wave velocity field as

$$u_w = \tilde{u}\mathbf{e}_x + \tilde{v}\mathbf{e}_y, \quad (2.20)$$

the wave motion is governed by

$$\frac{\partial u_w}{\partial t} = -\frac{1}{\rho} \frac{\partial \tilde{p}}{\partial x} \mathbf{e}_x - \frac{1}{\rho} \frac{\partial \tilde{p}}{\partial y} \mathbf{e}_y + \frac{\partial}{\partial z} \left[\rho \nu_T \frac{\partial u_w}{\partial z} \right]. \quad (2.21)$$

Outside the wave boundary layer the wave motion can be assumed to be irrotational, leading to the solution provided in Airy linear wave theory u_A ,

$$\frac{\partial u_A}{\partial t} = -\frac{1}{\rho} \frac{\partial \tilde{p}}{\partial x} \mathbf{e}_x - \frac{1}{\rho} \frac{\partial \tilde{p}}{\partial y} \mathbf{e}_y \quad \text{for } z > \delta_{wc}. \quad (2.22)$$

When having an irregular wave field, linear decomposition may be applied and u_A can be obtained as

$$u_A = \sum_{n=1}^N \sum_{m=1}^M u_{Anm}, \quad (2.23)$$

where u_{Anm} is the monochromatic wave component of the n -th frequency and m -th direction.

Also, Eq. 2.21 in $z < \delta_{wc}$ is

$$\frac{\partial u_w}{\partial t} = -\frac{1}{\rho} \frac{\partial \tilde{p}}{\partial x} \mathbf{e}_x - \frac{1}{\rho} \frac{\partial \tilde{p}}{\partial y} \mathbf{e}_y + \frac{\partial}{\partial z} \left[\rho \kappa u_{*r} z \frac{\partial u_w}{\partial z} \right], \quad (2.24)$$

with the pressure gradient imposed by the external flow u_A . The velocity defect $u_w - u_A$ is governed by

$$\frac{\partial(u_w - u_A)}{\partial t} = \frac{\partial}{\partial z} \left[\rho \kappa u_{*r} z \frac{\partial(u_w - u_A)}{\partial z} \right], \quad (2.25)$$

leading to a solution that can be written as

$$u_w = \sum_{n=1}^N \sum_{m=1}^M u_{wnm}, \quad (2.26)$$

where u_{wnm} is obtained from the real part of

$$u_{wnm} = \left[1 - \frac{\ker 2\sqrt{\zeta_n} + \text{kei} 2\sqrt{\zeta_n}}{\ker 2\sqrt{\zeta_{n0}} + \text{kei} 2\sqrt{\zeta_{n0}}} \right] u_{Anm} e^{i\omega_n t}, \quad (2.27)$$

\ker and kei denote the zeroth order Kelvin functions,

$$\zeta_n = \frac{z\omega_n}{\kappa u_{*r}}, \quad (2.28)$$

ζ_{n0} the value of ζ_n at $z = z_0$, u_{Anm} the near bottom orbital velocity, ω_n the n -th wave angular frequency.

Each wave component has a bottom shear stress $\widetilde{\tau_{bnm}}$ that can be obtained by evaluating the real part of

$$\widetilde{\tau_{bnm}} = -\rho \kappa u_{*r} \sqrt{\zeta_{n0}} \frac{\ker' 2\sqrt{\zeta_{n0}} + \text{kei}' 2\sqrt{\zeta_{n0}}}{\ker 2\sqrt{\zeta_{n0}} + \text{kei} 2\sqrt{\zeta_{n0}}} \widetilde{u_{bnm}} e^{i\omega_n t}, \quad (2.29)$$

in which \ker' and kei' are the derivatives of \ker and kei respectively. The total bottom shear stress of the wave motion $\widetilde{\tau_b}$ can be obtained as

$$\widetilde{\tau_b} = \sum_{n=1}^N \sum_{m=1}^M \widetilde{\tau_{bnm}}. \quad (2.30)$$

Reducing the wave bottom shear stress $\widetilde{\tau_b}$ to a representative amplitude

vector

$$\tilde{\tau}_b = |\tilde{\tau}_b|(\cos \theta_w \mathbf{e}_x + \sin \theta_w \mathbf{e}_y)e^{i\omega_r t} \quad (2.31)$$

that oscillates with a representative angular frequency ω_r , the combined wave-current shear velocity u_{*r} can be obtained by the equation

$$\rho u_{*r}^2 = ||\tilde{\tau}_b|(\cos \theta_w \mathbf{e}_x + \sin \theta_w \mathbf{e}_y) + \bar{\tau}|. \quad (2.32)$$

The wave boundary layer height δ_{wc} is determined by the equation

$$\delta_{wc} = 2 \frac{\kappa u_{*r}}{\omega_r} \quad (2.33)$$

when turbulent ($u_A^2/\omega_r \nu > 10^5$), or $\delta_{wc} = k_N$ otherwise.

Nichols (2005) implements in a MatLab code, the convergent iteration procedure proposed by Madsen (1994) in order to obtain u_{*c} , u_{*r} and δ_{wc} when current and wave motion are specified at certain reference level.

2.2 Sediment dynamics

With the action of waves, significant amounts of sediment particles are eroded from the bed and entrained into the water column and thus may be transported by currents. At currents and wave motion over certain intensity, self-stratification induced by suspended sediments may modify the near bottom hydrodynamics, reducing the turbulent fluxes.

Sediment mass conservation may be expressed as

$$\frac{\partial c}{\partial t} + \nabla \cdot (c \vec{v}_s) = 0, \quad (2.34)$$

where c is the sediment mass concentration, —that equals to the mass of sediments in a sediment-water sample divided by the total volume of the sample—, and \vec{v}_s is the sediment velocity. In some literature, volume concentration ϵ , —the ratio between volume of sediments divided by the total volume—, is used instead of c . Both parameters can be related by the equation $c = \rho_s \epsilon$ in terms of the sediment density ρ_s . For certain ranges of sediment size and density, it is frequent to assume that the difference between the velocity of the sediment and its surrounding fluid is equal to the terminal fall velocity in

quiescent water $-w_s \mathbf{e}_z$,

$$\vec{v}_s = \vec{v} - w_s \mathbf{e}_z. \quad (2.35)$$

On the other hand, applying the same decomposition proposed for Eq. 2.1, Eq. 2.34 for the steady component becomes

$$\frac{\partial \bar{c}}{\partial t} + \frac{\partial(\bar{c}\bar{u} + \overline{c'u'})}{\partial x} + \frac{\partial(\bar{c}\bar{v} + \overline{c'v'})}{\partial y} + \frac{\partial(\bar{c}\bar{w} + \overline{c'w'} - \bar{c}w_s)}{\partial z} = 0, \quad (2.36)$$

where the terms $\overline{c'u'}$, $\overline{c'v'}$ and $\overline{c'w'}$ represent the sediment fluxes due to turbulence, also known as Reynold sediment fluxes. Using the mass balance of the steady motion (Eq. 2.5) Eq. 2.36 becomes

$$\frac{\partial \bar{c}}{\partial t} + \bar{c} \frac{\partial \bar{u}}{\partial x} + \bar{c} \frac{\partial \bar{v}}{\partial y} + \bar{c} \frac{\partial \bar{w}}{\partial z} = \frac{d\bar{c}}{dt} = -\frac{\partial \overline{c'u'}}{\partial x} - \frac{\partial \overline{c'v'}}{\partial y} - \frac{\partial(\overline{c'w'} - \bar{c}w_s)}{\partial z}, \quad (2.37)$$

where the term $\frac{d\bar{c}}{dt}$ represents the total derivative of the mean concentration in the steady motion component. Assuming equilibrium and horizontal homogeneity, Eq. 2.37 may be simplified as

$$\frac{\partial(\overline{c'w'} - \bar{c}w_s)}{\partial z} = 0, \quad (2.38)$$

that can be integrated into

$$\overline{c'w'} - \bar{c}w_s = \bar{F}_{sz}, \quad (2.39)$$

where \bar{F}_{sz} is the net vertical sediment flux (García, 2008). A common closure to represent the Reynold sediment flux, as with the $\overline{u'w'}$ flux in Section 2.1, is

$$\overline{c'w'} = -\nu_{T_m} \frac{\partial \bar{c}}{\partial z}, \quad (2.40)$$

with ν_{T_m} being the turbulent sediment diffusivity. It is commonly assumed that the structure of ν_{T_m} is proportional to the eddy viscosity ν_T , being σ the ratio between ν_T and ν_{T_m} a constant order unity over the whole water column. Based on a laboratory work by Coleman (1970), Rijn (1984) proposes an expression to predict the value of σ as a function of the relation between

the terminal fall velocity and shear velocity

$$\sigma = \left(1 + 2 \left(\frac{w_s}{u_*} \right)^2 \right)^{-1}. \quad (2.41)$$

When w_s is large enough, particle inertia biases the trajectories increasing the effective mixing, and σ can be lower than one. For small (or neutrally buoyant) particles, i.e. small fall velocities as expected in Río de la Plata suspended sediments, the particle has an appropriate response to velocity fluctuations with values of $\sigma \simeq 1$.

2.2.1 Boundary condition.

Just above the bed $z = a$, as proposed by Eq. 2.39, the net sediment flux $\overline{F}_{sz}|_{z=a}$ must equal the eroded entrainment rate E minus the deposition flux $\bar{c}w_s$. Using the condition that the sediment transport is in equilibrium

$$E = \bar{c}w_s|_{z=a}, \quad (2.42)$$

several authors express the entrainment rate as a bed concentration \bar{c}_a , by dividing E between $w_s|_{z=a}$.

Experiments on cohesive sediment erosion were conducted by Partheniades (1962, 1965) in a laboratory flume. Several beds were prepared using natural sediment from San Francisco Bay at the bottom of a recirculating flume. Flow velocity was increased (consequently bottom shear stress τ_b) in steps, each step hundreds of hours long. After reaching the equilibrium in each step, suspended sediment concentration was measured over time and the entrainment rate E was estimated. Ariathurai (1974) used a straight line to approximate the trend of Partheniades (1962) experiments, resulting in the so-called Ariathurai-Partheniades equation

$$E = e_{AP}(\tau_b - \tau_s), \quad (2.43)$$

with e_{AP} the slope and τ_s the root interpreted as a bed shear strength. The values in Ariathurai (1974) for San Francisco bay mud were $e_{AP} = 7.4 \times 10^{-6}$ s/m and $\tau_s = 0.33$ Pa.

On the other hand, by analyzing the non-cohesive sediment dynamics of

the bedload, [Yalin \(1963\)](#) proposes that the concentration near the bed \bar{c}_a must be a function \mathcal{F} of the form

$$\bar{c}_a = \mathcal{F}(c_0, \rho_s - \rho, g, 2a_s, \tau_b - \tau_{cr}), \quad (2.44)$$

where c_0 is the concentration of the seabed, $\rho_s - \rho$ the submerged density of the sediment, g the acceleration due to gravity, $2a_s$ the sediment grain size and $\tau_b - \tau_{cr}$ the excess of shear stress at the bed with τ_b the bottom shear stress amplitude and τ_{cr} the shear stress to sediment transport initiation. After applying the Buckingham theorem dependence may be reduced to a function \mathcal{G} , in the following manner

$$\bar{c}_a = c_0 \mathcal{G} \left(\frac{\tau_b - \tau_{cr}}{(\rho_s - \rho)g2a_s} \right). \quad (2.45)$$

[Yalin \(1963\)](#) proposes a linear function for \mathcal{G} leading to

$$\bar{c}_a = c_0 \vartheta \frac{(\tau_b - \tau_{cr})}{(\rho_s - \rho)g2a_s}, \quad (2.46)$$

with ϑ a dimensionless constant value. This function is commonly expressed in terms of the dimensionless excess of shear stress $s = (\tau_b - \tau_{cr})/\tau_{cr}$

$$\bar{c}_a = \frac{c_0 \gamma_0}{\tau_{cr}} (\tau_b - \tau_{cr}) = c_0 \gamma_0 s, \quad (2.47)$$

where $\gamma_0 = \vartheta \theta_{cr}$, and θ_{cr} is the critical Shields value in his honor ([Shields, 1936](#))

$$\theta_{cr} = \frac{\tau_{cr}}{(\rho_s - \rho)g2a_s}. \quad (2.48)$$

In Eq. 2.47 when $\gamma_0 s > 1$, \bar{c}_a can be larger than c_0 , thus the concentration above the bed would be larger than that in the seabed. This issue latter seen by the same author ([Yalin, 1972](#)) was solved by [Smith and McLean \(1977b\)](#) by dividing between $1 + \gamma_0 s$ leading to the entrainment formula of Smith and McLean

$$\bar{c}_a = \frac{c_0 \gamma_0 s}{1 + \gamma_0 s}. \quad (2.49)$$

The resemblance between Equations 2.43 and 2.47 previously reported by [Mehta](#)

(2013) is very remarkable. In order to obtain estimates for some parameters appearing on both expressions, the following relations are assumed

$$\begin{aligned} \tau_{cr} &= \tau_s, \\ \frac{c_0 \gamma_0}{\tau_{cr}} &= \frac{e_{AP}}{w_s|_{z=a}}. \end{aligned} \quad (2.50)$$

As part of the EuroStrataform project in the Po delta near the Adriatic sea sediment concentrations were registered using multi-frequency acoustic measurements during large wave events (Traykovski et al., 2007). A one-dimensional model was implemented to study the sediment fluxes, and the entrainment parameters of Eq. 2.49 used there were $c_0 = 530 \text{ kg/m}^3$, $\gamma_0 = 0.002$, $\tau_{cr} = 0.1 \text{ Pa}$. Estimates for $w_s|_{z=a}$ cannot be deduced from that work, but the expression by Wolanski et al. (1989) for flocculation and hindered settling fall velocities for concentrations near c_0 to have an order of magnitude ($w_s|_{z=a} = 1 \times 10^{-6} \text{ m/s}$), the Ariathurai-Partheniades slope parameter is $e_{AP} \sim 10 \times 10^{-6} \text{ s/m}$ in opposition to $7.4 \times 10^{-6} \text{ s/m}$ for San Francisco Bay muds obtained in laboratory experiments by Partheniades (1962). The value of $\gamma_0 = 2 \times 10^{-3}$ used by Traykovski et al. (2007) is relatively close to 1.95×10^{-3} as proposed by Smith and McLean (1977b) for bedloads of fine sands. One common factor between laboratory experiments by Partheniades (1962) and field works by Traykovski et al. (2007) is that values for the dimensionless excess of shear stress s times γ_0 are lower than 0.12, correcting \bar{c}_a by a factor of 0.9 when applying the Eq. 2.49.

Fossati (2013) implemented a numerical model of Río de la Plata estuary, where calibration with data collected in field works yields to $E = 4 \times 10^{-6} \text{ kg/m}^2\text{s}$ and $\tau_{ce} = 0.1 \text{ Pa}$, which indicate that $e_{AP} = 40 \times 10^{-6} \text{ s/m}$. Alternatively, after calibrating a 2D (3D) numerical model near Montevideo Bay, Santoro (2017) yields $E = 3 \times 10^{-6} \text{ kg/m}^2\text{s}$ ($E = 30 \times 10^{-6} \text{ kg/m}^2\text{s}$) and $\tau_{ce} = 0.15 \text{ Pa}$, which indicate that $e_{AP} = 20 \times 10^{-6} \text{ s/m}$ ($e_{AP} = 200 \times 10^{-6} \text{ s/m}$).

2.3 Hydrodynamics and Sediment dynamics

By coupling sediment mass conservation and Navier-Stokes equation using eddy diffusivity closure, Glenn and Grant (1987) propose an extension of the hydrodynamic model by Grant and Madsen (1979) presented in Chapter 2.1

in order to predict vertical profiles of suspended sediment concentration and sediment transport. The analytical solutions of steady motion show the importance of self-stratification when there are fine sediments during storms explained by wave related entrainment. Vertical density gradients (caused by temperature, salinity and/or suspended sediments) may modify vertical mixing, deeply affecting boundary-layer turbulence. The usual tendency is for smaller densities to overlie higher densities. This stabilizes the flow and decreases turbulence due to the work required to vertically move portions of fluids in the stratified flow, and diffusion decreases.

Smith and McLean (1977b) propose a closure formulation for self-stratification effects with suspended sediments. A first order approximation of turbulence kinetic energy dissipation in presence of suspended sediment (McLean, 1992), indicates that eddy viscosity ν_T may be expressed as

$$\nu_T = \frac{\nu_{TN}}{1 + \gamma\zeta}, \quad (2.51)$$

being ν_{TN} the eddy viscosity in the case without sediment, also called neutral case, γ a dimensionless constant roughly equal to 5 and ζ a stratification parameter defined as

$$\zeta = \frac{z}{L} = \frac{\nu_{TN}}{u_*^4} \frac{g}{\rho_m} \overline{\rho'_m w'}, \quad (2.52)$$

being L the Monin-Obukov length, u_* a characteristic shear velocity and ρ_m the density of the water and sediment mixture given by $\rho_m = \rho + (1 - \rho/\rho_s)c$. ζ is interpreted by Glenn and Grant (1987) as the ratio between the buoyancy induced absorption of turbulent kinetic energy and the production of turbulent kinetic energy and McLean (1992) related it with the gradient Richardson number

$$Ri_g = \frac{(\sigma + \beta\zeta)\zeta}{(1 + \gamma\zeta)^2}, \quad (2.53)$$

with σ and β dimensionless parameters that allow to relate the eddy diffusivity of mass ν_{Tm} with the eddy viscosity under neutral conditions ν_{TN}

$$\nu_{Tm} = \frac{\nu_{TN}}{\sigma + \beta\zeta}. \quad (2.54)$$

When the production dominates over the buoyancy absorption, ζ is small having little effect on eddy viscosity. If buoyancy induced absorption dominates, large values of ζ reduce the eddy viscosity, inhibiting the vertical turbulent transports. No universal values are available for σ , β and γ , but the first one appears to be near 1 and the last two near 5. [Trowbridge and Lentz \(2018\)](#) review different approaches in the studies of stratification effects. Based on the theory of linear stability, the Miles-Howard theorem establishes that instabilities requires gradient Richardson number Ri_g to be less than 0.25. Theoretical considerations have shown that when Ri_g is over 0.25, mixing is significantly damped by stratification. Studies on atmospheric circulation established the Monin-Obukhov similarity theory which defines the stability parameter ζ . [Trowbridge and Lentz \(2018\)](#) indicate that those different approaches are consistent with each other, and replicate the different asymptotic regimes as well.

The discontinuity of the eddy viscosity at the top of the wave boundary layer, represented in the hydrodynamic model by [Grant and Madsen \(1979\)](#) (Eq. 2.13), may be problematic when attempting to obtain suspended sediment profiles. By running a series of laboratory experiments in a water tunnel with measurements in the wave boundary layer, [Lundgren \(1972\)](#) identified different zones where the turbulent interaction between waves and currents varies. [Fredsoe and Deigaard \(1992\)](#) summarize these regions into three: the upper zone $z_2 < z$, where turbulence is totally dominated by the current; the intermediate or transition zone $z_1 < z < z_2$ where the turbulent viscosity produced by waves gradually increase with depth; and the lower zone $z_0 < z < z_1$, where wave turbulence production is significantly larger. By generalizing the laboratory experiments in pure wave motion, [Lundgren \(1972\)](#) proposes a formulation for the average eddy viscosity with linear increasing near the bed and an exponential decrease as the top of the wave boundary layer is reached. In order to produce analytical solutions, [Glenn \(1983\)](#) simplifies the combined eddy viscosity suggested by [Lundgren \(1972\)](#) with the following formula

$$\nu_{TN} = \begin{cases} \kappa u_{*r} z & \text{for } z_0 < z < z_1 \\ \kappa u_{*r} z_1 & \text{for } z_1 < z < z_2 \\ \kappa u_{*c} z & \text{for } z_2 < z, \end{cases} \quad (2.55)$$

with z_1 and z_2 defining the lower and upper boundaries of the transition layer

where the eddy viscosity is constant. Continuity of ν_{TN} indicates that $z_2 = z_1 u_{*r}/u_{*c}$ and z_1 is proportional to the height of the wave boundary layer δ_{wc} ($z_1 = \alpha_G \delta_{wc}$). [Madsen and Wikramanayake \(1991\)](#) use α_G as a free fitting parameter to conclude that a single value fits all the data for current profiles in case of co-directional waves and currents. When waves and currents coexist at a certain angle, no predictor for α_G has been developed yet ([Styles et al., 2017](#)), but certain boundaries are established ($0 < \alpha_G < 1$).

This closure and other three different models (being one of them [Grant and Madsen \(1979\)](#)) were later compared by [Madsen and Wikramanayake \(1991\)](#) with data from laboratory experiments. One of the conclusions the referred work was that although the model by [Grant and Madsen \(1979\)](#) was very successful, the discontinuous eddy viscosity resulted in a poor representation of the velocity at the top of the wave boundary layer, and the model by [Glenn \(1983\)](#) was more appropriate. Based on the suspended sediment stratification model by [Glenn and Grant \(1987\)](#) and continuous time invariant turbulent eddy viscosity parametrization by [Glenn \(1983\)](#), [Styles and Glenn \(2000\)](#) propose an analytical solution for sediment transport in the wave-current boundary layer.

2.3.1 Current and Suspended sediment concentration solution.

Using the stratified eddy viscosity Eq. 2.51, [Styles and Glenn \(2000\)](#) arrive to the following solutions for the currents u_c and suspended sediment concentration c in each layer

$$u_c = \begin{cases} \frac{u_{*c}^2}{\kappa u_{*r}} \left[\ln(z/z_0) + \gamma \int_{z_0}^z 1/Ldz \right] & \text{for } z_0 < z < z_1 \\ \frac{u_{*c}^2}{\kappa u_{*r}} \left[\frac{z-z_1}{z_1} + \frac{\gamma}{z_1} \int_{z_1}^z z/Ldz \right] + u_c|_{z=z_1} & \text{for } z_1 < z < z_2 \\ \frac{u_{*c}}{\kappa} \left[\ln(z/z_2) + \gamma \int_{z_2}^z 1/Ldz \right] + u_c|_{z=z_2} & \text{for } z_2 < z, \end{cases} \quad (2.56)$$

$$c = \begin{cases} \bar{c}_a (z/z_0)^{-w_s/\kappa u_{*r}} e^{-\gamma w_s/\kappa u_{*r}} e^{\int_{z_0}^z 1/Ldz} & \text{for } z_0 < z < z_1 \\ c|_{z=z_1} e^{-w_s(z-z_1)/\kappa u_{*r} z_1} e^{-\gamma w_s/\kappa u_{*r} z_1} e^{\int_{z_1}^z z/Ldz} & \text{for } z_1 < z < z_2 \\ c|_{z=z_2} (z/z_2)^{-w_s/\kappa u_{*c}} e^{-\gamma w_s/\kappa u_{*c}} e^{\int_{z_2}^z 1/Ldz} & \text{for } z_2 < z. \end{cases} \quad (2.57)$$

The concentration near the bed \bar{c}_a may be calculated with the Eq. 2.49 using the bottom shear stress determined with the Grant and Madsen model presented in Section 2.1. Styles and Glenn (2000) state that the difference $\Delta\tilde{\tau}$ between the shear stress for waves in neutral case and with stratification may be written as

$$\Delta\tilde{\tau} = \nu_{TN} \frac{\partial u_w}{\partial z} \left[1 - \frac{1}{1 + \gamma\zeta} \right]. \quad (2.58)$$

Even with strong stratification, the stability parameter ζ near the bed is small, so the wave bottom shear stress is adequately prescribed with the Grant and Madsen model.

The author would like to thank Richard Styles for facilitating a MatLab code for stratified velocity and concentration profiles calculation. The code developed in this thesis for sediment transport estimations was based on this software.

Chapter 3

Hydroacoustics applied to sediment transport measurements

3.1 Linear theory

The sound is an oscillatory phenomenon, whose waves propagate due to the compressibility of the medium. Based on their frequency values, waves may be classified into infra-sound waves, with frequencies below 20 Hz; acoustic waves, with frequencies in the audible range from 20 Hz to 20 kHz; and ultrasound waves, with frequencies above 20 kHz. The frequencies of the instrumentation used in this work are in the range between 0.1 and 10 MHz within in the ultrasonic range.

Considering a Newtonian compressible fluid, mass conservation (Eq. 3.1), momentum equation under no force field (Eq. 3.2) and a linear barotropic constitutive law (Eq. 3.3) (Morse and Ingard, 1987) can be written as

$$\frac{d\rho}{dt} + \rho \nabla \cdot \vec{v} = 0, \quad (3.1)$$

$$\frac{d\vec{v}}{dt} = -\frac{1}{\rho} \nabla p + \frac{(\lambda + \mu)}{\rho} \nabla (\nabla \cdot \vec{v}) + \frac{\mu}{\rho} \Delta \vec{v}, \quad (3.2)$$

$$p - p_{eq} = c_s^2 (\rho - \rho_{eq}), \quad (3.3)$$

where $\frac{d\Phi}{dt}$ represents the variation on time of the fluid particles of a generic variable Φ (also equivalent to $\frac{\partial \Phi}{\partial t} + \vec{v} \cdot \nabla \Phi$), \vec{v} is the velocity, ρ the fluid density,

∇ the gradient operator, p the fluid pressure, λ the volume viscosity, μ the shear viscosity, $\nabla \cdot$ the divergence operator, Δ the Laplacian operator, p_{eq} and ρ_{eq} equilibrium pressure and density, and c_s the speed of sound. c_s can be related to the bulk modulus constant K as (2.15 GPa for water and 2.34 GPa for seawater) $c_s = \sqrt{K/\rho}$ (which produces sound speeds of 1465 m/s for water and 1530 m/s for seawater).

With a first order approximation for small-amplitude sound waves in a fluid at rest, pressure, density and velocity may be written as

$$p = p_0 + p_1, \rho = \rho_0 + \rho_1, \vec{v} = \vec{0} + \vec{v}_1, \quad (3.4)$$

where $_0$ represents the zero order and $_1$ the first order solutions. It can be seen that p_0 and ρ_0 are constant. So the first order equations are

$$\frac{\partial \rho_1}{\partial t} + \rho_0 \nabla \cdot \vec{v}_1 = 0, \quad (3.5)$$

$$\frac{\partial \vec{v}_1}{\partial t} = -\frac{1}{\rho_0} \nabla p_1 + \frac{(\lambda + \mu)}{\rho_0} \nabla (\nabla \cdot \vec{v}_1) + \frac{\mu}{\rho_0} \Delta \vec{v}_1, \quad (3.6)$$

$$p_1 = c_s^2 \rho_1. \quad (3.7)$$

Applying the divergence to Eq. 3.6 and substituting with 3.5 and 3.7 the following expression can be found

$$\frac{1}{c_s^2} \frac{\partial^2 p_1}{\partial t^2} = \Delta p_1 + \frac{(\lambda + 2\mu)}{\rho_0 c_s^2} \frac{\partial \Delta p_1}{\partial t}. \quad (3.8)$$

Searching solutions for the wave function p_1 of the form

$$p_1(x, y, z, t) = A(x, y, z)T(t), \quad (3.9)$$

Eq. 3.8 may be rewritten as

$$\frac{1}{c_s^2 T} \frac{\partial^2 T}{\partial t^2} = \frac{\Delta A}{A} + \frac{1}{\omega_0} \frac{\Delta A}{A} \frac{1}{T} \frac{\partial T}{\partial t}, \quad (3.10)$$

with

$$\omega_0 = \frac{\rho_0 c_s^2}{(\lambda + 2\mu)}. \quad (3.11)$$

When having mono frequency motion $T = e^{i\omega t}$ the wave equation is reduced

to (a Helmholtz equation with loss)

$$\Delta A + \mathbf{k}^2 A = 0, \quad (3.12)$$

due to the fact that the wave number \mathbf{k} is complex

$$\mathbf{k} = \frac{\omega}{c_s \left(1 + i \frac{\omega}{\omega_0}\right)^{\frac{1}{2}}} = k - i\alpha_{w\nu}. \quad (3.13)$$

In water $\omega_0 \approx 10^{12} s^{-1}$ resulting in $\omega/\omega_0 < 10^{-2}$ for frequencies below 10 MHz. In this range, k and $\alpha_{w\nu}$ may be approximated as

$$\alpha_{w\nu} = \frac{\omega}{c_s} \frac{1}{\sqrt{2}} \left[\frac{\sqrt{1 + \left(\frac{\omega}{\omega_0}\right)^2} - 1}{1 + \left(\frac{\omega}{\omega_0}\right)^2} \right]^{\frac{1}{2}} \approx \frac{\omega}{2c_s} \frac{\omega}{\omega_0}, \quad (3.14)$$

$$k = \frac{\omega}{c_s} \frac{1}{\sqrt{2}} \left[\frac{\sqrt{1 + \left(\frac{\omega}{\omega_0}\right)^2} + 1}{1 + \left(\frac{\omega}{\omega_0}\right)^2} \right]^{\frac{1}{2}} \approx \frac{\omega}{c_s} \left[1 - \frac{3}{8} \left(\frac{\omega}{\omega_0}\right)^2 \right]. \quad (3.15)$$

Equation 3.15 shows that wave numbers may be conveniently approximated with $k = \omega/c_s$. As Eq. 3.14 shows, the viscosity absorption coefficient for water $\alpha_{w\nu}$ scales with the square of the frequency.

In the case of spherical waves with spherical symmetry, Eq. 3.12 can be written as

$$\frac{1}{r} \frac{\partial^2(rA)}{\partial r^2} + \mathbf{k}^2 A = 0, \quad (3.16)$$

where r is the distance to the origin. The solution with physical interpretation for Eq. 3.16 is

$$A = \frac{P_1}{r} e^{-i\mathbf{k}r}, \quad (3.17)$$

and reconstructing the field pressure p_1

$$p_1 = \frac{P_1}{r} e^{i(\omega t - \mathbf{k}r)}, \quad (3.18)$$

where P_1 is a complex number whose modulus can be interpreted as the reference pressure amplitude p_{ref} at a certain distance from the origin r_0 , times r_0 . The argument of P_1 refers to the shift of the coordinate time reference frame and the phase of the acoustic wave. The other variables of interest are then

$$\rho_1 = \frac{P_1}{c_s^2 r} e^{i(\omega t - kr)}, \quad (3.19)$$

$$\vec{v}_1 = \frac{P_1 \omega}{\rho_0 c_s^2} e^{i(\omega t - kr)} \left(\frac{\mathbf{k}r - i}{(\mathbf{k}r)^2} \right) \mathbf{e}_r, \quad (3.20)$$

where \mathbf{e}_r is the radial versor. For long distances from the source, where $rk \gg 1$, the velocity field can be approximated as

$$\vec{v}_1 = \frac{P_1 \omega}{\rho_0 c_s^2 \mathbf{k}r} e^{i(\omega t - kr)} \mathbf{e}_r. \quad (3.21)$$

One point to note about the acoustic field is its symmetry respect to r and the coordinates of the source. In other words, the pressure at the measurement point r caused by a source in r_0 is equal to the pressure which would be measured at r_0 if the source was placed at r . This characteristic is known as the *principle of acoustic reciprocity* (Morse and Ingard, 1987).

Due to the way transducer's electronics sense the acoustic waves, a new field $p\vec{v}$ is introduced next. The mechanic energy balance in a compressive Newtonian fluid under no force field can be expressed as

$$\int_{\partial D} -p\vec{n} \cdot \vec{v} dA = \int_D \frac{\rho}{2} \frac{d\vec{v}^2}{dt} dV + \int_D -p(\nabla \cdot \vec{v}) dV + \int_D (\lambda \text{tr}^2 \mathbf{D} + 2\mu \text{tr} \mathbf{D}^2) dV, \quad (3.22)$$

where \mathbf{D} is the symmetric term of the velocity gradient defined as $\frac{1}{2} (\nabla \vec{v} + \nabla^T \vec{v})$ with T the transpose operator. The first term in this equation represents the work done by the external surface forces, the second term represents the changes in kinetic energy of the volume, the third term the work of volume expansion and the final term the power loss. Using the Gauss's theorem, the first term can be written as

$$\int_{\partial D} -p\vec{v} \cdot \vec{n} dA = - \int_D \nabla \cdot (p\vec{v}) dV. \quad (3.23)$$

Imposing Eq. 3.23 equality in Eq. 3.22 dividing by the volume of D and taking

the limit when the diameter of D tends to zero, the mechanical energy balance can be written in its differential form as

$$-\nabla \cdot (p\vec{v}) = \frac{\rho}{2} \frac{d\vec{v}^2}{dt} - p(\nabla \cdot \vec{v}) + (\lambda \text{tr}^2 \mathbf{D} + 2\mu \text{tr} \mathbf{D}^2), \quad (3.24)$$

where the field $p\vec{v}$ has a physical interpretation as instantaneous energy flux in the wave. The first order development of Eq. 3.24 has little interest as it states that

$$-p_0 \nabla \cdot \vec{v}_1 = 0 - p_0 \nabla \cdot \vec{v}_1 + (0). \quad (3.25)$$

On the other hand, the second order development of Eq. 3.24 is

$$-\nabla \cdot (p_1 \vec{v}_1) = p_0 \nabla \cdot \vec{v}_2 + \frac{\rho_0}{2} \frac{\partial \vec{v}_1^2}{\partial t} - p_1 (\nabla \cdot \vec{v}_1) - p_0 (\nabla \cdot \vec{v}_2) + (\lambda \text{tr}^2 \mathbf{D}_1 + 2\mu \text{tr} \mathbf{D}_1^2). \quad (3.26)$$

After some manipulation and using Eq. 3.5, Eq. 3.26 can be expressed as

$$\nabla \cdot (p_1 \vec{v}_1) + \frac{\rho_0}{2} \left[\frac{\partial \vec{v}_1^2}{\partial t} + \frac{1}{(\rho_0 c_s)^2} \frac{\partial p_1^2}{\partial t} \right] = - (\lambda \text{tr}^2 \mathbf{D}_1 + 2\mu \text{tr} \mathbf{D}_1^2). \quad (3.27)$$

When assuming perfect fluid (i.e. $\lambda = \mu = 0$) Eq. 3.27 becomes a differential form of conservation, where the conserved state

$$\frac{\rho_0 \vec{v}_1^2}{2} + \frac{p_1^2}{2\rho_0 c_s^2} \quad (3.28)$$

is the second order mechanical energy, composed by the kinematic and the potential elastic energy. The field $p_1 \vec{v}_1$, also symbolized as \vec{I}' ,

$$\vec{I}' = p_1 \vec{v}_1 = \frac{P_1^2 \omega}{\rho_0 c_s^2 k r^2} e^{2i(\omega t - kr)} \mathbf{e}_r, \quad (3.29)$$

is the instantaneous flux of this total mechanical energy. When Newtonian fluids in spherical waves are in consideration, by using Eqs. 3.5, 3.7 and 3.14 it is possible to rewrite Eq. 3.27 as

$$-2\alpha_{wv} \vec{I}' \cdot \mathbf{e}_r = - (\lambda \text{tr}^2 \mathbf{D}_1 + 2\mu \text{tr} \mathbf{D}_1^2), \quad (3.30)$$

stating that the power loss due to viscosity of the fluid is proportional to

twice the viscosity absorption coefficient $\alpha_{\omega\nu}$ times the radial component of \vec{I} . This expression is used also to parametrize other types of power losses such as internal molecular processes dissolved in the medium (see Section 3.3) or the presence of scatterers (see Section 3.5).

Transducers systems are in essence time and space integrators. The intensity they are able to measure is the mean square intensity amplitude $|\vec{I}|_{ms}$ which can be interpreted as the average of the instantaneous intensity over many time periods

$$|\vec{I}|_{ms} = \frac{\omega}{2\pi} \int_0^{\frac{2\pi}{\omega}} \vec{I} \cdot \vec{e}_r dt. \quad (3.31)$$

Far from the source, where spherical wave solution is a proper approximation and $|\vec{v}_1|$ is in phase with p_1

$$|\vec{I}|_{ms} = \frac{P_1^2}{2\rho_0 c_s r^2}. \quad (3.32)$$

3.2 Non-linear effects

Non linear quantification can be done by comparison with the viscous absorption, which is low for small amplitude waves, in Eq. 3.2. For simplicity, a planar wave equation is assumed

$$\frac{\partial u}{\partial t} + u \frac{\partial u}{\partial x} + \frac{1}{\rho} \frac{\partial P}{\partial x} = \frac{\lambda + 2\mu}{\rho} \frac{\partial^2 u}{\partial x^2}. \quad (3.33)$$

The orders of magnitude of the first and third term are the same, $U\omega$ and $P\omega/\rho c_s$. The order of magnitude of the non-linear term (the second one) is $U^2\omega/c_s$ and the one of the viscous term is $U\omega^2/\omega_0$. Dividing Eq. 3.33 into $U\omega$, the orders of magnitude of the terms are 1, U/c_s , 1 and ω/ω_0 . U/c_s can be rewritten as $P/\rho c_s^2$. With $P = 0.1$ Pa, the order of the nonlinear term is 10^{-10} while the lowest frequency in the range (0.1 MHz) leads to a viscous term of order 10^{-4} , allowing to omit in most cases the non-linear interactions in comparison with the viscous phenomena.

3.3 Absorption in the medium

Besides viscous losses there are other losses in the fluid. Two other loss phenomena should be considered: heat and losses associated with internal molecular processes if the fluid medium includes dissolved molecules. Thermal absorption in water also scales with the square of the frequency (see Eq. 3.14). Molecular losses are more complex, due to the fact that they are the result of conversion of the molecules kinetic energy into: 1) stored potential energy, 2) rotational and vibrational energies, and 3) energies association and dissociation between different ionic species and complex ionized solutions (Kinsler, 2000), depending on the molecules present on the medium. Some work in sea water, has proved the important role of two main responsible molecules in said molecular loss, namely boric acid and magnesium sulfate. In Francois and Garrison (1982) the total absorption for water is expressed as the sum of the absorption due to boric acid, magnesium sulfate and water

$$\alpha_w = \left(\frac{A_{BA}}{\omega_{BA}^2 + \omega^2} + \frac{A_{MS}}{\omega_{MS}^2 + \omega^2} + A_{water} \right) \omega^2, \quad (3.34)$$

where ω_{BA} and ω_{MS} are temperature dependent relaxation frequencies associated with the boric acid and magnesium sulfate correspondingly. A_{BA} , A_{MS} and A_{water} depend on temperature and hydrostatic pressure, while A_{BA} , ω_{BA} , A_{MS} and ω_{MS} depend on the salinity.

3.4 Radiation from a transducer

Circular piston like transducers are the most common, thus some insight of the radiation from these types of transducers is given. First, the acoustics generated by a pulsating sphere is studied. May the radius be $a = a_0 + a_1 e^{i\omega t}$, with $a_0 \gg a_1$, given the radial velocity magnitude on the sphere surface $ia_1 \omega e^{i\omega t}$, first order adherence boundary condition at $r = a_0$ yields

$$\vec{v}_1(a_0, t) = \frac{P_1 \omega}{\rho_0 c_s^2} e^{i(\omega t - ka_0)} \left(\frac{ka_0 - i}{(ka_0)^2} \right) \mathbf{e}_r = ia_1 \omega e^{i\omega t} \mathbf{e}_r. \quad (3.35)$$

If the mean radius of the sphere is small compared to the wavelength, $ka_0 \ll 1$, then $P_1 = -\rho_0 c_s^2 a_1 (\mathbf{k}a_0)^2$. The pressure field can be approximated as

$$p_1(r, t) = -\frac{\rho_0 c_s^2 a_1 (\mathbf{k}a_0)^2}{r} e^{i(\omega t - \mathbf{k}r)}. \quad (3.36)$$

Now let a rigid piston of radius a_t oscillate at a speed of $U_t e^{i\omega t}$, the resulting pressure field \mathbf{p} can be obtained by assuming that each element of area dS contributes as an infinitesimal sphere. The differential area of each element is equal to $2\pi a_0^2$, corresponding to half of a sphere surface area.

Using the coordinates as described in Fig. 3.1 this concept can be expressed

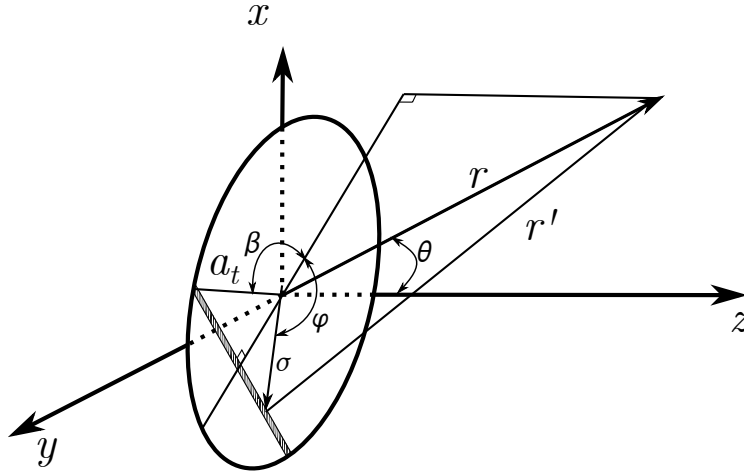


Figure 3.1: Circular plane piston of radius a_t .

as

$$\mathbf{p}(r, \theta, t) = \frac{i\rho_0 c_s^2 \mathbf{k}^2 U_t e^{i\omega t}}{2\pi\omega} \int_S \frac{e^{-ikr'}}{r'} dS, \quad (3.37)$$

where r' is the distance between the differential element and the point $r\mathbf{e}_r$

$$r' = \sqrt{r^2 + \sigma^2 - 2r\sigma \sin\theta \cos\varphi}. \quad (3.38)$$

. This integral is difficult to solve, but good approximations are developed for two regions, along the transducer axis ($\theta = 0$) and in the far field ($r \gg a_t$).

In the far field $r \gg a_t \geq \sigma$, the following infinitesimal equivalence can be used

$$\frac{e^{-ikr'}}{r'} \sim \frac{e^{-ik(r - \sigma \sin\theta \cos\varphi)}}{r}. \quad (3.39)$$

With $\sigma \cos \varphi = a_t \cos \beta$, Eq. 3.37 can be expressed as

$$\mathbf{p}(r, \theta, t) = \frac{i\rho_0 c_s^2 \mathbf{k}^2 U_t a_t^2}{\pi \omega r} e^{i(\omega t - \mathbf{k}r)} \int_0^\pi e^{i k a_t \sin \theta \cos \beta} \sin^2 \beta d\beta. \quad (3.40)$$

Usually $\alpha_w a_t \ll 1$, so

$$\int_0^\pi e^{i k a_t \sin \theta \cos \beta} \sin^2 \beta d\beta \approx \int_0^\pi e^{i k a_t \sin \theta \cos \beta} \sin^2 \beta d\beta, \quad (3.41)$$

and the pressure field of the piston \mathbf{p} tends to

$$\mathbf{p}(r, \theta, t) = i\rho_0 c_s U_t k a_t \frac{a_t J_1(k a_t \sin \theta)}{r k a_t \sin \theta} e^{i(\omega t - \mathbf{k}r)}, \quad (3.42)$$

where J_1 a Bessel function of the first kind. This particular type of Bessel functions (J_α when α is an integer) is also known as cylinder functions or cylindrical harmonics, because they appear in the solution to Laplace's equation in cylindrical coordinates. As shown in Eq. 3.42, pressure field can be expressed as the product of a function of r and a function of θ also called directional factor D , being

$$D(\theta) = \frac{2J_1(k a_t \sin \theta)}{k a_t \sin \theta}, \quad (3.43)$$

in the case of a circular piston like transducer. The factor of two is added in order to have the directional factor around the z axis equal to one. Figure 3.2 shows the directivity patterns of 500 kHz and 4 MHz AQUAscatter 1000R transducers.

Transducers with some symmetry, such as rectangular or elliptic ones, have a directional factor also depending on the other angle. Even in those cases, the amplitude of the pressure field has a maximum in the transducer axis. This maximum is called main lobe and measuring its width may be useful when trying to comprehend divergence of acoustic energy from the transducer. A common measure of the beam width is defined as the angle $\theta_{-3\text{dB}}$, also called half-beam angle, which is the angle from the center of the beam to the direction where the amplitude of the sound intensity $|\vec{I}|$ has decreased by half (~ -3 dB) in the far field

$$20 \log_{10} D(\theta_{-3\text{dB}}) = -3. \quad (3.44)$$

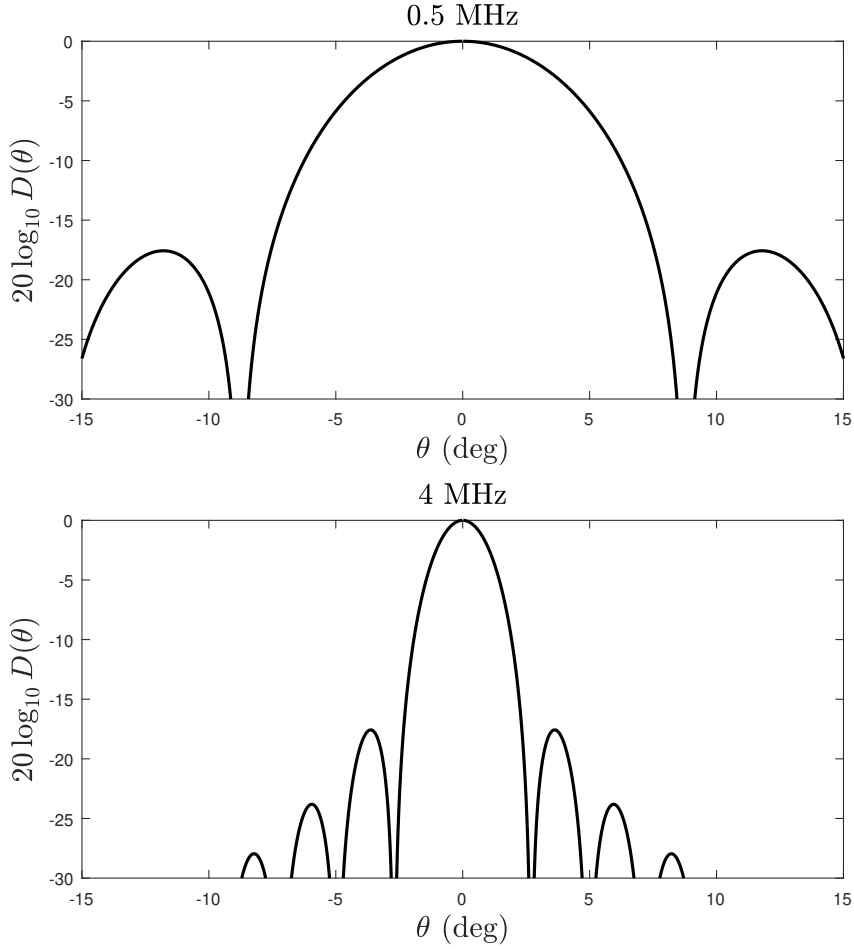


Figure 3.2: Directivity patterns of two AQUAscat 1000R transducers using factory values of a_t and f_s and sound speed c_s of 1500 m/s. f_s is the sound frequency ($2\pi f_s = \omega$).

As the power series of J_1 is $J_1(x) = \frac{x}{2}(1 - \frac{x^2}{8} + \dots)$, for a flat piston transducer an approximation of the beam divergence may be calculated as

$$\sin \theta_{-3\text{dB}} \approx \frac{\sqrt{8(1 - 10^{-3/20})}}{ka_t} \approx \frac{1.529}{ka_t}. \quad (3.45)$$

When the wavelength is small compared to the transducer geometry $ka_t \gg 1$ (as commonly occurs with commercial transducers), there are also other relative maximum pressure amplitude at other directions, called side lobes, as represented in Figure 3.2.

In the region near the transducer, often called the near field, pressure \mathbf{p} maintains a cumbersome form. For this reason theoretical studies have been avoiding this domain. When restricting the study to $\theta = 0$ only, the distance

Table 3.1: Transducer characteristics of the AQUAscat[®] 1000R provided by Aquatec Group Ltd. $c_s = 1500$ m/s is assumed in $k_{1.5}$

f_s (MHz)	a_t (mm)	$k_{1.5}a_t$	$\theta_{-3\text{dB}}$ ($^\circ$)
0.5	12.0	25	3.49
1	9.0	38	2.32
2	4.8	40	2.18
2.5	5.0	46	1.90
4	4.9	82	1.07
5	5.2	109	0.80

between the differential elements of the transducer and the point $r\mathbf{e}_r$ becomes simpler $r' = \sqrt{r^2 + \sigma^2}$ and Eq. 3.37 can be expressed as

$$\mathbf{p}(r, 0, t) = \frac{\rho_0 c_s^2 \mathbf{k}^3 U_t}{2\pi\omega} \left[1 - e^{-ikr(\sqrt{1^2 + (a_t/r)^2} - 1)} \right] e^{i(\omega t - kr)}, \quad (3.46)$$

where the real part of the term in square brackets is within the range between 0 and 1. As opposed to the behavior in the far field ($r \gg a_t$), several values of r can be found in the near field where the amplitude of $\mathbf{p}(r, 0, t)$ becomes zero

$$kr \left(\sqrt{1 + (a_t/r)^2} - 1 \right) = m_r \pi, \quad (3.47)$$

where m_r belongs to the non-negative integer numbers. When $m_r > 0$, Eq. 3.47 is equivalent to

$$2\frac{r}{a_t} = \frac{ka_t}{\pi m_r} - \frac{\pi m_r}{ka_t}. \quad (3.48)$$

The largest root r_1 , when $m_r = 1$, establishes a good idea of the limits between near and far field, being

$$r_1 = \frac{ka_t^2}{2\pi} \left[1 - \left(\frac{\pi}{ka_t} \right)^2 \right]. \quad (3.49)$$

As has been previously indicated, and also seen in Table 3.1, commercial transducers commonly have $ka_t \gg 1$, allowing to approximate

$$r_1 \approx \frac{ka_t^2}{2\pi}. \quad (3.50)$$

The Rayleigh length defined as $r_R = \pi r_1$ has been used to normalize r in

order to express the near field corrections of the pressure in a non dimensional form. [Downing et al. \(1995\)](#) compare observations of a series of laboratory experiments using different transducers and homogeneous suspensions, with their corresponding theoretical predictions. Defining ψ as a function which accounts for the departure of the backscattered signal from spherical spreading, the following formula was found to be in good agreement with the theory

$$\psi = 1 + \frac{1}{1 + \frac{1.35r}{r_R} + \left(\frac{2.5r}{r_R}\right)^{3.2}}. \quad (3.51)$$

Alternatively, Aquatec Group ([Aquatec, 2002](#)) proposes a ψ correction of the following form

$$\psi = \begin{cases} \frac{2}{3} \left[1 + \frac{r_R}{r}\right] & \text{for } r < 2r_R \text{ (near field)} \\ 1 & \text{for } r > 2r_R \text{ (far field).} \end{cases} \quad (3.52)$$

Both Eq. 3.51 ([Downing et al., 1995](#)) and Eq. 3.52 ([Aquatec, 2002](#)) were evaluated to estimate the near field correction ψ of each transducer. As the inversion technique in Section 3.8 proved to be sensitive to this correction, an empirical ψ was established for each transducer in an homogeneous sediment mixture with a known c in the mixing tank. Small changes (less than 10 %) have been applied to the factory reported a_t in Table 3.1 in order to change r_R and collapse the empirical curves to Eq. 3.51. Figure 3.3 shows the empirical curves and the theoretical curves. The proposed changes in the transducer radius a_t can be explained by the fact that the effective radius is generally 15%-30% lower ([Hay, 1991](#)) than the actual radius.

3.5 Scattering of sound

When sound waves propagate into a region with solid objects with different density and sound speed, some portion of incident acoustic intensity \vec{I} changes its direction, amplitude and phase. These changes in the incident wave caused by reflection, refraction, and diffraction are referred to as scattering. By convention the difference between the resulting wave and the one which would have been present with no obstacle is defined as the scattered wave.

Assuming an inviscid or Newtonian fluid medium, plane sound wave scat-

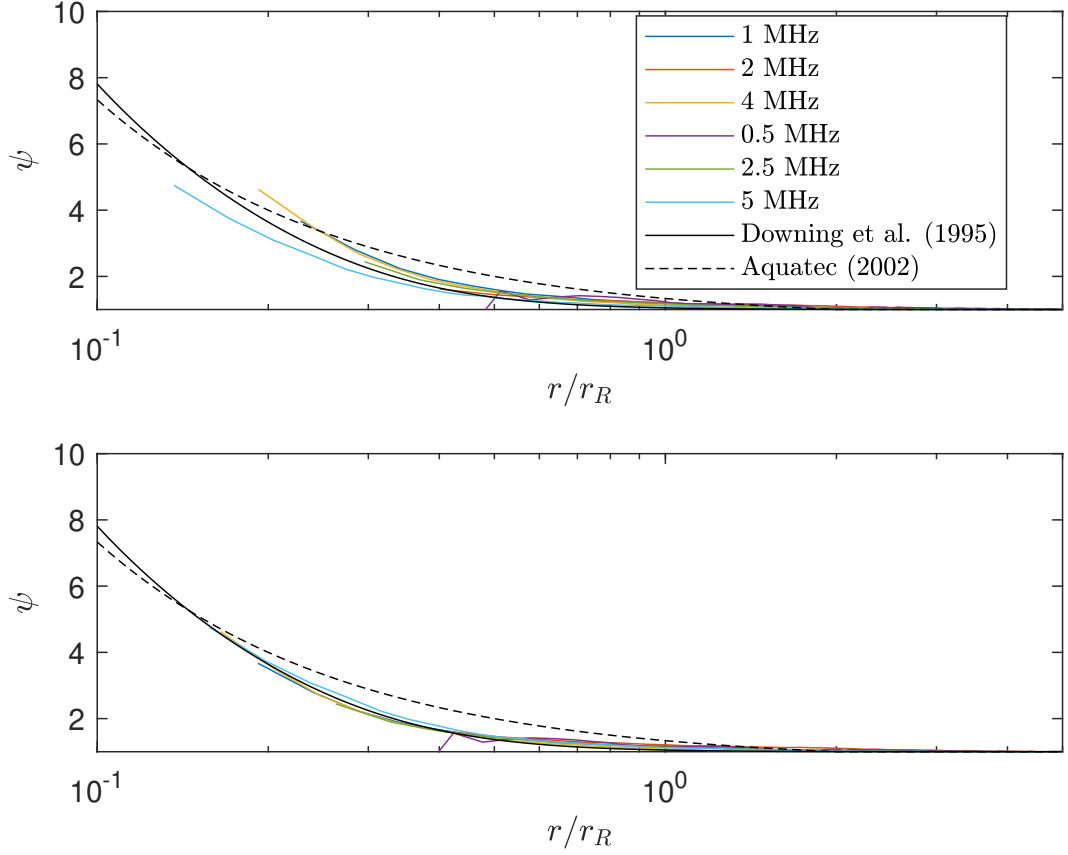


Figure 3.3: Upper panel: Near field determinations on laboratory (in colors) and theoretical curves (in black) with Rayleigh length r_R determined with the factory a_t . Lower panel: Changes of less than 10 % have been applied to a_t in order to approximate the empirical curves to Eq. 3.51 (Downing et al., 1995).

tering in presence of rigid, fluid or solid elastic simple geometrical objects have been extensively studied (King, 1934; Anderson, 1950; Faran Jr, 1951; Allegra and Hawley, 1972; Lin and Raptis, 1983; Hay and Mercer, 1985; Medwin, 2005). As the spherical case exhibit an azimuthally symmetric geometry, the incident wave in spherical coordinates facilitates the problem. Using the convention in Hay and Mercer (1985) for a sphere of radius a_s , the pressure field of the incident wave $p_{i,1}$ can be written as

$$p_{i,1} = p_{ref} e^{i(kr \cos \theta - \omega t)} = p_{ref} \sum_{m=0}^{\infty} i^m (2m+1) j_m(kr) P_m(\cos \theta) e^{-i\omega t}, \quad (3.53)$$

where p_{ref} is the complex reference pressure amplitude of the wave, P_m is a Legendre function and j_n spherical Bessel function of the first kind of order m respectively. The equation of dynamic elasticity, a wave equation inside the

scatterer ($r < a_s$) similar to Eq. 3.8 can be found

$$\frac{\rho_s}{G_s} \frac{\partial^2 \vec{d}_{1s}}{\partial t^2} = \Delta \vec{d}_{1s} + \frac{(3K_s + G_s)}{3G_s} \frac{\partial \nabla (\nabla \cdot \vec{d}_{1s})}{\partial t}, \quad (3.54)$$

where \vec{d}_{1s} is the displacement vector in the scatterer, and ρ_s , K_s and G_s are the density, bulk modulus and shear modulus of the scatterer. Imposing continuity of velocity and stress fields at $r = a_s$ as boundary conditions, the solution for the scattered wave pressure $p_{s,1}$ in the far field ($rk \gg 1$) is

$$p_{s,1} = p_{ref} \sum_{m=0}^{\infty} i^m (2m+1) A_m h_m(kr) P_m(\cos \theta) e^{-i\omega t}, \quad (3.55)$$

where h_m is the spherical Hankel function of order m and the coefficients A_m (Hay and Mercer, 1985) depend not only on the sediment size a_s and sound frequency ω but also on the parameters of the fluid (ρ , K , λ and μ) and solid media (ρ_s , K_s and G_s). In the far field, the spherical Hankel function can be approximated to

$$\lim_{kr \rightarrow \infty} h_m(kr) = -i \frac{e^{ikr}}{kr} (-i)^m, \quad (3.56)$$

allowing to rewrite Eq. 3.55 as

$$p_{s,1} = \frac{p_{ref}}{kr} e^{i(kr - \omega t)} \sum_{m=0}^{\infty} -i(2m+1) A_m P_m(\cos \theta). \quad (3.57)$$

Morse and Ingard (1987) indicate that far from the scatterer $kr \gg 1$, in the inviscid case ($\lambda, \mu \approx 0$) of the rigid immobile sphere ($K_s, G_s \gg K$), the scattered wave intensity amplitude $|I_{sM}|$ in the Geometric scattering regime $ka_s \gg 1$ can be written as

$$|I_{sM}| \simeq |I_i| \left[\frac{a_s^2}{4r^2} + \frac{a_s^2}{4r^2} \cot^2 \left(\frac{\theta}{2} \right) J_1^2(ka_s \sin \theta) \right], \quad (3.58)$$

where $|I_i|$ is the intensity amplitude of the incident wave. The first term inside the square brackets shows that half of the $|I_{sM}|$ is scattered equally in all directions, whereas the second term indicates that the other half is concentrated behind the scatterer, interfering destructively with the incident wave and generating a shadow zone (Morse and Ingard, 1987). Defining the tempo-

ral average power of the scattered wave Π_s as

$$\Pi_s = \int_S \vec{I}_s \cdot \mathbf{e}_r dA, \quad (3.59)$$

where S is the surface of a sphere of radius r centered in the scatter, [Morse and Ingard \(1987\)](#) obtain for the rigid scatterer in the Geometric scattering regime that

$$\Pi_{sM} \simeq |I_i| 2\pi a_s^2. \quad (3.60)$$

Both Eqs. [3.58](#) and [3.60](#) propose a scale for the acoustic parameters of the scatterers. Dividing $\vec{I}_s \cdot \mathbf{e}_r$ by the first term in Eq. [3.58](#) ($|I_i| \frac{a_s^2}{4r^2}$) defines a dimensionless reflectivity factor R_θ . Using the results in [Hay and Mercer \(1985\)](#), R_θ^2 can be written as

$$R_\theta^2 = \frac{\vec{I}_s \cdot \mathbf{e}_r}{|I_i|} \frac{4r^2}{a_s^2} = \frac{4}{(ka_s)^2} \left| \sum_{m=0}^{\infty} -i(2m+1)A_m P_m(\cos \theta) \right|^2. \quad (3.61)$$

Scattering from $\theta = \pi$, also called backscatter, has a particular interest in monostatic arrays (in which the transmitter and receiver are collocated) where $R_{\theta=\pi}$, sometimes called form function f , is

$$R_{\theta=\pi}^2 = f^2 = \frac{4}{(ka_s)^2} \left| \sum_{m=0}^{\infty} (-1)^m (2m+1) i A_m \right|^2. \quad (3.62)$$

Another important acoustic parameter of the scatterer is related to the energy losses. Attenuation in presence of scatter arises from conversion of acoustic energy into thermal energy due to viscosity and the reradiation of the incident acoustic energy out of the incident beam. Tracing back to Eq. [3.30](#), allows the use of Π_s in order to obtain the attenuation parameter due to sediment α_s

$$\Pi_s = 2\alpha_s |I_i| V, \quad (3.63)$$

where V is the volume of the sphere of radius r . When several scatterers are present in the volume V , the volume concentration ϵ defined in Section [2.2](#) can

useful since it enables to rewrite Eq. 3.63

$$\Pi_s = \frac{2\alpha_s}{\epsilon} |I_i| \frac{4\pi a_s^3}{3} N, \quad (3.64)$$

where $\frac{4\pi a_s^3}{3} N$ represents the volume of the scatterers in the volume, being N the number of scatterers. Dividing Π_s by N times Π_{sM} defines a dimensionless parameter χ called normalized total scattering cross-section

$$\frac{\Pi_s}{N\Pi_{sM}} = \chi = \frac{4}{3} \frac{\alpha_s a_s}{\epsilon}. \quad (3.65)$$

The total scattering cross-section χ may be seen as the sum of two different sources: scattering cross-section due to viscous dissipation χ_v attributed to the viscous drag between the fluid and the particles; and the scattering cross-section χ_s that resumes the scattering due to the scatterer geometry and material.

Measuring suspensions of irregular particles (sand and kaolin), [Urlick \(1948\)](#) compared the data with the expression by [Lamb \(1945\)](#) for spherical particles. The data indicated that in the Rayleigh scattering regime $ka_s \ll 1$ the viscous-drag loss ($\chi_v \propto ka_s$) is larger than the scattering loss ($\chi_s \propto (ka_s)^4$). Assuming the small scatterers are free to move in the sound field, [Urlick \(1948\)](#) arrives to the equation

$$\chi = \frac{(ka_s)^4}{9} + \frac{2}{3} \frac{s_U(\pi_\rho - 1)^2}{s_U^2 + (\pi_\rho + \tau_U)^2} ka_s, \quad (3.66)$$

where

$$\pi_\rho = \frac{\rho_s}{\rho}, \quad (3.67)$$

$$s_U = \frac{9}{4} \frac{\delta_S}{a_s} \left(1 + \frac{\delta_S}{a_s} \right), \quad (3.68)$$

$$\frac{\delta_S}{a_s} = \sqrt{\frac{2\nu}{\omega a_s^2}}, \quad (3.69)$$

$$\nu = \frac{\mu}{\rho}, \quad (3.70)$$

$$\tau_U = \frac{1}{2} + \frac{9}{4} \frac{\delta_S}{a_s}. \quad (3.71)$$

The first term in Eq. 3.66 is χ_s whereas the second term is χ_v . [Urlick \(1948\)](#)

uses the motion of a pendulum swinging in a viscous fluid, theoretically studied by G. G. Stokes, to show that s_U is proportional to the drag force and τ_U represents an addition to the sphere inertia. The Stokes length $\delta_S = \sqrt{2\nu/\omega}$ is the thickness of the laminar boundary layer, and the Stokes number a_s/δ_S (Eq. 3.69) is a dimensionless angular frequency.

With the acoustic scatterer parameters f and χ as a starting point, [Thorne and Meral \(2008\)](#) gathered published acoustic data on sandy sediment suspensions, and proposed a regression fit of the form

$$f = \frac{(ka_s)^2 \left(1 - 0.3e^{-\frac{(ka_s-1.5)^2}{0.49}}\right) \left(1 + 0.5e^{-\frac{(ka_s-1.8)^2}{4.84}}\right)}{1 + 0.9(ka_s)^2}, \quad (3.72)$$

$$\chi_s = \frac{0.29(ka_s)^4}{0.95 + 1.28(ka_s)^2 + 0.25(ka_s)^4}. \quad (3.73)$$

Adding the viscous loss proposed by [Urlick \(1948\)](#)

$$\chi_v = \frac{2}{3} \frac{s_U(\pi_\rho - 1)^2}{s_U^2 + (\pi_\rho + \tau_U)^2} ka_s, \quad (3.74)$$

with $\pi_\rho = 2.65$ and $\nu = 1 \times 10^{-6}$ m²/s, it is possible to obtain the total cross-section as $\chi = \chi_s + \chi_v$. [Betteridge et al. \(2008\)](#) use Ballotini glass spheres sieved to $\frac{1}{4}\phi$ which means that $\log_2\left(\frac{a_{s,M}}{a_{s,m}}\right) = \frac{1}{4}$ with $a_{s,M}$ being the maximum grain size and $a_{s,m}$ the minimum grain size of the ensemble. The presence of a population of scatterers with different sizes, even as narrow as $\frac{1}{4}\phi$, modifies the relation of the form factor f and the total scattering loss χ with the sound frequency, often flattens those functions. The use of glass spheres sieved in ranges of two consecutive ASTM E11 sieves is a common practice when calibrating the acoustic instruments. All ASTM sieve mesh sizes appear in <https://www.globalgilson.com/sieve-sizes>.

Figure 3.4 shows estimations of f and χ_s using [Betteridge et al. \(2008\)](#) and χ_v using [Urlick \(1948\)](#) for AQUAScat 1000R transducers frequencies used in this thesis. The \circ symbols represent the prediction for the calibration scatterers used in the factory, Ballotini glass spheres sieved to $\frac{1}{4}\phi$ with a mean radius of 59.25 μm .

Some authors use the sediment mass concentration instead of ϵ , as it gives more intuitive values for people who work in dredging. The relation between the sediment mass concentration M and ϵ is $M = \rho_s\epsilon$. The use of M instead

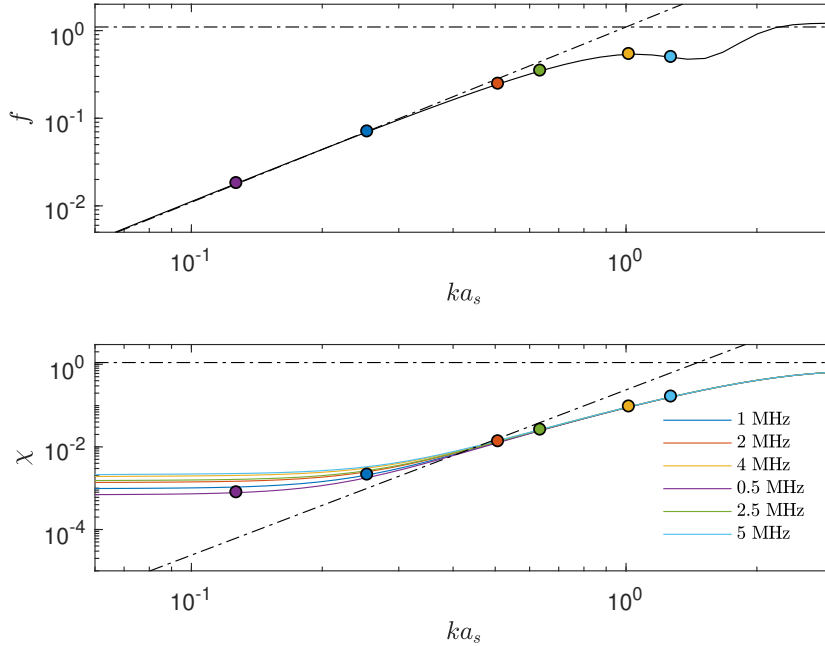


Figure 3.4: Estimations for f and χ using [Betteridge et al. \(2008\)](#) and [Urlick \(1948\)](#). The \circ symbols represent the predictions for all AQUAScat 1000R transducers with glass spheres with $a_s = 59.25 \mu\text{m}$.

of c to express sediment mass concentration is a reminder that they were estimated by acoustic techniques.

3.6 Incoherent backscatter of suspensions

With the ideas expressed in Sections 3.3, 3.4 and 3.5, the first order backscattered pressure $p_{s,1}$ of a particle at r and θ detected by a monostatic transducer (in which the transmitter and receiver are collocated) can be expressed as

$$p_{s,1} = \left[P_1 \frac{D(\theta)}{\psi r} e^{-\alpha r} \right] \left[\frac{f a_s}{2} \frac{D(\theta)}{\psi r} e^{-\alpha r} \right] e^{i(2kr - \omega t)}, \quad (3.75)$$

where the term within the first pair of square brackets represents the incident pressure amplitude on the particle, the term between within the second pair represents the fraction of the pressure amplitude that reaches the transducer, and α is the sum of the total absorption for water α_w and the attenuation due to sediment α_s along the path. As the transducer emits a pulse of certain duration τ_p , the presence of N particles disposed randomly in the irradiated

volume (thickness $c_s\tau_p/2$) produces an intensity that can be interpreted as the sum of each individual scatter. Following the theoretical considerations for the backscattered sound of a large number of particles in [Pedocchi and García \(2012\)](#), the acoustic intensity mean square amplitude $|\vec{I}|_{ms}$ reaching the transducer can be written as

$$|\vec{I}|_{ms} = \frac{P_1 P_1^*}{\rho c_s} \sum_{m=1}^N \sum_{n=1}^N \frac{f_n a_{s,n}}{2(\psi r_n)^2} \frac{f_m a_{s,m}}{2(\psi r_m)^2} D^2(\theta_n) D^2(\theta_m) e^{-2\alpha(r_n+r_m)} \cos [2k(r_n - r_m)], \quad (3.76)$$

where n and m refer to the particles.

The use of Eq. 3.76 to estimate the amount of particles N from a single measurement is an undetermined inverse problem. The main challenge resides not only on the several unknown form factors f_n or the total attenuation coefficient α , but also on the relative position of the particles $r_n - r_m$ over the irradiated volume. Two identical particles can be situated in a constructive configuration $\cos [2k(r_n - r_m)] = 1$ (quadrupling the backscattered intensity of a single particle), or in a destructive configuration $\cos [2k(r_n - r_m)] = 0$ (with zero backscattered intensity), significantly altering the backscattered wave.

Assuming that the scatterers have no preferential positions over the space allows to develop the so called Incoherent Backscattering hypothesis. When the particles adopt a random configuration, i.e. the spatial variables r_n and θ_n are randomly and uniformly distributed, it can be proved that the resulting pressure amplitude of the backscattered wave follows a Rayleigh probability distribution ([Bendat and Piersol, 2011](#)). Having statistical independent random variables r_n , θ_n , $f_n a_{s,n}$ and α_s and using [Thorne and Hanes \(2002\)](#) when $r \gg c_s\tau_p$ and $ka_t > 10$, Eq. 3.76 can be expressed as

$$\mathbb{E} \left(|\vec{I}|_{ms} \right) \approx \left[\frac{P_1 P_1^*}{\rho c_s} \frac{\pi}{4} \frac{c_s \tau_p}{(\psi r)^2} \left(\frac{0.96}{ka_t} \right)^2 e^{-4\alpha_w r} \right] \frac{N \mathbb{E}(f_n^2 a_{s,n}^2)}{V} e^{-4\mathbb{E}(\alpha_s r)}, \quad (3.77)$$

where V is the volume of the irradiated region ($V \approx c_s\tau_p\pi r^2$) and \mathbb{E} represents the expected value. The proportionality between the incoherent scattered intensity and N was previously indicated by [Morse and Ingard \(1987\)](#).

When the scatterers have different sizes

$$\frac{N}{V} = \frac{M}{\frac{4\pi}{3} \rho_s \mathbb{E}(a_{s,n}^3)}, \quad (3.78)$$

by defining n_{pdf} as the size probability density function (PDF) of the sediments the following expressions can be rewritten

$$\begin{aligned} \frac{\text{E}(f_n^2 a_{s,n}^2)}{\text{E}(a_{s,n}^3)} &= \frac{\int_0^\infty f^2 a_s^2 n_{pdf} da}{\int_0^\infty a_s^3 n_{pdf} da}, \\ \text{E}\left(\frac{\partial \alpha_s r}{\partial r}\right) &= \frac{3}{4\rho_s} \frac{\text{E}(\chi_i a_{s,i}^2)}{\text{E}(a_{s,i}^3)} M_i = \frac{3}{4\rho_s} \frac{\int_0^\infty \chi a_s^2 n_{pdf} da}{\int_0^\infty a_s^3 n_{pdf} da} M_i, \end{aligned} \quad (3.79)$$

where M_i is the expected sediment mass concentration at r . Representative values of the form function $\langle f \rangle$ and the normalized total scattering cross-section $\langle \chi \rangle$ of the suspension can be defined as

$$\begin{aligned} \langle f \rangle^2 &= \frac{\langle a_1 \rangle}{\langle a_3 \rangle} \int_0^\infty f^2 a_s^2 n_{pdf} da, \\ \langle \chi \rangle &= \frac{\langle a_1 \rangle}{\langle a_3 \rangle} \int_0^\infty \chi a_s^2 n_{pdf} da, \end{aligned} \quad (3.80)$$

where $\langle a_j \rangle$ is the j -th moment of n_{pdf} defined by

$$\langle a_j \rangle = \int_0^\infty a_s^j n_{pdf} da, \quad (3.81)$$

with $\langle a_0 \rangle = 1$ as n_{pdf} is a PDF. Definitions of Eqs. 3.80 and 3.81 allow to express Eq. 3.77 in a simplified form

$$|\vec{I}|_{ms} = \left[\frac{P_1 P_1^* \pi}{\rho c_s} \frac{c_s \tau_p}{4 (\psi r)^2} \left(\frac{0.96}{ka_t} \right)^2 e^{-4\alpha_w r} \right] \frac{3M}{4\pi\rho_s} \frac{\langle f \rangle^2}{\langle a_1 \rangle} e^{-4 \int_0^r \frac{3M}{4\rho_s} \frac{\langle \chi \rangle}{\langle a_1 \rangle} dr'}. \quad (3.82)$$

Introducing a transducer receive sensitivity R_t and a voltage transfer function of the system T_V , [Thorne and Hanes \(2002\)](#) arrive to the following expressions of the recorded root mean square voltage signal RMS (V_{rms})

$$\text{RMS}(V_{rms}) = \sqrt{2} K_t K_s \frac{\sqrt{M}}{\psi r} e^{-2r\alpha_w} e^{-2r\alpha_s}, \quad (3.83)$$

$$K_t = R_t T_V \frac{|P_1|}{\sqrt{\rho c_s}} \frac{0.96}{ka_t} \sqrt{\frac{3\tau_p c_s}{16}}, \quad (3.84)$$

$$K_s = \frac{\langle f \rangle}{\sqrt{\rho_s \langle a_1 \rangle}}, \quad (3.85)$$

$$r\alpha_s = \int_0^r \frac{3M}{4\rho_s} \frac{\langle \chi \rangle}{\langle a_1 \rangle} dr', \quad (3.86)$$

where K_s is determined by the size distribution and backscatter form factor of the suspended particles at r ; K_t resumes the dependence of the transducer geometry and frequency (ka_t), electronics (R_t and T_V) and configuration set up ($|P_1|$ and τ_p); and $e^{-2r\alpha_s}$ represents the correction for attenuation due to particles in suspension between the transducer and r .

Techniques designed to sample the amount of scatterers in a determined volume, such as gravimetric analysis, measure the mass concentration instead of the number of scatterers N . Relating the mass PDF m_{pdf} with n_{pdf}

$$m_{pdf} = \frac{a_s^3 n_{pdf}}{\langle a_3 \rangle}, \quad (3.87)$$

allows the use of m_{pdf} to calculate acoustic parameters

$$\begin{aligned} \langle f \rangle^2 &= \langle a_1 \rangle \int_0^\infty \frac{f^2}{a_s} m_{pdf} da, \\ \langle \chi \rangle &= \langle a_1 \rangle \int_0^\infty \frac{\chi}{a_s} m_{pdf} da, \end{aligned} \quad (3.88)$$

and

$$\langle a_j \rangle = \langle a_3 \rangle \int_0^\infty a^{(j-3)} m_{pdf} da. \quad (3.89)$$

3.7 Acoustic backscatter calibration

Calibration of acoustic instrumentation is required in order to quantify the accuracy and precision of the acquired data. Calibration methods can be categorized as component or system calibration. The first require the identification and performance evaluation of each component. Said methods need additional calibration instrumentation, expertise and time. System calibration methods evaluate the performance of the system (such as transmission and reception electronics, connectors, cables and transducers) as a whole (Demer et al., 2015).

The calibration of a multi-frequency system, as well as a single-frequency system, can be performed by measuring the backscatter suspensions. This approach incorporates both the electronic and acoustic calibration, but suspended scatterers should be selected carefully. Even though field multi-frequency systems are supposed to measure natural suspended sediments, it is recommended to perform calibration with scatterers of well-known properties (size,

shape, density, elasticity, mineralogy) in order to extrapolate the calibration parameters to a wide range of sediment mixtures. Glass spheres are commonly used due to their large documented properties (Gaunaud and Uberall, 1983; Hay, 1991; Thorne and Campbell, 1992; Betteridge et al., 2008), allowing to separate the effect of the scatters from the backscattered signal. In most cases, laboratory calibration facilities have mixing tanks that generate an homogeneous suspension of sediments over regions with no obstacles. Since air micro-bubbles are also scatterers, once the tank is filled with water, some hours to days are required to vent off the air dissolved in the water to the atmosphere and degas it. Moreover, it is common practice to measure the acoustic system in clear water to take account of the background noise.

Under Incoherent Backscattering hypothesis, the probability distribution of the backscattered amplitude presented in Eq. 3.83 leads to a Rayleigh distribution $V_{rms} \sim \text{Rayleigh}(\xi)$ (Bendat and Piersol, 2011; Thorne et al., 1993). The probability density function of the Rayleigh distribution is

$$p(V_{rms}) = \frac{V_{rms}}{\xi^2} e^{-V_{rms}^2/(2\xi^2)}, \quad (3.90)$$

where ξ is the scale parameter of the Rayleigh distribution. When having several independent profiles (with different scatterer configurations), sample statistics such as the mean or variance may be used to estimate ξ .

The recorded amplitude of the backscattered signal V_{rec} separates from V_{rms} as there is always noise V_{noise} . Thermal noise and other sources of noise such as electronic or ambient noise have been studied in acoustic systems (Rhyne, 1998; Deines, 1999). Three different ways to characterize noise have been documented: 1) since some equipment can operate in passive mode without transmitting pulses, the recorded voltage in said mode may be attributed to noise presence; 2) occasionally when measuring in laboratory, it is possible to run experiments with no scatterers in order to obtain the background noise; 3) during the measuring mode after the pulse was emitted, the returning signal starts to decay to a noise level. If the equipment was set to record acoustic profiles in a sufficiently wide range of r , the noise characteristics could be extracted from the end of the profiles. Since the acoustic instrumentation applied in this thesis cannot operate in passive mode, the second and third noise characterizations were performed. It should be noticed that with the third it is possible to determine the noise in every burst profiles, both in the

laboratory and in the field data.

The way the noise changes the recorded signal in a particular dataset is difficult to predict, as it depends on the noise source and equipment. Four sample statistics (Mean, Median, Variance and Mean square) and different noise addition hypothesis were explored for extracting the Rayleigh parameter ξ in the case of an AQUAscatter 1000R ABS manufactured by Aquatec Group. Table 3.2 shows the sample statistics and ξ relations

Table 3.2: Rayleigh distribution parameter estimators.

Mean	Mean (V_{rms}) = $\sqrt{\frac{\pi}{2}}\xi$
Median	Median (V_{rms}) = $\sqrt{2 \log 2}\xi$
Variance	Var (V_{rms}) = $\frac{4-\pi}{2}\xi^2$
Mean square	MS (V_{rms}) = $2\xi^2$

and the corresponding hypothesis of noise addition

$$\text{Mean}(V_{rec}) = \text{Mean}(V_{rms}) + \text{Mean}(V_{noise}), \quad (3.91)$$

$$\text{Median}(V_{rec}) = \text{Median}(V_{rms}) + \text{Median}(V_{noise}), \quad (3.92)$$

$$\text{Var}(V_{rec}) = \text{Var}(V_{rms}) + \text{Var}(V_{noise}), \quad (3.93)$$

$$\text{MS}(V_{rec}) = \text{MS}(V_{rms}) + \text{MS}(V_{noise}). \quad (3.94)$$

Figures 3.5 to 3.7 show histograms for No Sediment (V_{noise}) and $c = 0.391$ kg/m³ of Ballotoni glass spheres (V_{rec}) at different r . The ABS was configured to acquire 3200 profiles being each one the average of 4 different measurements at 4 Hz sampling rate. PDF distributions look Gaussian due to the selected averaging configuration in these measurements. The curves represent the PDF with the four different ξ estimates. Mean square estimates (which are the maximum likelihood sample statistics) provides better results, probably not due to the estimator itself but because of the noise addition hypothesis (see [Thorne and Campbell \(1992\)](#)). As the signal-to-noise ratio (SNR) is in most cases very high, i.e. the amplitude of the noise V_{noise} is lower than V_{rms} , departures from the expected probability distribution functions are detectable mainly in the lower values.

With ξ estimations, and knowing the sediment profile concentrations and

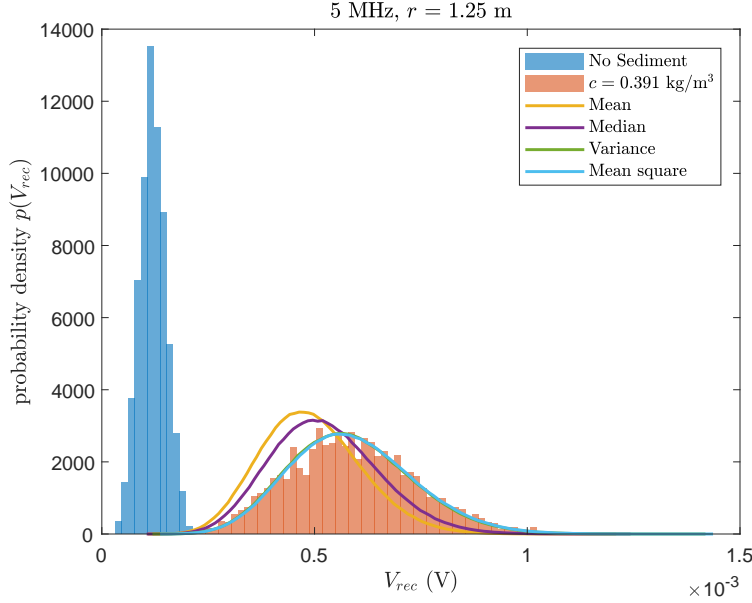


Figure 3.5: Histograms of the backscattered amplitude for No sediment and $c = 0.391 \text{ kg/m}^3$ of Ballotoni glass spheres $r = 1.25 \text{ m}$ distance of the 5 MHz transducer. Curves of mean, median, variance and mean square estimations of Rayleigh distribution parameter ξ .

acoustic scatterer parameters, the calibration parameter K_t may be obtained by rearranging Eq. 3.83

$$K_t = \frac{\xi \psi r}{K_s \sqrt{M}} e^{2r\alpha}. \quad (3.95)$$

Figure 3.8 describes K_t profiles (that are supposed to be constant in r) for 5 MHz transducer using Mean, Variance (Var) and Mean square (MS) estimators. The peak of SNR at $r = 1.9 \text{ m}$ occurs at the bottom of the tank.

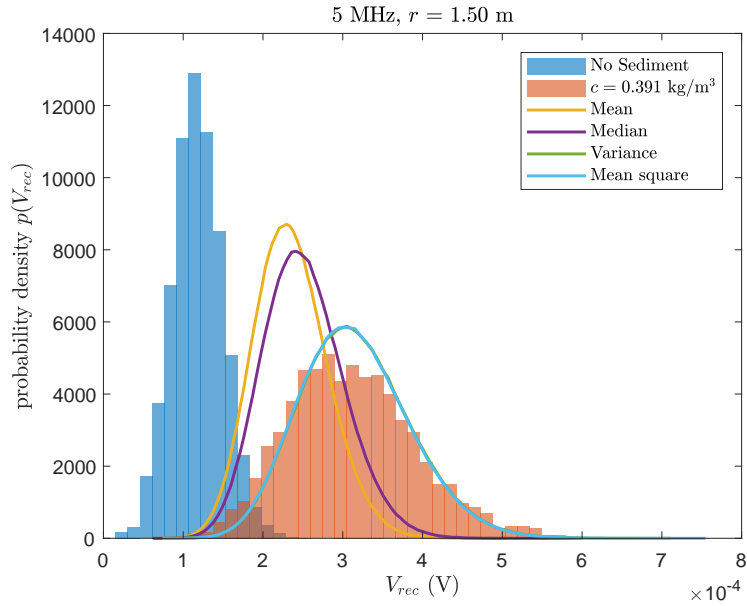


Figure 3.6: Histograms of the backscattered amplitude for No sediment and $c = 0.391 \text{ kg/m}^3$ of Ballotoni glass spheres $r = 1.50 \text{ m}$ distance of the 5 MHz transducer. Curves of mean, median, variance and mean square estimations of Rayleigh distribution parameter ξ .

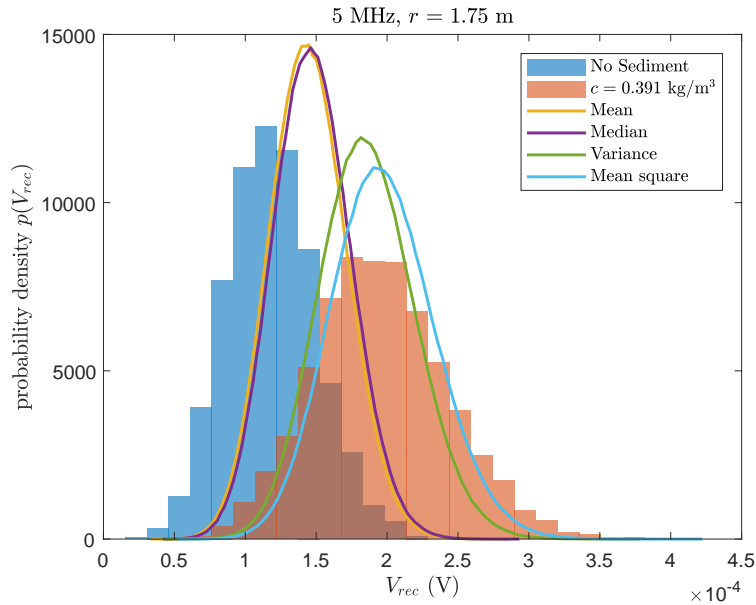


Figure 3.7: Histograms of the backscattered amplitude for No sediment and $c = 0.391 \text{ kg/m}^3$ of Ballotoni glass spheres $r = 1.75 \text{ m}$ distance of the 5 MHz transducer. Curves of mean, median, variance and mean square estimations of Rayleigh distribution parameter ξ .

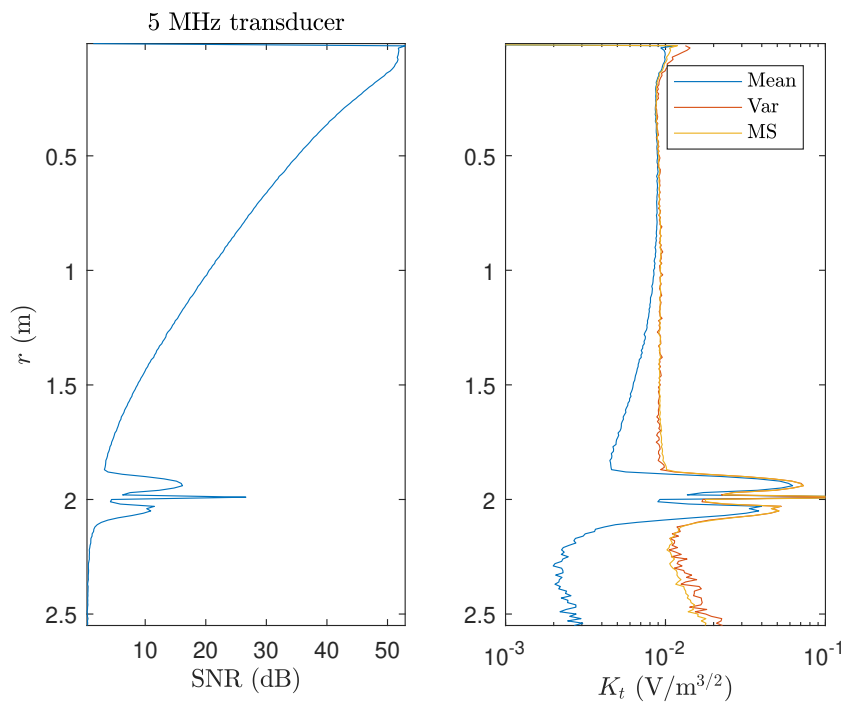


Figure 3.8: Estimations of K_t using mean, variance and root mean square.

3.8 Acoustic backscatter inversion

Different strategies have been proposed to determine suspended sediment quantities by using single (Thorne et al., 1993; Lee and Hanes, 1995) and multiple frequency (Hay and Sheng, 1992) acoustic backscatter data. As Eq. 3.83 shows, scattered acoustic signals depend on the amount and size distribution of particles as well as the acoustic frequency. When using a single sound frequency Thorne and Hanes (2002) present both implicit iterative and explicit methods that allow to extract M by adding some hypothesis of the sediment size distribution.

In Hay and Sheng (1992), both laboratory experiments and field measurements were used to evaluate multi-frequency algorithms in order to determine vertical profiles of suspended sand concentration M and size $\langle a_1 \rangle$. Multi-frequency acoustic data using 1, 2.25, and 5 MHz sound frequencies were compared with Optical Backscatter Sensors (OBS) data. Calculations were based on the ratios of $\langle f \rangle$ and $\langle \chi \rangle$ for the different sound frequencies. By rearranging Eq. 3.83 the following system of equations can be written

$$\frac{\langle f \rangle_n}{\langle f \rangle_m} = \frac{\xi_n \psi_n / K_{t,n}}{\xi_m \psi_m / K_{t,m}} e^{2r(\alpha_n - \alpha_m)}, \quad (3.96)$$

$$M = \frac{1}{N_f} \sum_{n=1}^{N_f} \left(\frac{\xi_n}{K_{s,n} K_{t,n}} \psi_n r e^{2r\alpha_n} \right)^2, \quad (3.97)$$

being sub-indexes n and m identifiers of the different frequencies with $n \neq m$ and N_f the number of sound frequencies. When adding some hypothesis of the sediment size distribution, Eq. 3.96 allows in principle to estimate other parameters besides M , such as $\langle a_1 \rangle$ and $\langle a_3 \rangle$.

The proposed iterative resolution of this system begins in the first range r , initiating the iterative cycle by determining $\langle a_1 \rangle$ using Eq. 3.96 and assuming $r(\alpha_n - \alpha_m) \approx 0$. When $\langle a_1 \rangle$ is found an estimation of M can be obtained with Eqs. 3.97. The next iteration cycle uses Eq. 3.96 to update $\langle a_1 \rangle$ having an estimation for $r(\alpha_n - \alpha_m)$, then, M is also updated using Eq. 3.97. After achieving a convergence criterion, the solution of $\langle a_1 \rangle$ and M in the first range is obtained, therefore iteration may begin in the next position r . This procedure is repeated until the last r is solved.

With a three frequency acoustic backscatter in laboratory experiments, the acoustic estimates obtained by Hay and Sheng (1992) of M were within 10 % of

the OBS estimates for c , which is within the uncertainty expected in the OBS technique. Instead, the acoustic estimates of suspended sediment size $\langle a_1 \rangle$ were within 10-20 %. The field measurements confirmed the accuracy found in laboratory for M , but no separate measurements of suspended particle size were made. The acoustic estimates of near-bottom mean size were within 6-18 % of the bottom sediment mean size at the deployment site. The size estimate variability was suspiciously high, with standard deviations between 30 and 50 % of the mean value and requiring long averaging times to achieve stable estimates. They concluded that one possible reason for this variability has to do with the fact that Eq. 3.96 involves the ratio of signals of different frequencies, which are subject to error, particularly for low amplitude signals in the denominator.

Wilson and Hay (2015) proposed a method for estimating both $\langle a_1 \rangle$ and M incorporating linearized statistical inversion theory and compared the results of a series of laboratory experiments. As this technique takes into account the ill conditioning of the inverse problem by using statistical regularizing assumptions, it shows improvements in the stability of the solution in cases with high acoustic attenuation in comparison with Hay and Sheng (1992) technique. The inversion multi-frequency method is a variant of that by Hay and Sheng (1992), where the function to be minimized in the first step is

$$\sum_{n \neq m} \left(\log \frac{\xi_n^p}{\xi_m^p} - \log \frac{\xi_n}{\xi_m} \right)^2, \quad (3.98)$$

where the superscript p refers to the prediction of the backscatter amplitude using Eq. 3.83. Once $\langle a_1 \rangle$ is obtained, the next function to be minimized is

$$\sum_n (\log \xi_n^p - \log \xi_n)^2, \quad (3.99)$$

in order to obtain the value of M .

Some of the sediments found in nature present a unimodal log-normal size distribution (Thorne et al., 2011; Lee et al., 2012), which can be expressed as

$$\frac{\partial C}{\partial \ln(a_s)} = \frac{c}{\sqrt{2\pi} \ln \sigma_g} e^{-\frac{1}{2} \left(\frac{\ln(a_s/a_g)}{\ln \sigma_g} \right)^2}, \quad (3.100)$$

where c is the mass concentration of the sediment, C the mass concentration of

each size, a_g the geometric mean radius, σ_g the geometric standard deviation and $C = c m_{pdf}$ with m_{pdf} defined in Eq. 3.87. As described in Chapter 5, the Particle Size Distribution (PSD) of the bed sediment extracted from the deployment site, may be simplified into four different sediment classes. The larger class (fine sand with geometric mean radius of 225.1 μm and geometric standard deviation of 1.42 in Table 5.1) dominates the backscatter whereas the other three dominate the attenuation due to sediment (Hanes, 2012). This multimodal PSD can be written as

$$\frac{\partial C}{\partial \ln(a_s)} = \sum_{j=1}^4 \frac{c_j}{\sqrt{2\pi} \ln \sigma_{gj}} e^{-\frac{1}{2} \left(\frac{\ln(a_s/a_{gj})}{\ln \sigma_{gj}} \right)^2}, \quad (3.101)$$

where c_j is the mass concentration, a_{gj} the geometric mean particle radius, which is equivalent to the median radius ($a_{50,j}$) for a log-normal distribution, and σ_{gj} the geometrical standard deviation of the j -th sediment class. In this case the mass concentration of sediments is

$$c = \sum_{j=1}^4 c_j. \quad (3.102)$$

In its most general form, Eq. 3.101 has twelve degrees of freedom, four c_j , four a_{gj} and four σ_{gj} . Assuming that the suspended material in the field may be expressed as some combination of the different classes determined in Section 5.1, i.e. fixing the eight values of a_{gj} and σ_{gj} , and due to the importance of the fine sediment in the acoustic backscattered signal on the attenuation vs backscatter phenomenon, i.e. linking the first three c_j , an acoustic parameter r_f can be defined as

$$r_f = \frac{1}{c} \sum_{j=1}^3 c_j, \quad (3.103)$$

where r_f represents the fine fraction mass proportion. The inversion implemented in this thesis applies Eqs. 3.98 and 3.99 to obtain r_f and M correspondingly. The reduction from the twelve sediment parameters seen in Eq. 3.101 to r_f and M , can be justified by the limitation on the four sound frequencies used in the field. Although the 0.5 MHz frequency transducer was useful to define the position of the seabed during high concentrated events,

this transducer data was not used in the acoustic backscatter inversion given the laboratory issues stated in Section 5.2. Due to this restriction only three separate equations (one for each frequency) remain available to determine sediment parameters. Because sediment acoustic parameter determination can be an ill-conditioned problem, an over-determined system of equations (three equations to obtain two parameters) was established leading to more stable solutions. Figures 3.9 and 3.10 present the results of the proposed inversion algorithm for different combinations of r_f and M in laboratory experiment data indicating good agreement with the expected values over the whole acoustic range.

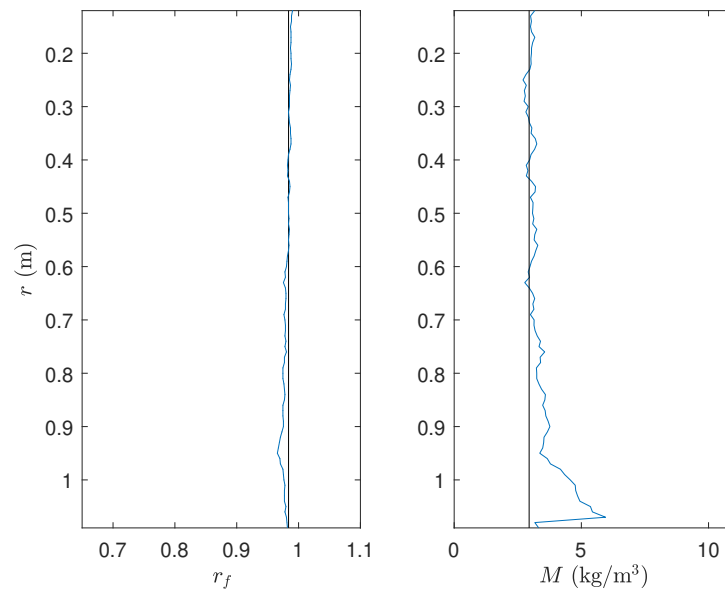


Figure 3.9: In blue, estimates of r_f and M using multifrequency inversion technique in Río de la Plata sediment in laboratory experiments. Black lines are independent measurements of those parameters using granulometry and gravimetric techniques.

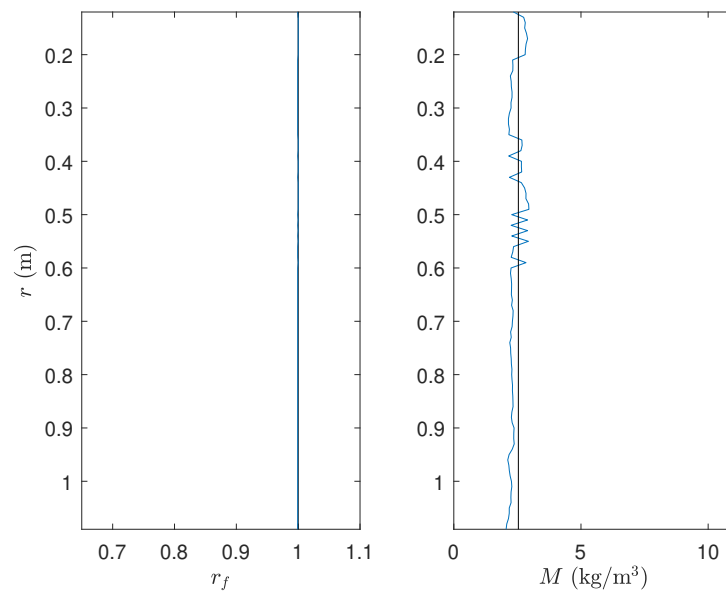


Figure 3.10: In blue, estimates of r_f and M using multifrequency inversion technique in Río de la Plata sediment sieved with No.200 ASTM in laboratory experiments. Black lines are independent measurements of those parameters using granulometry and gravimetric techniques

Chapter 4

Field Deployment

4.1 Field works

In order to reduce the interference with the data collection of the downward looking instruments, a thin and tall mooring structure was built at the IMFIA's workshop. It was designed to be deployed in a muddy bottom to study the near bed sediment transport mechanisms in the estuary under different wave, current and salinity conditions.

The sediment concentration profile was measured with downward looking AQUAScat 1000R multi-frequency Acoustic Backscatter Sensors (ABS) positioned 1 m above the bed. The near bed hydrodynamics was directly measured with an Acoustic Doppler Velocimeter (ADV) a few decimeters above the bed. The structure was deployed in summer, from December 8, 2017 to February 23, 2018. Water temperature varied between 20 and 26 °C, and water depth from 6 to 9 m. The largest significant wave height recorded during this deployment was 2.2 m and the maximum current registered was 1.4 m/s. In Chapter 6 there appears further information.

A few days before deployment, the structure was assembled in a shipyard property of Nitromar nearby. Once the structure was completed, the distances between the instruments and the bottom of the structure were measured, as presented in Fig. 4.1. The multicat Titón was sent to the study site once deployment permissions had been granted by the Oceanographic, Hydrographic and Meteorological Service of the National Army (SOHMA - Servicio de Oceanografía, Hidrografía y Meteorología de la Armada). Using a crane, divers from Techno Dive company deployed the structure in the muddy bot-

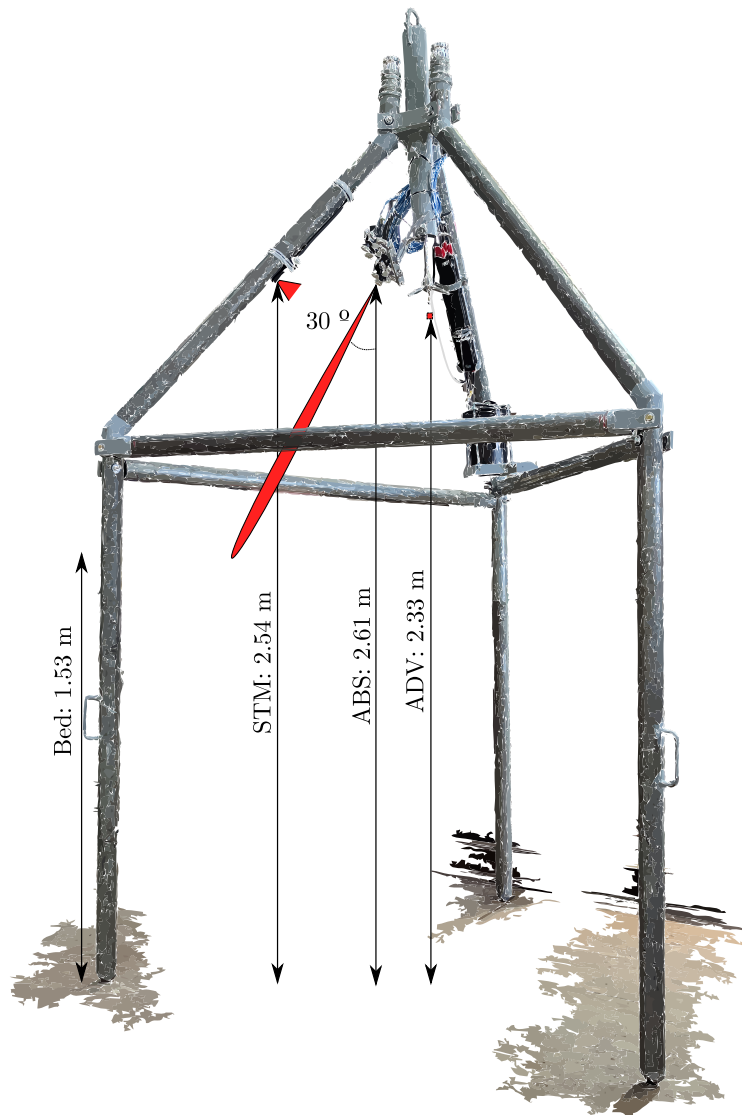


Figure 4.1: First deployment tripod.

tom. The penetration in the muddy bed of the tripod legs was registered, as shown in Fig. 4.1. The global position was marked with a Leica Viva CS15 dGPS and an antenna on the ground.

The deployment site was located 3.0 km South from the coast of Montevideo, and the mean water depth during the deployment was 7.5 m. The tripod was deployed on [Latitude 34°55'44.41"S](#), [Longitude 56°16'25.69"W](#), 3.0 km south of Punta Sayago, Montevideo, 100 meters away from the mooring dead weight of the oceanographic buoy, described in Section 4.7.

On February 22, 2018 on day before completing the first deployment the site, that had been previously marked with the dGPS, was reached by Zodiac

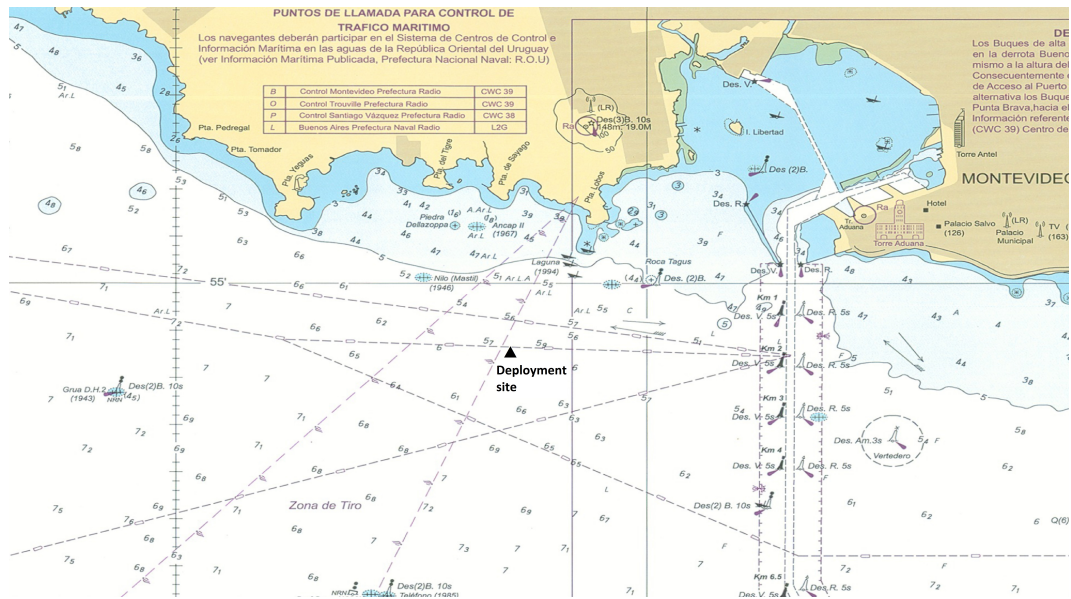


Figure 4.2: Location of the deployment site in the nautical chart 40 published in 2006 by SOHMA, Uruguay.

boat. A scuba diver descended to check the condition of the structure and registered the position of the structure in relation to the bed. A buoy with a stainless steel cable was tied to the lifting handle of the tripod. The following day Titón lifted the tripod at the site and returned it to the shipyard. Sediment and water samples were extracted and sent to the laboratory to calibrate the acoustic and optical sensors on the same day. The structure was cleaned, disassembled and sent to the IMFIA's facilities.

After completing the first deployment, the structure was modified in order to attach also a downward looking Sentinel V20 1 MHz Acoustic Doppler Current Profiler (ADCP) and a Seacat 19 plus V2 Conductivity, Temperature, and Depth sensor (CTD) with an OBS3+ Optical Backscatter Sensor (OBS). Zinc anodes for cathodic protection were placed as there appeared some signs of corrosion. This second structure was deployed in winter, from May 25 to August 23, 2018. The same procedures described for the first deployment were followed. Water temperature varied between 10 and 18 °C, salinity between 0 and 28 psu, and water depth between 6.5 and 9 m. The largest significant wave height recorded during this deployment was 2.0 m high and the maximum current registered was 1.1 m/s. In Chapter 6 there appears further information.

The data sets provided by these deployments are the first of this type in the Río de la Plata estuary.

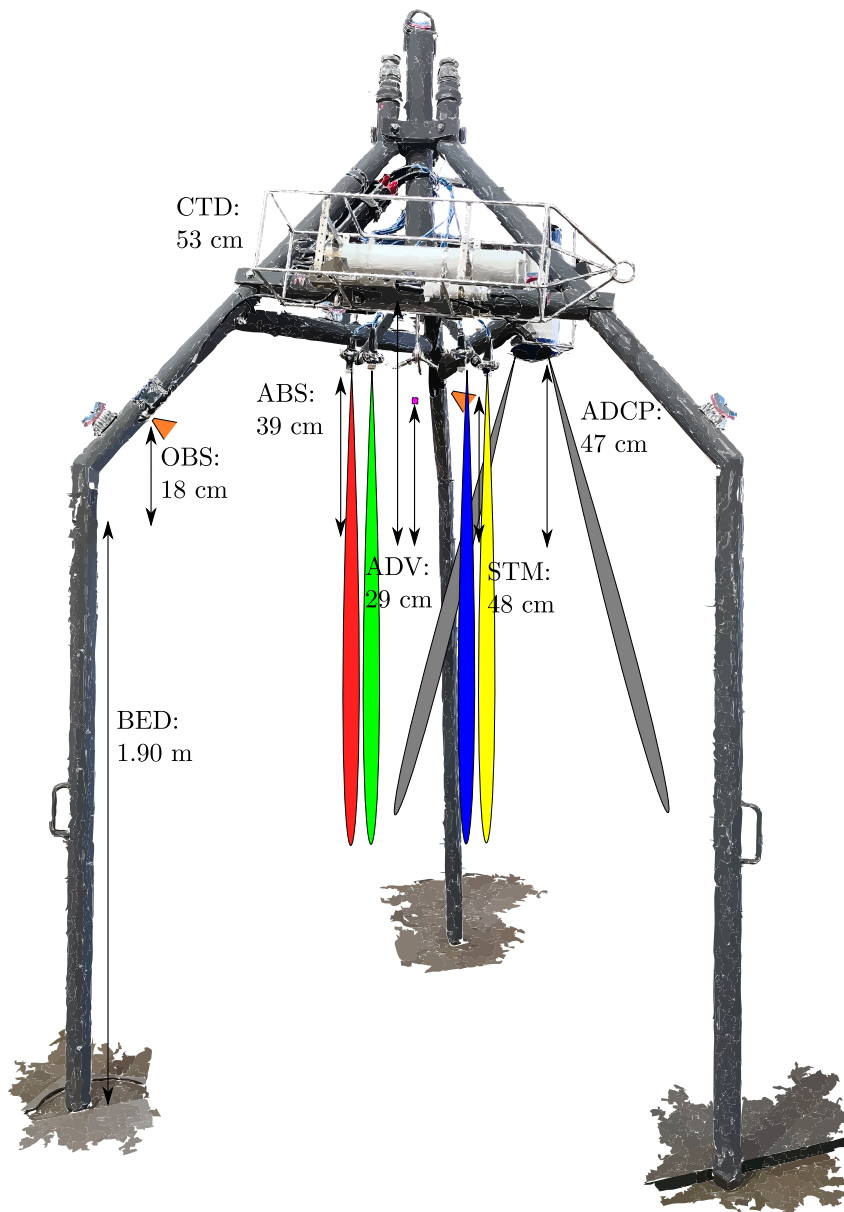


Figure 4.3: Second deployment tripod.

Figures 4.4 to 4.7 are some photos of the deployments and extractions of the structure.

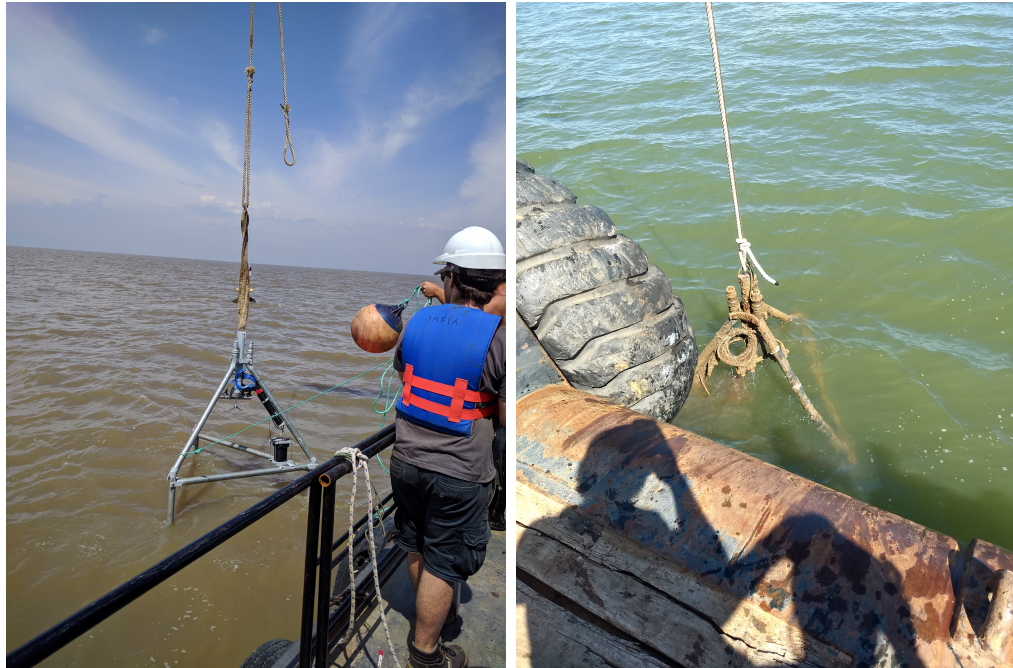


Figure 4.4: First mooring on December 8, 2017 and extraction on February 23, 2018.



Figure 4.5: Second mooring on May 25, 2018 after the structure has been assembled and during deployment.



Figure 4.6: Second tripod extraction on August 23, 2018.

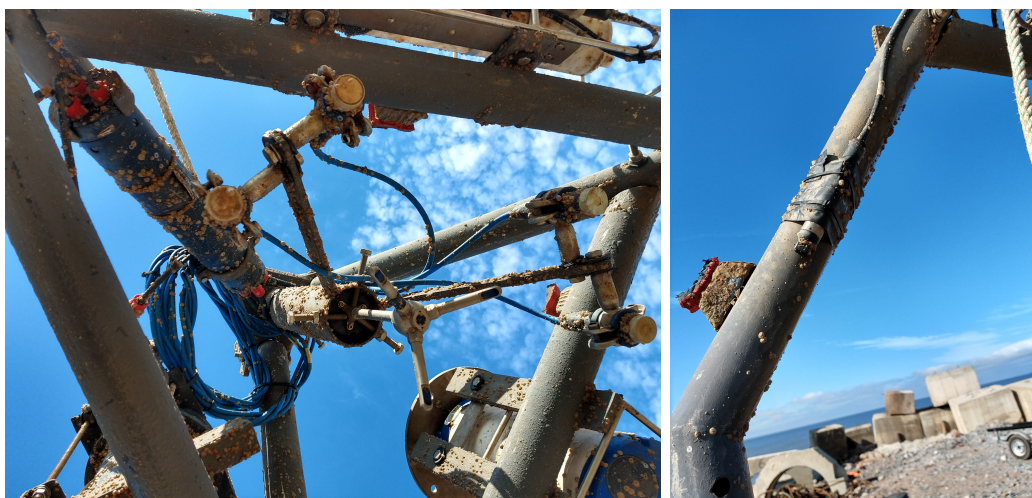


Figure 4.7: August 23, 2018. Details of the extracted tripod.

4.2 ABS

An AQUAscat 1000R ABS manufactured by Aquatec Group was attached to the tripod during both deployments. ABS register the echo amplitude profile of a short pulse emitted by each external transducer with up to four different sound frequencies within 0.5 to 5 MHz range. The profile, which may cover more than a meter, can be discretized into 1 centimeter cells accordingly to (Caine, 2014). Exterior to the data-logger case, a temperature sensor and a pressure port are also registering ambient data. With an analogical connection it is possible to install another auxiliary sensor.

During the first deployment, transducers operating in frequencies of 0.5, 1, 2.5 and 5 MHz were positioned at a 30 ° angle relative to the vertical. The instrument was set to register 2100 profiles every hour with a profile rate of 16 Hz (burst length longer than 2 minutes) at a range of 1.05 m and at each centimeter. Data was collected during 90 days given memory limitations. The recording period was from December 8, 2017 to February 23, 2018 and the distance between transducers and the seabed was 1.08 m.

The second deployment included transducers operating at frequencies of 0.5, 1, 2 and 4 MHz in downward looking position. The data-logger was set to register 4200 profiles every 30 minutes with a profile rate of 32 Hz (burst length longer than 2 minutes) at a range of 1.05 m, at each centimeter. Data was collected during 45 days given memory limitations. The distance between transducers and the seabed was 39 cm and the recording period was from May 25 to July 9, 2018.

4.3 ADV

A Vector ADV manufactured by Nortek was attached to the tripod during both deployments. The ADV is a bi-static sonar with a central transducer with pulse emission at 6 MHz sound frequency and a transducer on each of the three arms which receives the scattered signal. The pulse length may be adjusted between 2 and 8 mm and the sampling volume is located approximately 150 mm away from the central transducer accordingly to (Nortek, 2018). The ADV is a pulse coherent instrument, since the time lag of the pair of acoustic pulses used is known and their phase shift is determined with a covariance method. With this information found in relation to phase shifts associated

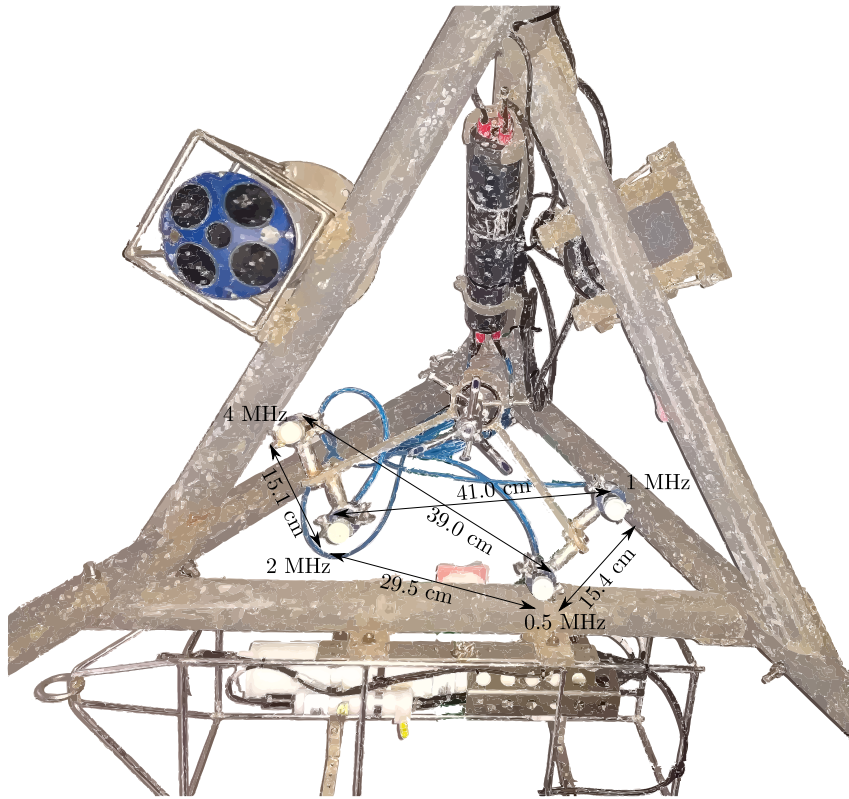


Figure 4.8: Downview of second tripod. Distances among ABS transducers are indicated.

with the motion of scatterers in the sampling volume, it is possible to obtain three-dimensional “instantaneous” velocity vector with a frequency of 64 Hz (Voulgaris and Trowbridge, 1998; Trowbridge, 1998; Rusello, 2009). This is defined as the pulse-to-pulse coherent method. Thermistor and piezoresistive sensors outside the data-logger case, and a magnetometer and a liquid level inside the case, provide temperature, pressure, heading, roll and pitch registers.

The Vector also runs an alternative test, known as Probe Check. Once the transmitter sends a pulse, all receivers record the acoustic amplitude profile of the echo for a long period of time. With the data provided by this test during deployments sound speed and salinity were estimated, as shown in Annex 1.

During the first deployment, the ADV was set to measure 6000 samples/hour with a sampling rate of 32 Hz (burst length longer than 3 minutes). The distance between the sampling volume and the bed was 80 cm and the recording period was from December 8, 2017 until February 23, 2018 given battery limitations.

During the second deployment, the ADV was set to measure 6000 samples/30

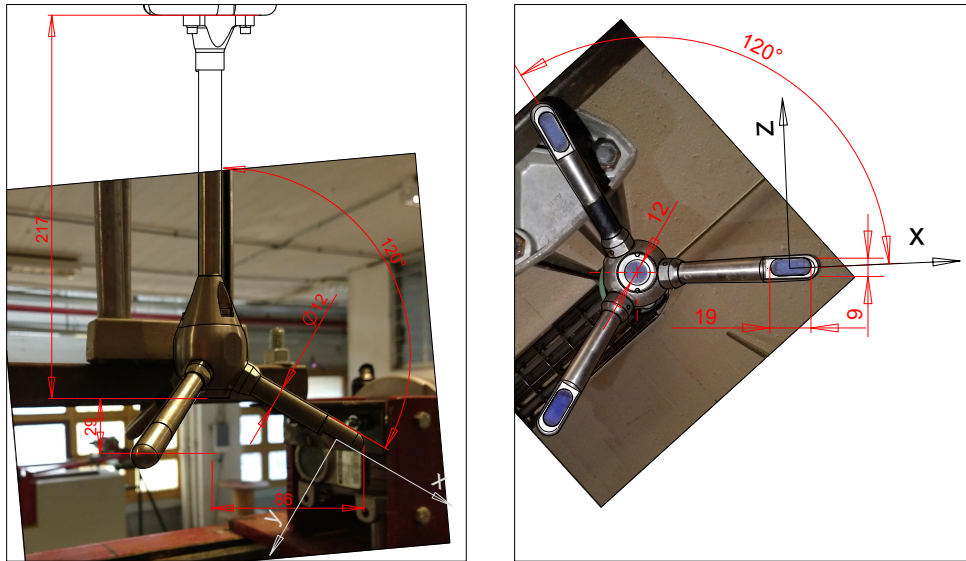


Figure 4.9: Vector manufactured by Nortek.

minutes with a sampling rate of 32 Hz (burst length longer than 3 minutes). The distance of the sampling volume from the bed was 29 cm and the recording period was from May 25 to August 11, 2018. In the period remaining until the structure was removed, more than 30 % of data in each burst was lost from the ADV due to power failure.

4.4 CTD

A SBE 19plus V2 SeaCAT CTD manufactured by Sea-Bird Electronics was fixed to the tripod during the second deployment. The CTD has conductivity, temperature, and depth sensors cased for protection inside an anti-foulant device. Water is refilled in the cavity with the sensors using a pump. Analogical connections are applied to install other auxiliary sensors (Sea-Bird, 2016). The equipment was set up to register every 10 minutes, collecting samples at 53 cm above the bed, from May 25 to August 23, 2018.

Derived variables, such as salinity and sound speed, were calculated in a post-processing software based on the international Equation Of State for seawater (EOS-80) by Unesco (1981) and Del Grosso (1974) formulations (Sea-Bird, 2014). The data provided by the CTD during this deployment was also used to estimate the errors of the proposed technique in Mosquera and Pedocchi (2019). Figure 4.10 describes a scatter plot of the CTD data using Del Grosso (1974) formulations to relate sound speed, salinity and temperature.

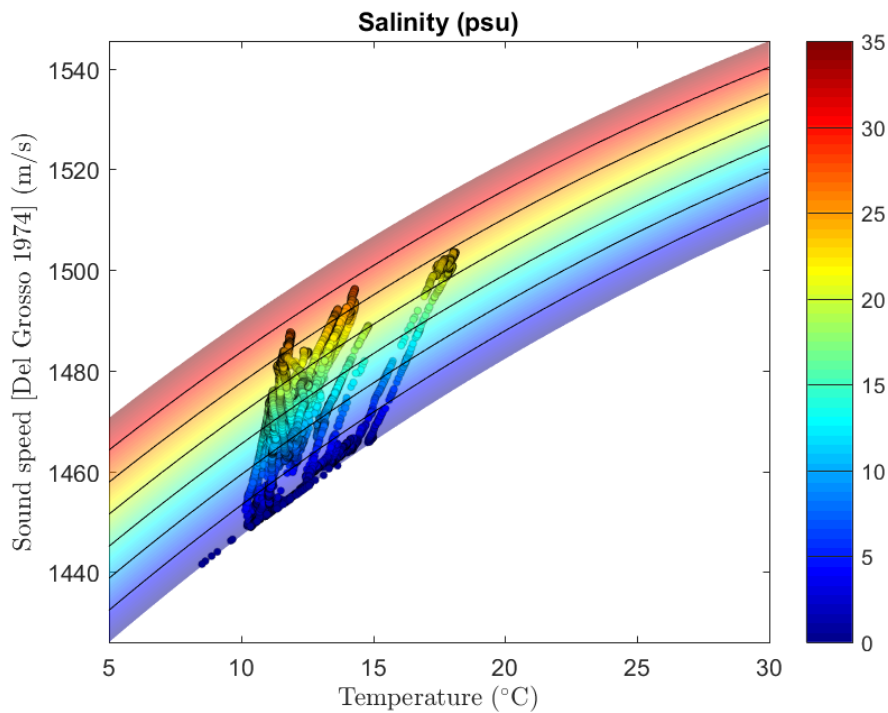


Figure 4.10: Sound speed, temperature and salinity relations applying Del Grosso (1974) formulations. The symbols \circ represent the CTD data.

4.5 Turbidity meters

In the first deployment a Seapoint Turbidity Meter (STM) manufactured by Seapoint was used. It was deployed 1.01 m above the bottom, and the data was registered the ABS data-logger. Turbidity measurements were registered every hour from December 8, 2017 to February 23, 2018. In the second deployment the STM was positioned 48 cm above the bed and an Optical Backscatter Sensor OBS-3+, manufactured by Campbell Scientific, was used. This was positioned 18 cm above the bed. Turbidity data was registered in the CTD data-logger. STM measurements were every 30 minutes from May 25 to July 10, 2018, while OBS measurements were every 10 minutes, from May 25 to July 25, 2018. Table 4.1 details specifications of the STM and the OBS provided by their corresponding manufacturers (Seapoint, 2013; Campbell, 2014).

Table 4.1: Turbidity sensor characteristics provided by the respective company

	OBS-3+
Light source wavelength	850 nm \pm 5 nm
Scattering Angles	15 - 150 °
Optical Power	2000 μ W
Turbidity Accuracy	2 % of reading or 0.5 NTU
Ranges (low/high)	1000/4000 NTU
	STM
Linearity	\pm 2 % 0-1250 FTU
Light Source Wavelength	880 nm
Scattering Angles	90 - 165 °
Power input	7 to 20 VDC and 3.5 mA average current
Sensitivity 1x gain	2 mV/FTU
Range 1x gain	4000 FTU (above 1250 FTU becomes non-linear)

4.6 ADCP

A Sentinel V20 ADCP manufactured by Teledyne RD Instruments was mounted downwards on the tripod during the second deployment. The ADCP includes five piezoelectric mono-static transducers operating at sound frequencies of 1 MHz. Once a coded pulse is emitted by transducers, the projected velocity profile of the scattering material is registered from each transducer by analyzing the backscattering signal. This method is referred to as broadband and improves the space and time resolution in relation to non-coded monochromatic

pulse methods (also called incoherent or narrowband methods). The Sentinel V20 measuring range may be over 20 meters being 25 cm its highest resolution (Teledyne, 2017). Currents may be reconstructed with all projected velocity profiles. Redundant data is used as a quality measurement of the registered signal. Accelerometers and magneto-inductive sensors are mounted inside the case to register heading, roll and pitch data. Temperature and pressure data are registered as well. The ADCP was set up to record 8 minutes bursts every 30 minutes. The frequency of samples was 2 Hz, resolution 25 cm and samples were collected 47 cm above the bed from May 25 to August 23, 2018.

4.7 Complementary data - Gas Sayago buoy

From 2016 to 2018 IMFIA's team assisted in maintenance and data processing of an AXYS WatchKeeper buoy, anchored 200 m away from the deployment site. This buoy included a series of meteorological sensors (anemometer, barometric pressure, humidity, rain gauge, temperature and visibility sensors) and oceanographic sensors, namely:

- A 600 kHz Workhorse Monitor ADCP facing downwards, manufactured by Teledyne RD Instrument. This ADCP was set up to record 2 min bursts/hour with 1 Hz frequency of samples and 50 cm resolution. The first cell was 2.6 m below the water surface.
- A SBE 37-SIP MicroCAT CT manufactured by Sea-Bird Electronic. The CT includes conductivity and temperature sensors located 70 cm below the water surface and was configured to register these variables every 30 minutes.
- TRIAXYS Next Wave II, a Directional Wave Sensor including accelerometers, angular rate and compass sensors. A post processor converts raw data into estimations within the directional wave spectra (AXYS, 2013). The wave sensor was set to measure every hour.

Once a year, the buoy was extracted for maintenance procedures, namely upgrading software, checking the status of batteries and solar panels, removing the bio-fouling and running some tests. Figures 4.11 and 4.12 include some photos of maintenance during February, 2018.



Figure 4.11: Gas Sayago buoy maintenance procedures in February 19 (extraction) and February 23 (mooring), 2018.



Figure 4.12: Bio-fouling of the buoy in February, 2018.

Chapter 5

Laboratory work

5.1 Sediment granulometry

Sediments of the Río de la Plata estuary were extracted from the bottom bed near the tripod deployment site (see Chapter 4) and Particle Size Distribution (PSD) of the fine sediment (passed through the No. 200 ASTM sieve with $75\ \mu\text{m}$ openings) was obtained with a Malvern Mastersizer 2000 size analyzer, property of the Laboratório de Dinâmica de Sedimentos Coesivos, Área Engenharia Costeira & Oceanográfica department of the Universidade Federal do Rio de Janeiro, Brazil. The Mastersizer 2000 applies a laser diffraction technique to determine particles sizes based on the angular intensity of the scattered light.

There were small quantities of sediments larger than the No. 200 ASTM sieve (mass fraction under 5 % (Pedocchi et al., 2012; Santoro, 2017)). Therefore, a combination of sieving and photography technique was required to determine the remaining part of PSD. After sieving with Nos. 30 ($600\ \mu\text{m}$), 40 ($425\ \mu\text{m}$), 70 ($212\ \mu\text{m}$), 140 ($106\ \mu\text{m}$) and 200 ($75\ \mu\text{m}$) ASTM sieve series, the retained material was photographed with a Nikon D5200 camera and an AF-S VR Micro-Nikkor 105 mm f/2.8G IF-ED lens. The Nikon camera has 24.1 million effective pixels and the lens is a single-servo autofocus type, with a minimum focus distance of 0.314 m for resolution as high as $3.7\ \mu\text{m}/\text{pixel}$.

Photographs as the one appearing in Fig. 5.1 were then analyzed, and the shape of the delimited areas of every sediment particle was characterized, once some transformations and filters had been applied. An example of the grain boundaries obtained is shown in Fig. 5.2.

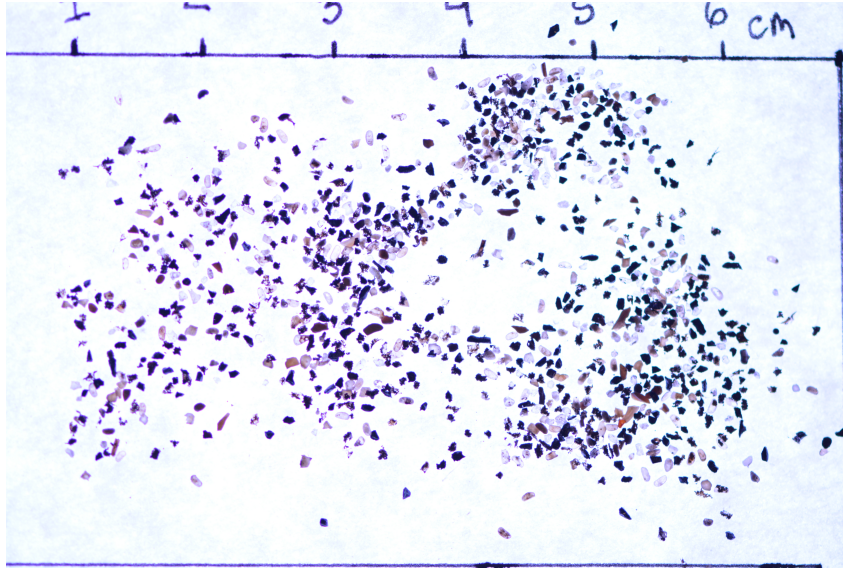


Figure 5.1: Photography of sediment retained by No. 40 ASTM sieve.

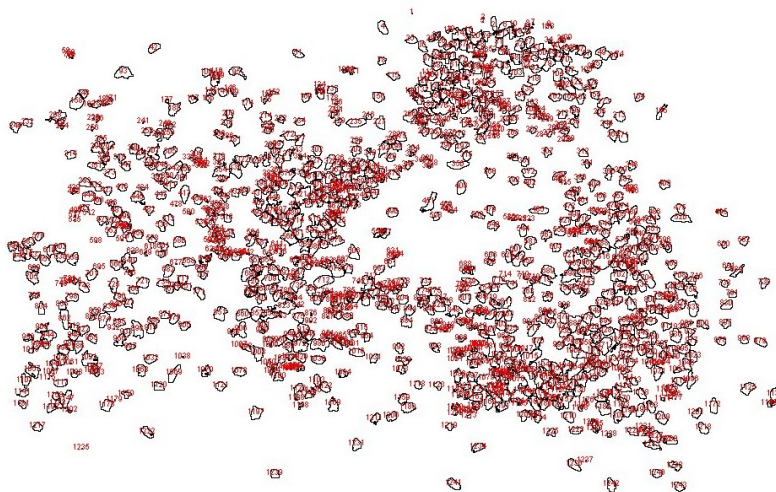


Figure 5.2: Grain boundaries of sediment retained by No. 40 ASTM sieve. The numbers in red particles numbered in the photography.

The PSD constructed with the Malvern Mastersizer and the sieve/photography techniques were fitted to three subordinate log-normal distributions in Table 5.1 (Classes 1, 2 and 4). The presence of sediment with radius in range from 10 to 100 μm could not be determined neither by Mastersizer nor by Nikon camera techniques. After a set of laboratory experiments in the mixing tank with ABS, a fourth sediment class within the same range ($a_{g3} = 29.40 \mu\text{m}$ and $\sigma_{g3} = 1.40$) was added to the PSD in order to fit the observed acoustic data. This acoustically determined sediment class, filled the gap of Malvern

Mastersizer and sieve/photography techniques as shown in Fig. 5.3. Using Eq. 3.101 proposed by Lee et al. (2012)

$$\frac{\partial C}{\partial \ln(a_s)} = \sum_{j=1}^4 \frac{c_j}{\sqrt{2\pi} \ln \sigma_{gj}} e^{-\frac{1}{2} \left(\frac{\ln(a_s/a_{gj})}{\ln \sigma_{gj}} \right)^2}, \quad (5.1)$$

and normalizing with $\sum_{j=1}^4 c_j = 100 \text{ g/m}^3$, the parameters of the different classes may be determined and are exhibited in Table 5.1.

Table 5.1: Fitted PSD parameters.

j	c_j (g/m ³)	a_{gj} (μm)	σ_{gj}
1	11.36	0.472	1.46
2	73.41	2.767	2.38
3	14.41	29.40	1.40
4	0.82	225.1	1.42

The data obtained with Mastersizer and Nikon camera techniques for the bottom sample appear as red dots in Figure 5.3. The four subordinate classes and their addition are shown as well. Even though the sediment Class 3 size is within the range size of flocculi (Lee et al., 2012), it was not possible to ensure its actual nature with the tools available during experiments. However, this sediment class resulted from the analysis of acoustic data and its detailed nature is not particularly relevant as long the scatterers in this class do not vary during measurements. This would be expected for fine sand or flocculi, which are composed of strongly bound clay particles and are considered to be extremely stable in nature.

5.2 ABS calibration and experiments

5.2.1 Ballotini glass spheres calibration.

AQUAscat[®] 1000R was delivered with calibration certificates for transducers, temperature and pressure gauges. Acoustic sensors were calibrated at the factory in a mixing tank with Ballotini glass spheres sieved to $\frac{1}{4}\phi$ with a sediment mean radius of 59.25 μm. ABS configuration included the following: bin size 1 cm; 0 dB gain in all channels; 4 profiles average; 4 Hz sampling rate. Water samples were collected to estimate the suspended sediment concentration at 0.57 m depth providing a mean sediment concentration of 0.391 g/l.

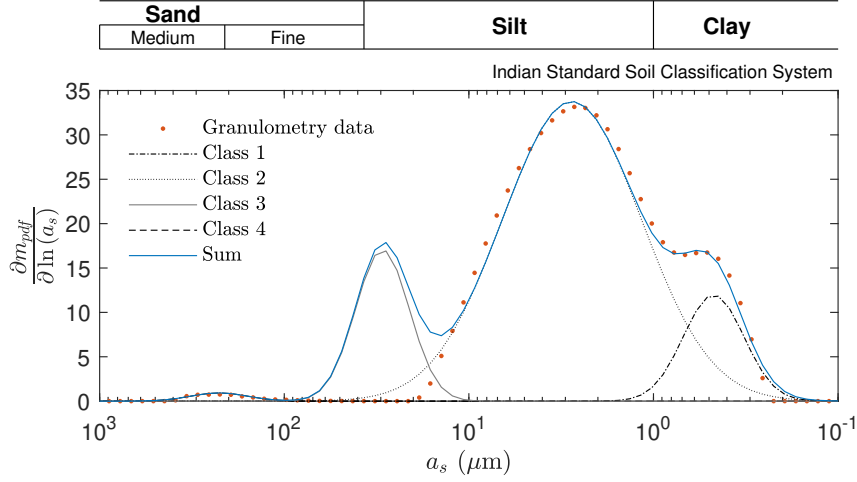


Figure 5.3: Bed granulometry data of both techniques (red dots), the different classes and the addition.

As the factory calibration constants determination procedure is not well documented, to avoid any bias the calibration files provided by AQUAtec were used to determine the constants K_t as described in Eq. 3.95 r within the range 0.5 to 1.5 m. This range was selected in order to avoid the transducers' near field as well as reflections coming from the bottom of the tank. Sound speed c_s and α_w were calculated using Francois and Garrison (1982) even though this formula was developed in the range of frequencies from 200 Hz to 1 MHz. The root mean square of the recorded backscatter signal profiles with No Sediment $\text{RMS}(V_{noise})$ and in presence of $c = 0.391 \text{ kg/m}^3$ $\text{RMS}(V_{rec})$, as well as the Theoretical curves using Eq. 3.95 for each transducer, are shown in Figures 5.4 and 5.5.

As K_t is an estimate of the observed data set of a Rayleigh distribution function, a 95 % Confidence Interval (95 % CI) for K_t can be determined as $[K_{tl}, K_{tu}]$

$$K_{tl} = \sqrt{\frac{2N_s}{b}} K_t, \quad K_{tu} = \sqrt{\frac{2N_s}{a}} K_t, \quad (5.2)$$

with N_s the number of samples used in the estimation, a and b such as

$$P(\chi^2(2N_s) \leq a^2) = 2.5\%, \quad P(\chi^2(2N_s) \leq b^2) = 97.5\%, \quad (5.3)$$

where χ^2 is the chi-squared distribution. The calibration results can be seen

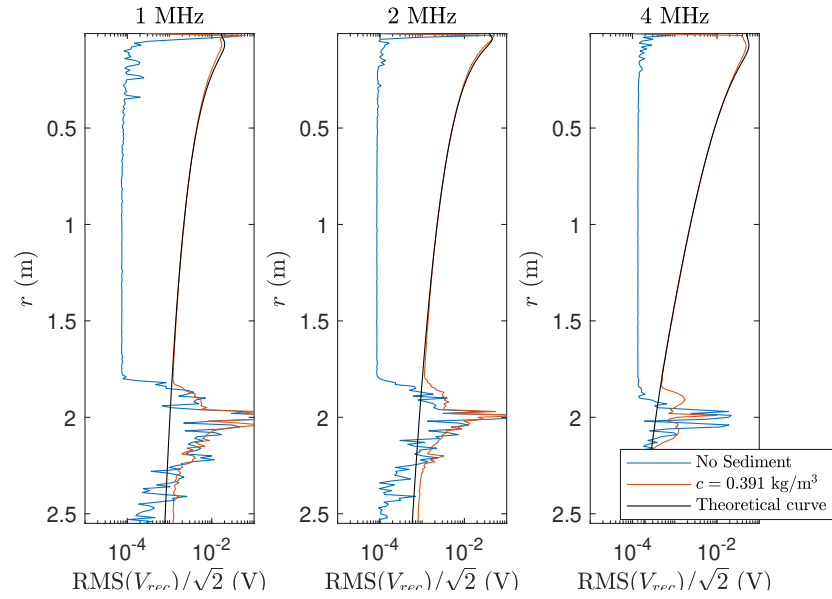


Figure 5.4: Measurements of acoustic backscatter of transducers 1, 2 and 4 MHz during the AQUAscatter[®] calibration.

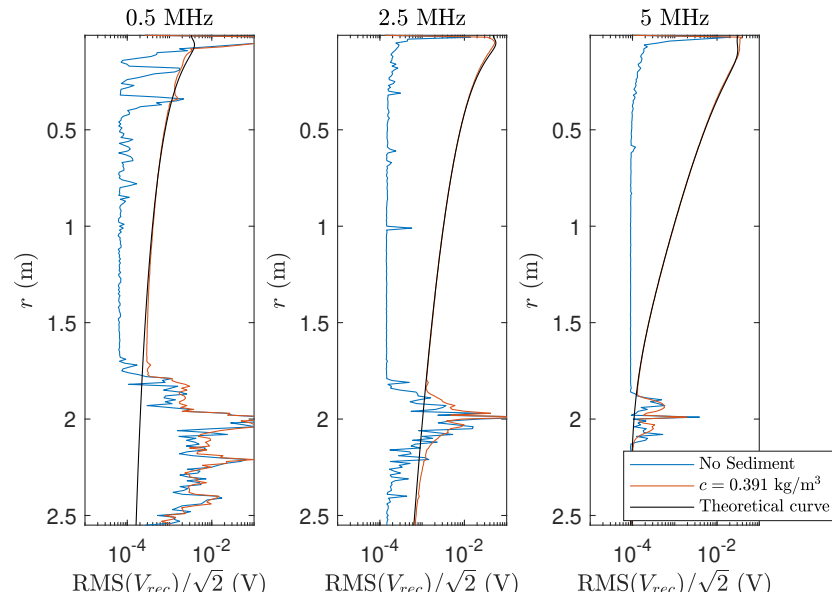


Figure 5.5: Measurements of acoustic backscatter of transducers 0.5, 2.5 and 5 MHz during the AQUAscatter[®] calibration.

in Table 5.2.

Table 5.2: Transducers calibration parameters K_t with the corresponding 95 % Confidence Intervals and mean square noise MS (V_{noise}) during calibration.

f_s (MHz)	K_t ($10^{-3}\text{Vm}^{3/2}$)	and 95 % CI	MS (V_{noise}) (10^{-9}V^2)
0.5	13.959	[13.926, 13.992]	7.627
1	20.974	[20.925, 21.023]	10.594
2	7.728	[7.710, 7.746]	14.180
2.5	9.206	[9.185, 9.228]	40.056
4	9.817	[9.794, 9.840]	35.274
5	9.217	[9.196, 9.239]	16.093

5.2.2 Río de la Plata sediment.

By means of laboratory experiments [Moate and Thorne \(2012\)](#) analyzed the variability of sediment acoustic parameters with different mineralogical compositions such as quartz, crushed shell fragments, aragonite, muscovite mica, olivine, zircon and magnetite. Measurements showed significant differences for $\langle f \rangle$ and $\langle \chi \rangle$ proving the relevance of mineralogical composition in acoustic scattering. In order to understand the differences and to avoid biases in the interpretation of acoustic field data, a series of laboratory experiments were performed using Río de la Plata sediment samples. The equipment included a transparent acrylic square prism mixing tank, whose base side is 60 cm side and its height 1.5 m. Four stainless steel paddles were used for mixing, whose dimensions are 1.2 m of height and 15 cm of width. They are positioned in each corner and are propelled by 4 engines powered by a variable-frequency drive. A peristaltic pump is applied to extract samples at different heights from seven water sampler ports. The AQUAscat[®] 1000R 0.5, 1, 2 and 4 MHz transducers were positioned at the top of the tank, facing downwards to insonify the central region as shown in [Fig. 5.6](#).

Approximately twenty four hours after the tank had been filled with tap water, in order to allow the water to degas and reach ambient temperature, ABS measurements were made to determine the background signal level. The dispersed material was incorporated into the mixing tank. One hour later, the mixture had been reached equilibrium and the paddles were stopped. The ABS initiated registration and water samples were collected. Suspended sediment concentration c was determined by gravimetric analysis of water samples. Water temperature was monitored using a standard alcohol-filled thermometer at middle depth.

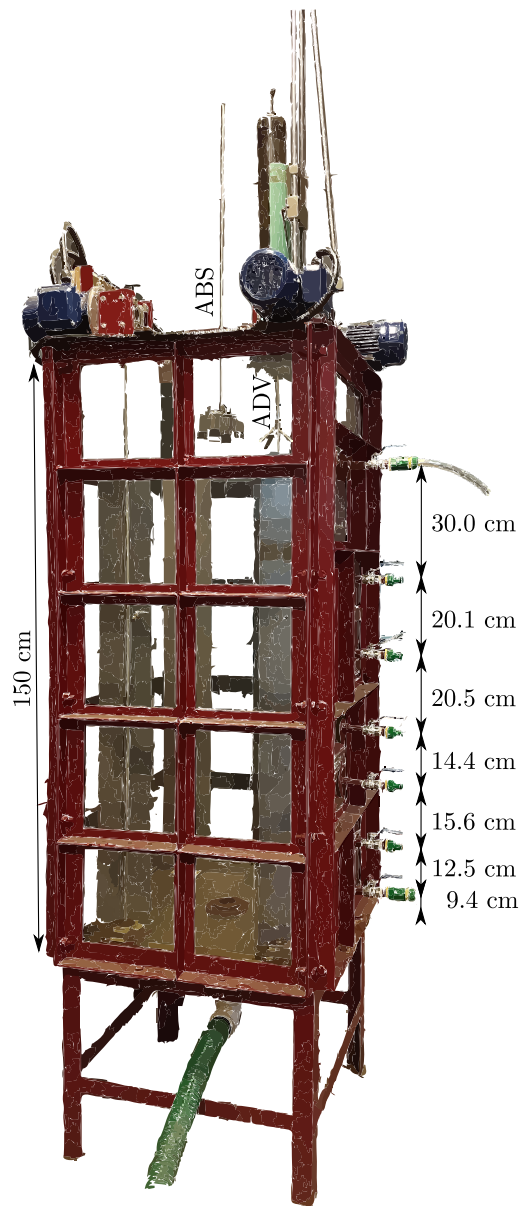


Figure 5.6: Acoustic sediment calibration set-up at the IMFIA's facilities.

Five different field scenarios were simulated in the laboratory:

- Firstly, during calm periods, when currents and waves are weak, the presence of suspended sand is negligible. The backscattered energy of some of the acoustic frequencies used in the deployment is very sensitive to the presence of sand. Thus, the material passing through No. 200 ASTM sieve was studied in the first place.
- Secondly, in order to understand changes caused by salinity, sodic chloride was incorporated into the mixture to observe variation in the ABS

data.

- Thirdly, the sediment was left to consolidate for a week and the re-suspended sediment was analyzed. It presented denser aggregates.
- Commercial flocculant was added to the tank mixture to complete the flocculated sediment analysis.
- Finally, the non-sieved Río de la Plata sediment was measured.

Also, high concentration sediment mixtures were acoustically irradiated in order to know learn about the scattering theory applicability limitations.

Using Eqs. 3.72, 3.73 and 3.74, theoretical curves of the acoustic parameters f and χ were calculated assuming the presence of quartz sediment classes in the water column shown in the upper panels of Figures 5.8, 5.10, 5.12, 5.14 and 5.16. Combining them with Eq. 3.88, Eq. 3.89 and the corresponding m_{pdf} (see Table 5.1), the acoustic parameters $\langle f \rangle$ and $\langle \chi \rangle$ of the sediment PSD were calculated and labeled as Theoretical parameters \circ in the upper and middle panel of Figures 5.8, 5.10, 5.12, 5.14 and 5.16 and Tables 5.3 to 5.7. As both $\langle f \rangle$ and $\langle \chi \rangle$ are the result of integrating f^2 and χ times $\frac{m_{pdf}}{a_s} da_s$, $m_{pdf} \Delta a_s / a_s$ curves for each frequency were also calculated and are shown in the lower panel of said Figures. Independent estimations of $\langle f \rangle$ and $\langle \chi \rangle$ using only the acoustic data from the laboratory experiments were obtained by fitting the acoustic profiles to Eq. 3.83, and labeled as fitted parameters \diamond in Figures and Tables mentioned above.

Figures 5.7, 5.9, 5.11, 5.13 and 5.15 show the acoustic profiles of each transducer and simulated scenario with Theoretical and Fitted curves obtained with the corresponding acoustic parameters. Theoretical and Fitted acoustic parameters and curves were calculated assuming that both sediment mass concentration and granulometry remain unchanged in the entire water column.

The $MS(V_{noise})$ in the laboratory experiments was determined by analyzing the end of sufficiently large acoustic data profiles, as explained in Section 3.7. As r increases, V_{rms} decreases due to attenuation, and only the noise in the recorded signal V_{rec} remains. This can be appreciated in the acoustic profiles, as those appearing in Fig. 5.7, since $MS(V_{rec})$ tends to be a constant far from the transducer.

Río de la Plata fine sediment

The mean square root registered for recorded voltage $\text{RMS}(V_{rec})$ with a fine sediment mass concentration $c = 2.539 \text{ kg/m}^3$ is shown in Fig. 5.7. Theoretical profiles were determined separately from the experiment, and are consistent with the acoustic data registered and with the fitted curves. This indicates that Classes 1 and 2 shown in Table 5.1 explain the scattering observed in the laboratory. It appears that the 500 kHz frequency acoustic profile is noisy. This issue may also be observed in the calibration data shown in Fig. 5.5. The directivity pattern (see $\theta_{-3\text{dB}}$ in Table 3.1) for this transducer is wide, considering that both calibration tanks are rather narrow.

Figure 5.8 shows estimations of $\langle f \rangle$ and $\langle \chi \rangle$ of the sediment PSD for transducers 0.5, 1, 2 and 4 MHz, and the fitted parameters. The 95 % Confidence Interval of the fitted parameters, calculated with the usual hypothesis of the least-squares regression (Wilks, 2011), is also shown. Table 5.3 summarizes the dimensionless $k \langle a_1 \rangle$, $\langle f \rangle$ and $\langle \chi \rangle$ values presented in Fig. 5.8 for each transducer.

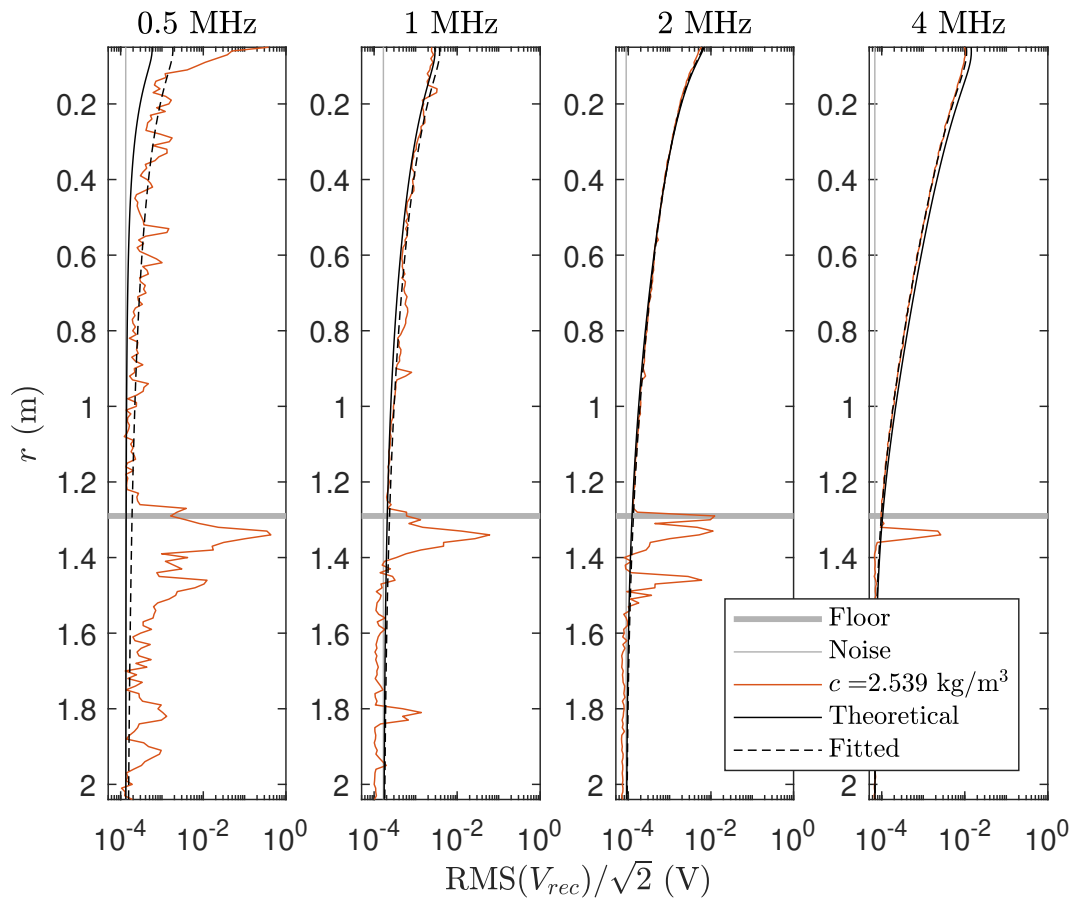


Figure 5.7: Measurements of acoustic backscatter of 0.5, 1, 2 and 4 MHz transducers with Río de la Plata sediment sieved with No. 200 ASTM. The thick gray line indicates the position of the tank floor.

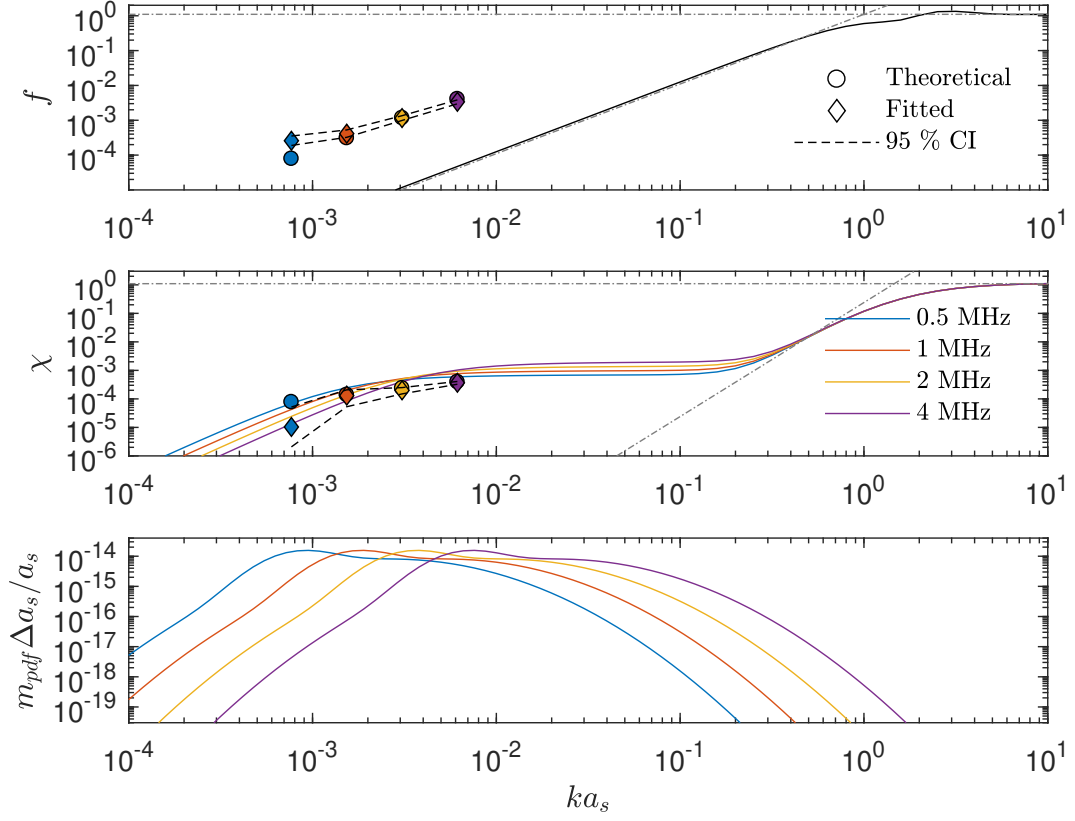


Figure 5.8: The symbol \circ represents estimations of theoretical $\langle f \rangle$ and $\langle \chi \rangle$ for 0.5, 1, 2 and 4 MHz transducers using Eqs. 3.88. The symbol \diamond represents the result of the fitted curve of each acoustic profile using Eqs. 3.83 and the dashed line for the corresponding 95 % CI.

Table 5.3: Numerical values of acoustic parameters in Figure 5.8

f_s (MHz)	$k \langle a_1 \rangle$	Theoretical		Fitted	
		$\langle f \rangle$	$\langle \chi \rangle$	$\langle f \rangle$	$\langle \chi \rangle$
0.5	7.67×10^{-4}	7.91×10^{-5}	7.80×10^{-5}	2.58×10^{-4}	1.04×10^{-5}
1	1.53×10^{-3}	3.10×10^{-4}	1.39×10^{-4}	4.13×10^{-4}	1.30×10^{-4}
2	3.07×10^{-3}	1.17×10^{-3}	2.39×10^{-4}	1.16×10^{-3}	1.99×10^{-4}
4	6.14×10^{-3}	4.09×10^{-3}	3.95×10^{-4}	3.38×10^{-3}	3.68×10^{-4}

Río de la Plata fine sediment and salt

In this experiment, sodic chloride was also incorporated into the mixture increasing salinity to 10.4 psu. Results are shown in Figures 5.9 and 5.10.

Although flocculation induced by sodic chloride had an effect on the behavior of the sediment mixture, namely, it accelerated the sedimentation process, the acoustic parameters were similar to those from tap water. In other words, when taking samples with the ABS, both fitted $\langle f \rangle$ and $\langle \chi \rangle$ parameters were in the range of uncertainty of the previous experiment. Nevertheless, after the mixing ended, the settling phase was visually faster than the fresh water experiment, indicating that the salt induced flocculation changed the suspended matter aggregation.

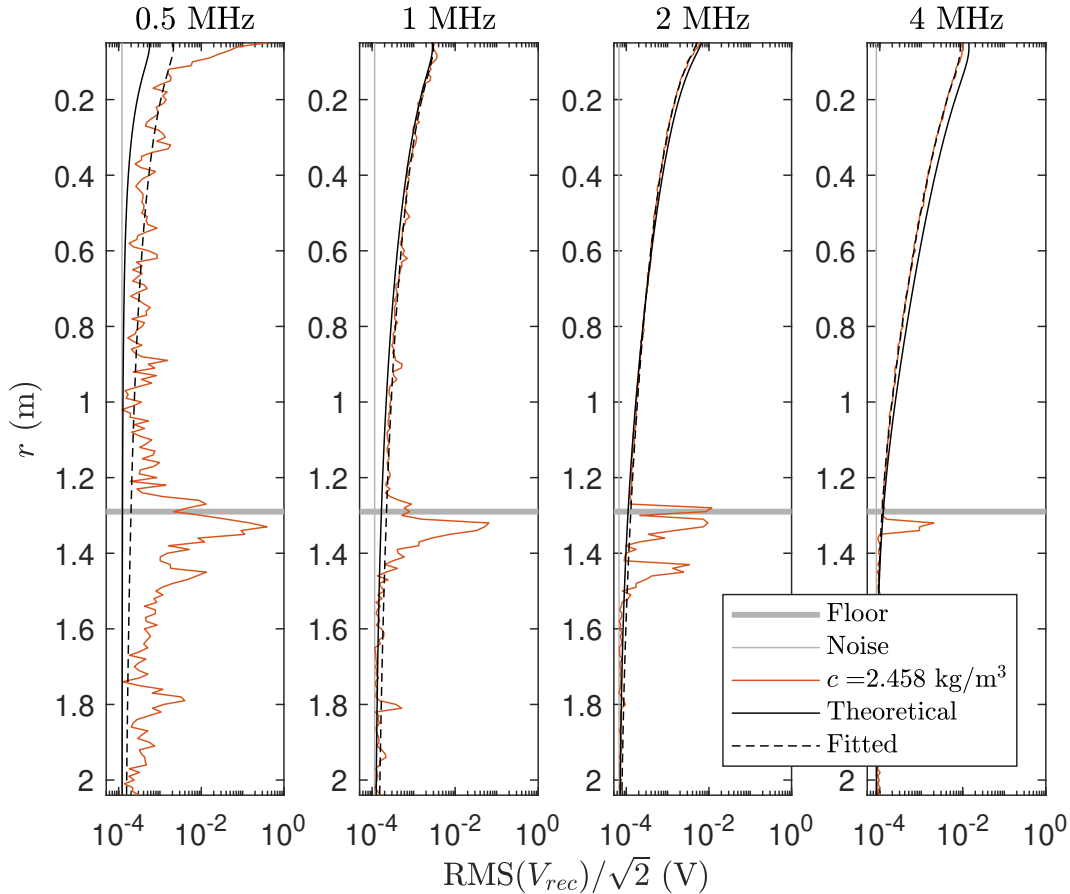


Figure 5.9: Measurements of acoustic backscatter of 0.5, 1, 2 and 4 MHz transducers with Río de la Plata sediment sieved with No. 200 ASTM and salinity of 10.4 psu. The thick gray line indicates the position of the tank floor.

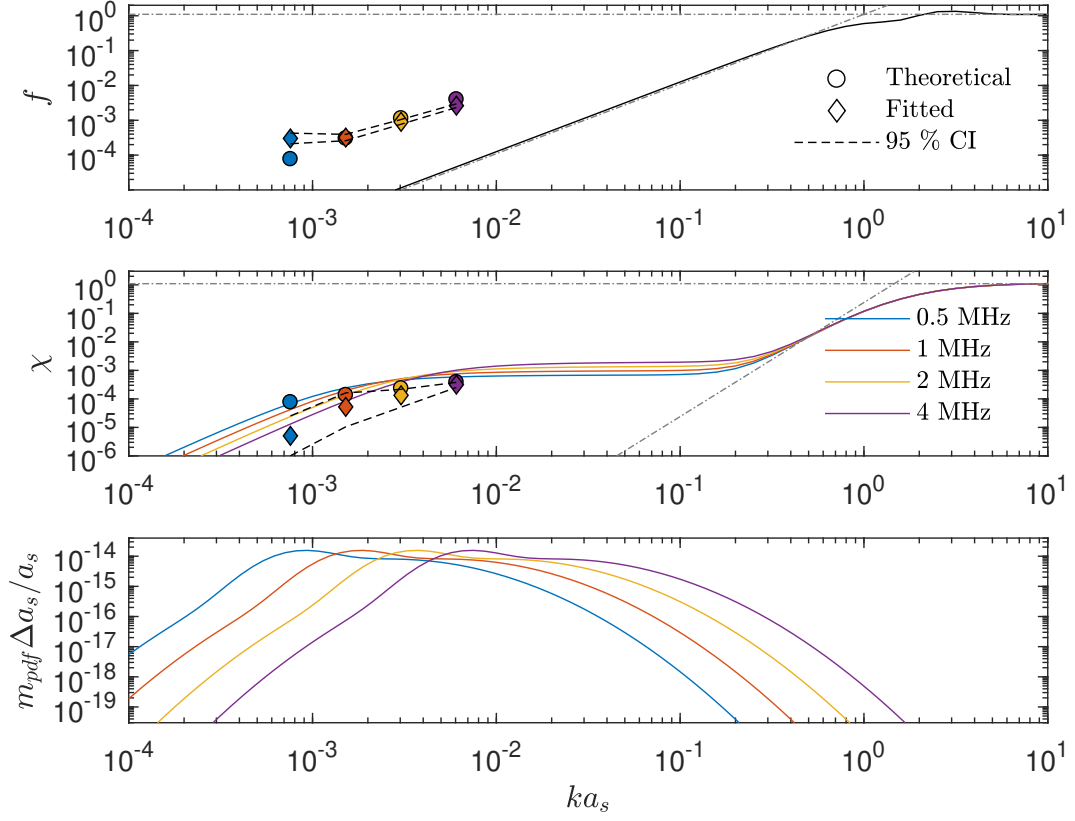


Figure 5.10: The symbol \circ represents estimations of theoretical $\langle f \rangle$ and $\langle \chi \rangle$ for 0.5, 1, 2 and 4 MHz transducers using Eqs. 3.88. The symbol \diamond represents the result of the fitted curve of each acoustic profile using Eqs. 3.83 and the dashed line for the corresponding 95 % CI.

Table 5.4: Numerical values of acoustic parameters in Figure 5.10

f_s (MHz)	$k \langle a_1 \rangle$	Theoretical		Fitted	
		$\langle f \rangle$	$\langle \chi \rangle$	$\langle f \rangle$	$\langle \chi \rangle$
0.5	7.58×10^{-4}	7.72×10^{-5}	7.70×10^{-5}	3.01×10^{-4}	5.05×10^{-6}
1	1.52×10^{-3}	3.03×10^{-4}	1.37×10^{-4}	3.19×10^{-4}	5.24×10^{-5}
2	3.03×10^{-3}	1.14×10^{-3}	2.36×10^{-4}	9.00×10^{-4}	1.34×10^{-4}
4	6.06×10^{-3}	4.00×10^{-3}	3.90×10^{-4}	2.62×10^{-3}	3.16×10^{-4}

Río de la Plata fine sediment, salt and consolidation-resuspension cycle

To analyze one additional aggregation state, consolidation of sediments was allowed during one week and then re-suspension was achieved by the stainless steel paddles, emulating some of the cycles occurring in the field data. Associated results are shown in Figures 5.11 and 5.12.

Similarly, acoustic parameters did not vary in relation to the previous ones. Thus, the ABS estimations of suspended sediments are not biased by “natural” flocculation in the Río de la Plata.

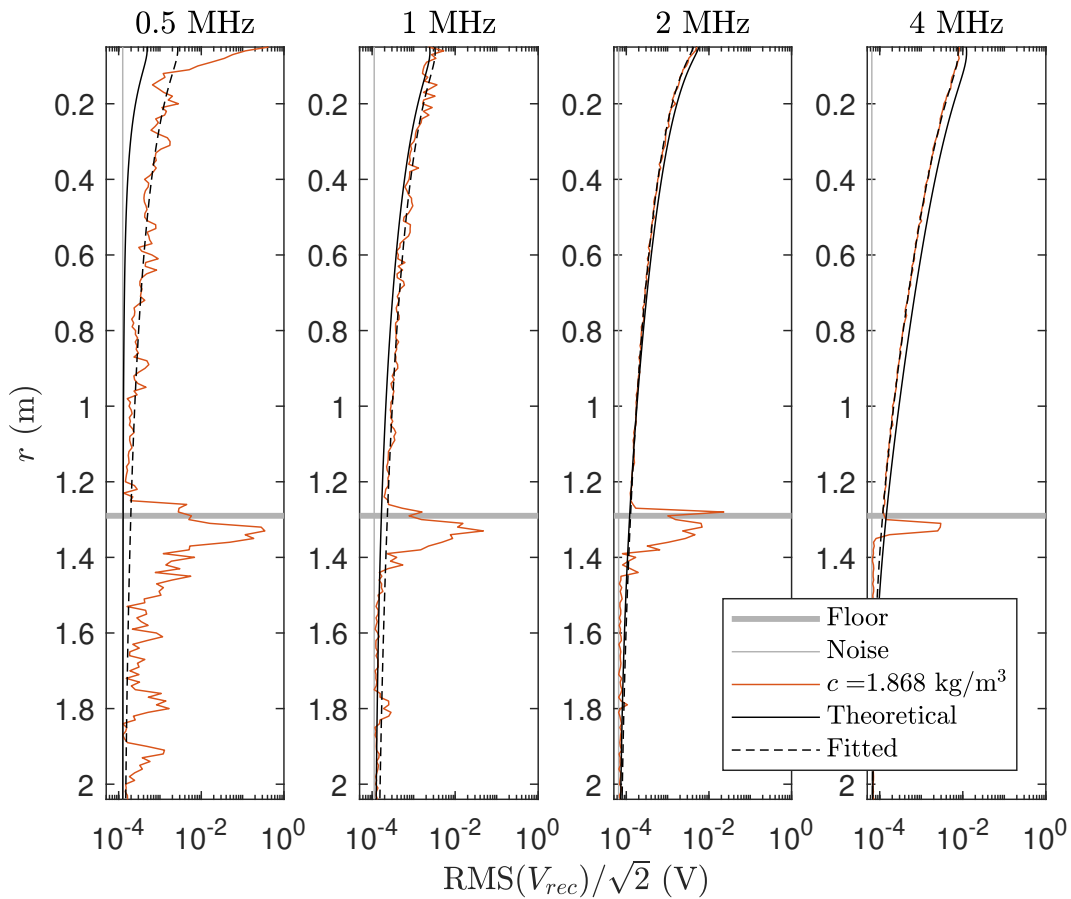


Figure 5.11: Measurements of acoustic backscatter of 0.5, 1, 2 and 4 MHz transducers with Río de la Plata sediment sieved with No. 200 ASTM, salinity of 10.4 psu and a consolidation-resuspension cycle. The thick gray line indicates the position of the tank floor.

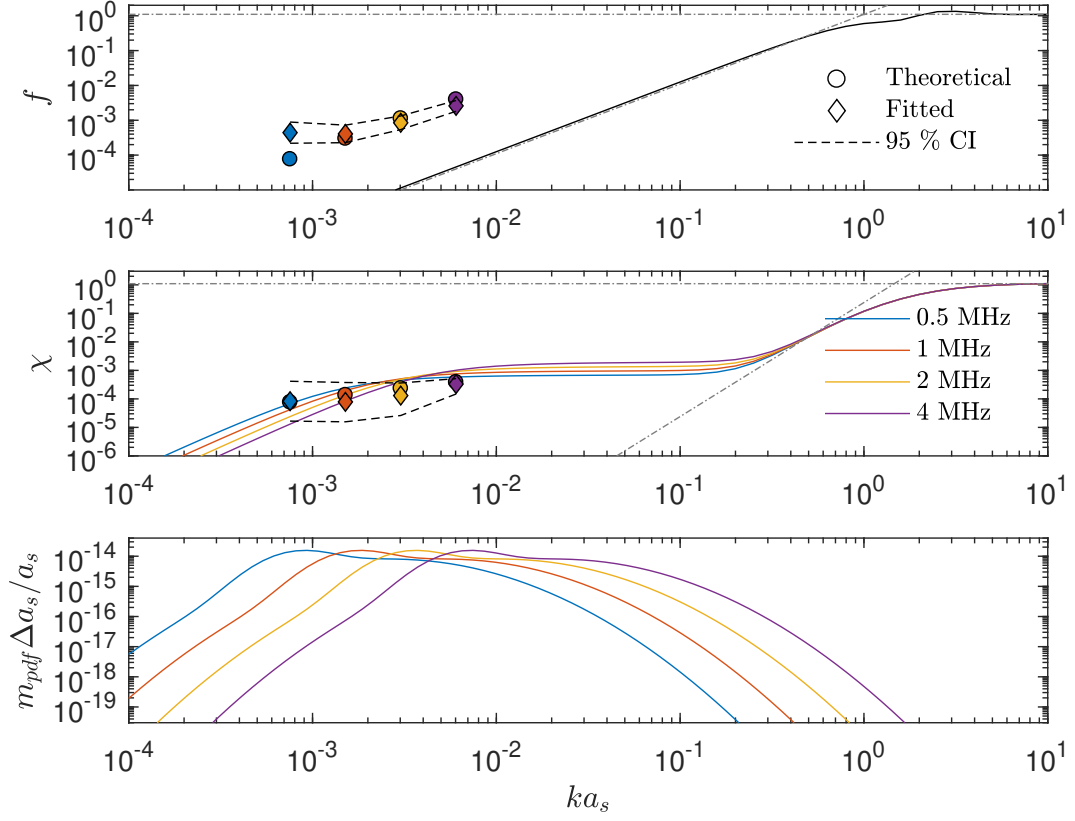


Figure 5.12: The symbol \circ represents estimations of theoretical $\langle f \rangle$ and $\langle \chi \rangle$ for 0.5, 1, 2 and 4 MHz transducers using Eqs. 3.88. The symbol \diamond represents the result of the fitted curve of each acoustic profile using Eqs. 3.83 and the dashed line for the corresponding 95 % CI.

Table 5.5: Numerical values of acoustic parameters in Figure 5.12

f_s (MHz)	$k \langle a_1 \rangle$	Theoretical		Fitted	
		$\langle f \rangle$	$\langle \chi \rangle$	$\langle f \rangle$	$\langle \chi \rangle$
0.5	7.55×10^{-4}	7.65×10^{-5}	7.67×10^{-5}	4.41×10^{-4}	8.31×10^{-5}
1	1.51×10^{-3}	3.01×10^{-4}	1.37×10^{-4}	4.06×10^{-4}	7.85×10^{-5}
2	3.02×10^{-3}	1.14×10^{-3}	2.35×10^{-4}	8.47×10^{-4}	1.31×10^{-4}
4	6.04×10^{-3}	3.97×10^{-3}	3.88×10^{-4}	2.59×10^{-3}	3.31×10^{-4}

Río de la Plata fine sediment and flocculant

After performing a number of laboratory experiments with kaolin suspensions and commercial flocculant, [MacDonald et al. \(2013\)](#) concluded that scattering properties of cohesive fine sediments are affected by aggregation due to flocculation processes. In these experiments, calculations of the scattering parameters under the assumption that only primary particles are to be considered, leads to incorrect estimations. In the referred work, two models are introduced to indicate range limits for the scattering parameters of the flocculated particles. Since in all three previous experiments, acoustic parameters could be explained solely with primary particles, a commercial flocculant was added to register variations caused by aggregation. Results are shown in Figures 5.13 and 5.14.

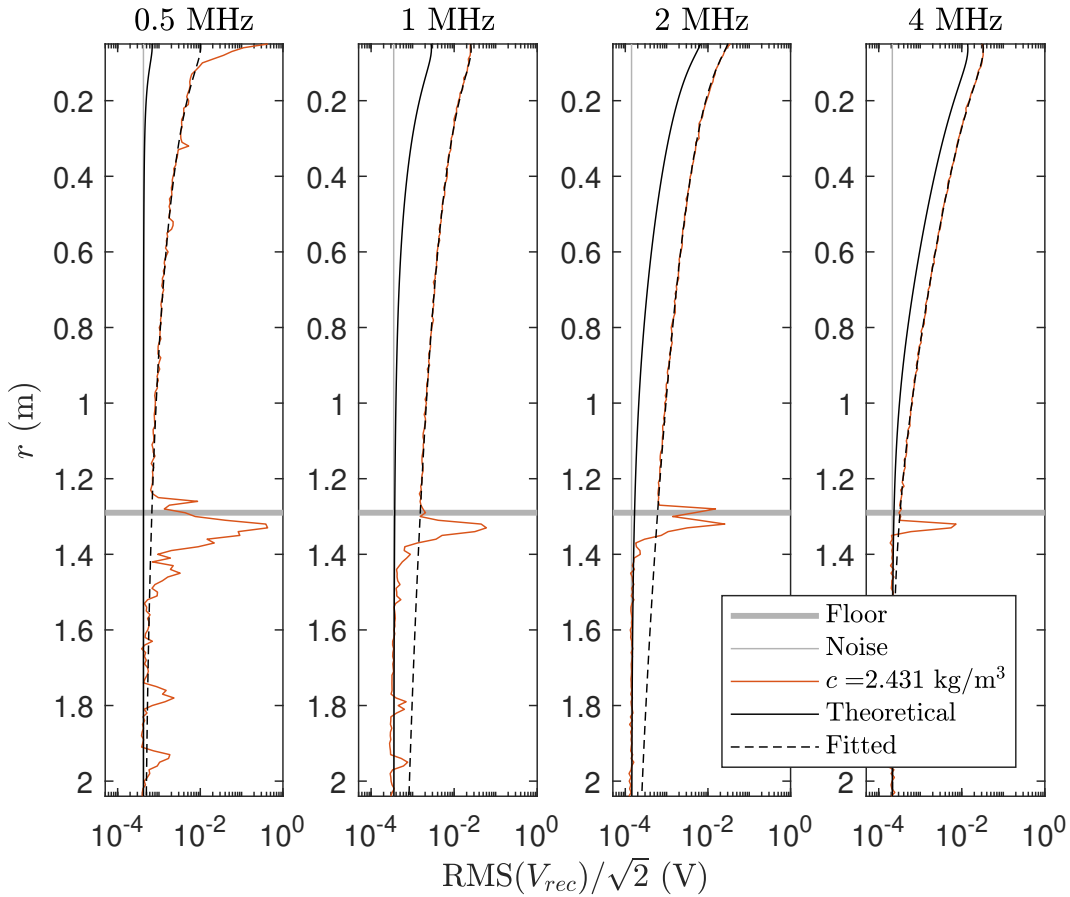


Figure 5.13: Measurements of acoustic backscatter of 0.5, 1, 2 and 4 MHz transducers with Río de la Plata sediment sieved with No. 200 ASTM and commercial flocculant. The thick gray line indicates the position of the tank floor.

In this case, fitted estimations of $\langle f \rangle$ are higher than theoretical ones. As proposed by [MacDonald et al. \(2013\)](#), this artificially flocculated mixture

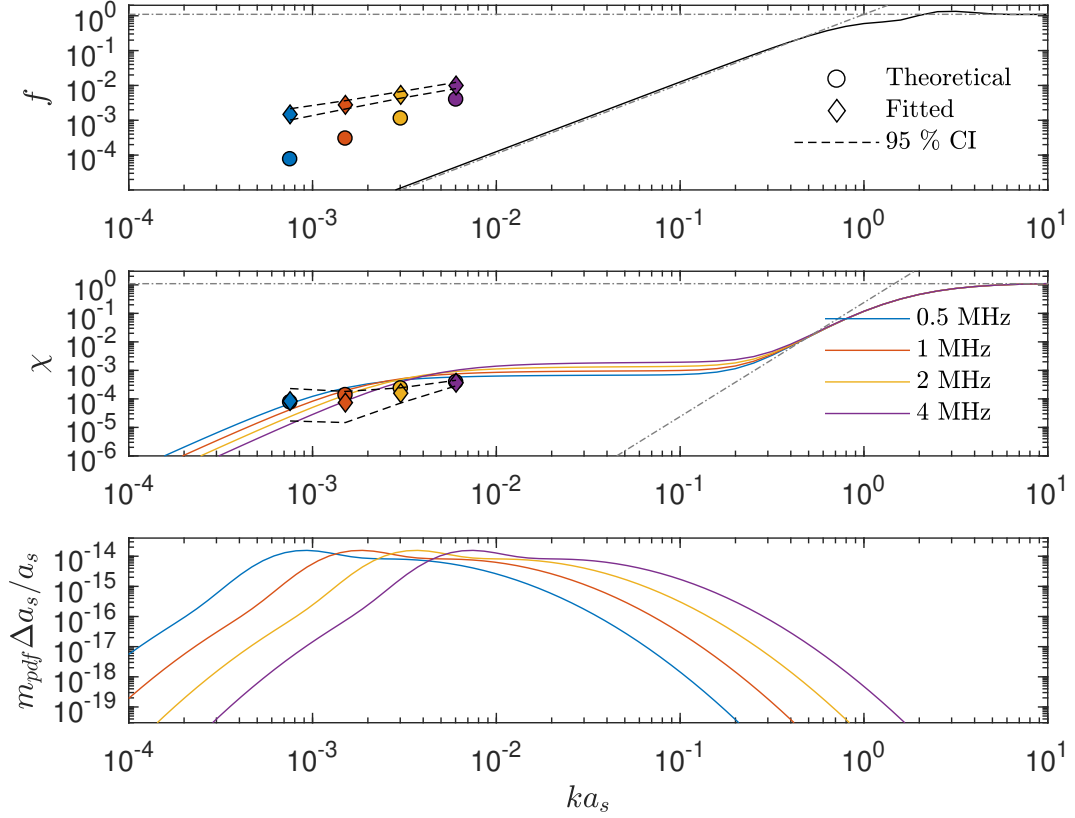


Figure 5.14: The symbol \circ represents estimations of theoretical $\langle f \rangle$ and $\langle \chi \rangle$ for 0.5, 1, 2 and 4 MHz transducers using Eqs. 3.88. The symbol \diamond represents the result of the fitted curve of each acoustic profile using Eqs. 3.83 and the dashed line for the corresponding 95 % CI.

Table 5.6: Numerical values of acoustic parameters in Figure 5.14

f_s (MHz)	$k \langle a_1 \rangle$	Theoretical		Fitted	
		$\langle f \rangle$	$\langle \chi \rangle$	$\langle f \rangle$	$\langle \chi \rangle$
0.5	7.55×10^{-4}	7.65×10^{-5}	7.67×10^{-5}	1.47×10^{-3}	8.40×10^{-5}
1	1.51×10^{-3}	3.01×10^{-4}	1.37×10^{-4}	2.77×10^{-3}	7.39×10^{-5}
2	3.02×10^{-3}	1.14×10^{-3}	2.35×10^{-4}	5.35×10^{-3}	1.58×10^{-4}
4	6.04×10^{-3}	3.97×10^{-3}	3.88×10^{-4}	9.97×10^{-3}	3.68×10^{-4}

has some emergent properties because of the aggregation configuration. The lower panel of Fig. 5.14 shows that $m_{pdf}\Delta a_s/a_s$ curves are mainly within the Rayleigh regime, as in previous experiments. When all sediment particle backscattering are within the Rayleigh regime ($ka_s \ll 1$), different $\langle f \rangle$ of each sound frequency in the Log-Log plot should draw a parallel line relative to $(ka_s)^2$ as predicted in Eq. 3.72 (Thorne and Meral, 2008). The most remarkable feature in this experiment is that, although the fitted estimations of $\langle f \rangle$ vs $k \langle a_1 \rangle$ are aligned, the line no longer parallel to $(ka_s)^2$, suggesting that the aggregation state backscatters as a larger “particle” beyond the Rayleigh regime.

Río de la Plata sediment

Non-sieved Río de la Plata sediment mixture was used for this experiment. Each one of the four classes described in Section 5.1 (Table 5.1) was used for the theoretical estimations. Although theoretical and fitted estimates there appears a wider CI. Fluctuations in fine sand (Class 4) concentrations explain the wide 95 % CI registered in the experiment.

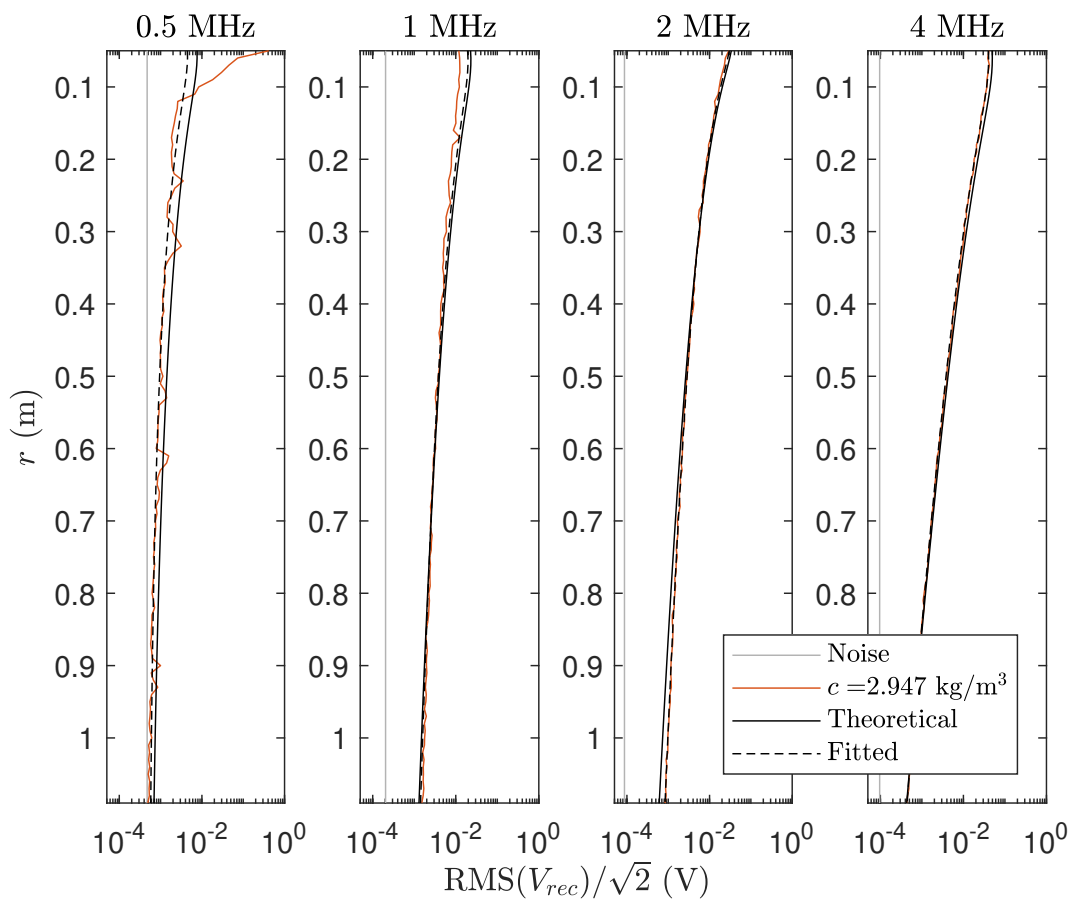


Figure 5.15: Measurements of acoustic backscatter of 0.5, 1, 2 and 4 MHz transducers with Río de la Plata sediment.

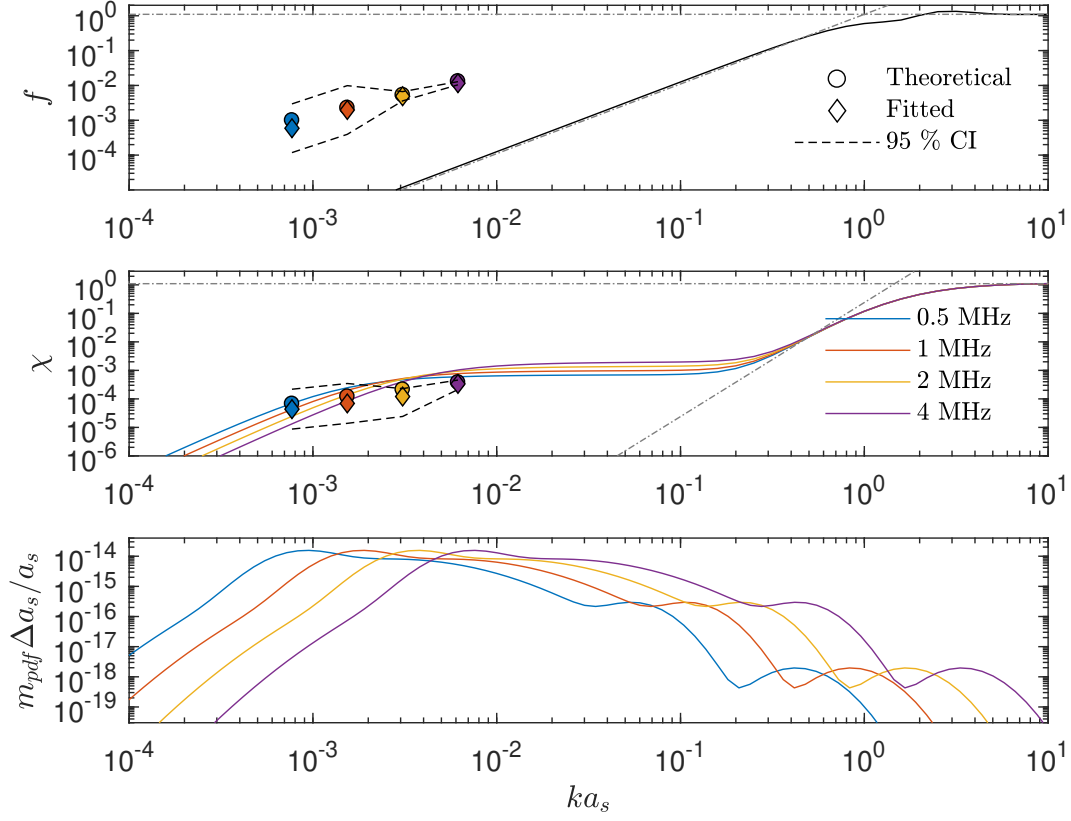


Figure 5.16: The symbol \circ represents estimations of theoretical $\langle f \rangle$ and $\langle \chi \rangle$ for 0.5, 1, 2 and 4 MHz transducers using Eqs. 3.88. The symbol \diamond represents the result of the fitted curve of each acoustic profile using Eqs. 3.83 and the dashed line for the corresponding 95 % CI.

Table 5.7: Numerical values of acoustic parameters in Figure 5.16

f_s (MHz)	$k \langle a_1 \rangle$	Theoretical		Fitted	
		$\langle f \rangle$	$\langle \chi \rangle$	$\langle f \rangle$	$\langle \chi \rangle$
0.5	7.69×10^{-4}	1.00×10^{-3}	6.78×10^{-5}	5.90×10^{-4}	4.36×10^{-5}
1	1.54×10^{-3}	2.29×10^{-3}	1.22×10^{-4}	1.97×10^{-3}	6.93×10^{-5}
2	3.08×10^{-3}	5.34×10^{-3}	2.14×10^{-4}	4.89×10^{-3}	1.21×10^{-4}
4	6.15×10^{-3}	1.32×10^{-2}	3.82×10^{-4}	1.16×10^{-2}	3.35×10^{-4}

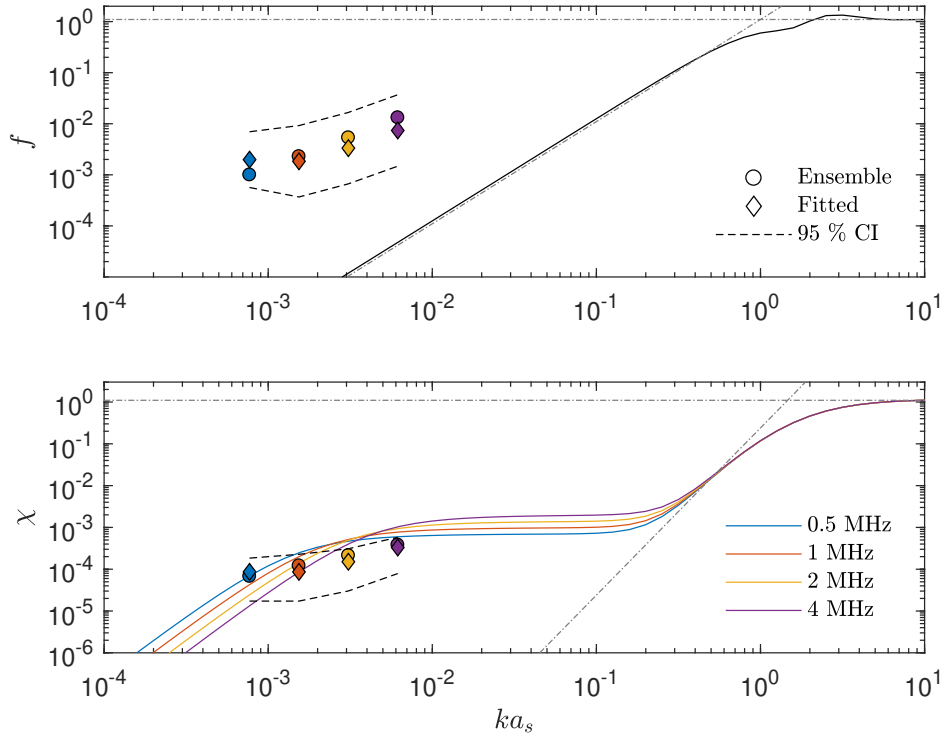


Figure 5.17: The symbol \circ represents estimations of theoretical $\langle f \rangle$ and $\langle \chi \rangle$ for 0.5, 1, 2 and 4 MHz transducers using Eqs. 3.88. The symbol \diamond represents the result of the fitted curve of each acoustic profile with $c = 75 \text{ kg/m}^3$ using Eqs. 3.83 and the dashed line for the corresponding 95 % CI.

Scattering parameter limits

In order to comprehend the limitations of the acoustic theory used in this work, high concentrated non-sieved Río de la Plata sediment mixtures were measured in the laboratory. With a small container of 40 cm of height, $c = 75 \text{ kg/m}^3$ and 155 kg/m^3 were achieved. Theoretical and fitted estimates of both $\langle f \rangle$ and $\langle \chi \rangle$ were calculated with satisfactory consistency for $c = 75 \text{ kg/m}^3$ (see Figure 5.17). The symbol \circ represents estimations of theoretical $\langle f \rangle$ and $\langle \chi \rangle$ for 0.5, 1, 2 and 4 MHz transducers using Eqs. 3.88. The symbol \diamond represents the result of the fitted curve of each acoustic profile using Eqs. 3.83 and the dashed line for the corresponding 95 % CI.

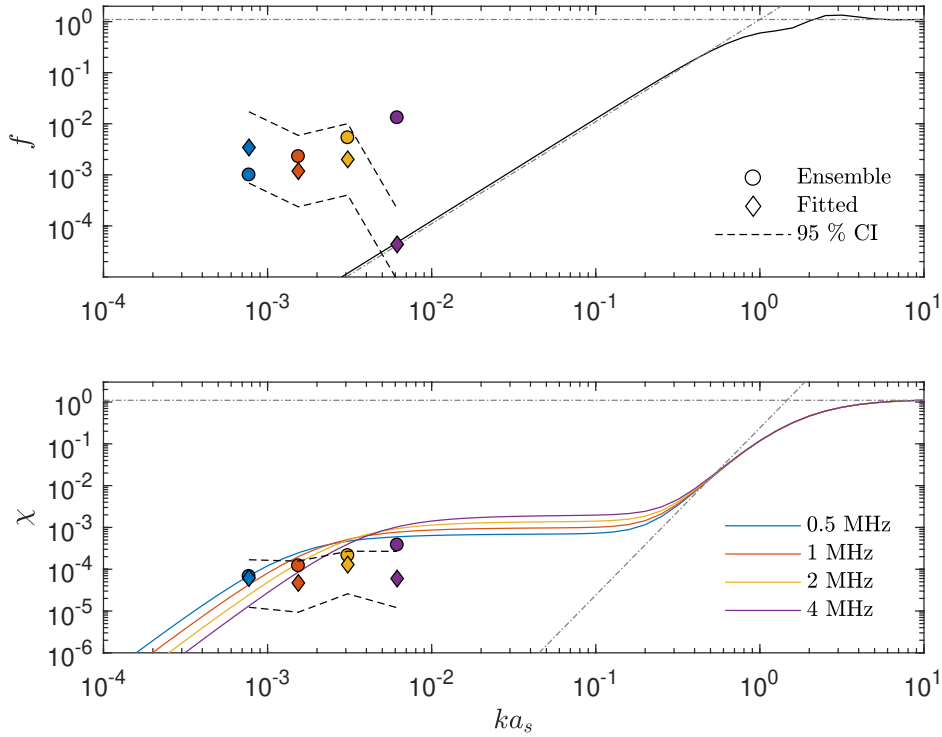


Figure 5.18: The symbol \circ represents estimations of theoretical $\langle f \rangle$ and $\langle \chi \rangle$ for 0.5, 1, 2 and 4 MHz transducers using Eqs. 3.88. The symbol \diamond represents the result of the fitted curve of each acoustic profile with $c = 155 \text{ kg/m}^3$ using Eqs. 3.83 and the dashed line for the corresponding 95 % CI.

Instead, higher sediment concentration $c = 155 \text{ kg/m}^3$ registers a significant bias on both acoustic parameters as show in Figure 5.18.

5.3 Turbidity meters calibration

Turbidity is associated to optical properties which result in lack of transparency of water since suspended and dissolved matter scatters and absorbs light. In general, mineral-based solids reflect more light, while organic particles tend to absorb it. The higher concentration of suspended matter in water, the higher its turbidity. Turbidity sensors use near infrared (NIR) electromagnetic radiation (from 780 to 2500 nm) and photodiode for detecting the intensity of the light scattered by suspended particles in water. NIR is rarely absorbed, therefore it is not affected by dissolved colored material. The distance traveled by scattered light also alters the turbidity readings. The longer the light path between source and detector, the better the instrument resolution at low turbidity levels. However, increasing the light path length compromises measurement range.

Several different units may be defined to quantify turbidity depending on the type of light source, detector, angle of measurement, standard substance and equipment. After the development of formazin, it has been used as a calibration standard substance and Formazin Turbidity Units (FTU) have been adopted. These units, however, do not specify the instrument source-sensor array. Nephelometry consists of the measurement of light scattered by suspended particles in perpendicular direction to the incident beam. NTU stands for Nephelometric Turbidity Unit implying that the sensor measures scattered light from the sample at a 90 ° angle from the incident light. Although NTU and FTU may be based on calibrations that apply the same formazin primary standard, the value on water samples with suspended sediment might differ significantly. AMCO Clear is another primary standard which is used in OBS-3+ Campbell Scientific calibration of turbidity.

Analogously to acoustic scattering (Section 3.5), when a particle is considerably smaller than the wavelength of light, the scattering is fairly symmetrical in every direction. Larger particles scatter more light away from the light beam. This is one of the reasons why turbidity measurements made through different methods are often not comparable, because when the light source differs, light scattering will differ. As in every other optical turbidity sensor, Seapoint Turbidity Meter (STM) and Optical Backscatter Sensor (OBS) responses depend on the size, composition, and shape of suspended particles. Therefore, Río de la Plata sediments from the deployment site were used to establish the relation

between turbidity units and sediment mass concentration c . The sediment calibration procedure is described by Campbell (2014). It was performed in a 43 l, container as appears in Figure 5.19. Considering the range of the field data collected with both turbidimeters, five different mixtures of up to 2000 g/m^3 were measured with OBS-3+ and STM. Figure 5.20 includes results for both instruments and the calibration curves.



Figure 5.19: Turbidity calibration set-up.

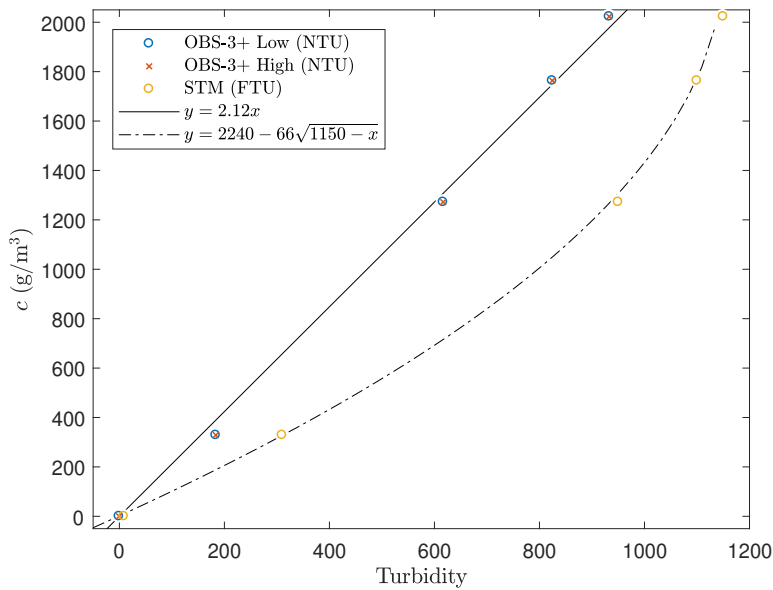


Figure 5.20: Turbidity calibration curves.

Chapter 6

General view of collected data

This chapter presents a general view of the data obtained during the deployments on a weekly time window. The data shown here have not been highly processed, they are in line with the raw data registered by the corresponding instrument. Despite this, the ensembles provide a good overview allowing the identification of very interesting hydrodynamics and sediment dynamics activity events. Only one week of the first deployment is shown, since the analysis tools were designed mainly for the second deployment. Nevertheless, the complete data set of this deployment is presented in Appendix 1.

During the first deployment, the ABS transducers were 108 cm above the seabed and the ADV sampling volume was 80 cm above the seabed. As mentioned in Section 4.1, after the first deployment the structure was modified in order to attach a conductivity, temperature, depth and optical backscatter sensors and an acoustic Doppler current profiler. During the second deployment both ADV and ABS were closer to the seabed than during the first deployment (the ABS transducers was 39 cm and the ADV sampling volume 29 cm above the seabed). Avoiding large sound attenuation induced by the sediments when high concentrations are present, more detailed data of the first decimeters near the bottom are provided by the ABS data during this period of time. There is no description of the second deployment events here, but the black boxes in the second and third weeks are analyzed in detail in Chapter 8.

6.1 First deployment

Figure 6.1 in this Section shows the collected data on the sixth week of first deployment.

- First panel: East projection of the currents U_E (which is generally the most significant direction) measured by the ADCP in the buoy. As the ADCP was placed facing downwards, the depth d minus z is in the ordinate. Black line shows the pressure of the ADV in mH₂O in order to indicate the boundary of the velocity profiles.
- Second panel: East projection of the mean velocity U_E measured by the ADV.
- Third panel: Significant wave height H_S measured by the ADV both with the pressure p and velocity \vec{v} data obtained as established in Section 7.3.1. The H_S measured by the TRIAXYS sensor in the buoy is also shown.
- Fourth panel: Temperature θ measured by the ABS at the bottom and by the ADCP buoy at the surface. Salinity s estimated with the ADV and using technique presented in Annex 1 is also shown.
- Fifth panel: Sediment mass concentration c obtained with the STM and with the ADV.
- Sixth panel: ADV Probe Check raw data.
- Seventh panel: Acoustic backscatter profiles of 2.5 MHz ABS transducer corrected by spreading, near field and water absorption as explained in Chapter 3. Each profile showed here is the average of corrected recorded voltage over the 2.2 min every half an hour. As can be seen in the next Chapter, Section 7.5, due to the presence of waves and other non-stationary motion component, the estimation of sediment concentration M requires more computation.
- Eighth panel: Acoustic backscatter profiles of 5 MHz ABS transducer corrected by spreading, near field and water absorption as explained in Chapter 3. The same considerations made in the previous panel apply to this one.
- Ninth panel: Acoustic backscatter profile of one beam of the ADCP in the buoy corrected by spreading, near field and water absorption.

As of Jan 14, 2018, there starts to occur an erosive event of about 2 days long after a day and 12 hours of low current velocity and a week of low wave

energy (see Fig. 1.5 in Appendix 1). An abrupt increment in all three acoustic backscatter signals (seventh to ninth panels) as well as the ADV Probe Check raw data (sixth panel) is seen, which indicates the presence of suspended sediment in the water column. Peak mass concentrations of around 0.10 kg/m^3 were measured 80 cm above the seabed (as seen in the fifth panel). Halfway through the event (on Jan 14, 2018, at 20:00), as currents become weaker and wave energy is maximum, a high echo 10 cm above the seabed was registered in both 2.5 (seventh panel) and 5 MHz (eighth panel) ABS transducers. These local maximums on the backscatter acoustic profiles suggest a gradient on the acoustic impedance induced by a sharp variation in the suspended sediment concentration, indicating the presence of a lutocline. An interesting feature that all acoustic instruments show when lutocline is present, is the reduction of the acoustic signal above this layer. Consequently, the concentration 80 cm above the bed drops to under 0.04 kg/m^3 (fifth panel) which indicates less suspended sediment. During the second half of the event, once the current velocities begin to increase, the lutocline signal is erased and the suspended sediment concentration increases again.

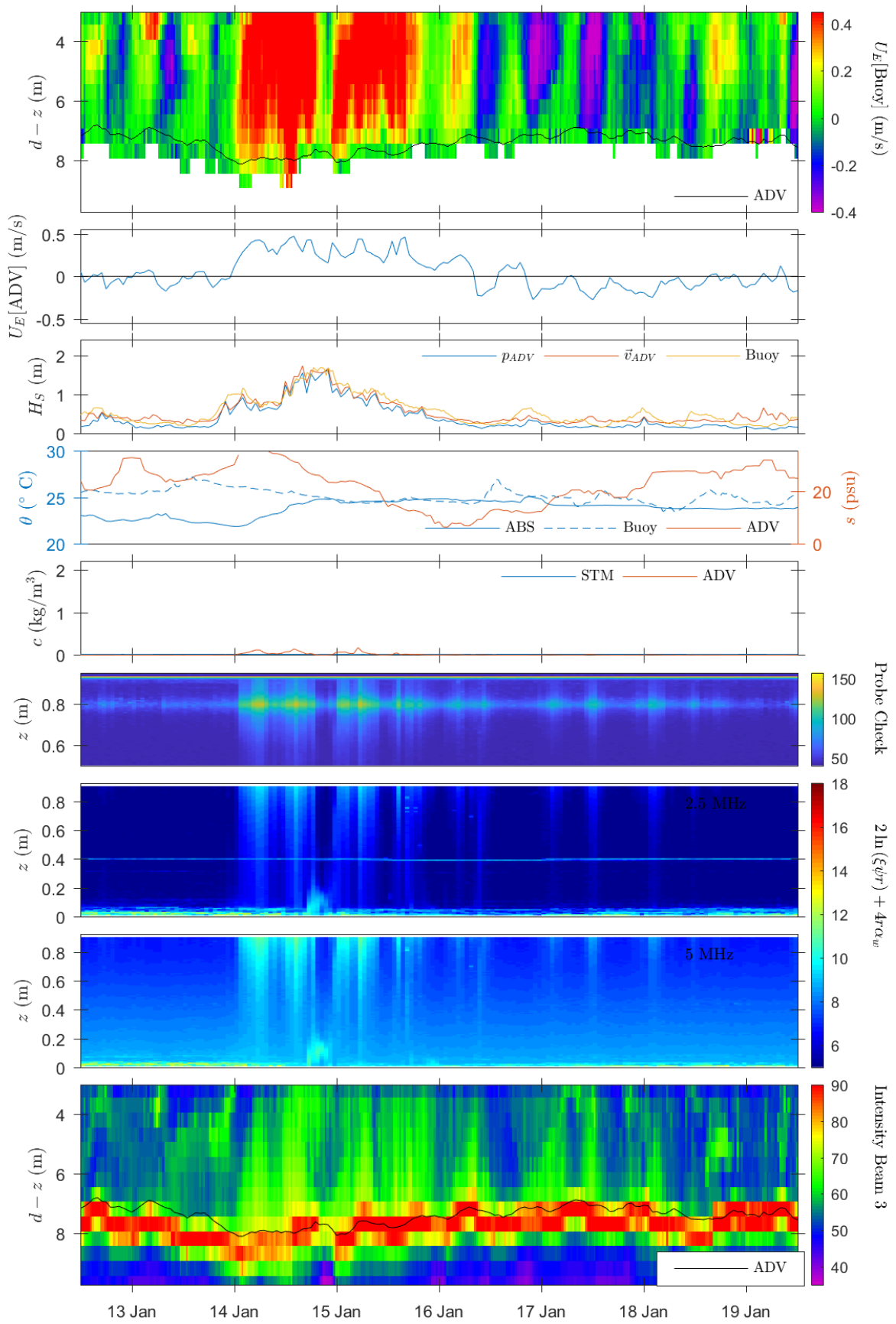


Figure 6.1: First deployment, sixth week.

6.2 Second deployment

Figures 6.2 to 6.8 in this Section show the collected data during the second deployment. The black boxes in Figures 6.3 and 6.4 are discussed in detail on Chapter 9.

- First panel: East projection of the currents U_E (which is generally the most significant direction) measured by the ADCP in the buoy. As the ADCP was placed facing downwards, the depth d minus z is in the ordinate. Black line shows the pressure of the CTD in mH₂O in order to indicate the boundary of the velocity profiles.
- Second panel: East projection of the mean velocity U_E measured by the ADV and friction velocity U_* obtained as established in Section 7.4.
- Third panel: Significant wave height H_S measured by the ADV both with the pressure p and velocity \vec{v} data obtained as established in Section 7.3.1. The H_S measured by the TRIAXYS sensor in the buoy is also shown.
- Fourth panel: Temperatures θ measured by the CTD at the bottom and by the ADCP buoy at the surface. Salinity s measured by the CTD and estimated with the ADV and using technique presented in Annex 1 is also shown.
- Fifth panel: Suspended sediment concentration c obtained with the STM and the OBS turbidity meters.
- Sixth panel: ADV Probe Check raw data.
- Seventh panel: Acoustic backscatter profile of 1 MHz ABS transducer corrected by spreading, near field and water absorption as explained in Chapter 3. Each profile showed here is the average of corrected recorded voltage over the 2.2 min every half an hour. As can be seen in the next Chapter, Section 7.5, due to the presence of waves and other non-stationary motion component, the estimation of M requires more computation. The acoustic inversion technique proposed in this work to estimate sediment mass concentration was applied to some selected “instants” inside the black rectangles of Figs. 6.3 and 6.4, and presented in Chapter 8.
- Eighth panel: Acoustic backscatter profile of 4 MHz ABS transducer corrected by spreading, near field and water absorption as explained in Chapter 3. The same considerations made in the previous panel apply

to this one.

- Ninth panel: Acoustic backscatter profile of one beam of the ADCP in the buoy corrected by spreading, near field and water absorption.

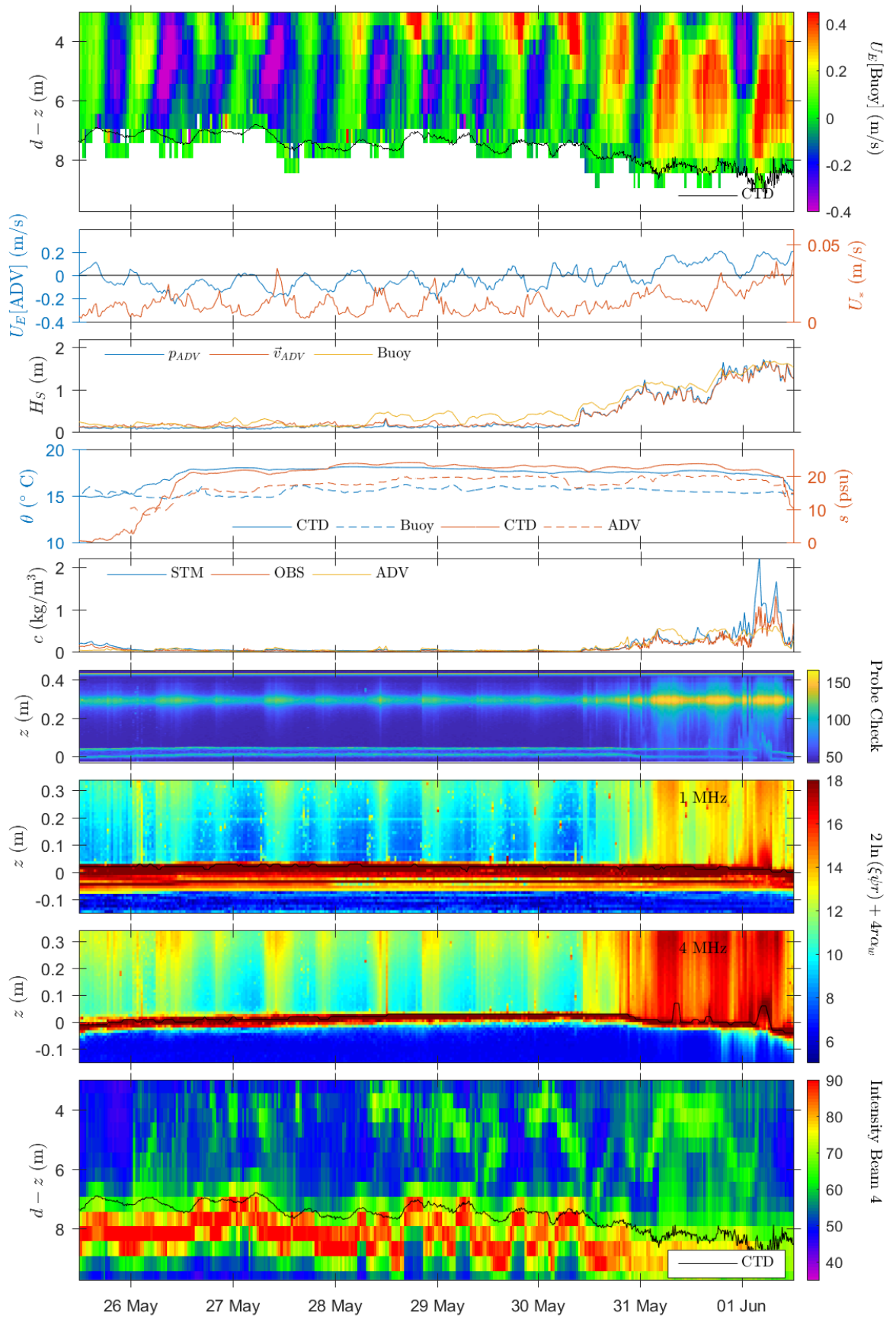


Figure 6.2: Second deployment, first week.

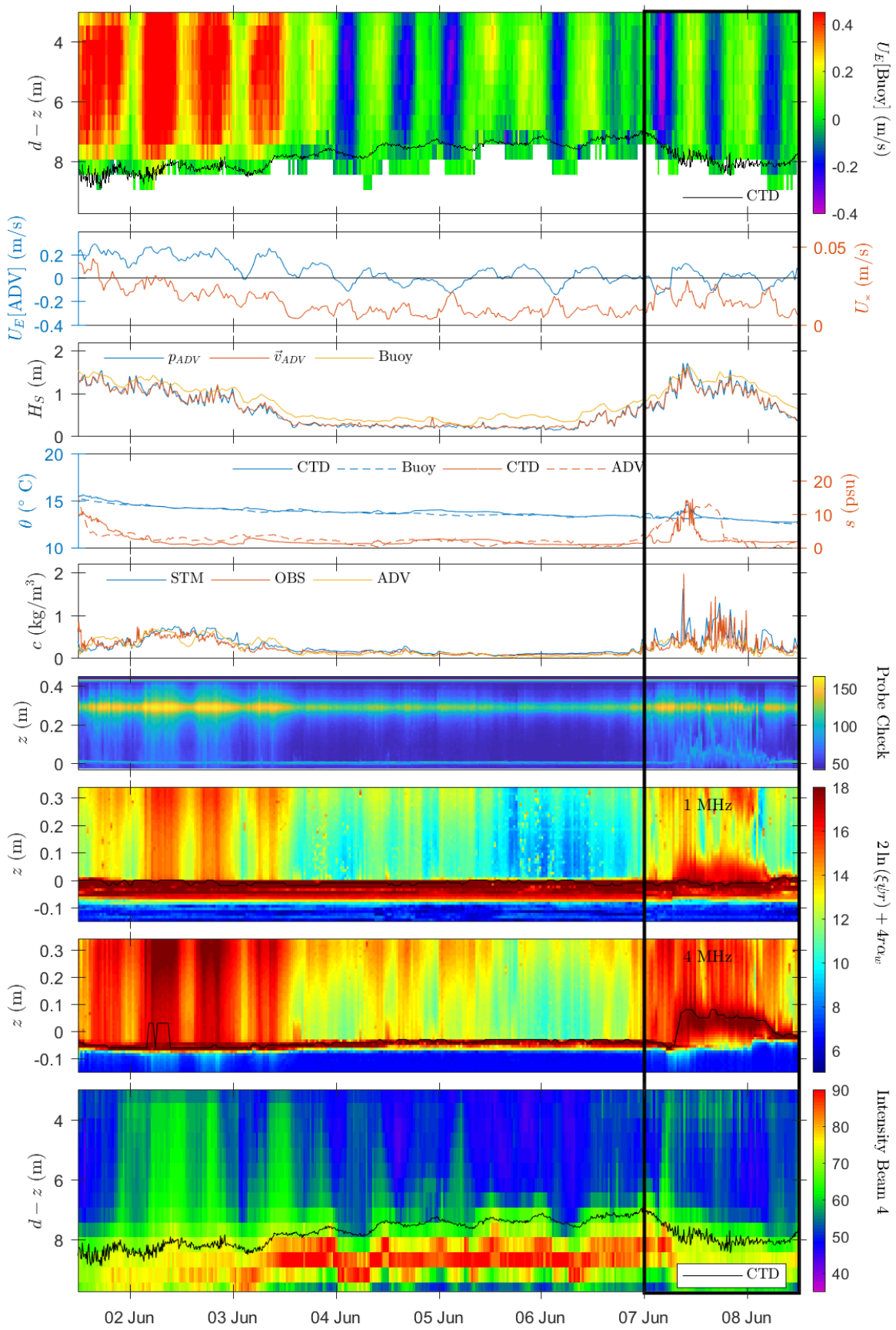


Figure 6.3: Second deployment, second week.

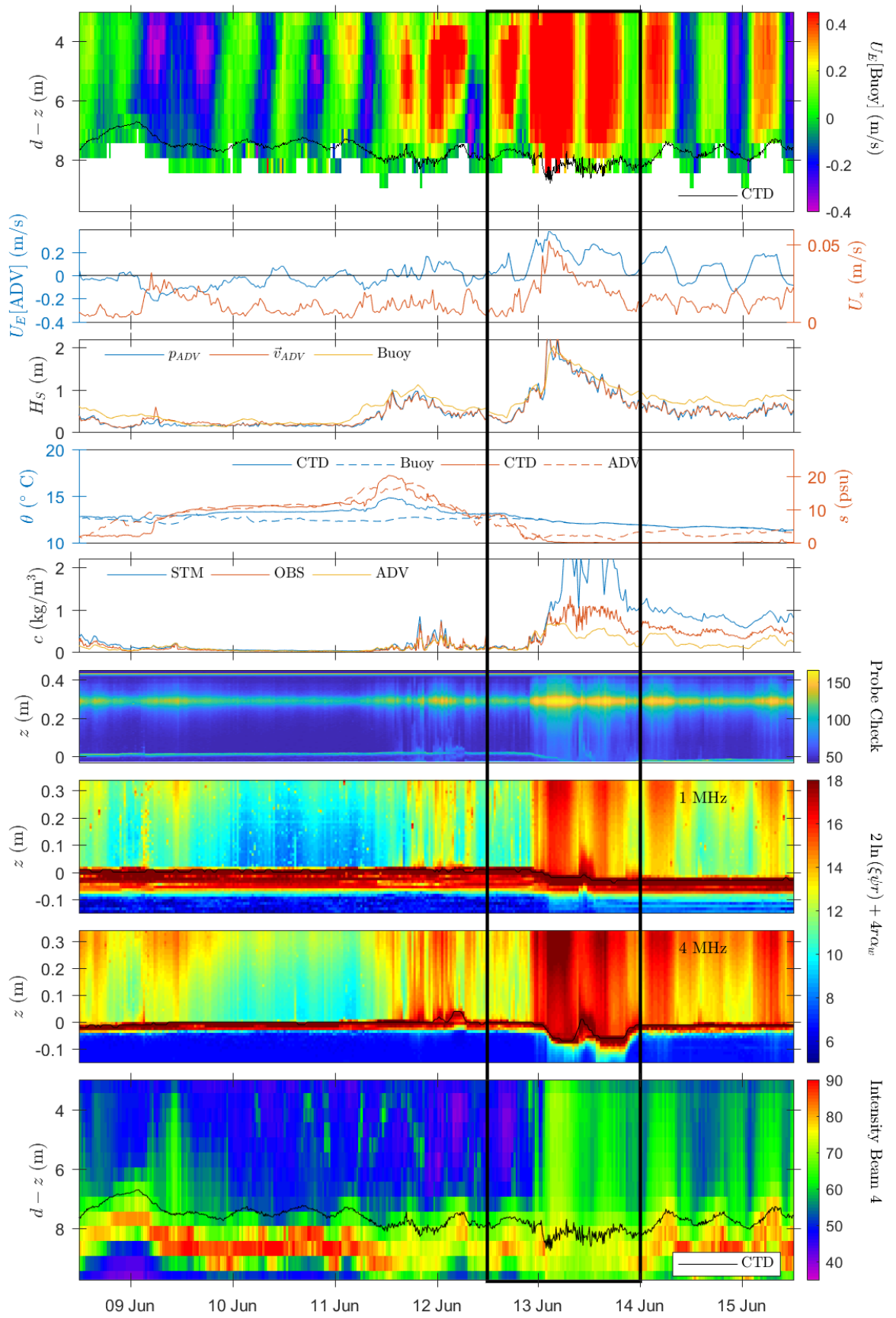


Figure 6.4: Second deployment, third week.

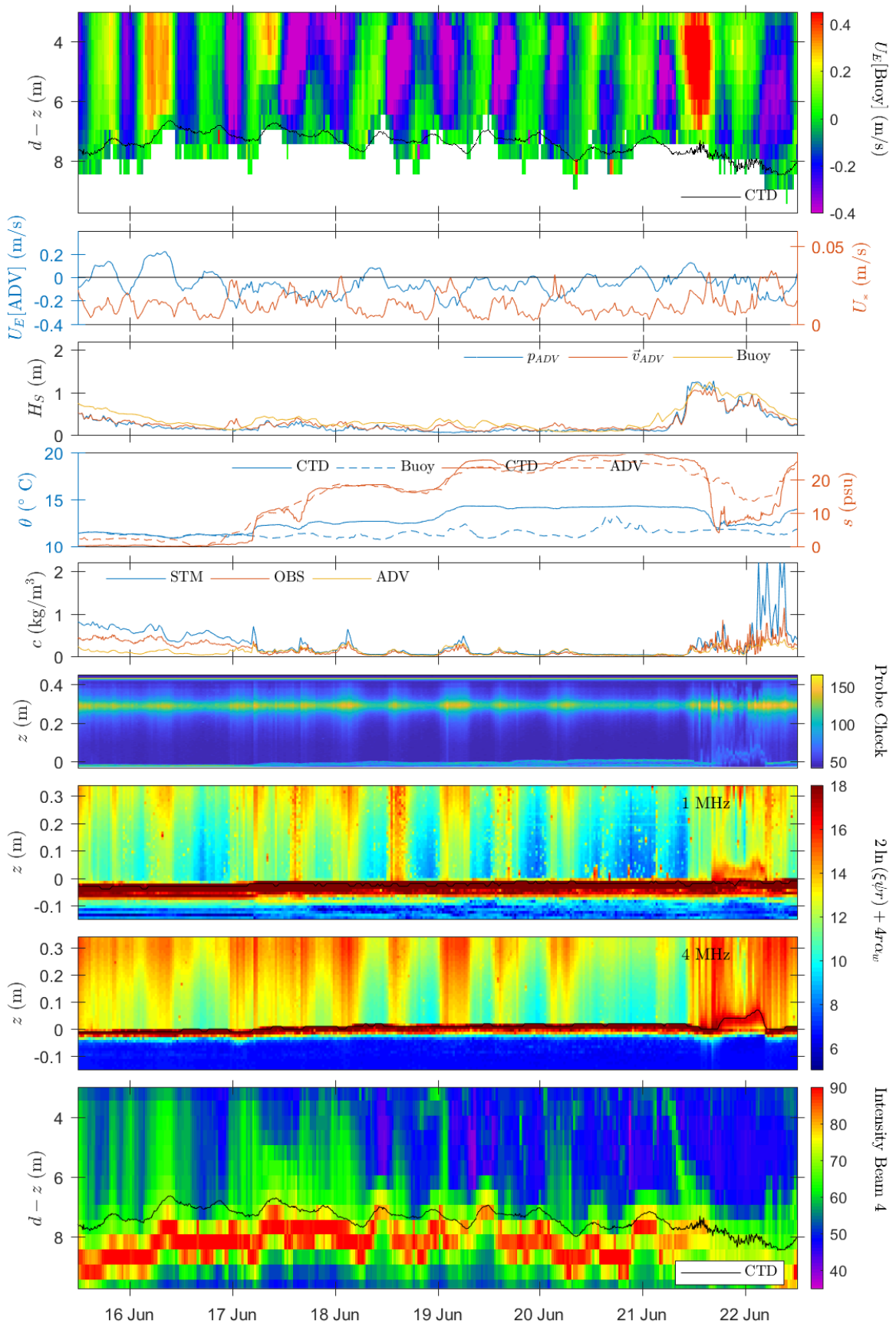


Figure 6.5: Second deployment, fourth week.

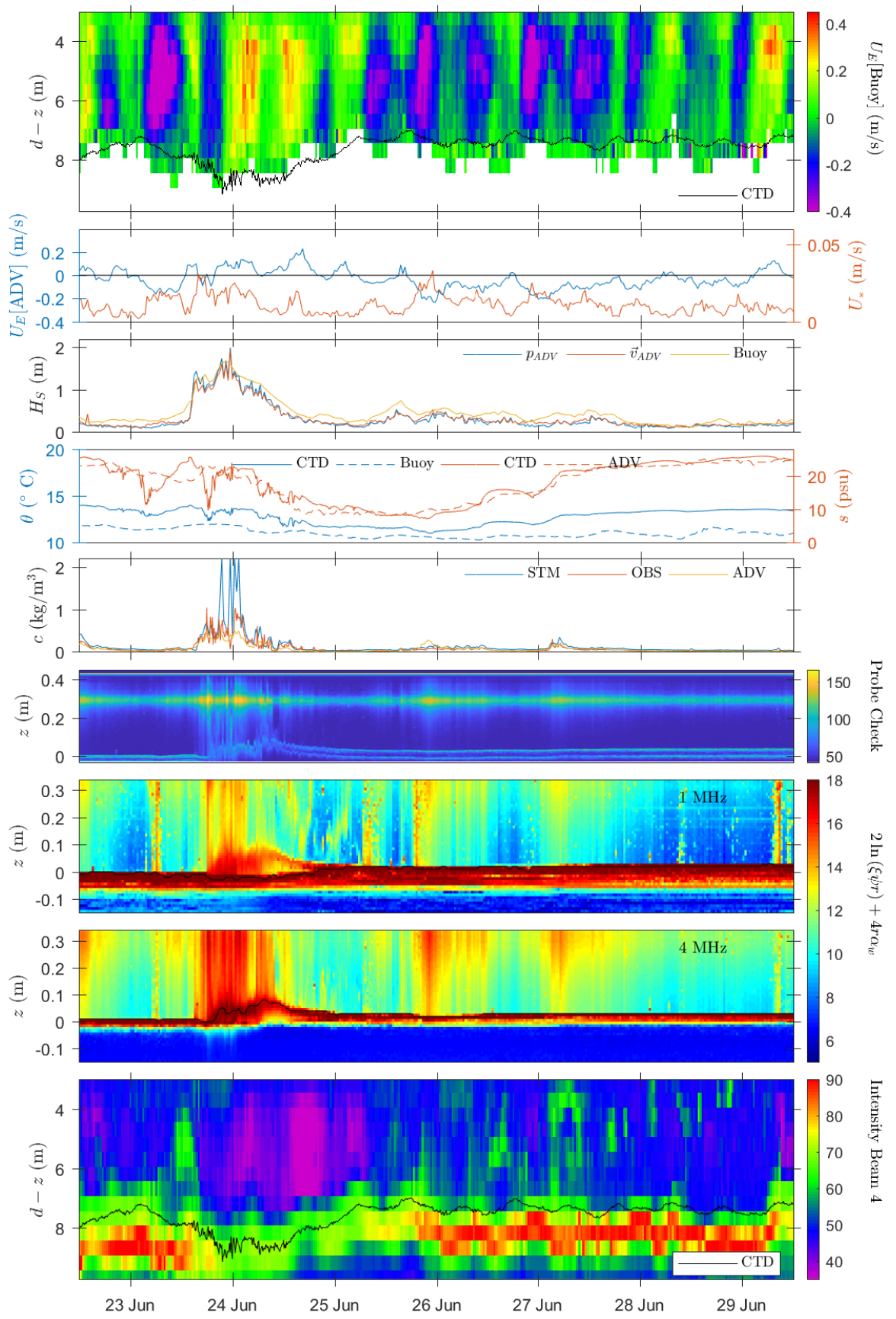


Figure 6.6: Second deployment, fifth week.

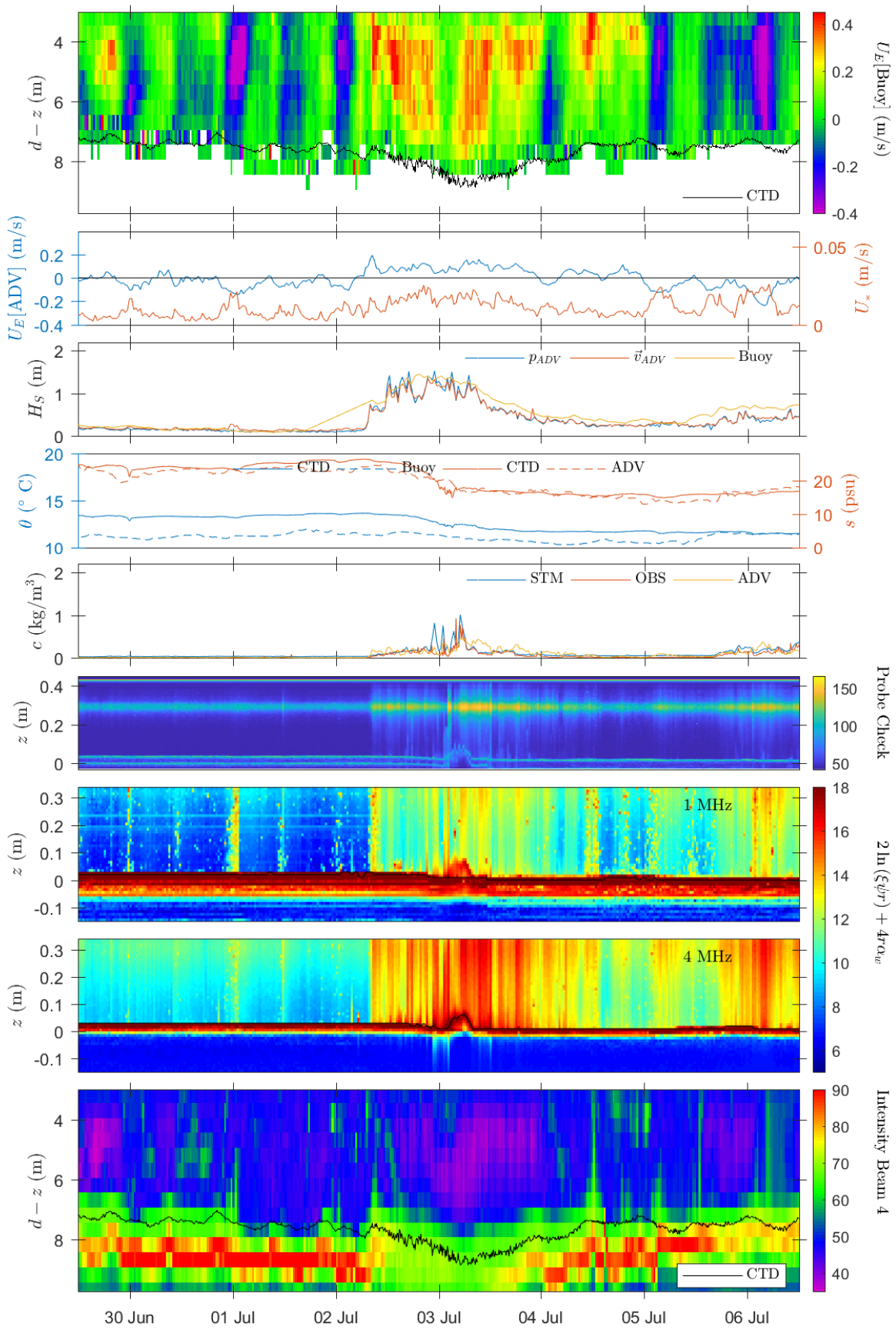


Figure 6.7: Second deployment, sixth week.

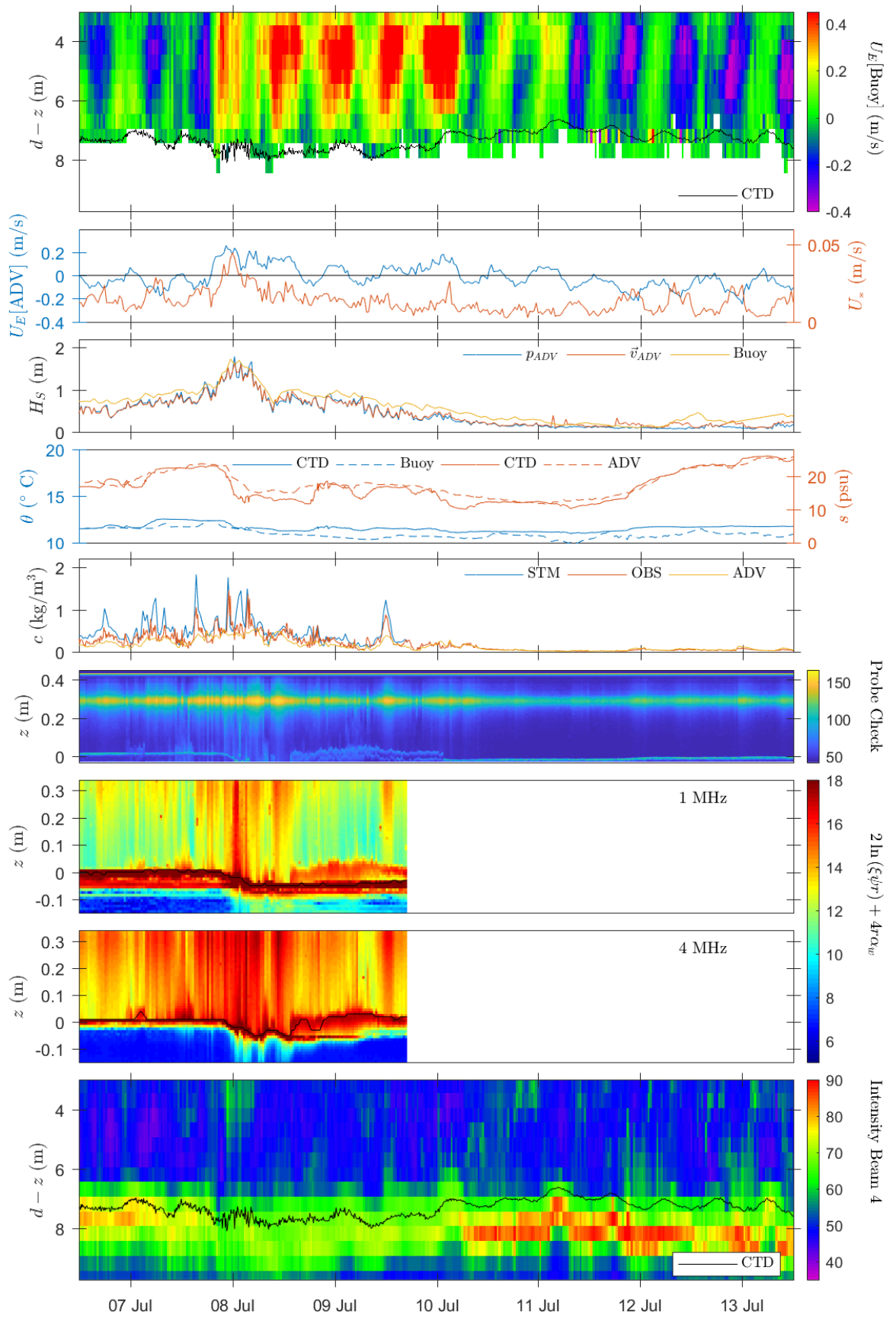


Figure 6.8: Second deployment, seventh week.

Chapter 7

Field data analysis

7.1 Lutocline

After correcting the ABS signal by spreading, near field and water sound absorption, in calm conditions every transducer data of the downward looking array present a peak in the transition to the motionless bottom. The vertical coordinate z of this peak can be seen in black lines on the seventh panel of Figures 6.2 to 6.8 as well as in the second panel of the zoom-in shown in Fig 7.1.

During some combinations of high waves and moderate currents, a second peak in the backscatter signal can be observed in the higher frequencies (eighth panel of Figs. 6.2 to 6.8 and third panel of Fig. 7.1). ADV Probe Check raw data also present the acoustic peaks as can be seen in the sixth panels of Figs. 6.2 to 6.8. The sharp gradient of the acoustic backscatter data is an indicator of a lutocline (defined in Chapter 1), whose height δ_L can be more than a decimeter. Figure 7.1 shows two different lutocline events associated to the waves. Even more, δ_L is observed to be proportional to H_S under low U_E .

A closer look over the acoustic bursts shows an oscillation of the lutocline, associated to surface waves that make the concentration fluctuate strongly during the measuring time window. Deviations of the statistical distribution of V_{rec} from incoherent backscattering of suspensions (Section 3.6) can be associated either to a fix bed or to significant concentration fluctuations during the burst. Figure 7.2 show the probability density distributions of V_{rec} inside one burst at four different heights, from highest ($z = 0.12$ m) to lowest ($z = -0.01$ m): above the lutocline; in the lutocline; below the lutocline but

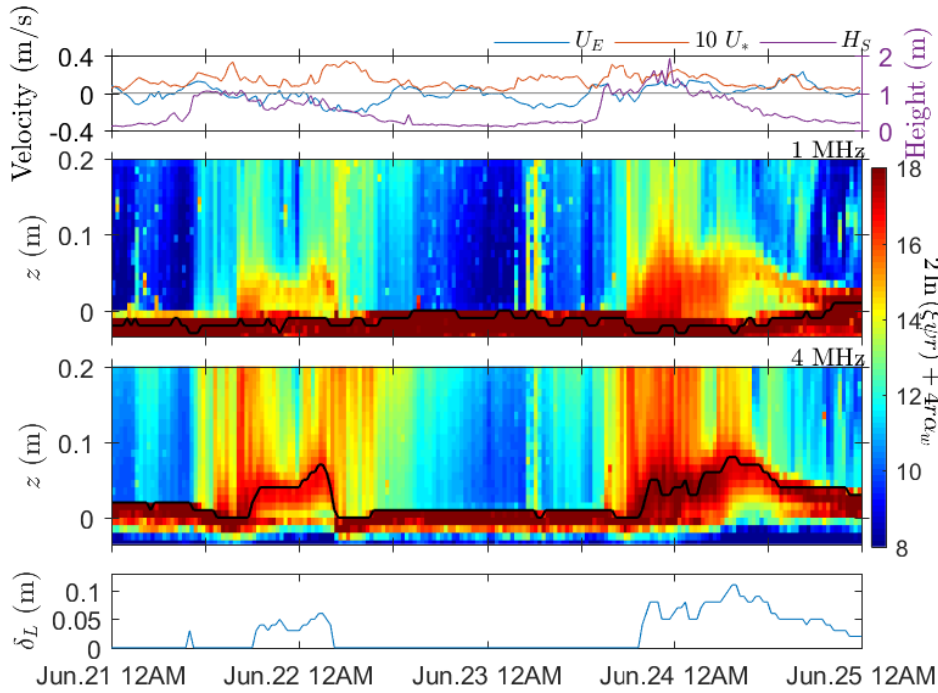


Figure 7.1: First panel: Time series of U_E , U_* and H_S , all three obtained with the ADV velocity data. Second panel: Acoustic backscatter profile of 1 MHz ABS transducer corrected by spreading, near field and water absorption. The black line indicates the position of the peak in the profile. Third panel: Acoustic backscatter profile of 4 MHz ABS transducer with the same consideration made in the previous panel. Fourth panel: Time series of δ_L obtained as the difference of peak heights in 4 and 1 MHz acoustic profiles.

above the seabed; and in the seabed. Lines correspond to incoherent backscatter distribution hypothesis maintaining the color code. The interface position was determined in two ways, by finding the acoustic backscatter peak, and by analyzing the goodness of fit of the signal pdf at each z with an incoherent backscatter pdf. These techniques provided similar result both for the lutocline and for the seabed interface positions. Even though, finding the maxima in a profile is faster than estimating the goodness of fit to an incoherent backscatter pdf, both techniques complement each other. Under high attenuation conditions the peaks may be hard to observe, and the second technique can throw some light on the location of those interfaces. The presence of a lutocline and the estimation of δ_L are milestones that justify this work as it has been discussed in Chapter 1

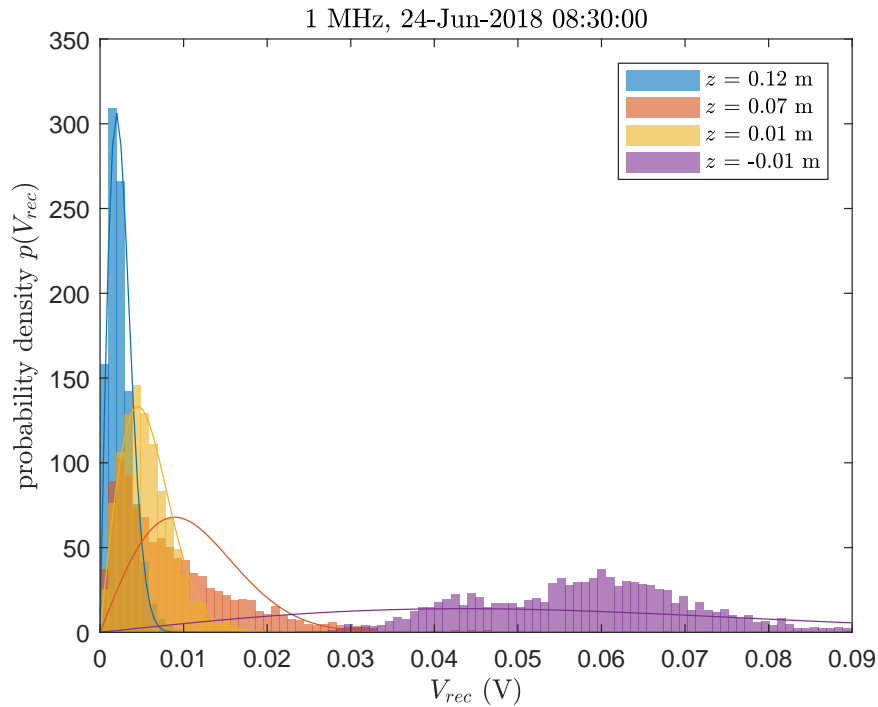


Figure 7.2: Histograms of the 1 MHz transducer V_{rec} on Jun 24 at 08:30 of four positions: **above the lutocline** $z = 0.12$ m; **in the lutocline** $z = 0.07$ m; **below the lutocline and above the seabed** $z = 0.01$ m; **in the seabed** $z = -0.01$ m. Curves correspond to incoherent backscatter distribution fits maintaining the color code.

7.2 Currents

Currents in the water column were obtained every hour with a 50 cm resolution using ADCP facing downwards located at the buoy. Due to the acoustic rays divergence, the buoy motion and the side lobes, near the bottom the velocity values provided by the ADCP are biased. [Teledyne \(2019\)](#) recommends discarding approximately the lower 6 % of the distance from the transducers to the sea bed (approximately 0.5 m). Under certain hydrodynamic conditions, the sediment mass concentration c has particular patterns or “textures”, which can be captured by the different ABS transducers as shown in Fig. 7.3.

Because the transducers were positioned 15 to 40 cm apart from each other (see Fig. 4.8) the advection of the sediments may be observed as a repetition of the concentration pattern in the different transducers, and the time lags among the patterns in the different transducers may be used to estimate the flow velocity. Using pairs of images separated by a fixed time delay, [Meinhart](#)

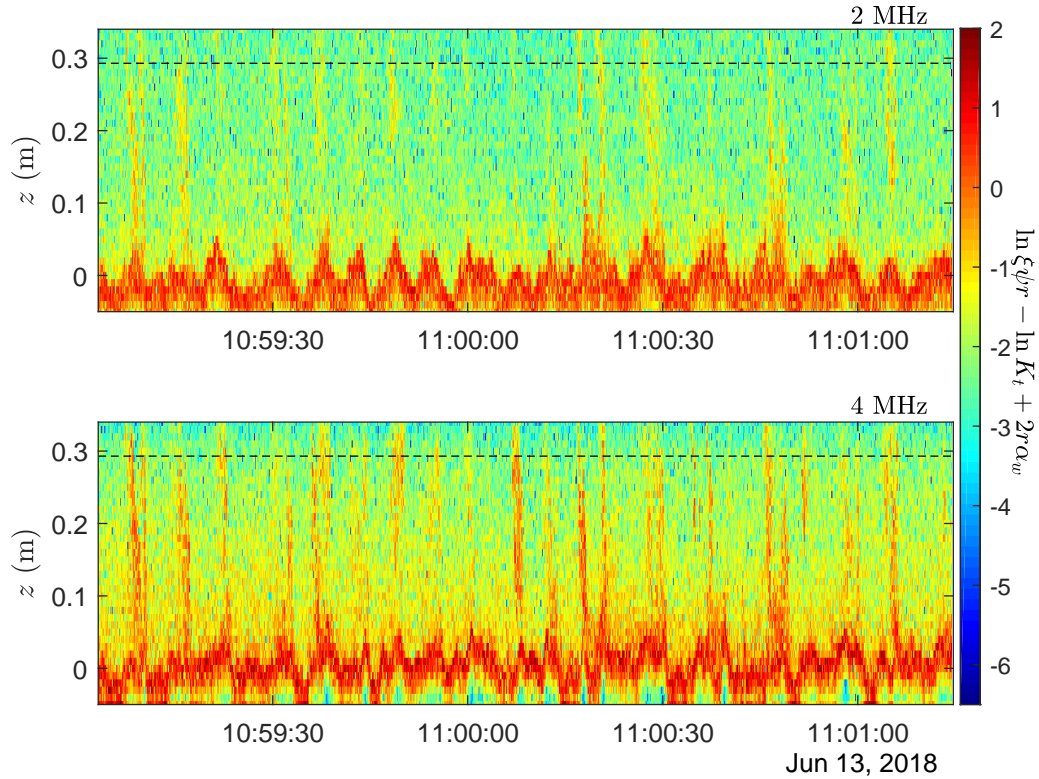


Figure 7.3: Acoustic backscatter bursts of 2 (upper panel) and 4 MHz (lower panel) transducers corrected by spreading, near field and water absorption. The dashed black line indicates the position z of the sampling volume of the ADV.

[et al. \(2000\)](#) present three different particle image velocimetry algorithms for estimating time averaged velocity fields. It is possible to adapt said ideas, in order to obtain a time-averaged velocity projection by determining the peak in the correlation function between pairs of points at the same height on different transducers. By calculating the correlation function of the different heights, it is possible to relate the time-averaged velocity projection profile with the peak in the correlation function. Similar ideas can be found in works by [Thorne and Holdaway \(1997\)](#); [Thorne and Hanes \(2002\)](#). Figure 7.4 shows the cross-covariance function of 0.5 and 1 MHz transducers $\text{cov}(V_{rec,0.5 \text{ MHz}}, V_{rec,1 \text{ MHz}})$ as well as 2 and 4 MHz transducers $\text{cov}(V_{rec,2 \text{ MHz}}, V_{rec,4 \text{ MHz}})$, normalized so that autocovariance at zero lag equals 1.

The ADV determines the “instantaneous” velocity vector with a sampling rate of 32 Hz for more than 3 minutes every half an hour, 29 cm above the bed (Section 4.3). Currents, waves and shear velocity extracted from those records

were used as boundary conditions in the hydrodynamics and sediment dynamics model presented in Section 2.3 which provides currents u_c and suspended sediment concentration c profiles. Selecting a pair of transducers, the black full line in Fig. 7.4 shows the separation distance divided by the projection of u_c in the transducers' plane. Even though the covariance technique seems not to be the panacea for current velocity profiles estimation, particularly close to the bed, it serves as a verification of the u_c calculated as established by [Styles and Glenn \(2000\)](#) as may be seen in Fig. 7.4.

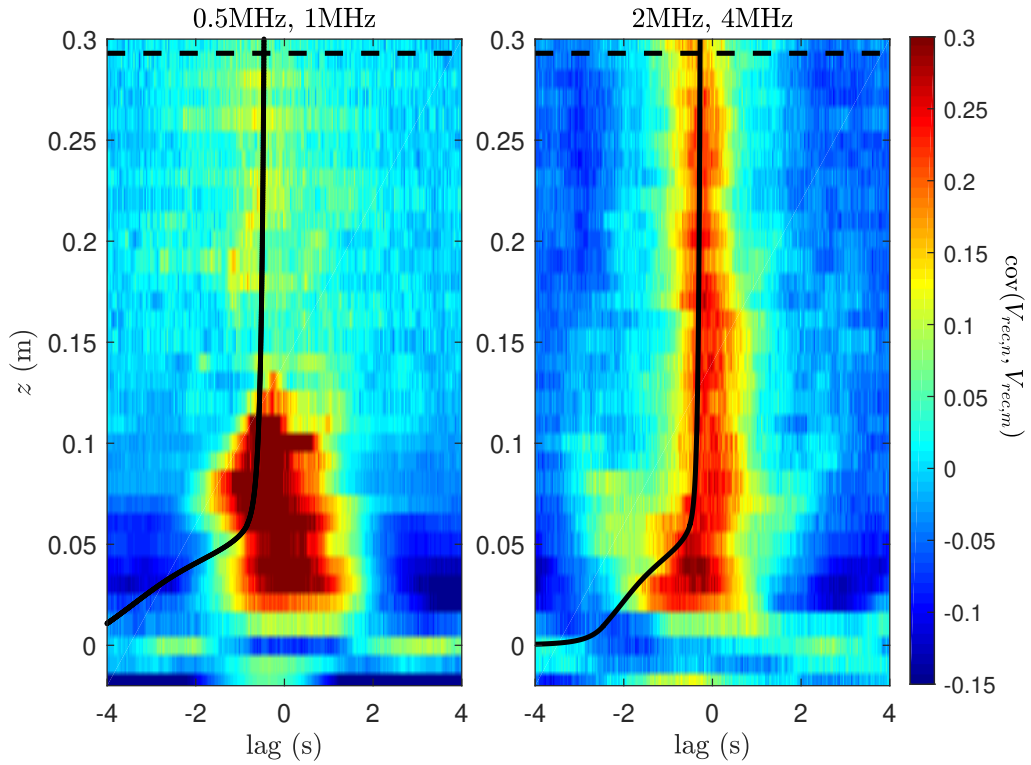


Figure 7.4: Left panel: Cross-covariance of 0.5 and 1 MHz transducers. Right panel: Cross-covariance of 2 and 4 MHz transducers. The angle between the two planes is 65° . The black full line is the distance between the pair of transducers divided by the projection of u_c as established calculated by [Styles and Glenn \(2000\)](#) in the transducers' plane. The dashed black line indicates the position z of the ADV sampling volume.

7.3 Non-stationary motion components

7.3.1 Waves.

Wave parameters such as significant wave height H_S , peak wave period T_P and mean wave direction D_m were estimated every hour by the directional wave sensor in the buoy detailed in Section 4.7. Near the sea bed, pressure and orbital velocity induced by waves were captured by the ADV every 30 minutes. The pressure $S_{\bar{p}}$, East $S_{\bar{v}_E}$ and North $S_{\bar{v}_N}$ horizontal velocity projections power spectra of the wave component extracted from the ADV data, can be used to estimate the wave energy spectrum S_η using the Airy wave theory. Two different and independent ways of estimating S_η are expressed in the following formulas

$$S_\eta = \left[\frac{\cosh kd}{\cosh kz} \right]^2 \frac{S_{\bar{p}}}{(\rho g)^2}, \quad (7.1)$$

$$S_\eta = \left[\frac{\sinh kd}{\cosh kz} \right]^2 \frac{S_{\bar{v}_E} + S_{\bar{v}_N}}{\omega^2}, \quad (7.2)$$

where k is the wave number, d the water depth, z the vertical distance from the seabed to the measuring point, ρ the water density, g the gravity acceleration and ω the wave angular frequency. Wave number and angular frequency can be related with the dispersion relationship equation

$$\omega^2 = gk \tanh kd. \quad (7.3)$$

Both H_S and T_P can be extracted from S_η . On the other hand, the mean direction for each frequency $D(f)$ can be estimated as

$$D(f) = \arctan \frac{S_{\bar{v}_E}}{S_{\bar{v}_N}}. \quad (7.4)$$

The ADV wave component estimations were more suitable for the purposes of this thesis than the buoy estimation as they were measured more frequently (ADV estimations are every 30 minutes against the hourly measure of the buoy); their measurement was performed near the bottom, a few centimeters above the formation of the lutocline; not only the wave sample statistic such as H_S , T_P and D_m were obtained, but also the motion component such as \tilde{u} and \tilde{v} . When referring to wave direction, according to convention the approaching

direction of the waves is provided. When degrees (radians) are used as angle units, from true North, increasing clockwise, North is 0 (zero) degrees and East is 90° ($\pi/2$ rad).

The ADV data was used to estimate the hydrodynamic wave boundary conditions of both hydrodynamic models, based on works by [Madsen \(1994\)](#) and [Styles and Glenn \(2000\)](#), presented in Chapter 2. In Fig. 7.5 there appears a scatter plot comparing the ADV and buoy H_S estimations. It can be seen that the H_S obtained with the buoy is systematically 20 cm above the ADV ones. Even though the source of such bias is not well comprehended, it is probably associated to the velocity and pressure wave amplitude decrease of the high frequency wave components near the seabed.

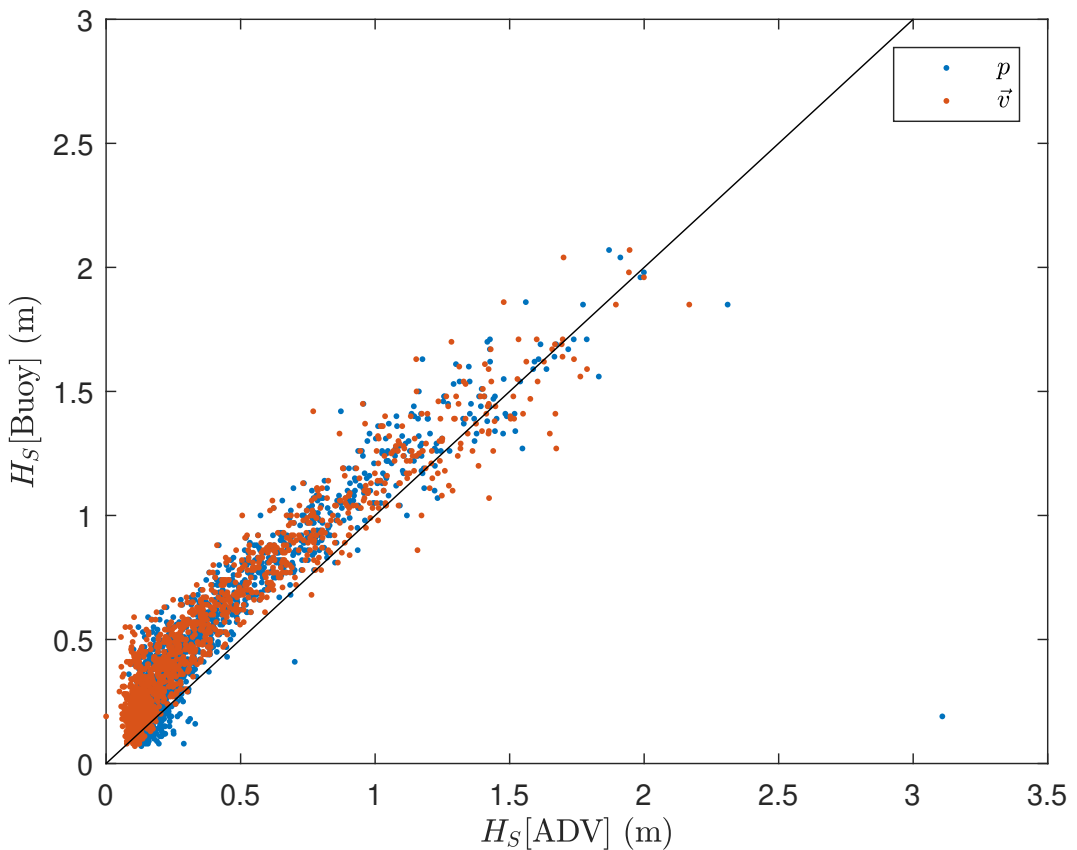


Figure 7.5: Scatter plot between H_S estimated with the pressure p and the velocity \vec{v} data of the ADV vs H_S estimated with the buoy.

7.3.2 Turbulence.

Wave motion component can produce large biases when trying to obtain turbulent estimations using velocity measurements in a single point (Grant et al., 1984; Trowbridge, 1998; Trowbridge and Elgar, 2001; Sherwood et al., 2006). Distinguishing between wave \tilde{w} and turbulent w' motion components, as introduced in Eq. 2.1, based on a single-sensor velocity measurements is often difficult, as the frequency range where both motion components have energy may overlap (Grant and Madsen, 1986). Nevertheless, as near the sea bed the vertical projection of the wave-induced velocity \tilde{w} is small, the energy spectrum resembles a pure turbulent motion and “estimates of quantities such as $\langle w'^2 \rangle / U_*^2$ agree well with classical expectations” (Grant and Madsen, 1986), being $\langle w'^2 \rangle$ the mean square of the turbulent component of the vertical velocity w' . The Airy theory predicts that the amplitude of \tilde{w} decays with $\sinh kz$. Because the ADV during the second deployment measured the velocity 29 cm above the bottom in a depth d around 7.5 m, the vertical velocity of the wave component \tilde{w} is expected to be very small. The ratios of theoretical amplitudes extracted from Airy theory for \tilde{w} at the ADV measuring point and at water surface are less than 4 %, with wave periods from 5 to 20 s. Only the most energetic ones were measured.

In the upper panel Fig. 7.6 shows in the upper panel a typical time series of the pressure p and East v_E , North v_N and vertical w velocity projections measured by the ADV. It can be seen that w is very small in comparison with the other two velocity projections. In the second panel the same color code is used for the spectrum of each time series. Each energy spectrum was calculated with 50 % overlapping 41 s Hamming windows sub-sampled at a 32 Hz frequency, resulting in averaging 8 spectra over the 3.1 min duration. Wave energy in Fig. 7.6 is distributed in the 0.05 - 0.3 Hz range and v_E , v_N and p power spectral densities present an abrupt change in the slope in 0.3 Hz. Assuming fully developed wind-generated waves, the high frequency tails of the wave spectra is proportional to f^{-5} (Holthuijsen, 2007). With Eq. 7.2 this limit can be expressed in the velocity spectrum as $f^{-3} \left[\frac{\cosh kz}{\sinh kd} \right]^2$ being k the wave number calculated using Eq. 7.3 and the relation $\omega = 2\pi f$. The full black line of $f^{-5/3}$ corresponds to the turbulence inertial sub-range spectra with the usual Taylor frozen turbulence hypothesis.

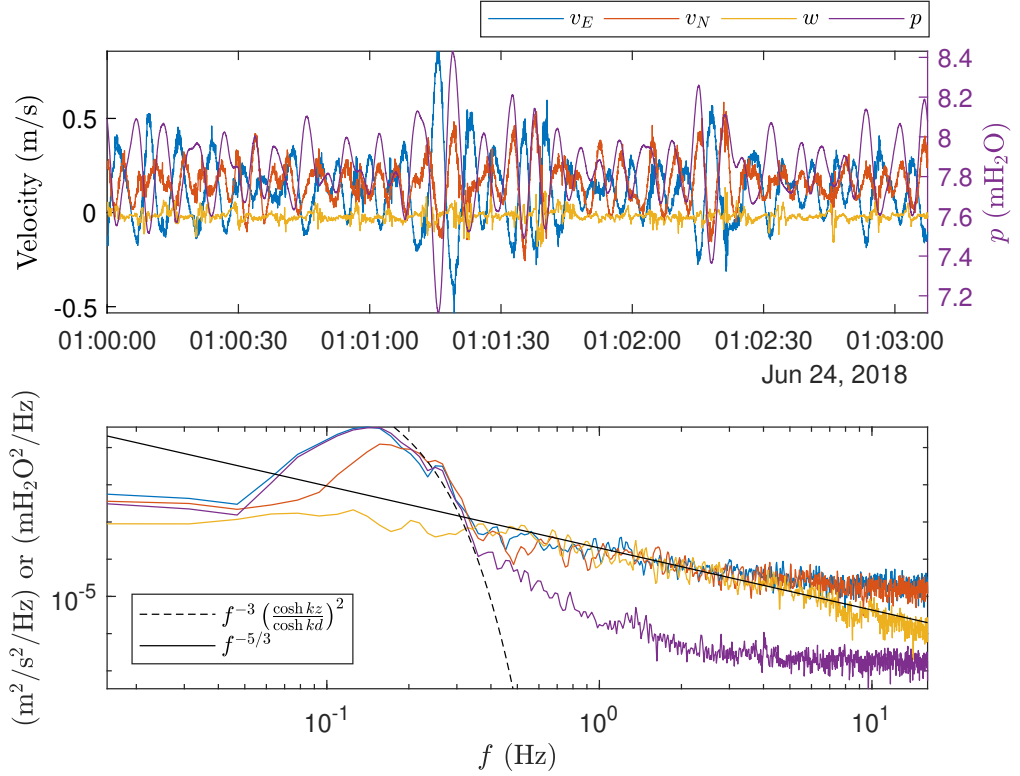


Figure 7.6: Upper panel: East, north and vertical velocity projections (v_E , v_N and w correspondingly) and pressure p records. Lower panel: Color coded v_E , v_N , w and p power spectral densities.

Using velocity and surface elevation measurements in the field, [Thornton \(1979\)](#) separates the turbulence spectrum velocity $S_{v'}$ from the wave-induced spectrum velocity $S_{\bar{v}}$. The spectrum of any velocity projection can be expressed, in its most generic form, in terms of wave-induced and turbulent contributions

$$S_v = S_{\bar{v}} + S_{v'} + C_{\bar{v}v'}, \quad (7.5)$$

where $C_{\bar{v}v'}$ is coincident spectral density function (co-spectrum), being also in this case twice the real part of the cross-spectrum between the wave-induced velocity and the surface elevation $S_{\bar{v}v'}$ ([Bendat and Piersol, 2011](#)). Even though the primary generation of turbulence may occur at wave breaking, where the size of the vortices generated are of the same scale as the orbital motion induced by the wave, as a first approximation, wave-induced and turbulent velocity spectral components are assumed to be statistically independent, so the

spectrum of the velocity S_v simplifies to (Thornton, 1979)

$$S_v = S_{\tilde{v}} + S_{v'}. \quad (7.6)$$

The turbulence generated by waves at the bed results in smaller spatial scales than the waves scales, with two sensors near the bed, separated by a distance longer than the correlation scale of the turbulence, but shorter than the coherence structure of the wave motion. Therefore, the contribution of the turbulence in the cross spectrum between velocity and surface elevation records becomes zero. In other words

$$S_{v\eta} = S_{\tilde{v}\eta}, \quad (7.7)$$

where $S_{v\eta}$ is the cross spectrum between the velocity and surface elevation and $S_{\tilde{v}\eta}$ the cross spectrum between the wave-induced velocity and the surface elevation. When assuming that surface elevation and wave-induced velocities are described by a linear process, as the Airy wave theory does, coherence $\gamma_{\tilde{v}\eta}^2$ is identically equal to unity

$$\gamma_{\tilde{v}\eta}^2 = \frac{|S_{\tilde{v}\eta}|^2}{S_{\tilde{v}}S_{\eta}} \equiv 1, \quad (7.8)$$

and it is possible to calculate $S_{\tilde{v}}$ using

$$S_{\tilde{v}} = \gamma_{v\eta}^2 S_v. \quad (7.9)$$

During the second deployment, the ADV had the pressure port 37.4 cm above the velocity measurement point (67 cm above the bottom). As velocity and pressure were obtained at different z , turbulent $S_{v'}$ and wave-induced $S_{\tilde{v}}$ spectral components of each velocity projection can be differentiated due to the vertical coherent structures using the cross spectrum between velocity, pressure S_{vp} and the relation between S_{η} and $S_{\tilde{p}}$ of Eq. 7.1. The upper panel in Fig. 7.7 shows in the upper panel, the cross spectrum between the pressure and the different velocity projections. In the lower panel the coherence is also shown. Even though velocity and pressure measurements are 37.4 cm apart, coherence between w and p is very low in the whole frequency range, validating the hypothesis that the \tilde{w} is negligible.

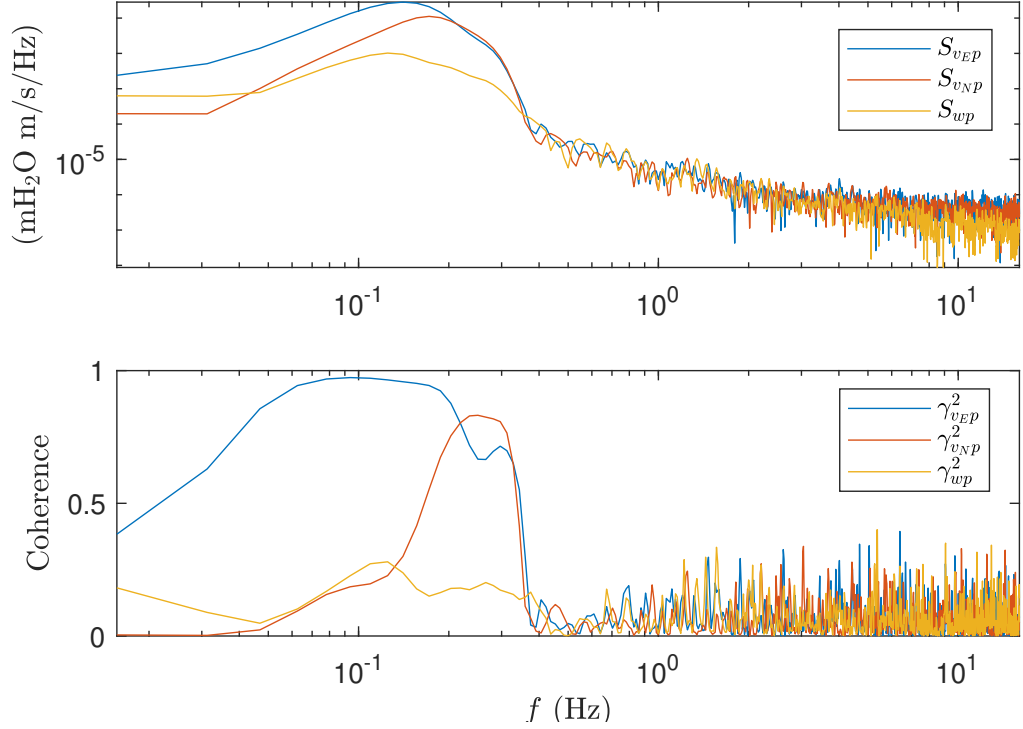


Figure 7.7: Upper panel: S_{vEP} , S_{vNP} and S_{wp} cross spectra of ADV measurements during June 24, 2018 at 1:00 am. Lower panel: Same color code for coherence as in the upper panel.

7.3.3 Wave-Turbulence interaction.

Mass sediment changes can be observed in timescales of a few seconds (see Figs. 7.3 or 7.13) suggesting that some wave dependent mechanism governs those events. Laboratory studies by Jensen et al. (1989) and numerical model by Pedocchi et al. (2011) with regular monochromatic waves show the dependence of phase average turbulence quantities on the wave cycle. By calculating the root mean squared orbital velocity amplitude U_{orb} as

$$U_{orb} = \sqrt{2 \int (S_{\bar{v}_E} + S_{\bar{v}_N}) df}, \quad (7.10)$$

the oscillatory Reynolds number can be defined as

$$Re_w = \frac{U_{orb}^2}{\omega_r \nu}, \quad (7.11)$$

with ω_r a representative angular wave frequency taken as

$$\omega_r = \frac{\int \omega(S_{\tilde{v}_E} + S_{\tilde{v}_N}) df}{\int (S_{\tilde{v}_E} + S_{\tilde{v}_N}) df}. \quad (7.12)$$

Analyzing wave friction coefficient and phase lead between the maximum bed shear stress over the maximum velocity, [Jensen \(1988\)](#) identifies different flow regimes. Using Re_w as an indicator of the flow regimes over smooth walls, [Pedocchi et al. \(2011\)](#) acknowledge four different regimes: a laminar regime for $Re_w < 5.0 \times 10^3$, a disturbed laminar regime for $5.0 \times 10^3 < Re_w < 1.5 \times 10^5$, an intermittent turbulent regime for $1.5 \times 10^5 < Re_w < 1.0 \times 10^6$, and a fully developed turbulent regime for $1.0 \times 10^6 < Re_w$. Direct Numerical Simulations (DNS) reported in that work had Re_w as high as 1.41×10^6 exceeding the lower limit for fully developed regime. Despite finding significant levels of turbulent kinetic energy (TKE) away from the near-wall region, it is concluded that turbulence decays significantly in the near-wall region ($zu_{*max}/\nu < 100$) when the wave velocity away from the wall drops to zero. Nevertheless, the TKE production by the shear layer during weak wave velocity “plays a key role in maintaining relatively important levels of turbulent intensity in the flow, which has a seeding effect on further development of turbulence” ([Pedocchi et al., 2011](#)) when strong wave velocity is present. Other studies use a Reynolds number defined with the Stokes viscous wave boundary thickness Re_δ , which can be related to the oscillatory Reynolds number $Re_\delta = \sqrt{2Re_w}$.

As proposed in [Section 7.3.2](#), vertical velocity ADV records can be interpreted as w' , enabling its use as an indicator of turbulence intensity. Sometimes the vertical velocity data, as shown in [Fig. 7.8](#) shows, presents a slow varying envelope. [Mark and Fischer \(1976\)](#) suggest that the vertical component of non-stationary turbulence records can be written as

$$w' = a_{w'}W, \quad (7.13)$$

where $a_{w'}$ is a deterministic function, an envelope that represents the non-stationary variance whereas W is a stationary random process with zero mean value and variance of unity. [Bendat and Piersol \(2011\)](#) use the Hilbert transform to obtain the envelope $a_{w'}$ of this type of non-stationary data. Defining

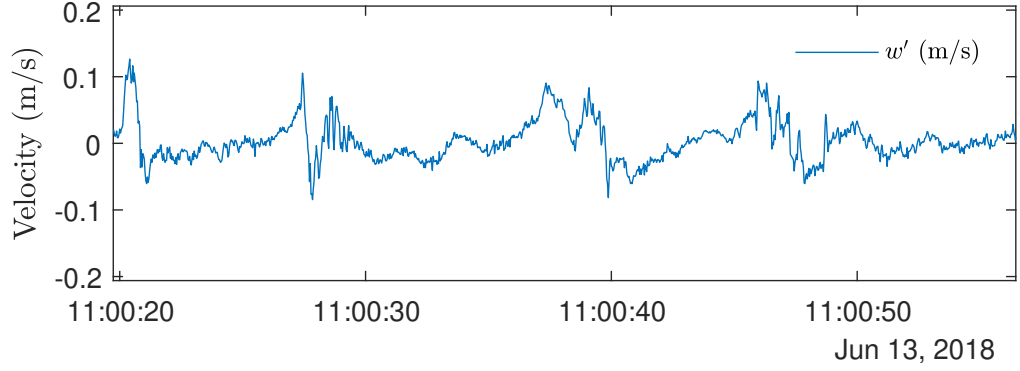


Figure 7.8: ADV vertical velocity record.

an analytic signal \mathcal{W} as

$$\mathcal{W} = w' + iH(w'), \quad (7.14)$$

where $H(w')$ is the Hilbert transform of w' and i is the imaginary unit $i^2 = -1$; \mathcal{W} could also be expressed as

$$\mathcal{W} = a_{w'}(t)e^{i\theta(t)}, \quad (7.15)$$

where $a_{w'}$ can be obtained with the following formula

$$a_{w'}(t)^2 = w'^2 + H(w')^2. \quad (7.16)$$

Figure 7.9 presents the envelope obtained by this methodology.

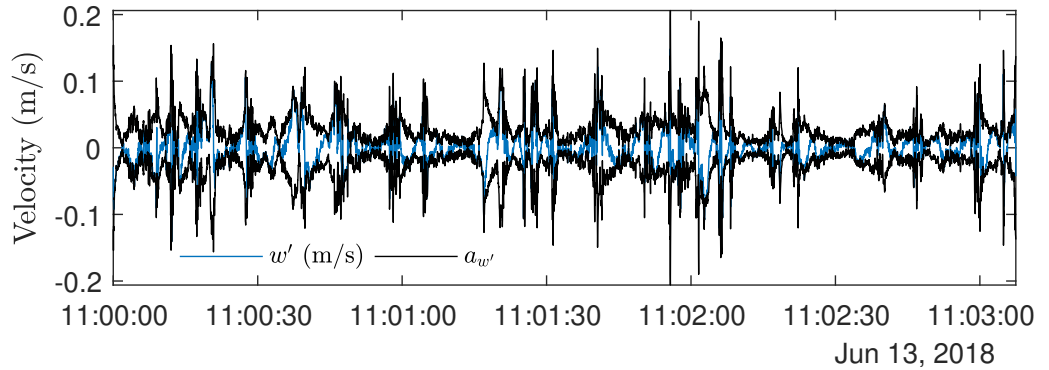


Figure 7.9: ADV vertical velocity record and Hilbert transform envelope $a_{w'}$.

Once $a_{w'}$ is determined, cross-covariance functions of this turbulence indica-

tor with wave variables, such as the horizontal velocity of the wave component projected in the mean wave direction \tilde{v}_{D_m} or bottom shear stress of the wave motion $\tilde{\tau}_b$ calculated with Eq. 2.30, can be obtained as Fig. 7.10 shows.

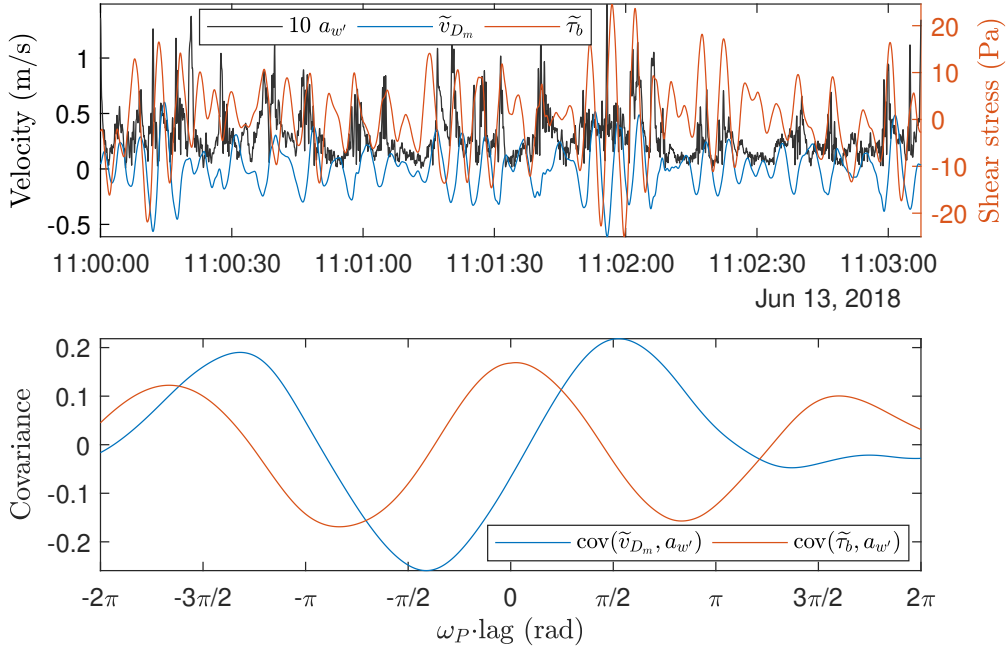


Figure 7.10: Upper panel: $a_{w'}$, \tilde{v}_{D_m} and $\tilde{\tau}_b$ time series. Lower panel: Cross-covariance of \tilde{v}_{D_m} and $a_{w'}$ as well as cross-covariance of $\tilde{\tau}_b$ and $a_{w'}$.

Taking into account that cross-covariance is less than 0.2, $\text{cov}(\tilde{v}_{D_m}, a_{w'})$ presents a maximum at $\omega_P \cdot \text{lag} = \pi/2$ indicating that \tilde{v}_H is delayed a quarter of the peak wave period T_P with respect to $a_{w'}$. On the other hand, $\tilde{\tau}_b$ and $a_{w'}$ are in phase. In this case $U_{orb} = 0.329$ m/s, $U_* = 3.03$ cm/s and $T_P = 6.1$ s providing $zU_{*max}/\nu = 8.8 \times 10^3$ and $Re_w = 8.6 \times 10^4$ in the disturbed laminar regime (Pedocchi et al., 2011). In the monochromatic smooth bed wave flume experiments presented by Jensen et al. (1989), the logarithmic hydrodynamic layer comes into existence at this phase, $\omega_P \cdot \text{lag} = \pi/2$, with $Re_w > 1 \times 10^6$. The presence of turbulence intensity in the present measurements at such low Re_w may be explained by the fact that the current motion also induces turbulence.

The amplitude $a_{w'}$, which can be interpreted as an indicator of the instantaneous turbulence intensity, is compared with sediment concentration profiles M in Section 7.5.

7.4 Current shear velocity

Shear velocity of the current U_* can be estimated with the ADV data by using expressions for turbulence intensity as proposed by [Nezu and Nakagawa \(1993\)](#)

$$U_* = \frac{\sqrt{\langle w'^2 \rangle}}{1.27} e^{\frac{z}{d}}. \quad (7.17)$$

In Fig. 7.11 a scatter plot comparing these estimations with calculations of u_{*c} provided by [Madsen \(1994\)](#) implemented in a MatLab code by [Nichols \(2005\)](#) (see Section 2.1) and by [Styles and Glenn \(2000\)](#) also implemented in a MatLab code based on software provided by Richard Styles (see Section 2.3).

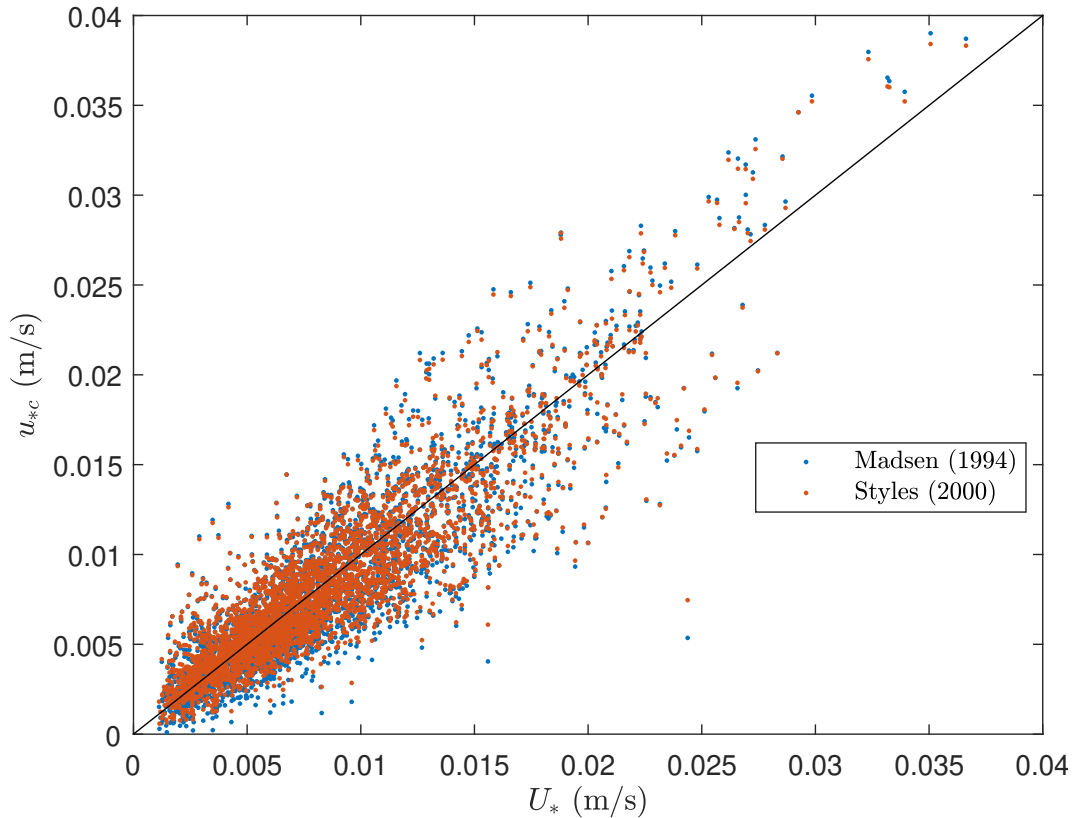


Figure 7.11: Scatter plot of U_* estimated with [Nezu and Nakagawa \(1993\)](#) vs u_{*c} obtained with [Madsen \(1994\)](#) and vs u_{*c} obtained with [Styles and Glenn \(2000\)](#).

Even though, both abscissa and ordinate in Fig. 7.11 of the scatter clouds were obtained with the ADV data, as Eq. 7.17 indicates, U_* was obtained with the vertical velocity projection of the turbulent component w' . On the other hand, u_{*c} were obtained using models by [Madsen \(1994\)](#) and [Styles et al. \(2017\)](#) with the following inputs: U_{orb} (in Eq. 7.10); T_P extracted from

S_η ; and $U_c = \sqrt{U_E^2 + U_N^2}$, all three inputs completely independent from the vertical velocity projection. With Fig. 7.11 both mathematical models are verified. This would be the first time the referred theories have been verified, as far as the author is concerned.

As has been previously mentioned in Section 2.3.1, the difference between the bottom shear stress in neutral case and with stratification $\Delta\tilde{\tau}$ is small. This enables to apply the $\tilde{\tau}_b$ obtained with the model by Madsen (1994) instead of the model by Styles et al. (2017) which imply time consuming calculations.

7.5 Mobile sediments

The ADV and ABS data were also analyzed as a whole. Even though every instrument clock was synchronized with the same clock at the beginning of each deployment, a small drift was registered in the ADV and the ABS clocks. Both instruments were set to measure every half an hour, the ABS for 2.1 min and the ADV for 3.1 min. Fortunately, the pressure signal of each instrument was very useful to determine the clock shift between time series. The ABS recorded the pressure data with a rate of 1 Hz and the ADV recorded the pressure data with a rate of 64 Hz. In order to obtain better time shift resolution, the ADV pressure data was interpolated to 64 Hz in the frequency domain by zero-padding the Fast Fourier Transform (FFT). With the ABS interpolated data, the peak in the cross-covariance maxima of both pressure signals was used to estimate the clock shift. Figure 7.12 show both ADV and ABS raw data, as well as the ABS pressure data interpolated with the zero-padding FFT method. The time shift was used to correct the ABS clock.

Mehta (2013) indicates that at the boundary between mobile fluid mud and the suspension of sediment, upward sediment entrainment depends on the kinetic energy of the turbulent eddies. Figure 7.13 presents profiles of M with a sampling rate of 2 Hz using the methodology proposed in Section 3.8. This figure shows the variability of sediment mass concentration when waves with $U_{orb} = 0.329$ m/s and $T_P = 5.8$ s are present with currents of $U_c = 0.328$ m/s. This variability compels to more time consuming acoustic inversions, in order to ensure constant sediment mass concentration in the selected time window, 0.5 seconds in this figure. The time series of M at $z = 0.05$ m is plotted with $a_{w'}$, where $a_{w'}$ was averaged to match the same time steps as M . Some correlation can be seen when comparing between M and $a_{w'}$, even though

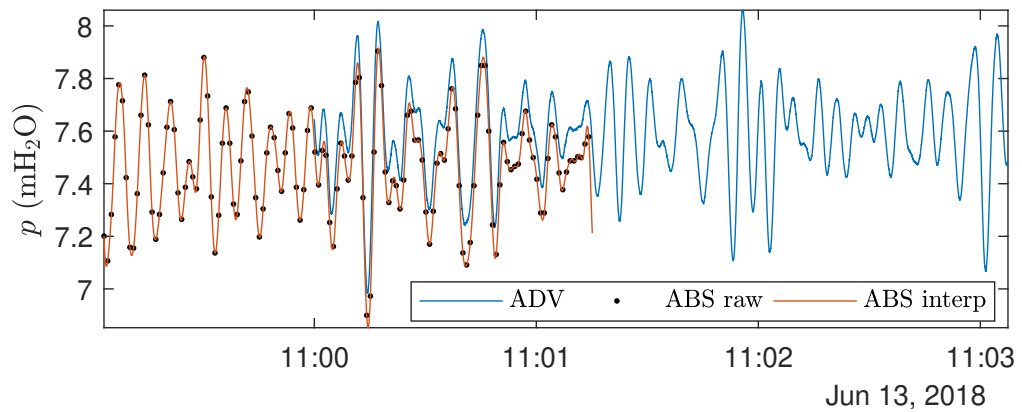


Figure 7.12: ADV and ABS pressure raw data. The interpolated ABS data is shown as a full red line. Both ABS raw and interpolated data were corrected by the time shift.

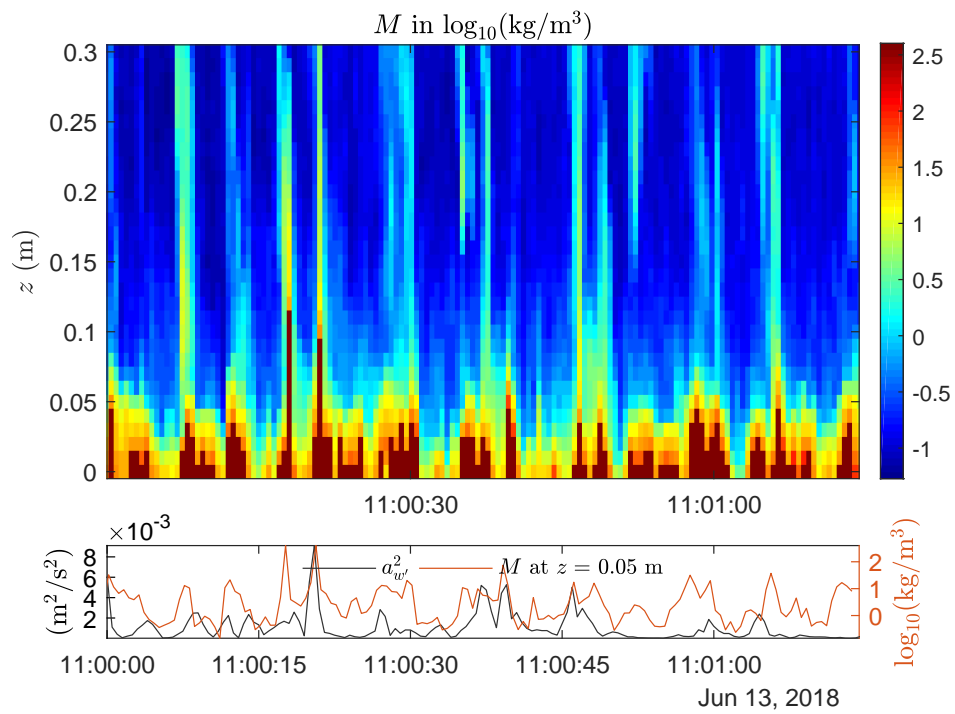


Figure 7.13: Upper panel: Sediment concentration profiles M obtained with the ABS. Lower panel: time series of M at $z = 0.05$ m and the averaged amplitude $a_{w'}$.

sediment burst can happen without a corresponding turbulence intensity burst registered at the ADV sampling volume at $z = 0.29$ m.

The concentration near the bed was obtained with the acoustic technique

\overline{M}_a , by evaluating the time average of M at $z = 1$ cm, which is the nearest measured point to the bottom (as from now, \overline{M} refers to the time average of M at each z). On the other hand, depth integrated sediment transport near the bottom Q_{sb} can be obtained by integrating the sediment concentration profile M times the current solution of the model by [Styles and Glenn \(2000\)](#) in the acoustic range with the following formula

$$Q_{sb} = \int \overline{M} u_c dz'. \quad (7.18)$$

Figure 7.14 shows the time average mass sediment concentration using the methodology proposed in Section 3.8 and the solutions of the model by [Styles and Glenn \(2000\)](#) presented in Section 2.3. The solutions were obtained using U_{orb} , T_P and U_c parameters obtained with the ADV data as well as \overline{M}_a obtained with the ABS data. The ratio of the first layer height z_1 with the wave boundary layer δ_{wc} named $\alpha_G = z_1/\delta_{wc}$, whose values are between 0 and 1, was the only tuning parameter when running the model by [Styles and Glenn \(2000\)](#).

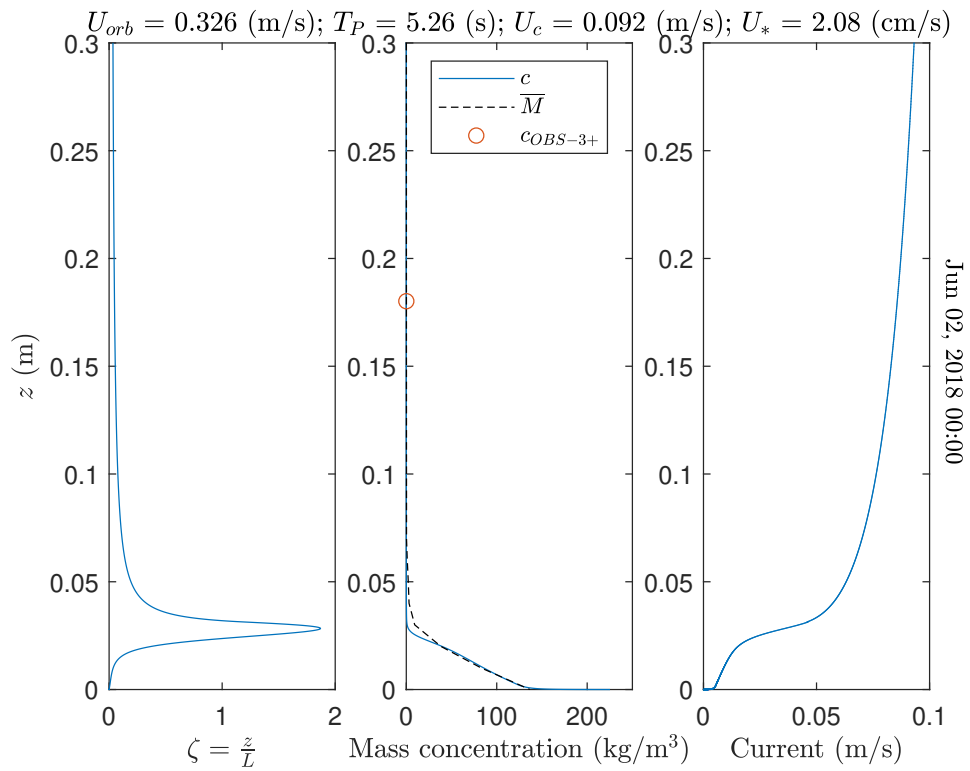


Figure 7.14: ζ , c and u_c profiles obtained using the model by [Styles and Glenn \(2000\)](#) (Eqs. [2.52](#), [2.57](#) and [2.56](#)) from Jun 02, 2018 00:00. In dashed black line averaged sediment concentration profile \bar{M} obtained with the ABS data are represented. The \circ symbol indicates the mass concentration estimated with the OBS-3+.

Chapter 8

Results and discussion

8.1 Results

This Section describes two time intervals or events each one of approximately one day 12 hours. One begins on Jun 7 and the other one begins on Jun 12, 2018. Both events had very intense waves, currents and bottom sediment activity. The first event captured a persistent lutocline, with a duration of approximately one day, associated with strong waves from the west and moderate currents. The second event presents higher wave energy than the previous one, it approaches from the southwest and has stronger currents. Instead, the presence of lutocline is restricted to a few hours when the currents weaken in the middle of the event. Details of the hydrodynamic conditions and sediment response during both events are discussed below.

To facilitate the analysis all the forcings, orbital velocities U_{orb} , bottom shear stresses $|\tilde{\tau}_b|$, the mean square of the turbulent component of the vertical velocities $\langle w'^2 \rangle$ (as a proxy for turbulent kinetic energy) as well as the sediment transports Q_{sb} are classified according to Table 8.1.

Table 8.1: Ranges for low, moderate and strong values.

	Low	Moderate	Strong
U_c (m/s)	< 0.100	0.100 – 0.300	> 0.300
U_{orb} (m/s)	< 0.100	0.100 – 0.300	> 0.300
$ \tilde{\tau}_b $ (Pa)	< 10.0	10.0 – 20.0	> 20.0
$\langle w'^2 \rangle$ (cm ² /s ²)	< 5.0	5.0 – 20.0	> 20.0
Q_{sb} (kg/ms)	< 0.100	0.100 – 0.300	> 0.300

8.1.1 First event: June 7-8, 2018

After three consecutive days of currents below 0.200 m/s, significant wave heights below 0.30 m and orbital velocities below 0.100 m/s, resulting from the action of winds of about 10 m/s coming from the northwest, on June 7, a wave-dominated event approaching from the west begins, which increases sediment activity. This is framed with a black rectangle in Fig. 6.3. During the first 2 hours and 30 minutes of this event, moderate wave energies (U_{orb} from 0.151 to 0.161 m/s and H_s from 0.85 to 0.96 m) combined with a sustained increment in current velocities from low ($U_c = 0.027$ m/s) to moderate ($U_c = 0.197$ m/s) can be seen in the first and third panel of Fig. 8.1.

During the following two hours (from 2:30 AM to 4:30 AM), while current velocities and wave energies present small increments, the acoustic backscatter profile over the whole water column shown in the second panel of Fig. 8.1, increases as more sediment is entrained into suspension (correction of near field, water absorption and spreading were applied when presenting the acoustic backscatter profile of Acoustic Doppler Current Profiler (ADCP) beams (Chapter 6)). The mean sediment concentration \bar{M} determined with the multi-frequency acoustic inversion of the Acoustic Backscatter Sensor (ABS) data, displayed in the fourth panel of Fig. 8.1, also presents this increment in the upper centimeters (with values of \bar{M} at $z = 27$ cm increasing from 0.2 kg/m³ at 2:30 AM to 0.7 kg/m³ at 5:30 AM).

On June 7, from 4:30 AM to 9:00 AM, currents became weaker ($U_c = 0.214$ m/s to $U_c = 0.109$ m/s) and both wave energies and bottom shear stresses increased from moderate ($U_{orb} = 0.172$ m/s, $H_s = 1.06$ m and $|\tilde{\tau}_b| = 4.0$ Pa at 4:30 AM) to strong ($U_{orb} = 0.355$ m/s, $H_s = 1.45$ m and $|\tilde{\tau}_b| = 16.2$ Pa at 9:00 AM). During this period, the bed sediment is entrained into suspension forming a concentrated sediment layer (fluid mud) above 50 kg/m³, and a lutocline at the top of the layer 7 cm high. The height of the lutocline δ_L , detected by the ABS can be seen in the fourth panel of Fig. 8.1. The Acoustic Doppler Velocimeter (ADV) Probe Check data seen in the sixth panel of Fig. 6.3 confirms this. As shown in the second panel of Fig. 8.1, any changes in the bottom sediment concentration profiles were also registered by the ADCP acoustics, as the local maximum of the acoustic backscatter near the seabed decreases over this period, demonstrating a gentler transition in terms of sediment concentration.

From early in the day until 7:30 AM, both low frequency ABS transducers,

0.5 MHz (not shown) and 1 MHz (shown in Fig. 6.3, seventh panel), registered a descent of two centimeters in the position of the seabed. This is evidence of erosion. However, it is important to recall that the spatial resolution of the ABS was 1 cm. Only Beam 3 of the buoy ADCP not shown here registered an abrupt descent of the bottom approximately 2:30 AM. This value was of almost 1 meter. Most likely, the motion of the buoy by hydrodynamic forcing explains this register, indicating once again that bottom sediment dynamics require more dedicated measurements than the ones provided by the buoy.

The fifth panel of Fig. 8.1 shows the depth-integrated sediment transport near the bottom Q_{sb} , using the sediment concentration \overline{M} presented in the fourth panel, the velocity current profiles determined with Styles and Glenn (2000) model and Eq. 7.18. The parameter α_G in Styles and Glenn (2000) model simulations was set in the range of 0.15 to 0.40. Although δ_L is approximately 7 cm, after Jun 7 at 4:00 PM the sediment transport begins to decline, in line with a reduction in U_c . At the end of the event, starting on Jun 8 at 2:00 AM a reduction of δ_L is recorded, completely disappearing at 5:00 AM of the same day. The last panel of Fig. 8.1 indicate a good agreement of the OBS and ABS (at the same z than the OBS sensor) sediment concentration estimations. The dashed black line indicates the laboratory turbidity calibration limit. The OBS is located right in the middle of the acoustic range of the ABS (OBS position was $z = 0.18$ m and ABS transducers were $z = 0.39$ m).

In the following sub-sections, particular instants of this event are analyzed and described in detail. The upper left panels of Figs. 8.2 to 8.8 show the sediment concentration profiles M obtained using the multi-frequency acoustic technique presented in Section 7.5. The middle left panels of those figures present the raw data collected by the ADV, used to calculate $a_{w'}$, \tilde{v}_{D_m} , $\tilde{\tau}_b$ displayed in the lower left panels, as well as the values of U_E , U_N , U_c , H_S , T_P , D_m , U_{orb} , U_* , $\langle w'^2 \rangle$ and $|\tilde{\tau}_b|$ of those time intervals. More details of this calculations are provided in Chapter 7. The mean sediment concentration profile \overline{M} appears in the second upper panels. It is calculated as the time average of M at each z , $M_{95\%}$, the 2.5th and 97.5th percentiles of M at each z , and $M_{50\%}$, the 25th and 75th percentiles. The sediment concentration profile c resulting from the model simulations by Styles and Glenn (2000) and the concentration estimated by the OBS-3+ can be seen also in those panels. The third and fourth upper panels show the results of the stability parameter ζ and current velocities u_c of the model by Styles and Glenn (2000).

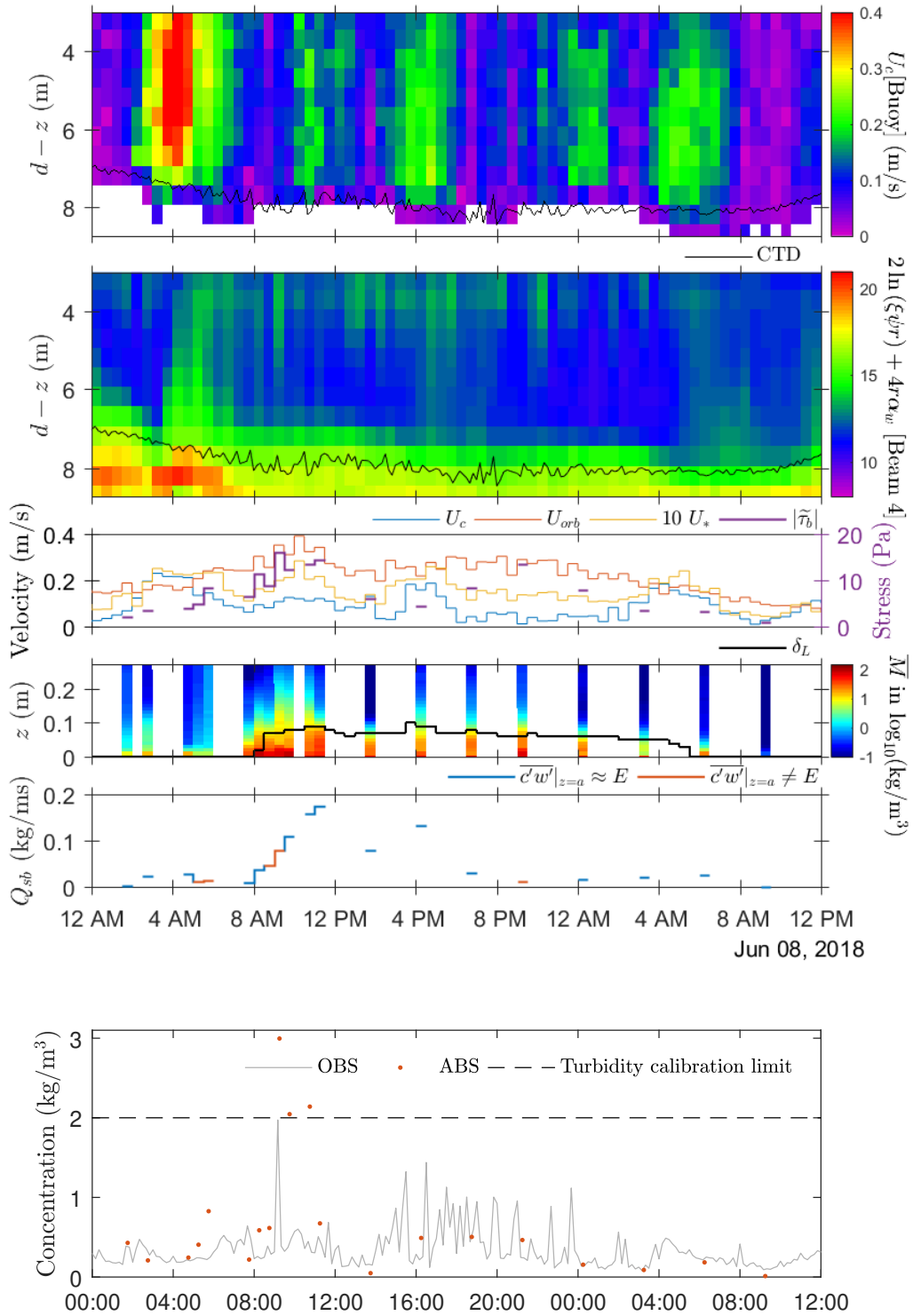


Figure 8.1: Registered values on June 7 and on the first 12 hours of June 8, 2018. Wave-dominated event.

Jun 7 at 2:30 AM.

At the beginning of this event, there is low shear stress caused by moderate currents with a southwest direction combined with moderate waves approaching from the west, which form an angle of 132 degrees. In the upper left panel of Fig. 8.2, pulses of high sediment concentration on the lower decimeter appear to be correlated with $a_{w'}$. The amplitude of w' is calculated using Eq. 7.16 and it is used as a proxy of the instantaneous turbulent intensity. In the second upper panel, $M_{50\%}$ and $M_{95\%}$ ranges indicate high sediment concentration variability in the lower 2 cm. \overline{M} together with c indicate a gradient on the mean sediment concentration profile at $z = 2$ cm, where the stability parameter ζ presents a local maximum (third upper panel). The current velocity profile presented in the fourth upper panel decays from $u_c = 0.197$ m/s at $z = 29$ cm to around 0.050 m/s at the referred lower 2 cm.

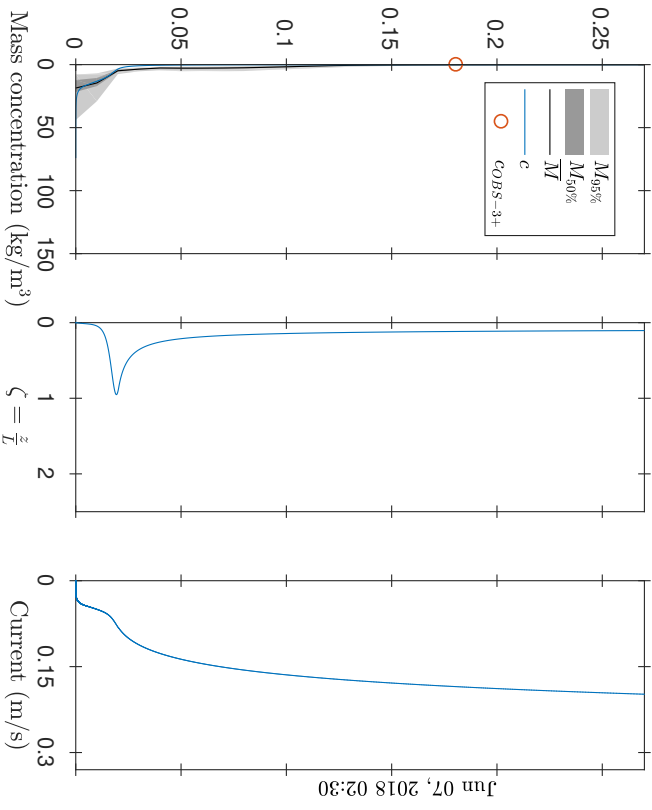
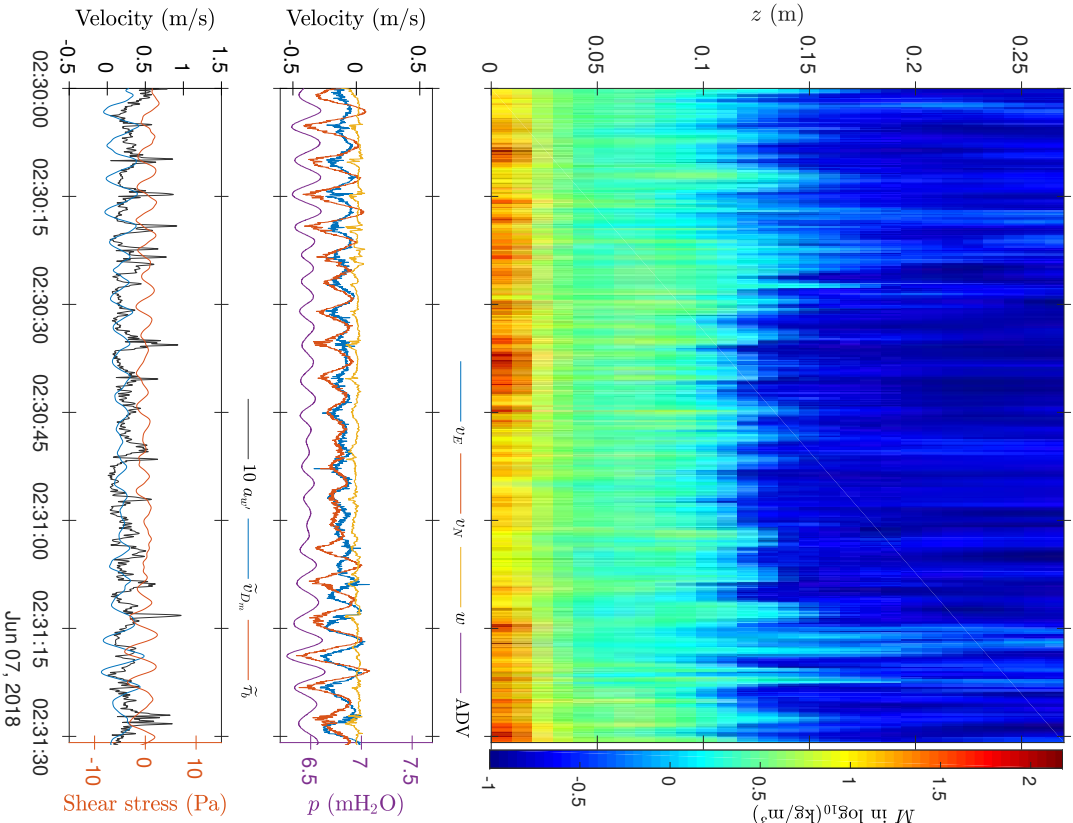


Figure 8.2: Near bed currents of $U_E = -0.113$ m/s and $U_N = -0.161$ m/s ($U_c = 0.197$ m/s) and waves with $H_S = 0.96$ m, $T_P = 4.5$ s and $D_m = 264$ (near bed orbital velocity of $U_{orb} = 0.161$ m/s) $U_* = 2.0$ cm/s, $\langle w'^2 \rangle = 6.0$ cm²/s², $|\tilde{\tau}_b| = 3.7$ Pa and $Q_{sb} = 0.023$ (kg/ms).

Jun 7 at 4:30 AM.

There are low shear stresses caused by small increments on the hydrodynamic conditions in relation to the previous two hours, moderate currents with a southwest direction and moderate waves approaching from the west, which form an angle of 119 degrees. When comparing with values at 2:30 AM (Fig. 8.2, stability parameter ζ is slightly higher, as shown in the third upper panel of Fig. 8.3. This indicates a more stratified condition. There is also no evidence of pulses in the sediment concentration profiles, as shown in the upper left panel. Larger sediment concentrations in the lower 2 cm ($\bar{M} = 17.1 \text{ kg/m}^3$ at $z = 1 \text{ cm}$) in comparison with the previous two hours ($\bar{M} = 14.6 \text{ kg/m}^3$ at $z = 1 \text{ cm}$) and similar u_c profiles result in an increment of Q_{sb} from 0.023 to 0.028 kg/ms.

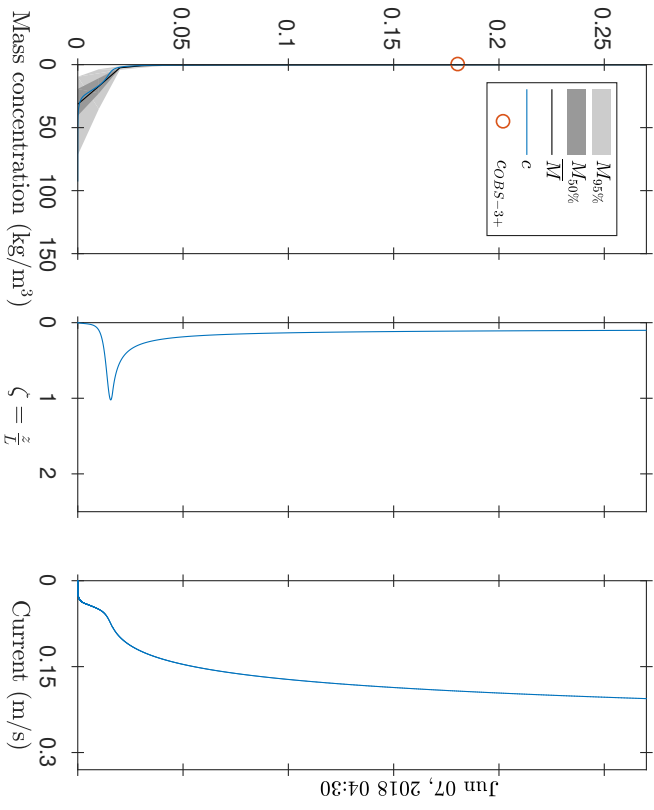
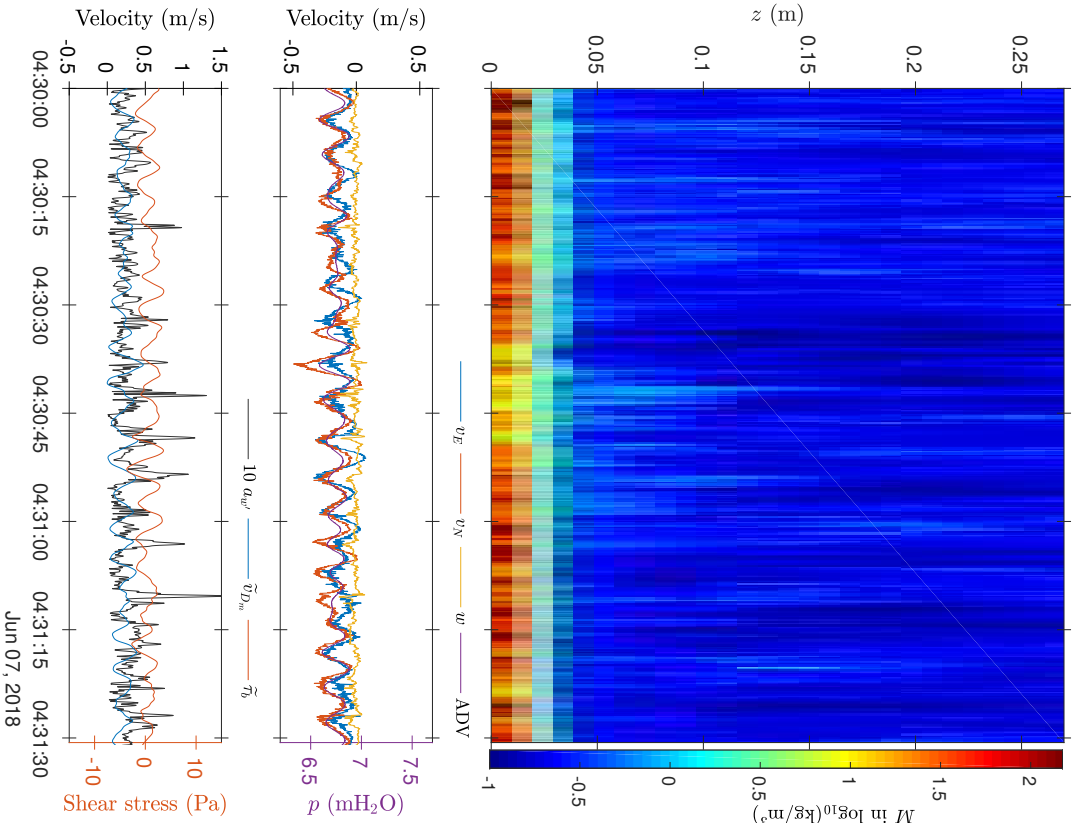


Figure 8.3: Near bed currents of $U_E = -0.120$ m/s and $U_N = -0.177$ m/s ($U_c = 0.214$ m/s) and waves with $H_G = 1.06$ m, $T_P = 4.8$ s and $D_m = 275$ ° (near bed orbital velocity of $U_{orb} = 0.172$ m/s) $U_* = 2.4$ cm/s, $\langle w'^2 \rangle = 8.6$ cm²/s², $|\tilde{\tau}_b| = 4.0$ Pa and $Q_{sb} = 0.028$ (kg/ms).

Jun 7 at 7:30 AM.

Low shear stresses and turbulent kinetic energy cause low currents with east direction and moderate waves approaching from the west, which form an angle of 1 degree. The upper left panel of Fig. 8.4 indicates an evident increment in sediment dynamics compared with the previous hours. Pulses of high concentration in the lower decimeter appear to be related with the shear stress $\tilde{\tau}_b$, as $a_{w'}$ is quite smaller than the value at 2:30 AM and 4:30 AM. In the second upper panel, $M_{50\%}$ and $M_{95\%}$ indicate high sediment concentration variability in the lower 5 cm portion and \bar{M} of 31.5 kg/m^3 at $z = 1 \text{ cm}$. The sediment concentration gradient in $z = 5 \text{ cm}$ corresponds with a peak in ζ , which proves stratified conditions. The small current velocities u_c result in very small Q_{sb} (0.010 kg/ms).

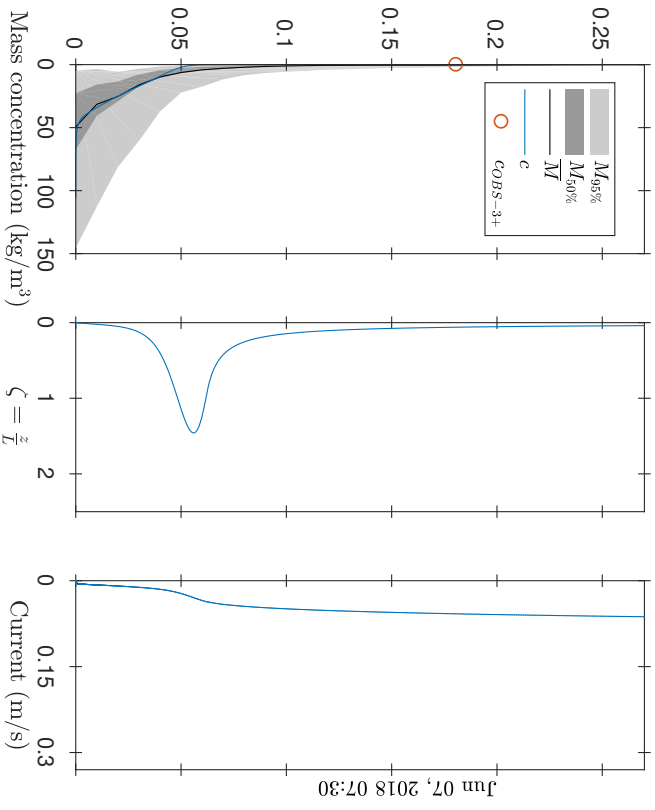
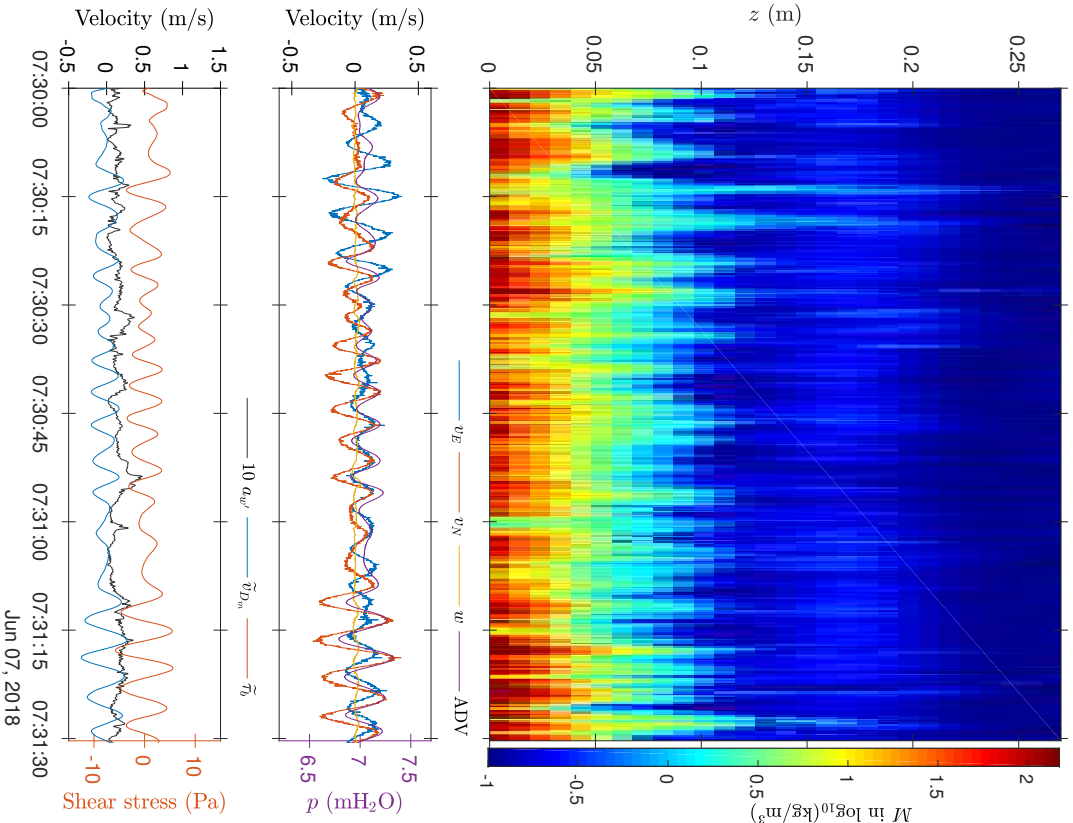


Figure 8.4: Near bed currents of $U_E = 0.064$ m/s and $U_N = 0.000$ m/s ($U_c = 0.064$ m/s) and waves with $H_S = 1.33$ m, $T_P = 5.1$ s and $D_m = 269^\circ$ (near bed orbital velocity of $U_{orb} = 0.244$ m/s) $U_* = 1.2$ cm/s, $\langle w'^2 \rangle = 2.1$ cm²/s², $|\overline{\tau_b}| = 6.5$ Pa and $Q_{sb} = 0.010$ (kg/ms).

Jun 7 at 8:00 AM.

At this stage, moderate shear stresses and low kinetic energy are caused by currents and waves stronger than the previous 30 minutes, low currents with east-southeast direction and strong waves approaching from the west, which form an angle of 14 degrees. In the upper left panel of Fig. 8.5, pulses of high sediment concentration appear to be related with the wave shear stresses $\tilde{\tau}_b$ (shown in the lower left panel) comparable to what was seen at 7:30 AM. In the second upper panel of that figure, $M_{50\%}$ and $M_{95\%}$ ranges indicate high sediment concentration variability in the lower 7 cm layer. For the first time in this event, a sharp change in the suspended sediment concentration profile (lutocline) can be appreciated near $z = 3$ cm. The stability parameter ζ (third upper panel) has a maximum at the referred z value. This indicate a reduced vertical turbulent transport. The sediment concentration profile c was not able to predict the acoustic sediment concentration \overline{M} in the 7 cm layer above the lutocline. Despite the high concentrated sediment suspensions induced by the strong wave mixing, it is possilbe to estimate low sediment transport due to the low currents. This is represented in the fourth upper panel.

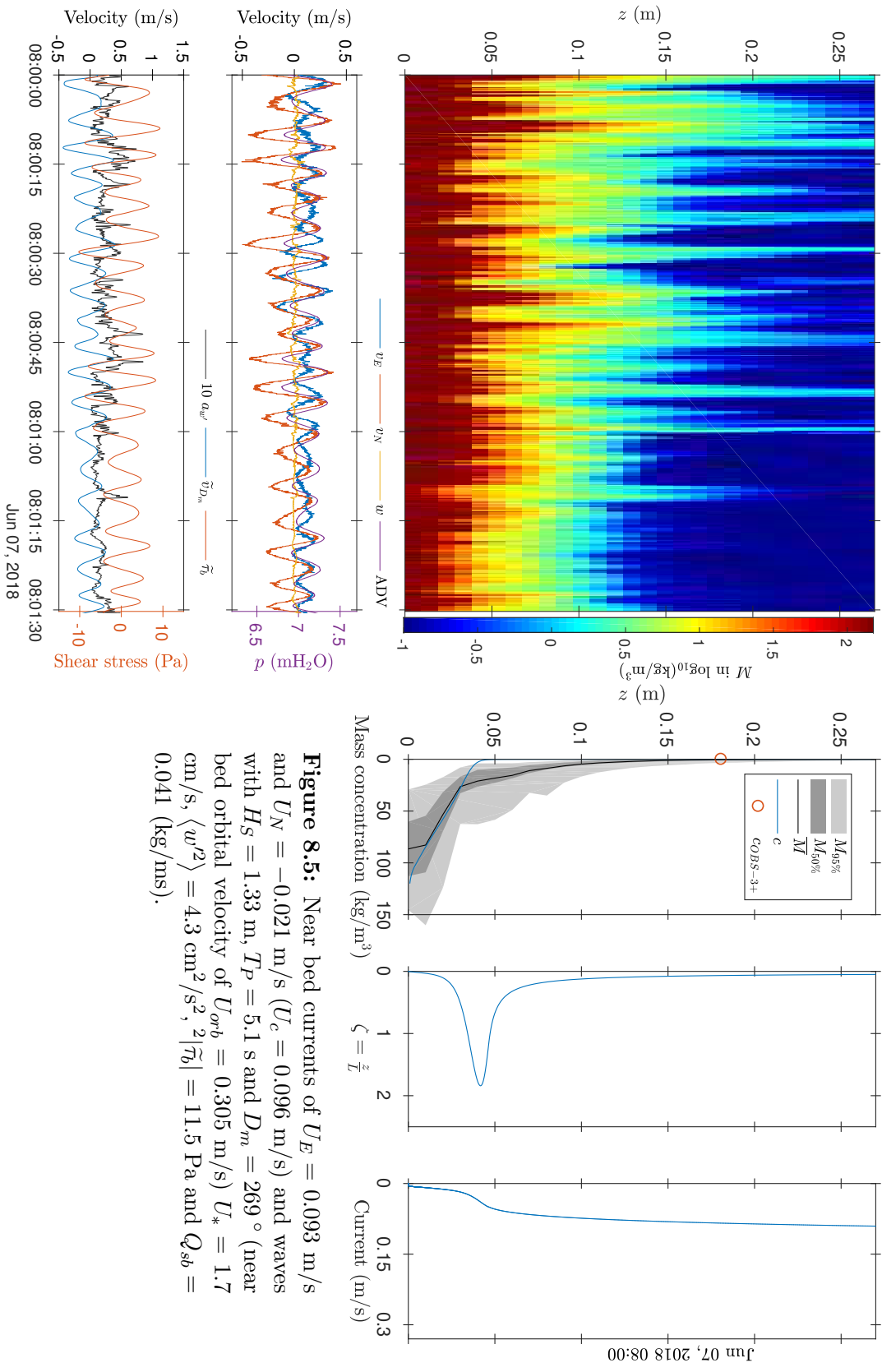


Figure 8.5: Near bed currents of $U_E = 0.093$ m/s and $U_N = -0.021$ m/s ($U_c = 0.096$ m/s) and waves with $H_S = 1.33$ m, $T_P = 5.1$ s and $D_m = 269^\circ$ (near bed orbital velocity of $U_{orb} = 0.305$ m/s) $U_* = 1.7$ cm/s, $\langle w'^2 \rangle = 4.3$ cm²/s², $2|\overline{\tau_b}| = 11.5$ Pa and $Q_{sb} = 0.041$ (kg/ms).

Jun 7 at 9:00 AM.

Moderate shear stresses and turbulent kinetic energy caused by stronger currents than those occurring at 8:00 AM moderate currents with east-southeast direction and similar strong wave energy approaching from the west, which form an angle of 21 degrees. The upper left panel of Fig. 8.6 shows pulses of high sediment concentration in the entire 27 cm layer of the ABS range. This appears to be related with both turbulent intensity and shear stresses variability produced by the wave groups. A high sediment concentration variability in the lower 15 cm is indicated by $M_{50\%}$ and $M_{95\%}$ in the second upper panel of that figure. There is a consistent sharp gradient around $z = 3$ cm. As currents became stronger in relation to the previous hour, apparently the sediment dynamics has not reached equilibrium so far. This explains the fact that no results for c and ζ from the model by [Styles and Glenn \(2000\)](#) are presented here. However, some particular patterns or “textures” of the sediment concentration may be seen in the upper left panel. Therefore, 0.5 and 1 MHz ABS transducer cross-covariance function $\text{cov}(V_{rec,0.5 \text{ MHz}}, V_{rec,1 \text{ MHz}})$ is shown in the third upper panel of Fig. 8.6. Section 7.2 explains in more detail the calculations of this function. The fourth panel shows $\text{cov}(V_{rec,2 \text{ MHz}}, V_{rec,4 \text{ MHz}})$, a good comparison with the velocity profile predicted by the model by [Styles and Glenn \(2000\)](#) is appreciated and drawn with a thick black line. This seems to indicate that hydrodynamics, represented by the current velocity profiles u_c , achieves equilibrium earlier than sediment dynamics. A larger sediment transport is caused by the stronger velocity currents.

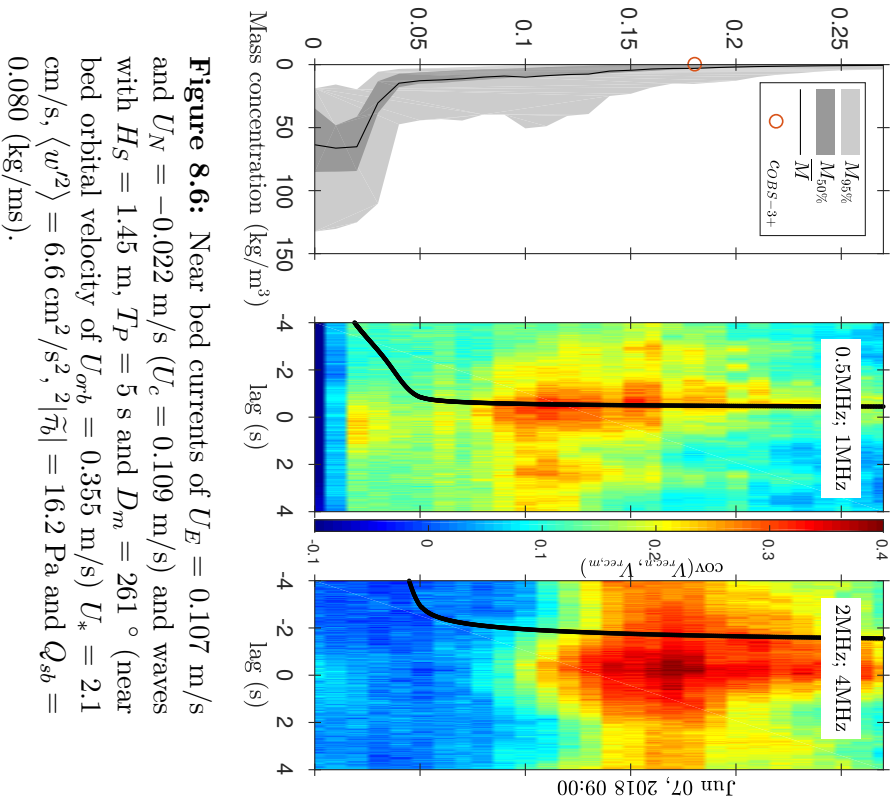
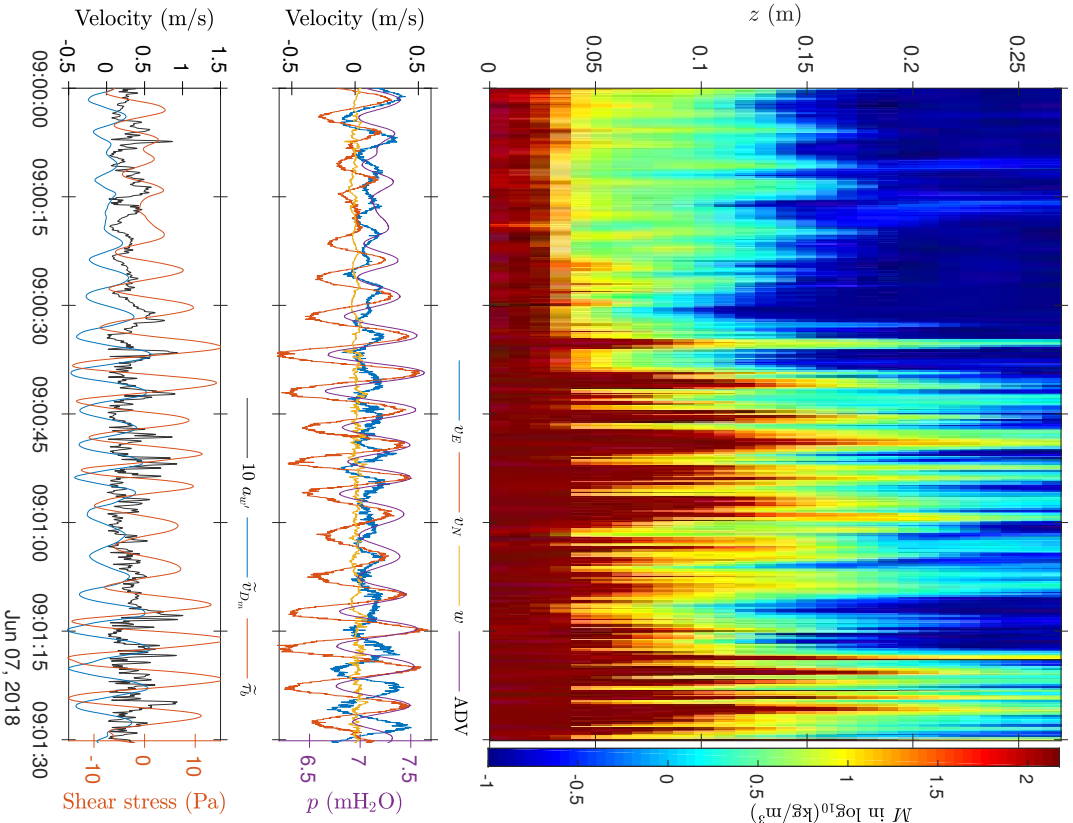


Figure 8.6: Near bed currents of $U_E = 0.107$ m/s and $U_N = -0.022$ m/s ($U_c = 0.109$ m/s) and waves with $H_S = 1.45$ m, $T_P = 5$ s and $D_m = 261^\circ$ (near bed orbital velocity of $U_{orb} = 0.355$ m/s) $U_* = 2.1$ cm/s, $\langle w'^2 \rangle = 6.6$ cm²/s², $2|\tilde{\sigma}| = 16.2$ Pa and $Q_{sb} = 0.080$ (kg/ms).

Jun 7 at 9:30 AM.

Compared with the previous 30 minutes, less shear stresses and larger turbulent kinetic energy (both moderate) are caused by stronger currents with east-southeast direction (moderate currents) and smaller wave energy (strong waves) approaching from the west-southwest, which form an angle of 30 degrees. In the upper left panel of Fig. 8.7, pulses of high sediment concentration appear to be related mostly with $\tilde{\tau}_b$. High sediment concentration variability in the lower 15 cm and a consistent sharp gradient at approximately $z = 4$ cm is also indicated by ζ . The sediment concentration profile c in the model by [Styles and Glenn \(2000\)](#) could not predict the 10 cm layer above the lutocline of \bar{M} . This is probably because the sediments are still falling from the previous intense hydrodynamic conditions, and are not in equilibrium in that range of z . Compared with data from 9:00 AM, there is an increase in the sediment transport (moderate Q_{sb}).

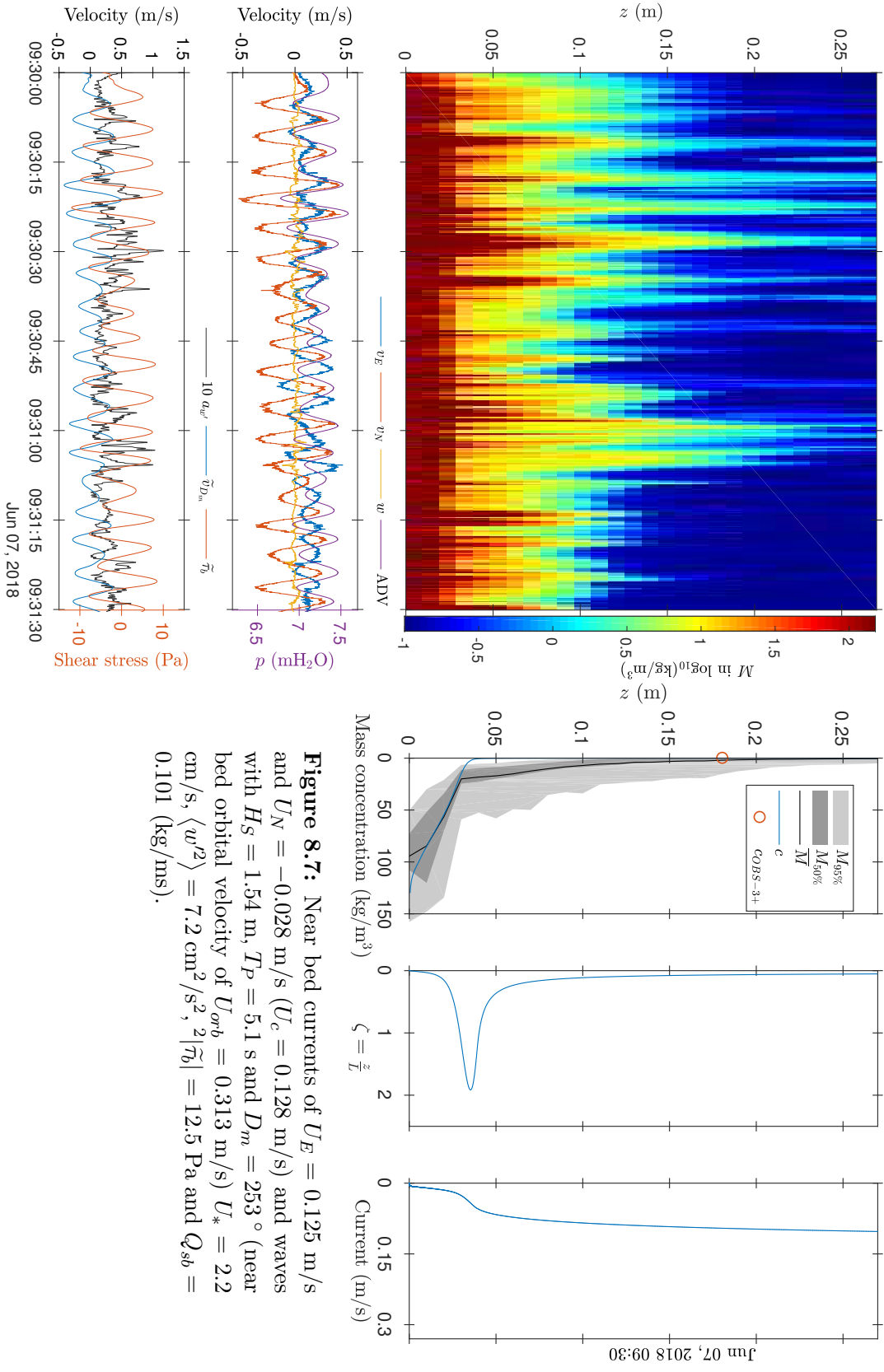


Figure 8.7: Near bed currents of $U_E = 0.125$ m/s and $U_N = -0.028$ m/s ($U_c = 0.128$ m/s) and waves with $H_S = 1.54$ m, $T_P = 5.1$ s and $D_m = 253^\circ$ (near bed orbital velocity of $U_{orb} = 0.313$ m/s) $U_* = 2.2$ cm/s, $\langle w'^2 \rangle = 7.2$ cm²/s², $2|\overline{\tau_0}| = 12.5$ Pa and $Q_{sb} = 0.101$ (kg/ms).

Jun 7 at 11:00 AM.

Moderate shear stresses and turbulent kinetic energy are caused by moderate currents with southeast direction and strong waves approaching from the west-southwest, which form an angle of 69 degrees. The upper left panel of Fig. 8.8 shows pulses of high concentration mostly related to $\tilde{\tau}_b$. $M_{50\%}$ and $M_{95\%}$ in the second upper panel indicate high sediment concentration variability over the lower 10 cm layer, where the lutocline is registered. This is the stage of the event with higher intensity in terms of sediment dynamics.

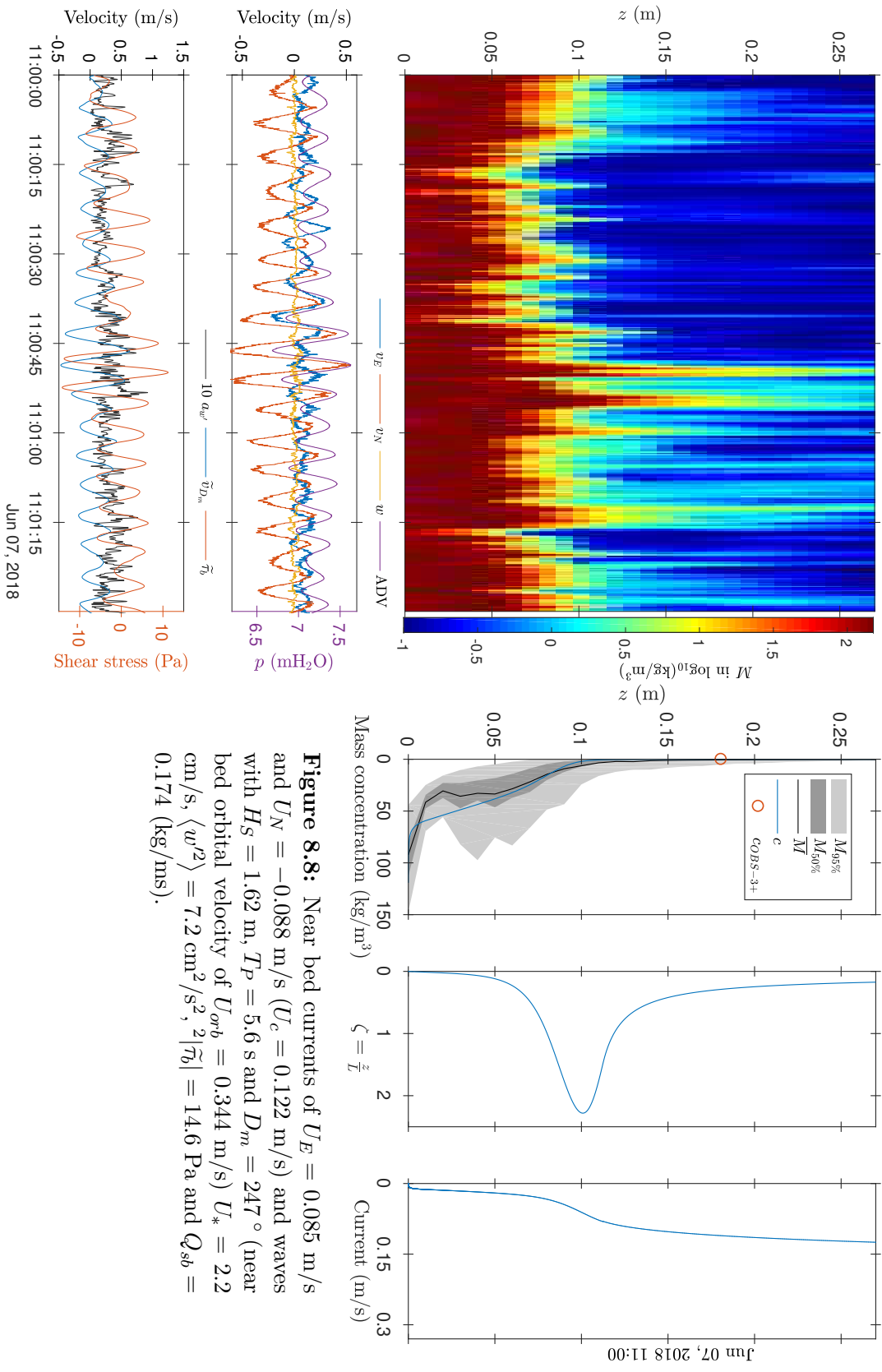


Figure 8.8: Near bed currents of $U_E = 0.085$ m/s and $U_N = -0.088$ m/s ($U_c = 0.122$ m/s) and waves with $H_S = 1.62$ m, $T_P = 5.6$ s and $D_m = 247^\circ$ (near bed orbital velocity of $U_{orb} = 0.344$ m/s) $U_* = 2.2$ cm/s, $\langle w'^2 \rangle = 7.2$ cm²/s², $2|\overline{\tau_b}| = 14.6$ Pa and $Q_{sb} = 0.174$ (kg/ms).

8.1.2 Second event: June 12-13, 2018

There follows the detailed analysis of the second event. Preceded by a day with low to moderate hydrodynamic conditions, with currents U_c and U_{orb} orbital velocities below 0.200 m/s and H_S below 0.90 m (see Fig. 6.4) 0.200 m/s, a 34 hour erosive event was registered. This event started on Jun 12 at 10:00 AM and ending Jun 13 at 8:00 PM and is shown in Fig. 8.9. This was a current-dominated event, despite having some wave predominance from 8:00 AM to 2:00 PM on June 13, around the time the current velocities presented a local minimum. At this point, lutocline was captured by the ABS as well as the ADV. As soon as the currents became stronger, there was an increment in the vertical mixing entrained sediment from the concentrated fluid mud layer up into the water column, reducing the lutocline and the sediment concentration. In the corrected acoustic backscatter profile of the Beam 4 of the buoy shown in the second panel there is an increase in the intensity at approximately 11:00 AM on June 12 caused by the suspended sediments.

Currents U_c and orbital U_{orb} velocities near the bed started to increase, reaching 0.623 m/s and 0.564 m/s correspondingly, at 2:30 AM on June 13 is shown in the third panel of Fig. 8.9. At this time, also the shear velocity U_* and the bottom shear stress of the wave motion $|\tilde{\tau}_b|$ reached their highest value. Following these peaks on the same day, U_c presented a local minimum at 9:30 AM of 0.108 m/s and a local maximum at 2:00 PM of 0.336 m/s, with current direction varying within the small range from northeast to north-northeast. Wave energy, on the other hand, decreased monotonically until the end of the day, with a starting direction perpendicular to the current but then rotating abruptly to become co-linear with it over the first few hours.

As can be seen in the fourth panel, the ABS acoustic inversion presented similar features to the corrected acoustic backscatter profile of the buoy. Because of the high sound attenuation in presence of high sediment concentration (see Section 5.2.2), the sediment concentration profiles obtained with the ABS were cut when \overline{M} exceeded 155 kg/m³ as can be seen on Jun 13 at 2:00 AM to 10:30 AM. Using the lower sediment concentration predicted by the [Smith and McLean \(1977b\)](#) (further discussed in Section 8.2) as an input for the model by [Styles and Glenn \(2000\)](#), c , ζ and u_c profiles were calculated. Sediment transport Q_{sb} , was calculated using c instead of \overline{M} when high sound attenuation is present.

Both 1 and 4 MHz sound frequency ABS transducers, as well as the ADV Probe check data (see Fig. 6.4), indicated that the seabed lowered gradually during 3 hours and 30 minutes starting on Jun 12 at 11:00 PM and ending on Jun 13 at 2:30 AM when both U_c and U_{orb} maxima were registered, presenting a total scour of 6 cm. The depth of the seabed remained constant over the next seventeen hours as indicated by the 1 MHz ABS transducer. The lutocline height δ_L is also shown here. At 8:00 PM, the position of the 4 MHz transducer peak, indicating the sea bed, gradually recovered the initial height over the next four hours. It took one week for the 1 MHz peak to recover the height presented by the 4 MHz peak, indicating a hardening of the bottom due to the consolidation process. From 2:00 AM to 8:00 AM on June 13 (indicated in a gray area of the last panel of Fig. 8.9), as the hydrodynamic forces become stronger, the concentration estimated by the ABS at the position of the OBS is higher than 10 kg/m^3 (consistent with the bottom shear stresses), whereas the concentration estimated by the OBS is lesser than 1 kg/m^3 . This indicate that the OBS sensor was in a high concentrated sediment layer where the calibration maximum (2 kg/m^3) was exceed and the strong optical attenuation provide incorrect optic inversions.

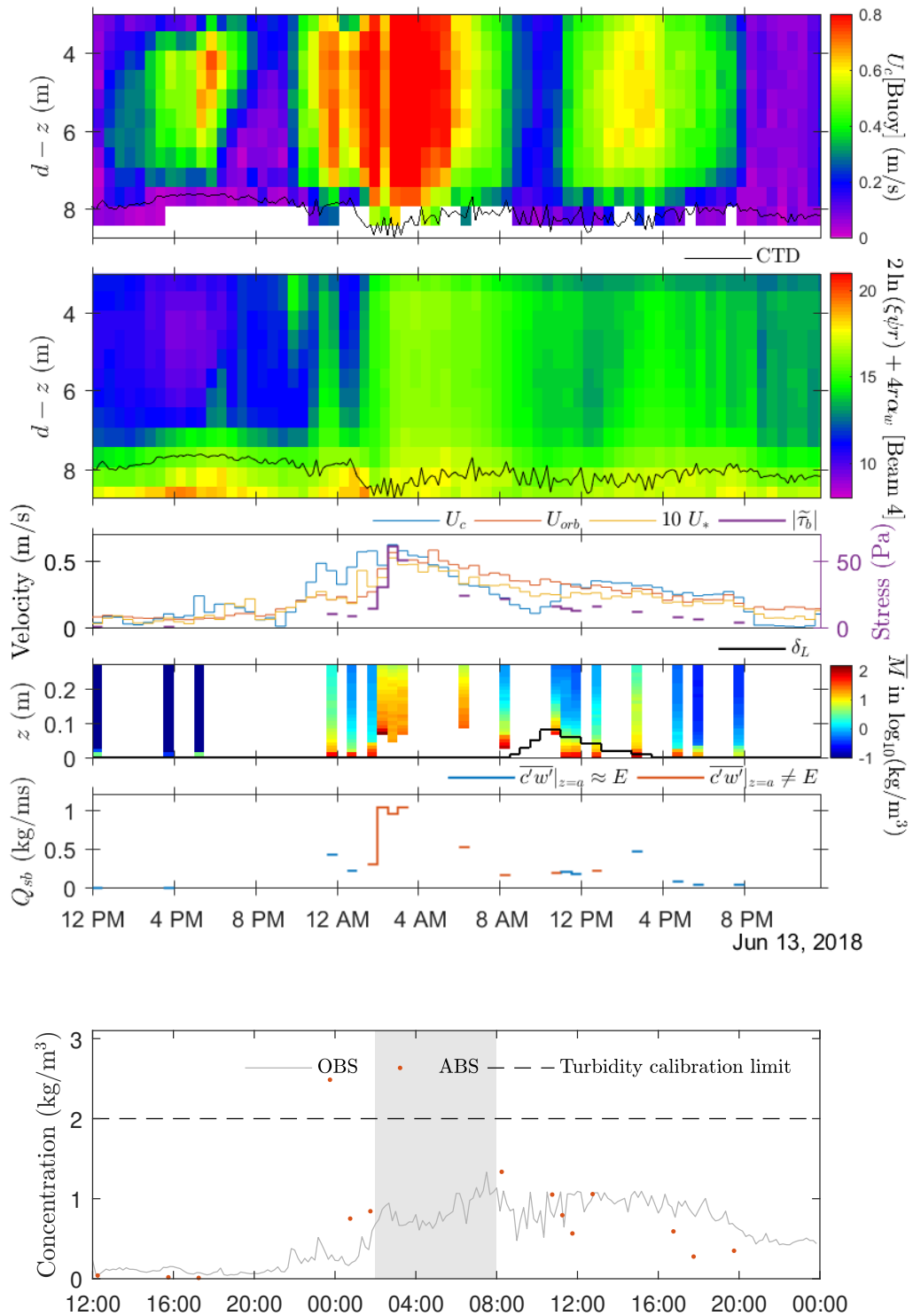


Figure 8.9: The last 12 hours on June 12 and June 13, 2018. Current dominated event.

Jun 13 at 1:30 AM.

During the first 4 hours and 30 minutes (Jun 12 at 9:00 PM) currents were very low ($U_c = 0.011$ m/s) and waves were moderate ($U_{orb} = 0.142$ m/s). Hydrodynamics began to increase until strong currents with north-northeast direction and wave velocities approaching from the southwest, which form an angle of 19 degrees, caused moderate shear stresses and strong turbulent kinetic energy. High concentration pulses are difficult to recognize in the upper left panel of Fig. 8.10. Nevertheless, resuspension events near the bottom have a large concentration variability indicated by $M_{50\%}$ and $M_{95\%}$ in the lower 5 cm layer.

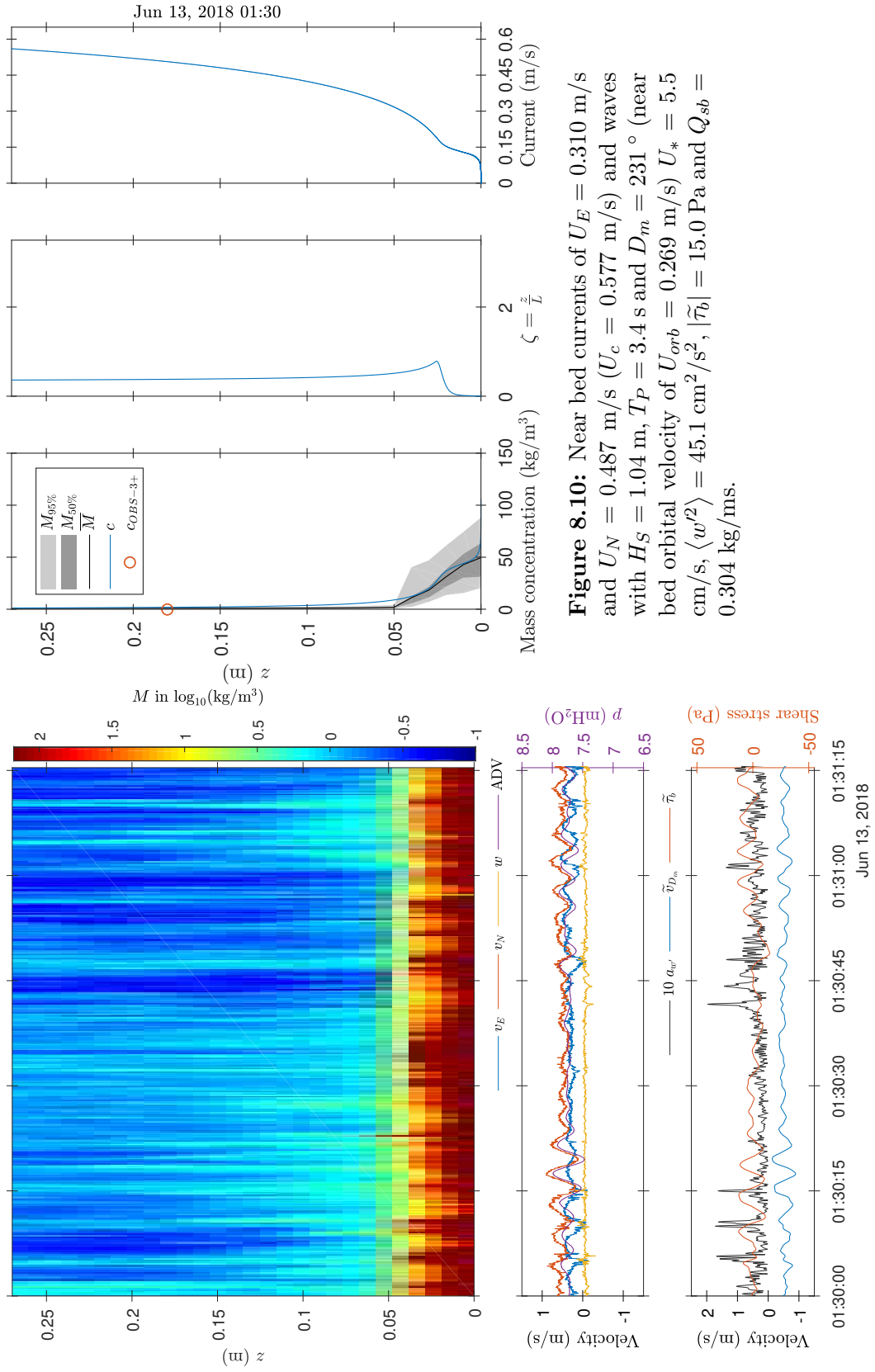


Figure 8.10: Near bed currents of $U_E = 0.310$ m/s and $U_N = 0.487$ m/s ($U_c = 0.577$ m/s) and waves with $H_S = 1.04$ m, $T_P = 3.4$ s and $D_m = 231^\circ$ (near bed orbital velocity of $U_{orb} = 0.269$ m/s) $U_* = 5.5$ cm/s, $\langle w'^2 \rangle = 45.1$ cm²/s², $|\tilde{\tau}_b| = 15.0$ Pa and $Q_{sb} = 0.304$ kg/ms.

Jun 13 at 2:30 AM.

Currents were stronger and wave velocities higher compared to these values at 1:30 AM. Currents were strong with a northeast direction and strong waves approaching from west-southwest, which form an angle of 23 degrees, and caused high shear stresses and turbulent kinetic energy at this point. In Fig. 8.11, the pulses of high concentration shown in the upper left panel seem to be correlated with a_w and $\tilde{\tau}_b$ appearing in the lower left panel. The acoustic inversion was intentionally cut over when $\bar{M} > 155 \text{ kg/m}^3$, in the lower 5 cm layer. Due to the high sound attenuation, the inversion technique may have biased solutions on z lower range. With a sediment mass concentration of 260 kg/m^3 in the lower sediment concentration expected by the Smith and McLean (1977b) as an input for the model by Styles and Glenn (2000), c , ζ and u_c solutions can be seen in the second, third and fourth upper panel respectively. In order to estimate the sediment transport, instead of using \bar{M} as indicated in Eq. 7.18, the sediment concentration predicted by Styles and Glenn (2000) c was used. This profile shows a 5 cm height layer of high sediment concentration and strong Q_{sb} .

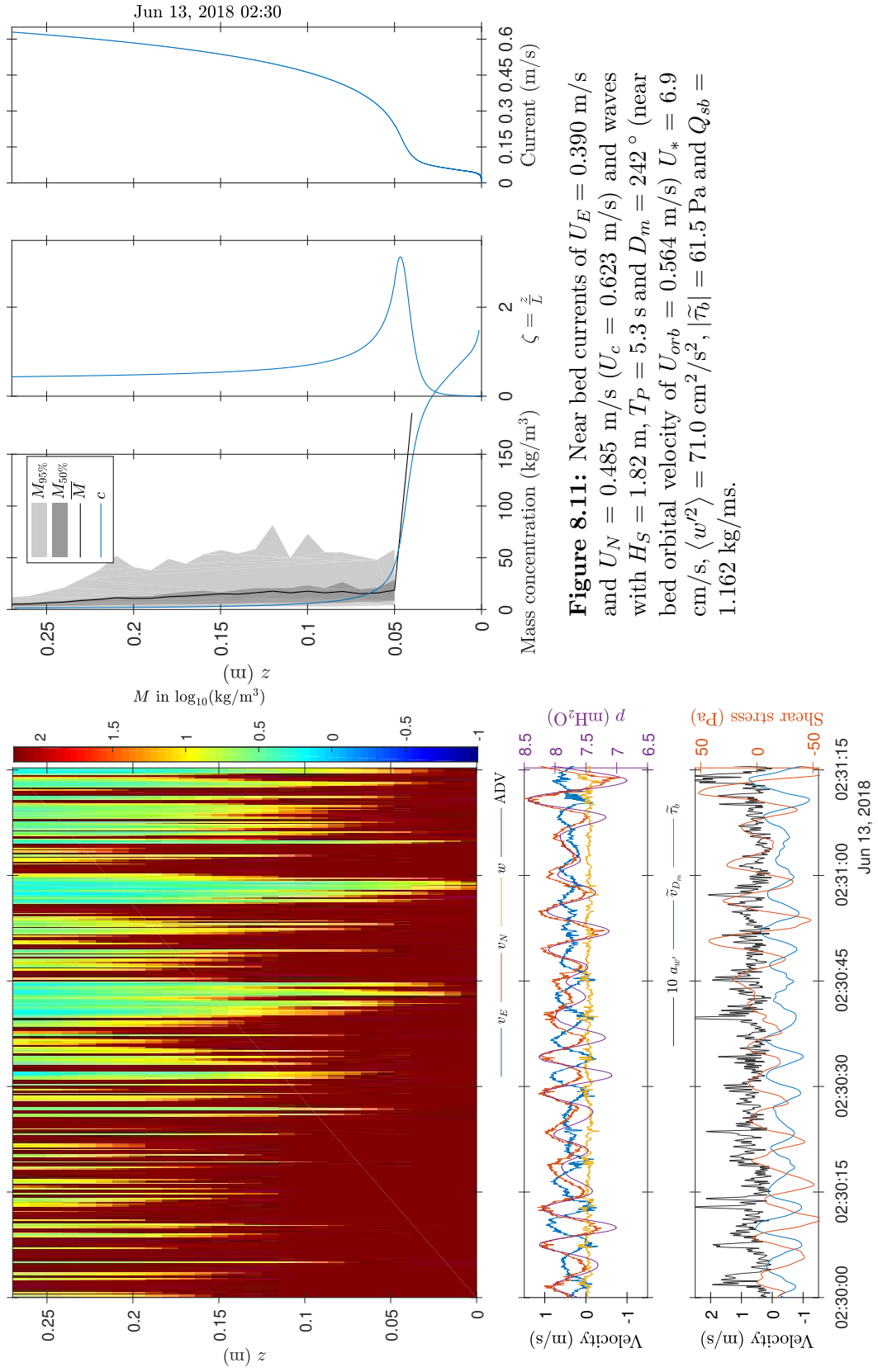


Figure 8.11: Near bed currents of $U_E = 0.390$ m/s and $U_N = 0.485$ m/s ($U_c = 0.623$ m/s) and waves with $H_S = 1.82$ m, $T_P = 5.3$ s and $D_m = 242^\circ$ (near bed orbital velocity of $U_{orb} = 0.564$ m/s) $U_* = 6.9$ cm/s, $\langle w'^2 \rangle = 71.0$ cm²/s², $|\tilde{\tau}_b| = 61.5$ Pa and $Q_{sb} = 1.162$ kg/ms.

Jun 13 at 10:30 AM.

Moderate shear stresses and turbulent kinetic energy were caused by currents and waves that were weaker than those registered at 2:30 AM, and moderate current velocities with a northeast direction and strong waves approaching from the south-southwest, which form an angle of 12 degrees. In Fig. 8.12, pulses of high concentration shown in the upper left panel appear to be correlated with $\tilde{\tau}_b$ in the lower left panel. The acoustic inversion was intentionally cut over when $\bar{M} > 155 \text{ kg/m}^3$, near $z = 7 \text{ cm}$, where a concentration gradient over the period shows lutocline distinguishable also in Fig. 8.9. At a sediment mass concentration of 117 kg/m^3 at the lower sediment concentration expected by the Smith and McLean (1977b) as an input for the model by Styles and Glenn (2000), c , ζ and u_c solutions appear in the second, third and fourth upper panel, respectively. Due to similar restrictions as the 2:30 AM burst, the sediment transport Q_{sb} was estimated using c instead of \bar{M} . This profile corresponds to a 6 cm thick layer with high sediment concentration.

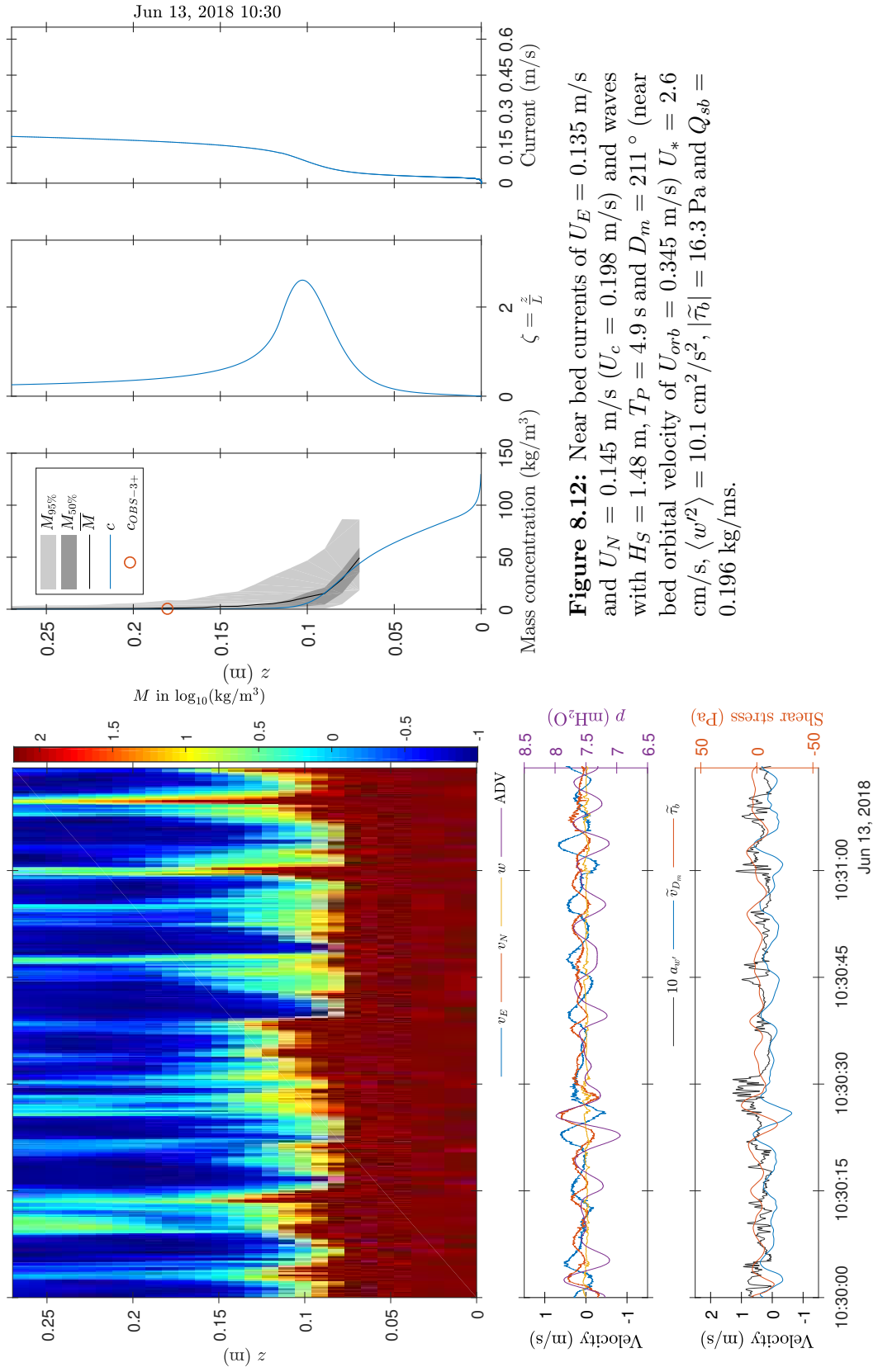


Figure 8.12: Near bed currents of $U_E = 0.135$ m/s and $U_N = 0.145$ m/s ($U_c = 0.198$ m/s) and waves with $H_S = 1.48$ m, $T_P = 4.9$ s and $D_m = 211^\circ$ (near bed orbital velocity of $U_{orb} = 0.345$ m/s) $U_* = 2.6$ cm/s, $\langle w'^2 \rangle = 10.1$ cm²/s², $|\tilde{\tau}_b| = 16.3$ Pa and $Q_{sb} = 0.196$ kg/ms.

Jun 13 at 2:30 PM.

Moderate shear stress and strong turbulent kinetic energy were caused by stronger currents than those registered at 10:30 AM (strong current velocities) with a northeast direction and moderate waves approaching from the southwest, which form an angle of 6 degrees. In Fig. 8.13 pulses of high concentration shown in the upper and lower left panels appear to be correlated with the turbulent intensity a_w . In the second upper panel, $M_{50\%}$ and $M_{95\%}$ indicate high sediment concentration variability in the lower 20 cm layer. Lutocline is no longer present as the waves are smaller and currents are larger than those registered at 10:30 AM.

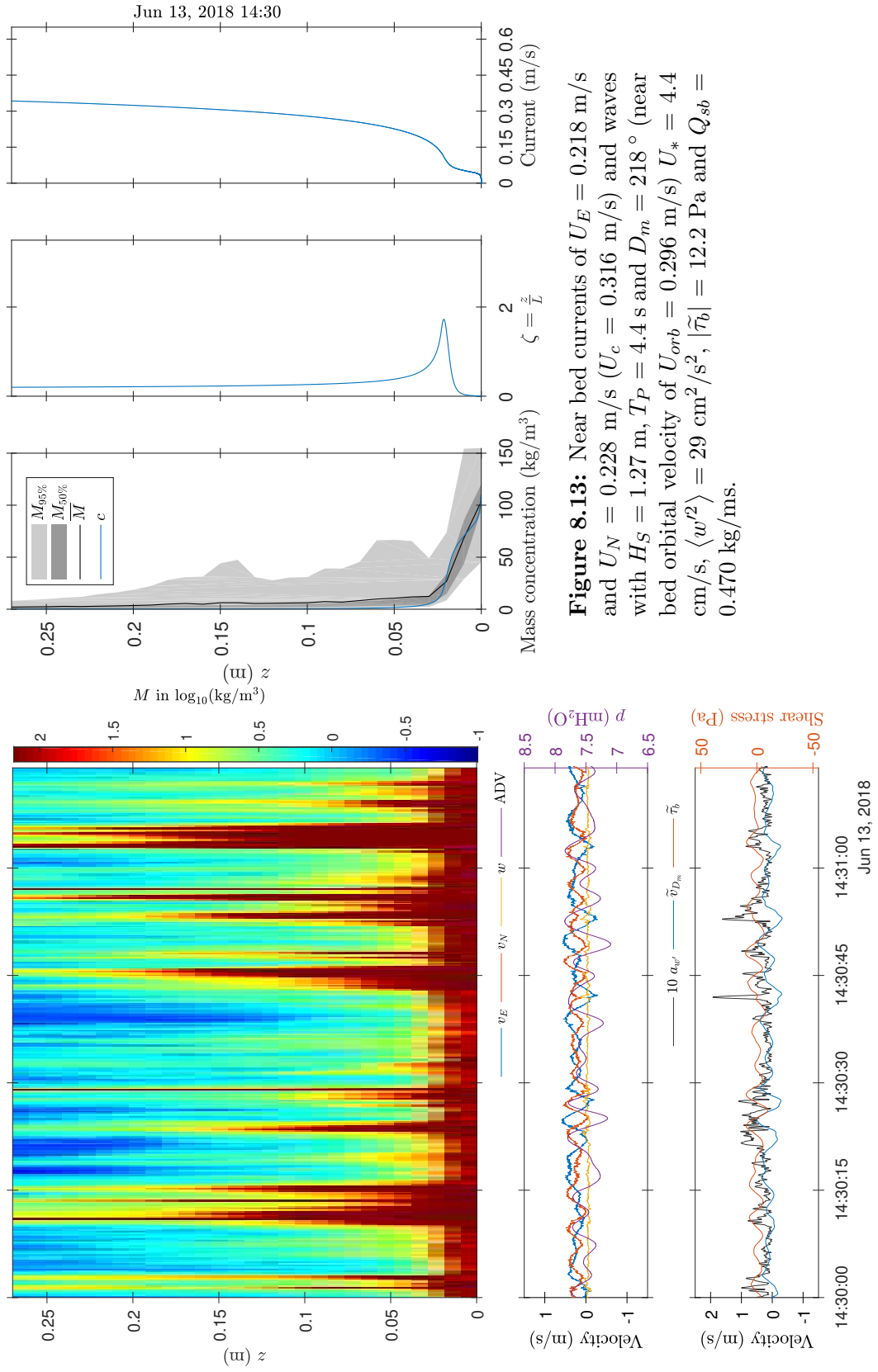


Figure 8.13: Near bed currents of $U_E = 0.218$ m/s and $U_N = 0.228$ m/s ($U_c = 0.316$ m/s) and waves with $H_S = 1.27$ m, $T_P = 4.4$ s and $D_m = 218^\circ$ (near bed orbital velocity of $U_{orb} = 0.296$ m/s) $U_* = 4.4$ cm/s, $\langle w'^2 \rangle = 29$ cm²/s², $|\tilde{\tau}_b| = 12.2$ Pa and $Q_{sb} = 0.470$ kg/ms.

8.2 Discussion

Two strong sediment dynamic events were described above: in Section 8.1.1 the first event from June 7 to 8 and in Section 8.1.2 the second event from June 12 to 13. Erosion was most significant in the second event of the entire second deployment. Erosion was 6 cm after more than 3 hours of strong shear stresses generated by waves of significant wave height, i.e. 2.3 m as can be seen in Fig. 6.4, and orbital and current velocities above 0.60 m/s as can be seen in Fig. 8.9. Table 8.2 summarizes the main forcings during the particular instances discussed above.

Table 8.2: Summary of the main parameters of the instances in both events on June 7 to 8 and June 12 to 13, 2018.

Date and Time	U_c (m/s)	U_{orb} (m/s)	U_* (cm/s)	$\langle w'^2 \rangle$ (m ² /s ²)	$ \tilde{\tau}_b $ (Pa)	Q_{sb} (kg/ms)
Jun 7 at 2:30 AM	0.197	0.161	2.0	6.0	3.7	0.023
Jun 7 at 4:30 AM	0.214	0.172	2.4	8.6	4.0	0.028
Jun 7 at 7:30 AM	0.064	0.244	1.2	2.1	6.5	0.010
Jun 7 at 8:00 AM	0.096	0.305	1.7	4.3	11.5	0.041
Jun 7 at 9:00 AM	0.109	0.355	2.1	6.6	16.2	0.080
Jun 7 at 9:30 AM	0.128	0.313	2.2	7.2	12.5	0.101
Jun 7 at 11:00 AM	0.122	0.344	2.2	7.2	14.6	0.174
Jun 13 at 1:30 AM	0.577	0.269	5.5	45.1	15.0	0.304
Jun 13 at 2:30 AM	0.623	0.564	6.9	71.0	61.5	0.957
Jun 13 at 10:30 AM	0.198	0.345	2.6	10.1	16.3	0.196
Jun 13 at 2:30 PM	0.316	0.296	4.4	28.9	12.2	0.470

In both events it can be seen that under strong waves and low currents (Figs. 8.5 to 8.8 and Fig. 8.12) the eroded sediment remains near the seabed, staying in motion for more than a day if the hydrodynamic conditions remain favorable. The high sediment concentrations generate strong density gradients produce stratification of the flow, usually inhibiting the turbulent mix imposed by currents along the rest of the water column as seen during Jun 13 at 10:30 AM (the presence of high sediment concentration pulses over the first 30 cm layer above the bed are correlated with the wave shear stresses during said hydrodynamic conditions). This mechanism enables the development of fluid mud layers whose concentrations could surpass 100 kg/m³ and their heights could be higher than a decimeter.

During the second event, when strong currents and waves were registered

(Figs. 8.11 and 8.13), more sediment is entrained from the lower highly concentrated layer into the water column (entrainment). The vertical mix imposed by the currents breaks the stratification of the flow. This results in suspended sediment concentration up in the water column of one order of magnitude higher than suspended sediment concentration registered during the first event (the presence of high sediment concentration pulses over the first 30 cm layer above the bed is correlated mainly with the turbulent kinetic energy proxy $\langle w'^2 \rangle$ during those hydrodynamic conditions).

As mentioned in Section 7.2, when ABS' signal presented some particular pattern or "texture", a particle image velocimetry technique was applied in order to obtain mean velocity profiles over the lower 40 cm layer near the bottom. Using these mean velocities and the sediment mean concentration profiles provided by the ABS, it was possible to compute the bulk Richardson number Ri_0 , and classify the mixing conditions of said instances. If the flow is composed by only two layers, the upper layer with density ρ_1 and velocity v_1 , and the lower layer with density ρ_2 and velocity v_2 , both having the same height h , Ri_0 can be computed as

$$Ri_0 = \frac{4(\rho_2 - \rho_1)gh}{(\rho_1 + \rho_2)(v_1 - v_2)^2}, \quad (8.1)$$

where g is the gravitational acceleration. Mehta (2013) showed that Ri_0 can be seen as a relation between the potential energy that is needed to maintain a fully-mixed water column, and the kinetic energy that this mixing condition would obtain from the fluid. When $Ri_0 > 1$ water columns are under mixed conditions, while when $Ri_0 < 1$ water columns are under mixed conditions. In order to show the variability of the mixing conditions present in the deployment site, two different instances are presented, June 13, 2018 at 10:30 AM and 2:30 PM. During Jun 13 at 10:30 AM, $\rho_1 = 1003 \text{ kg/m}^3$ (sediment concentration of 4.8 kg/m^3), $v_1 = 0.16 \text{ m/s}$, $\rho_2 = 1025 \text{ kg/m}^3$ (sediment concentration of 40 kg/m^3), $v_2 = 0.07 \text{ m/s}$, and $h = 0.10 \text{ m}$, resulting in $Ri_0 = 5.2 > 1$. The sediment concentration profile in Fig 8.12 shows small variation in the position of the peak concentration gradients, and the Ri_0 value indicates that this was a stratified water column condition. Four hours later, at 2:30 PM, $\rho_1 = 1009 \text{ kg/m}^3$ (sediment concentration of 14 kg/m^3), $v_1 = 0.30 \text{ m/s}$, $\rho_2 = 1031 \text{ kg/m}^3$ (sediment concentration of 50 kg/m^3), $v_2 = 0.15 \text{ m/s}$, and $h = 0.03 \text{ m}$, resulting in $Ri_0 = 0.56 < 1$. Figure 8.13 shows large variability in the

sediment concentration profiles as well as the lutocline position, indicating a mixed water column condition as suggested also by the value of Ri_0 .

Using the mean sediment concentration in the lower cm layer obtained by the ABS \overline{M}_a , the orbital velocity U_{orb} , the bottom wave excursion amplitude U_{orb}/ω_r , the mean current U_c and the angle between waves and currents extracted from the ADV's instantaneous velocity data, an analytical model was implemented in order to quantify the sediment transport in the lower 30 cm layer above the seabed. Based on Glenn (1983), Styles and Glenn (2000) developed an analytical model for non-cohesive sediments in presence of waves and currents, where three different layers were defined, one next to the seabed where the eddy viscosity is dominated by the wave motion; another one very far from the seabed in which the eddy viscosity is completely governed by the currents; and an intermediate transition layer between the other two which is limited by two heights z_1 and z_2 . In addition to currents and wave action, the analytical model considers the inhibition of turbulent diffusion due to the presence of concentration gradients that stratify the flow by implementing the turbulent closure for sediment self-stratification proposed by Smith and McLean (1977a). In this closure a stratification parameter ζ is used. ζ is the ratio between the distance from the bottom and the Monin-Obukov length. The height where the transition layer ends is z_2 , which can be determined as

$$z_2 = \alpha_G \frac{u_{*r}}{u_{*c}} \delta_{wc}. \quad (8.2)$$

It is where the maximum of ζ and the maximum sediment concentration gradient $\frac{\partial c}{\partial z}$ are located.

In the simulations presented here, the value for the terminal fall velocity was equal to 1 mm/s based on the concentrations estimated by the ABS and previous numeric (Fossati, 2013; Santoro, 2017) and field-laboratory works (Ponce de León et al., 2019). α_G in this model was used as a tuning parameter for z_2 and lutocline δ_L to have similar heights. Concentration profiles described by Styles and Glenn (2000) collapse with those obtained by the ABS in the entire range. This is shown in Figs. 8.2, 8.3, 8.4, 8.8 and 8.10.

Figures 8.5, 8.7 and 8.13 show good consistency between \overline{M} and c in the lower centimeters until the sharp sediment concentration gradient. In the decimeter above, the profile c obtained with Styles and Glenn (2000) underestimates the sediment concentration. The acoustic inversion on that region

indicates that the suspended sediment is mainly fine material as the fine fraction mass proportion r_f (defined in Eq. 3.103) is about 0.96 and 1.00. The analytical model assumes equilibrium in terms of sediment dynamics, the upper boundary sediment condition is no flux in the water surface ($z = 8.0$ m in these simulations). In order to explain this situation, the vertical depth was changed to simulate another sediment flux in $z = 29$ cm, but the bias could not be reduced. Nevertheless, the sediment conditions in the previous hours over of those instances, could explain the gap between \overline{M} and c within that range (Fig. 8.6 and Fig. 8.7). α_G in all the field experiments adopted values between 0.15 and 0.40.

McLean (1992) related ζ with the gradient Richardson number Ri_g

$$Ri_g = \frac{(\sigma + \beta\zeta)\zeta}{(1 + \gamma\zeta)^2}, \quad (8.3)$$

with σ and β being dimensionless parameters that relate the eddy diffusivity of mass ν_{T_m} with the eddy viscosity under neutral conditions ν_{T_N}

$$\nu_{T_m} = \frac{\nu_{T_N}}{\sigma + \beta\zeta}, \quad (8.4)$$

and γ being a parameter that relates the eddy viscosity with and without sediments as seen in Eq. 2.51. No universal values are available for σ , β or γ . Considering that Ri_g should be above 0.25 at the lutocline during stratified flows conditions and values of Ri_g should be below 0.25 during mixed conditions, the following values $\gamma = 5$, $\sigma = 2.7$ and $\beta = 6.2$ were calibrated using the results of ζ profiles for this dataset. McLean (1992) indicates that σ is order 1 whereas the order of β and γ is about 5.

Because some of the selected intervals appear to be under non-equilibrium conditions in terms of sediment dynamics (see Fig. 8.6), the analytical model by Styles and Glenn (2000) does not strictly apply. However, the current velocity profiles u_c present similarities when compared to the cross-covariance technique proposed in Section 7.2, indicating that hydrodynamics reach equilibrium before sediment dynamics does. During those conditions Q_{sb} was also calculated using Eq. 7.18.

Because of the laboratory experiments shown on Section 5.2.2, the sediment concentration \overline{M} was cut when it exceeded 155 kg/m^3 (as shown in Figs. 8.11 and 8.12). There is no acoustic estimation of the sediment concentration

near the bed, so another source for the sediment boundary condition \bar{c}_a of the model by [Styles and Glenn \(2000\)](#) is needed in those instances (Eq. 2.57). There are several formulations that relate the concentration of sediments near the bottom under equilibrium conditions \bar{c}_a (when the vertical net flow of the sediment is assumed to be zero), with bed shear strength, bed concentration and stresses generated by the flow of water in the seabed. As seen in Section 2.2.1, there is a similarity between the formulation proposed by Ariathurai-Partheniades widely used in cohesive sediments, and that proposed by [Smith and McLean \(1977b\)](#). Using a common value for γ_0 of 2×10^{-3} and values extracted from numerical models ([Fossati, 2013](#)) and field works ([Pedocchi et al., 2012](#)) of the study site for seabed concentration c_0 of 480 kg/m^3 and τ_s and τ_{cr} of 0.1 Pa , Eq. 2.50 establishes that $\frac{e_{AP}}{w_s|_{z=a}}$ equals $9.6 \text{ s}^2/\text{m}^2$. Using the results of the mean sediment concentration obtained by the ABS \bar{M}_a , under equilibrium conditions, and applying the model by [Grant and Madsen \(1979\)](#) presented in Section 2.1 to estimate the bottom shear stress, Ariathurai-Partheniades and [Smith and McLean \(1977b\)](#) were compared with the data. Figure 8.14 presents a scatter plot for sediment mass concentration near the bed against γ_0 times the dimensionless excess of shear stress s (where $s = (\tau_b - \tau_{cr})/\tau_{cr}$), as well as the curves predicted by in the models by [Smith and McLean \(1977b\)](#) and Ariathurai-Partheniades. Blue dots indicate instances where equilibrium condition could be assumed, whereas red dots are conditions where the net vertical sediment flux is nonzero as on June 07 at 9:30 AM (Fig. 8.6) where the $\bar{M}_a = 67 \text{ kg/m}^3$ and the mass concentration expected by [Smith and McLean \(1977b\)](#) is equal to 117 kg/m^3 . For values of $\gamma_0 s$ under 0.15 (small τ_b), models by Smith and McLean and Ariathurai-Partheniades behave quite similarly. As $\gamma_0 s$ becomes large enough, [Smith and McLean \(1977b\)](#) and Ariathurai-Partheniades formulations diverge mainly because [Smith and McLean \(1977b\)](#) model does not allow values for \bar{c}_a above the seabed concentration. The collapsing of the data and the formulation by [Smith and McLean \(1977b\)](#) is outstanding.

The high stresses and the continuous agitation that are generated in the wave boundary layer, limit the development of bonds between sediment particles. Therefore, small flocs in relation to large and less strong flocs prevail. The rheological behavior of the fine sediment mixtures in the vicinity of the bottom does not necessarily match that one expected under calm conditions. This reason explains why the proposed cohesionless sediment model by [Smith and McLean \(1977b\)](#) had such a good performance.

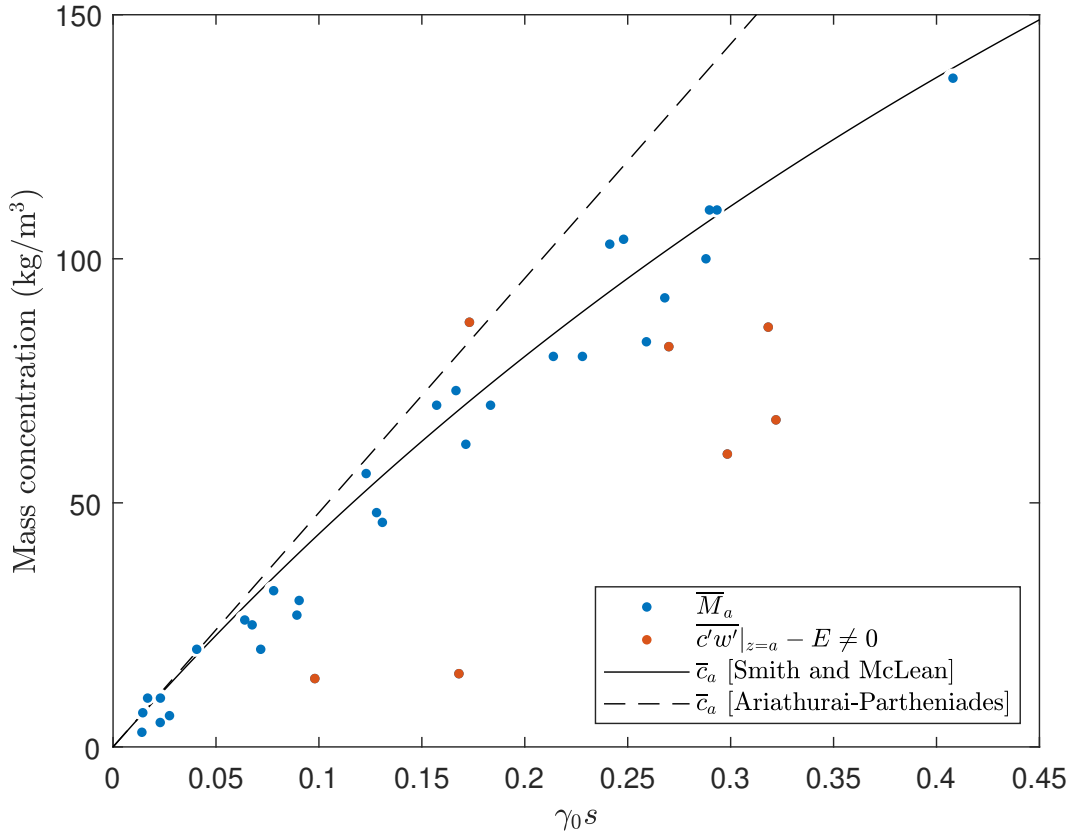


Figure 8.14: Scatter plot of mass concentration estimated by the ABS in the first centimeter over the seabed vs $\gamma_0 s$. The full black line represents the model by Smith and McLean (1977b) with the parameters proposed here. The dashed black line represents the model by Ariathurai-Partheniades with the parameters proposed here.

As shown in Fig. 8.15, the sediment concentration estimated by the ABS at the OBS height $\overline{M}(z = z_{OBS})$ is strongly dominated by the wave shear stress near the seabed $|\tilde{\tau}_b|$. When the currents U_c are medium or strong the depth integrated sediment flux near the bottom Q_{sb} is intensified by the wave motion that keeps high sediment concentration in suspension. At the beginning of June 7, during the first eight hours, low shear stresses even with moderate currents result in low sediment flux. As wave bottom stresses begin to rise around 8:00 AM, also the sediment transport increase. After 4 hours of strong bottom stresses, the sediment is more easily transported by the currents. With currents and waves stronger during June 12 to 13, the same relations can be found. In the second event, the influence of the shear stress on the sediment flux is more evident. Considering the small portion of the data analyzed here, those results agree with the work done by Santoro (2017). In that work it was concluded

that despite that the suspended sediment flux is related to the water flux, it is strongly enhanced during storms because of the high suspended sediment concentrations. Santoro found a relationship between the highest sediment flux values and the strong storms events with SW-NE wind direction (which are the directions of the waves on both events analyzed in this Chapter).

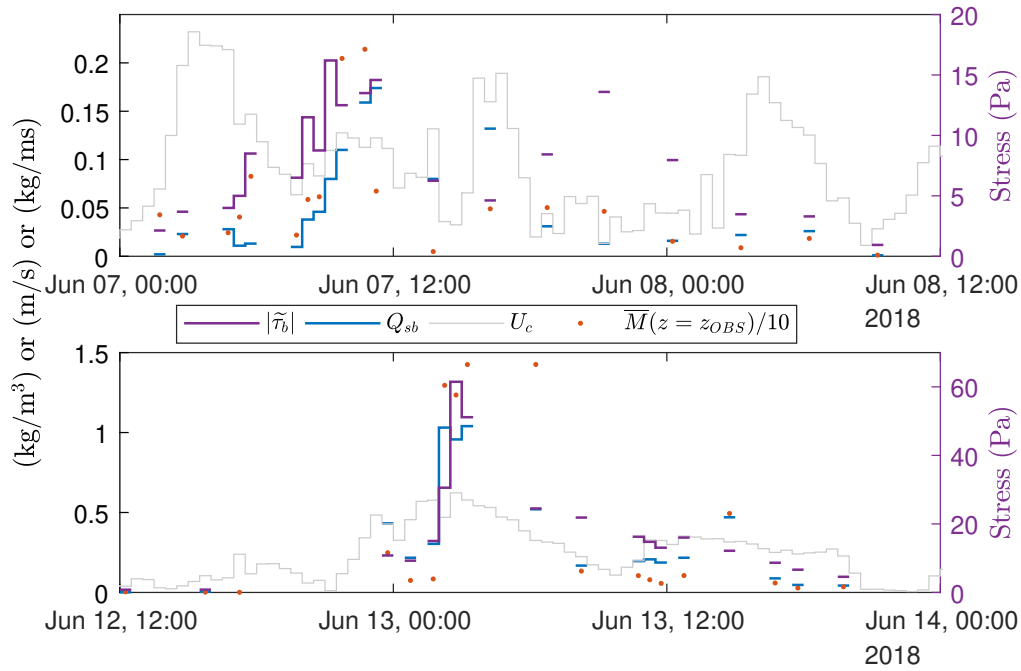


Figure 8.15: Sediment flux and related variables for both events on June 7 to 8 and June 12 to 13, 2018.

Interpolating Q_{sb} in the entire first event (from June 7 at 12:00 AM to June 8 at 12:00 PM), it can be estimated that 5.3 tons of sediment per meter width were transported from the west to the east, perpendicular to the Montevideo’s port access channel seen in Fig. 4.2. If it is assumed that all this sediment is captured into this channel, with a concentration of 300 kg/m^3 for the freshly deposited sediments inside the channel as previous studies have suggested, the shoaling would be approximately 7 cm. Also, the simulations of the model by Styles and Glenn (2000) of instances where the acoustic inversion technique was not within the range of applicability (concentrations above 155 kg/m^3), allowed us to compute the sediment transport during highly erosive events, as the event from June 12 to June 13, 2018. During this particular event (from June 12 at 12:00 PM to Jun 13 at 11:30 PM), 32 tons per meter width of sediment were transported towards the Montevideo’s port access channel.

If this sediment transport had been completely captured in the channel, the shoaling would have been approximately 38 cm. The annual siltation rate in this particular reach of the access channel is about 1 m per year if navigation is present. In the access channel to Gas Sayago Port, which is abandoned, measurements showed siltation rates of approximately 2 m per year.

One feature that the model by [Styles and Glenn \(2000\)](#) does not consider is the change in the viscosity due to the high concentrated mixtures of cohesive sediments. In the lower layer ($z_0 < z < z_1$) where the maximum sediment concentrations are expected, the viscosity proposed in the model by [Styles and Glenn \(2000\)](#) is lower (Eq. 2.55, $\nu_{TN} = \kappa u_{*r} z$ in the lower layer). In order to have realistic simulations of this model, a correction of the viscosity profile induced by the sediment concentration would be advisable. Adapted from [Mignot \(1968\)](#), [Mehta \(2013\)](#) showed the dependence of the viscosity with the sediment concentration of several mud samples from different locations. Taking as an example the data collected on June 7 at 9:30 AM (Fig. 8.7), it could be seen that for concentrations of fine sediments of approximately 100 kg/m^3 , the viscosity was expected to be between 5×10^{-6} and $50 \times 10^{-6} \text{ m}^2/\text{s}$. The simulation in that instant was $z_1 = 1.2 \text{ cm}$, $u_{*r} = 3.3 \text{ cm/s}$ providing a value of $\kappa u_{*r} z_1 = 160 \times 10^{-6} \text{ m}^2/\text{s}$. The simulations on both events presented in this work had minimum values for $\kappa u_{*r} z_1$ of $\sim 100 \times 10^{-6} \text{ m}^2/\text{s}$ with $z_1 < 2 \text{ cm}$. If the viscosity was corrected due to concentration, only the first centimeter near the bottom would present appreciable variations, reducing the velocity flow.

Chapter 9

Conclusions and future work

9.1 Conclusions - Methodology

The seabed close to Montevideo is composed of mud whose thickness can be above 15 m thick, complicating some mooring strategies experienced previously in the area. It is common practice to add weight to the mooring structure in order to prevent it from moving with the efforts imposed by hydrodynamics. These structures are usually buried in places where there are such amounts of mud, which complicates the search and rescue of the structure, and affects the quality of the data that can be obtained during the deployment. Considering this, a new structure was designed for this work. It included three slender legs that buried 1.5 m in the mud to keep the structure motionless upon events of strong agitation. The first deployment was very successful: an ABS and an ADV were set one meter above the bottom, and the structure remained fixed during almost three months, without sinking down into the soft mud. After the deployment, the structure was modified to incorporate a CTD and an ADCP to the deployment. In the second deployment, measurements were taken much closer to the bed, the time between samples of the ADV was reduced to thirty minutes and the ABS was set to take samples more frequently. During a total period of five months and fifteen days including both deployments, data was collected in several scenarios: conditions in which currents dominated; conditions in which waves dominated; and conditions of waves and currents combined.

In the first deployment there was no CTD attached to the structure. Therefore, salinity estimations with this instrument near the bottom were lacking.

However, the transducers array of the ADV enabled the determination of the sound speed using Probe Check information. Combining said estimations with the temperature and pressure measurements obtained also with the ADV and the formulation by [Del Grosso \(1974\)](#), it is possible to estimate salinity as described by [Mosquera and Pedocchi \(2019\)](#) in Annex 1. Salinity estimations obtained by the ADV were comparable to the CTD estimations during the second deployment. This demonstrates that the proposed methodology can be confidently used to estimate the salinity in estuarine environments as the Río de la Plata.

The granulometry of the sediment extracted from the study area indicates that the fraction larger than $75\ \mu\text{m}$ (sieve No. 200 of the ASTM standard), despite representing less than 5 % of mass fraction, has a strong impact on the form function acoustic parameter $\langle f \rangle$ (Eq. 3.88). This was corroborated in laboratory measurements with ABS shown in Chapter 5. The amount of coarse sediment ($> 75\ \mu\text{m}$) in relation to total sediment in suspension was expected to be still less than 5 % in calm instances, since coarse material has a higher falling velocity than fine sediments ($< 75\ \mu\text{m}$). In order to consider possible variations in the granulometry of suspended material in storm and calm events, a multi-frequency acoustic inversion was designed (see Section 3.8), considering that these two classes of sediment can occur in different proportions. As far as the author of this work is concerned, this is the first time that an approach by class is delved into multi-frequency acoustic inversion.

Several laboratory works were made using the fine sediment fraction ($< 75\ \mu\text{m}$) only in order to understand the relation between the aggregates and the acoustic response. Firstly, a recently sieved sediment and tap water mixture was measured. The acoustic parameters extracted from said measurements corresponded with theoretical values of completely disaggregated material with the same granulometry. Secondly, salinity events of 10.4 psu, with consolidation and resuspension cycles of approximately one week, were also simulated in order to reproduce the study site collected data. Aggregation could be appreciated with the naked eye. However, since falling velocities of the suspended material were higher than those with tap water, the acoustic backscatter signal provided similar acoustic parameters. This indicates that the aggregation conditions that the fine material may present in the area of interest do not lead to a significant change in the acoustic parameters of the frequencies used by ABS. This hypothesis was used during the acoustic inversion performed in

the present work, since the acoustic parameters were not adjusted by flocculation. Only after adding a commercial flocculant values of $\langle f \rangle$ were significantly different from the disaggregated material ones. Finally, high concentrations of sediment were used in order to explore the application limitations of the acoustic theory used. It was found out that concentrations higher than 155 kg/m^3 show a significant deviation in acoustic backscatter parameters. Therefore, in those cases the theory of incoherent backscatter does not apply.

9.2 Conclusions - Cohesive sediment dynamics in the Río de la Plata

Various mechanisms that explain the formation of fluid mud layers are described in the existing literature. The most commonly described mechanisms are those where an abrupt reduction in the flow velocity occurs. This could be caused by spatial or temporal variations. For example as a widening of the flow boundaries slack waters during the tide cycle, respectively. This deceleration reduces the flow capacity to retain the suspended sediment. Consequently, sedimentation generates an increase in the sediment concentration at the bottom of the water column. However, the data collected during five months and 15 days demonstrated that the formation of fluid mud layer in the Río de la Plata is accountable to a different process. Even though acknowledging this phenomenon is key to understand the interaction between waves, currents and sediments, it is not simple to capture it in situ, due to the lack of collocated measurements, with high temporal resolution of waves, currents and sediment dynamics near the bottom. This work confirms, for the first time, the presence of a fluid mud layer with a very high concentration of fine sediments in two very different events (see Section 8), with the ability to move, in the proximity of Montevideo bay. Depending on currents, this layer could be transported towards the port, which would explain the sedimentation rates observed by the port's authorities (1 m/year or larger when the port traffic is low) as discussed in Section 8.2.

During events with waves of significant wave height H_S , above than 1.3 m (moderate and strong waves), that occur weekly, a process of erosion starts in the first centimeters of the cohesive bottom, incorporating a significant amount of sediment to the movement. During the deployments erosion and

also deposition were detected, by determining the position of the seabed with the 1 MHz Acoustic Backscatter Sensor Profiler (ABS) frequency transducer. In the event captured on June 12 and June 13, 2008, the highest erosion of approximately 6 cm was registered. There had been more than three hours of strong shear stresses caused by strong waves and currents in this event.

When analyzing instants with moderate waves and moderate to low currents, like the ones presented on Section 8.1.1, the eroded sediment remains near the bottom. This indicates that the vertical mix imposed by the waves occurs in the lower layers. The high sediment concentrations generated during those instances, impose strong density gradients that result in flow stratification, usually inhibiting the turbulent mix imposed by currents over the entire water column. This mechanism enables the occurrence of fluid mud layers with concentrations that could surpass 100 kg/m^3 and stable lutoclines of 10 cm of thickness, as registered during the event from June 7 to June 8, 2018. In various instances along the deployments (Figs. 6.1 to 6.8), a local maximum of the ABS' 4 MHz transducer acoustic signal remained stable a few centimeters over the bottom during the two minutes of measuring. This evidences a shift in the acoustic impedance that can be associated with a lutocline, i.e. an abrupt change in the sediment concentration that exists between the fluid mud and the water column.

The event registered from June 12 to June 13 presented in Section 8.1.2 had higher current and waves velocities than the one registered from June 7 to June 8. Consequently, a greater sediment exchange occurred between the fluid mud layer and the water column during the latest of these two events. The vertical mix imposed by this hydrodynamic conditions, destabilizes the lutocline, breaking the stratification. This results in higher concentrations in the water column compared with scenarios with similar wave energy but weaker current velocities. The sediment concentrations presented in this thesis were determined by the multi-frequency inversion of the ABS measurements. Due to the intrinsic random nature of the acoustical backscatter measurements it is necessary to have various acoustic profiles to estimate a sediment concentration profile. Also, the sediment concentration profiles can present fluctuations due to the water flux, for example in the presence of waves, where variations in the sediment concentration profile may be associated with the action of each wave. To estimate the sediment concentration, it was assumed that the sediment concentration profiles were constant at 0.5 s intervals. Under this

assumption, the concentration variability captured under waves included at least 16 measures by profile.

Occasionally, depending on the texture of the sediment concentrations captured by the ABS signal, it was possible to apply a particle image velocimetry technique in order to obtain mean velocity profiles in the lower 40 cm layer near the bottom. Using these mean velocities and the sediment mean concentration profiles given by the ABS, the bulk Richardson number Ri_0 was computed, to confirm the mixing conditions that were observed by the acoustic inversion (discussed in Section 8.2). In order to illustrate the variability of the mixing conditions present in the deployment site, two different instances were presented, one with stratified water column conditions (June 13, 2018 at 10:30 AM) and another one with mixed water column conditions (June 13, 2018 at 2:30 PM) with a 4 hour difference.

Using the mean concentration profiles obtained with the ABS and the velocity measurements obtained with the ADV, an analytical model proposed by [Styles and Glenn \(2000\)](#) and presented in Section 2.3 was implemented, in order to quantify the sediment transport in the lower 30 cm layer above the seabed. This model also considers the inhibition of turbulent diffusion by presence of concentration gradients that stratify the flow and the turbulent closure for sediment self-stratification proposed by [Smith and McLean \(1977a\)](#). The value of α_G in this model was used as a tuning parameter, for the lower bottom of the region where the eddy viscosity is governed by the currents to have a height comparable to the height of the lutocline, collapsing the [Styles and Glenn \(2000\)](#) concentration profiles with the profiles obtained with the ABS. α_G in the field experiments adopted values between 0.15 and 0.40, being the values proposed by [Styles and Glenn \(2000\)](#) in the range within 0 and 1. The stratification parameter ζ , the ratio between the distance from the bottom and the Monin-Obukov length, reported in the model by [Styles and Glenn \(2000\)](#) could be compared with the gradient Richardson number as discussed in Section 8.2.

There are several formulations in the literature that relate the concentration of sediments near the bottom \bar{c}_a under equilibrium conditions (when the vertical net flow of the sediment is assumed to be zero), with bed shear strength, bed concentration and stresses generated by the flow of water in the seabed. With the results of the mean sediment concentration obtained by the ABS and the bottom shear stress estimated by the ADV, two different for-

mulations were compared. The entrainment formulation proposed by [Smith and McLean \(1977a\)](#) included a good comparison with the field data, and provided a boundary condition for the model by [Styles and Glenn \(2000\)](#) when the acoustics could not do it.

The [Styles and Glenn \(2000\)](#) model was calibrated, reproducing the variability seen in the collected data, providing a relation between the sediment concentration profiles and the hydrodynamics forcing (wave and currents). The analytical model simulations can capture the near bed dynamics, and provide a good estimation of the sediment concentration profiles measured by the ABS. Moreover, it was possible to compare the current profiles obtained with the model with a particle image velocimetry technique (proposed in [Section 7.2](#)), indicating also consistency in the hydrodynamics. This model provided mean velocity profiles, that combined with the concentration profiles of the ABS, resulted in an estimation for the sediment transport during different events (from June 7 to 8, 2018, 5.3 tons/m of sediment were transported and from June 12 to 13, 2018, 32 tons/m sediment were transported as presented in [Section 8.2](#)). As far as the author is concerned, this is the first time this model has been verified with field data.

9.3 Future work

Two major lines of work are envisioned to obtain a better quantification of the dynamics of fine sediments in the surroundings of the bottom of cohesive beds in presence of waves and currents

The first line of work, using mooring strategies comparable to those presented in this work, is to collect data of this phenomenon focusing on the fluid mud hydrodynamics. In the present work, the dynamics were mainly estimated using analytical models that consider hydrodynamics in the presence of waves, current and self-stratification by sediment concentration. In this way, the more dedicated measurements would capture not only the sediment exchanges in the first layers close to the bottom, but also the transport of that highly concentrated sediment layer. Based on field work in similar environments, to capture the first few decimeters above the seabed [Traykovski et al. \(2015\)](#) recommends the use of pulse-coherent acoustic Doppler profilers technology. Based on field observations, an array of 4 to 5 synchronized ADVs vertically separated by 5 cm may be used instead. Regarding backscat-

ter acoustics, ABS's low-frequency transducers, such as the 500 kHz one have a small diameter, leading to a relatively large half-beam angle in comparison with the other transducers. Similar issues were detected with the 300 kHz transducer of that instrument. Although at this frequency it is not expected to achieve improvements in acoustic inversion given the acoustic return of small sediment particles in the area, it is possible to capture the position of the bottom and the large sediment concentration gradients, which are often masked by the significant attenuation that high sediment concentrations provide.

In relation to the numerical simulations of these layers of fluid mud, two possible scenarios are foreseen. The most advisable would be, considering the results produced by the Styles model, to improve the resolution of the lowest layers of the numerical models in the boundary layer. For formulations based on the high concentrations measured in strong agitation events, Smith and McLean entrainment formulation is preferred. It is understood that there is already an adequate simulation of stratified flows based on the gradient Richardson number, as well as the combination of waves and currents, on models such as the ones already implemented in the Montevideo bay based on the Telemac numerical code (Santoro, 2017). This could be an excessively optimistic strategy considering the size of the study area. Although approximately 10 layers separated by 2 to 3 cm near the bottom would be required, the gradients as well as the temporal dynamics observed, may incur in a reduction of the calculation steps, and this would require high calculation resources in order to avoid numerical modes that add instability to the simulations. Being this the case, a battery of simulations using a Computational Fluid Dynamics code is suggested. It would be necessary to incorporate the presence of mass particles that would allow the inclusion of turbulence damping due to stratification by particle concentration in the model. With these simulations, analyzing the results that consider various combinations of waves and currents seen in the field, a parameterization of the fluid mud, its height, concentration and transport could be obtained.

A priori, exploration through laboratory experimentation of the phenomenon is discouraged, since the wave energies required to simulate this type of phenomenon in the laboratory require large laboratory facilities to reduce the scale effects. The lower layer can present laminar movements in part of its motion since the oscillatory Reynolds numbers are in the transition regime.

Bibliography

- Allegra, J. R. and Hawley, S. A. (1972). Attenuation of Sound in Suspensions and Emulsions: Theory and Experiments. *The Journal of the Acoustical Society of America*, 51(5B):1545–1564.
- Anderson, V. C. (1950). Sound scattering from a fluid sphere. *The Journal of the Acoustical Society of America*, 22(4):426–431.
- Aquatec (2002). Application Note AN4. Technical report, Aquatec Group.
- Ariathurai, C. R. (1974). *A finite element model for sediment transport in estuaries*. PhD thesis, University of California, Davis.
- AXYS (2013). *TRIAXIS Next Wave II Directional Wave Sensor - DN 40200600Z*. AXYS Technologies.
- Bellón, D. (2005). Determinación de sedimento fino en suspensión a través de métodos acústicos. Master's thesis, Facultad de Ingeniería, Universidad de la República.
- Bellón, D. and Piedra-Cueva, I. (2009). Estimating suspended solids concentrations from Acoustic Doppler Current Profiles measurements on the coast of Montevideo, Uruguay. In Vionnet, C., García, M. H., Latrubesse, E. M., and Perillo, G. M. E., editors, *River, Coastal and Estuarine Morphodynamics RCEM 2009*, pages 1045–1050.
- Bendat, J. S. and Piersol, A. G. (2011). *Random data: analysis and measurement procedures*, volume 729. John Wiley & Sons.
- Betteridge, K. F. E., Thorne, P. D., and Cooke, R. D. (2008). Calibrating multi-frequency acoustic backscatter systems for studying near-bed suspended sediment transport processes. *Continental Shelf Research*, 28(2):227–235.

- Caine, S. (2014). *AQUAscat 1000 User Manual*. Aquatec Group Limited.
- Campbell (2014). *OBS-3+ and OBS300 Suspended Solids and Turbidity Monitors*. Campbell Scientific.
- Coleman, N. L. (1970). Flume studies of the sediment transfer coefficient. *Water Resources Research*, 6(3):801–809.
- Deines, K. L. (1999). Backscatter estimation using Broadband acoustic Doppler current profilers. In *Proceedings of the IEEE Sixth Working Conference on Current Measurement (Cat. No.99CH36331)*, pages 249–253.
- Del Grosso, V. A. (1974). New equation for the speed of sound in natural waters (with comparisons to other equations). *The Journal of the Acoustical Society of America*, 56(4):1084–1091.
- Demer, D. A., Berger, L., Bernasconi, M., Bethke, E., Boswell, K., Chu, D., Domokos, R., Dunford, A., Fassler, S., Gauthier, S., et al. (2015). Calibration of acoustic instruments. Technical Report No. 326. 133 pp, International Council for the Exploration of the Sea (ICES).
- Downing, A., Thorne, P. D., and Vincent, C. E. (1995). Backscattering from a suspension in the near field of a piston transducer. *The Journal of the Acoustical Society of America*, 97(3):1614–1620.
- Faran Jr, J. J. (1951). Sound scattering by solid cylinders and spheres. *The Journal of the acoustical society of America*, 23(4):405–418.
- Fossati, M. (2013). *Dinámica Global de Sedimentos Finos en el Río de la Plata (Global fine sediment dynamics in Río de la Plata)*. PhD thesis, Facultad de Ingeniería, Universidad de la República.
- Fossati, M., Santoro, P., Mosquera, R., Martínez, C., Ghiardo, F., Ezzatti, P., Pedocchi, F., and Piedra-Cueva, I. (2014). Dinámica de flujo, del campo salino y de los sedimentos finos en el Río de la Plata. *Ribagua*, 1(1):48–63.
- Francois, R. E. and Garrison, G. R. (1982). Sound absorption based on ocean measurements: Part I: Pure water and magnesium sulfate contributions. *The Journal of the Acoustical Society of America*, 72(3):896–907.

- Fredsøe, J. and Deigaard, R. (1992). *Mechanics of Coastal Sediment Transport*. Advanced Series on Ocean Engineering. World Scientific Publishing Company.
- Fromant, G., Floc'h, F., Lebourges-Dhaussy, A., Jourdin, F., Perrot, Y., Dantec, N. L., and Delacourt, C. (01 Aug. 2017). In situ quantification of the suspended load of estuarine aggregates from multifrequency acoustic inversions. *Journal of Atmospheric and Oceanic Technology*, 34(8):1625 – 1643.
- Fugate, D. C. and Friedrichs, C. T. (2002). Determining concentration and fall velocity of estuarine particle populations using ADV, OBS and LISST. *Continental Shelf Research*, 22(11-13):1867–1886.
- García, M. H., editor (2008). *Sedimentation Engineering: processes, measurements, modeling, and practice*. American Society of Civil Engineers.
- Gaunaurd, G. C. and Uberall, H. (1983). RST analysis of monostatic and bistatic acoustic echoes from an elastic sphere. *Journal of the Acoustical Society of America*, 73(1):1–12.
- Glenn, S. M. (1983). *A continental shelf bottom boundary layer model: The effects of waves, currents, and a movable bed*. phdthesis, Massachusetts Institute of Technology and Woods Hole Oceanographic Institution.
- Glenn, S. M. and Grant, W. D. (1987). A suspended sediment stratification correction for combined wave and current flows. *Journal of Geophysical Research: Oceans*, 92(C8):8244–8264.
- Grant, W. D. and Madsen, O. S. (1979). Combined wave and current interaction with a rough bottom. *Journal of Geophysical Research: Oceans*, 84(C4):1797–1808.
- Grant, W. D. and Madsen, O. S. (1986). The Continental-Shelf Bottom Boundary Layer. *Annual Review of Fluid Mechanics*, 18(1):265–305.
- Grant, W. D., Williams III, A. J., and Glenn, S. M. (1984). Bottom stress estimates and their prediction on the northern California continental shelf during CODE-1: the importance of wave-current interaction. *Journal of Physical Oceanography*, 14(3):506–527.

- Guarga, R., Borghi, J., Vinzón, S., Piedra-Cueva, I., and Kaplan, E. (1988). Control y seguimiento de los estudios hidráulicos del puerto de Montevideo efectuado por INTECSA. Technical report, IMFIA.
- Hanes, D. M. (2012). On the possibility of single-frequency acoustic measurement of sand and clay concentrations in uniform suspensions. *Continental Shelf Research*, 46:64–66.
- Hay, A. E. (1991). Sound scattering from a particle-laden, turbulent jet. *The Journal of the Acoustical Society of America*, 90(4):2055–2074.
- Hay, A. E. and Mercer, D. G. (1985). On the theory of sound scattering and viscous absorption in aqueous suspensions at medium and short wavelengths. *The Journal of the Acoustical Society of America*, 78(5):1761–1771.
- Hay, A. E. and Sheng, J. (1992). Vertical profiles of suspended sand concentration and size from multifrequency acoustic backscatter. *Journal of Geophysical Research: Oceans*, 97(C10):15661–15677.
- Holthuijsen, L. H. (2007). *Waves in Oceanic and Coastal Waters*. Cambridge University Press.
- INTECSA (1987). Plan de desarrollo a largo plazo para el Puerto de Montevideo, incluyendo un estudio de las condiciones hidráulicas de la Bahía de Montevideo y del canal de acceso. Technical report, Estudios Hidráulicos y sedimentológicos, INTECSA.
- Jaramillo, S. (2008). *Observations of Wave-Sediment Interactions on a Muddy Shelf*. PhD thesis, University of Florida.
- Jensen, B. L. (1988). *Experimental Investigation of Turbulent Oscillatory Boundary Layers*. PhD thesis, Institute of Hydrodynamics and Hydraulic Engineering, Technical University of Denmark.
- Jensen, B. L., Sumer, B. M., and Fredsøe, J. (1989). Turbulent oscillatory boundary layers at high Reynolds numbers. *Journal of Fluid Mechanics*, 206:265–297.
- King, L. V. (1934). On the acoustic radiation pressure on spheres. *Proceedings of the Royal Society of London. Series A-Mathematical and Physical Sciences*, 147(861):212–240.

- Kinsler, L. E. (2000). *Fundamentals of acoustics*. Wiley.
- Lamb, H. (1945). Hydrodynamics. *Dover Publications, New York*, pages 361 – 363.
- Lee, B. J., Fettweis, M., Toorman, E., and Molz, F. J. (2012). Multimodality of a particle size distribution of cohesive suspended particulate matters in a coastal zone. *Journal of Geophysical Research: Oceans*, 117(C3).
- Lee, T. H. and Hanes, D. M. (1995). Explicit solution to the acoustic backscatter equation to measure the concentration of uniform, suspended particles. *Journal of Geophysical Research: Oceans*, 100(C2):2649–2657.
- Lin, W. H. and Raptis, A. C. (1983). Acoustic scattering by elastic solid cylinders and spheres in viscous fluids. *The Journal of the Acoustical Society of America*, 73(3):736–748.
- Lundgren, H. (1972). Turbulent currents in the presence of waves. In *13th Coastal Engineering Conference*, volume 1, pages 623–634. American Society of Civil Engineers.
- MacDonald, I. T., Vincent, C. E., Thorne, P. D., and Moate, B. D. (2013). Acoustic scattering from a suspension of flocculated sediments. *Journal of Geophysical Research: Oceans*, 118(5):2581–2594.
- Madsen, O. S. (1994). Spectral wave-current bottom boundary layer flows. In *Coastal Engineering 1994*, volume 24, pages 384–398.
- Madsen, O. S. and Wikramanayake, P. N. (1991). Simple models for turbulent wave-current bottom boundary layer flow. resreport DRP-91-1, Massachusetts Institute of Technology.
- Mark, W. and Fischer, R. (1976). Investigation of the effects of nonhomogeneous (or nonstationary) behavior on the spectra of atmospheric turbulence. Technical report, NASA.
- McAnally, W. H., Friedrichs, C., Hamilton, D., Hayter, E., Shrestha, P., Rodriguez, H., Sheremet, A., Teeter, A., and null null (2007). Management of Fluid Mud in Estuaries, Bays, and Lakes. I: Present State of Understanding on Character and Behavior. *Journal of Hydraulic Engineering*, 133(1):9–22.

- McLean, S. R. (1992). On the calculation of suspended load for noncohesive sediments. *Journal of Geophysical Research: Oceans*, 97(C4):5759–5770.
- Medwin, H. (2005). *Sounds in the sea: From ocean acoustics to acoustical oceanography*. Cambridge University Press.
- Mehta, A. J. (1989). On estuarine cohesive sediment suspension behavior. *Journal of Geophysical Research: Oceans*, 94(C10):14303–14314.
- Mehta, A. J. (2013). *An introduction to hydraulics of fine sediment transport*, volume 38. World Scientific Publishing Company.
- Meinhart, C. D., Wereley, S. T., and Santiago, J. G. (2000). A PIV algorithm for estimating time-averaged velocity fields. *Journal of Fluids Engineering*, 122(2):285–289.
- Mignot, C. (1968). A study of the physical properties of various very fine sediments and their behaviour under hydrodynamic action. *La Houille Blanche*, 23(7):591–620.
- Moate, B. D. and Thorne, P. D. (2012). Interpreting acoustic backscatter from suspended sediments of different and mixed mineralogical composition. *Continental Shelf Research*, 46:67–82.
- Morse, P. M. and Ingard, K. U. (1987). *Theoretical Acoustics*. Princeton University Press.
- Mosquera, R., Groposo, V., and Pedocchi, F. (2014). Acoustic measurements of a liquefied cohesive sediment bed under waves. *Advances in Geosciences*, 39:1–7.
- Mosquera, R. and Pedocchi, F. (2012). Avances para el estudio de la dinámica de sedimentos cohesivos en el laboratorio. Master’s thesis, Facultad de Ingeniería, Universidad de la República.
- Mosquera, R. and Pedocchi, F. (2013). Decomposition of incident and reflected surface waves using an Ultrasonic Velocity Profiler. *Coastal Engineering*, 71:52 – 59.
- Mosquera, R. and Pedocchi, F. (2019). Salinity estimation from Acoustic Doppler Velocimeter measurements. *Continental Shelf Research*, 180:5–95.

- Mosquera, R., Pedocchi, F., Bellón, D., and Piedra-Cueva, I. (2012). Medición del oleaje con un ADCP frente a la costa de Montevideo, Uruguay. In *XXV Congreso Latinoamericano de Hidráulica*, pages 1–10. IAHR.
- Nezu, I. and Nakagawa, H. (1993). *Turbulence in Open-Channel Flows*. IAHR Monographs. A.A. Balakema.
- Nichols, C. S. (2005). *Evaluation of Wave-Current Bottom Boundary Layer Models*. PhD thesis, The Ohio State University.
- Nielsen, P. (1992). *Coastal bottom boundary layers and sediment transport*, volume 4. World scientific.
- Nortek (2018). Vector 300 m Specifications. Technical report, Nortek Group.
- Partheniades, E. (1962). *A study of erosion and deposition of cohesive soils in salt water*. PhD thesis, University of California, Berkeley.
- Partheniades, E. (1965). Erosion and deposition of cohesive soils. *Journal of the Hydraulics Division*, 91(1):105–139.
- Pedocchi, F., Cantero, M. I., and García, M. H. (2011). Turbulent kinetic energy balance of an oscillatory boundary layer in the transition to the fully turbulent regime. *Journal of Turbulence*, 1(12):1–27.
- Pedocchi, F. and García, M. H. (2012). Acoustic measurement of suspended sediment concentration profiles in an oscillatory boundary layer. *Continental Shelf Research*, 46:87–95.
- Pedocchi, F., Groposo, V., Mosquera, R., and Piedra-Cueva, I. (2012). Estudio de la profundidad náutica del puerto de Montevideo. Technical report, IMFIA - Facultad de Ingeniería - Universidad de la República.
- Pedocchi, F. and Mosquera, R. (2015). Medición de la pluma de sedimentos generada durante el dragado de apertura de la Terminal de la Planta Regasificadora. Technical Report IMFIA_2015.0001.04, IMFIA - Facultad de Ingeniería - Universidad de la República.
- Pedocchi, F., Solari, S., and Fossati, M. (2015). Evaluación de la sedimentación en los canales y área de maniobra de la Terminal de la Planta Regasificadora. Technical Report IMFIA_2015.0002.01, IMFIA - Facultad de Ingeniería - Universidad de la República.

- Piedra-Cueva, I. (1993). On the response of a muddy bottom to surface water waves. *Journal of Hydraulic Research*, (5):681–696.
- Piedra-Cueva, I. and Fossati, M. (2007). Residual currents and corridor of flow in the Río de la Plata. *Applied Mathematical Modelling*, 31(3):564–577.
- Ponce de León, L. A., Maciel, F., Santoro, P., and Pedocchi, F. (2019). Estimación de velocidades de sedimentación de sólidos en suspensión y su variación con la salinidad. In Nardin, A., Szupiany, R., Pedocchi, F., and García, C. M., editors, *VI Simposio sobre Métodos Experimentales en Hidráulica*.
- Rhyne, T. L. (1998). Characterizing ultrasonic transducers using radiation efficiency and reception noise figure. *IEEE Transactions on Ultrasonics, Ferroelectrics, and Frequency Control*, 45(3):559–566.
- Rijn, L. C. v. (1984). Sediment transport, part II: suspended load transport. *Journal of Hydraulic Engineering*, 110(11):1613–1641.
- Rusello, P. J. (2009). A Practical Primer for Pulse Coherent Instruments. Tn-027, Nortek USA.
- Safak, I., Sheremet, A., Davis, J., and Kaihatu, J. M. (2017). Nonlinear wave dynamics in the presence of mud-induced dissipation on atchafalaya shelf, louisiana, usa. *Coastal Engineering*, 130:52 – 64.
- Sahin, C., Safak, I., Hsu, T.-J., and Sheremet, A. (2013). Observations of suspended sediment stratification from acoustic backscatter in muddy environments. *Marine Geology*, 336:24 – 32.
- Santoro, P. (2017). *Numerical modeling of Montevideo Bay hydrodynamics and fine sediment dynamics*. PhD thesis, Facultad de Ingeniería, Universidad de la República.
- Santoro, P., Fossati, M., Tassi, P., Huybrechts, N., Van Bang, D. P., and Piedra-Cueva, J. C. I. (2017). A coupled wave–current–sediment transport model for an estuarine system: Application to the Río de la Plata and Montevideo Bay. *Applied Mathematical Modelling*, 52:107–130.

- Santoro, P. E., Fossati, M., and Piedra-Cueva, I. (2013). Study of the meteorological tide in the Río de la Plata. *Continental Shelf Research*, 60:51 – 63.
- Sea-Bird (2014). *Seasoft V2: SBE Data Processing - User's Manual*. Sea-Bird Electronics.
- Sea-Bird (2016). *SBE 19plus V2 SeaCAT Profiler CTD - User Manual*. Sea-Bird Electronics, 012 edition.
- Seapoint (2013). *Seapoint Turbidity Meter - User Manual*. Seapoint Sensors.
- Sherwood, C. R., Lacy, J. R., and Voulgaris, G. (2006). Shear velocity estimates on the inner shelf off Grays Harbor, Washington, USA. *Continental Shelf Research*, 26(17-18):1995–2018.
- Shields, A. (1936). Anwendung der Aechichkeits-Mechanic und der Turbuleng Forschung auf dir Geschiebewegung' Mitt Preussische. *Versuchsanstalt fir Wasserbau and Schiffbau, Berlin, Germany (translated to English by WP Ott and JC van Uchelen, California Institute of Technology, Pasadena, California, USA)*.
- Smith, J. D. and McLean, S. R. (1977a). Boundary layer adjustments to bottom topography and suspended sediment. In Nihoul, J. C. J., editor, *Elsevier Oceanography Series*, volume 19, pages 123–151. Elsevier.
- Smith, J. D. and McLean, S. R. (1977b). Spatially averaged flow over a wavy surface. *Journal of Geophysical research*, 82(12):1735–1746.
- Styles, R. and Glenn, S. M. (2000). Modeling stratified wave and current bottom boundary layers on the continental shelf. *Journal of Geophysical Research: Oceans*, 105(C10):24119–24139.
- Styles, R., Glenn, S. M., and Brown, M. E. (2017). An optimized combined wave and current bottom boundary layer model for arbitrary bed roughness. Technical report, US Army Engineer Research and Development Center, Coastal and Hydraulics
- Teledyne (2017). *Sentinel V Operation Manual*. Teledyne RD Instruments, p/n 95d-6002-00 edition.

- Teledyne (2019). *WinRiver II, Software User's Guide*. Teledyne RD Instruments, p/n 957-6231-00 edition.
- Thorne, P. D. and Campbell, S. C. (1992). Backscattering by a suspension of spheres. *The Journal of the Acoustical Society of America*, 92(2):978–986.
- Thorne, P. D. and Hanes, D. M. (2002). A review of acoustic measurement of small-scale sediment processes. *Continental Shelf Research*, 22(4):603–632.
- Thorne, P. D., Hardcastle, P. J., and Soulsby, R. L. (1993). Analysis of acoustic measurements of suspended sediments. *Journal of Geophysical Research: Oceans*, 98(C1):899–910.
- Thorne, P. D. and Holdaway, G. P. (1997). Interpretation of acoustic backscatter measurements using a cross-correlation technique to evaluate near-bed current velocities. In *Oceans' 97. MTS/IEEE Conference Proceedings*, volume 1, pages 457–461. IEEE.
- Thorne, P. D., Hurther, D., and Moate, B. D. (2011). Acoustic inversions for measuring boundary layer suspended sediment processes. *The Journal of the Acoustical Society of America*, 130(3):1188–1200.
- Thorne, P. D. and Meral, R. (2008). Formulations for the scattering properties of suspended sandy sediments for use in the application of acoustics to sediment transport processes. *Continental Shelf Research*, 28(2):309–317.
- Thornton, E. B. (1979). Energetics of breaking waves within the surf zone. *Journal of Geophysical Research: Oceans*, 84(C8):4931–4938.
- Traykovski, P., Geyer, W. R., Irish, J. D., and Lynch, J. F. (2000). The role of wave-induced density-driven fluid mud flows for cross-shelf transport on the Eel River continental Shelf. *Continental Shelf Research*, 20(16):2113–2140.
- Traykovski, P., Trowbridge, J., and Kineke, G. (2015). Mechanisms of surface wave energy dissipation over a high-concentration sediment suspension. *Journal of Geophysical Research: Oceans*, 120(3):1638–1681.
- Traykovski, P., Wiberg, P. L., and Geyer, W. R. (2007). Observations and modeling of wave-supported sediment gravity flows on the Po prodelta and comparison to prior observations from the Eel Shelf. *Continental Shelf Research*, 27(3-4):375–399.

- Trowbridge, J. and Elgar, S. (2001). Turbulence measurements in the surf zone. *Journal of Physical Oceanography*, 31(8):2403–2417.
- Trowbridge, J. H. (1998). On a technique for measurement of turbulent shear stress in the presence of surface waves. *Journal of Atmospheric and Oceanic Technology*, 15(1):290–298.
- Trowbridge, J. H. and Lentz, S. J. (2018). The bottom boundary layer. *Annual review of marine science*, 10:397–420.
- Unesco (1981). Background papers and supporting data on the international equation of state of seawater 1980. Technical report, Unesco technical papers in marine science.
- Urlick, R. J. (1948). The absorption of sound in suspensions of irregular particles. *The Journal of the acoustical society of America*, 20(3):283–289.
- Vincent, C. E. and MacDonald, I. T. (2015). A flocculi model for the acoustic scattering from flocs. *Continental Shelf Research*, 104:15–24.
- Voulgaris, G. and Trowbridge, J. H. (1998). Evaluation of the Acoustic Doppler Velocimeter (ADV) for Turbulence Measurements. *Journal of Atmospheric and Oceanic Technology*, 15(1):272–289.
- Wilks, D. S. (2011). *Statistical methods in the atmospheric sciences*, volume 100. Academic press.
- Wilson, G. W. and Hay, A. E. (2015). Acoustic backscatter inversion for suspended sediment concentration and size: A new approach using statistical inverse theory. *Continental Shelf Research*, 106:130–139.
- Wolanski, E., Asaeda, T., and Imberger, J. (1989). Mixing across a lutocline. *Limnology and Oceanography*, 34(5):931–938.
- Yalin, M. S. (1963). *An expression for bed-load transportation*. 89. Proc. ASCE.
- Yalin, M. S. (1972). *Mechanics of sediment transport*. Pergamon Press.

APPENDICES

Appendix 1

First deployment

Figures in this Section show the collected data during the first deployment.

- First panel: East projection of the currents U_E (which is generally the most significant direction) measured by the ADCP in the buoy. As the ADCP was placed in a downward looking position, the depth d minus z is in the ordinate. Black line shows the pressure of the ADV in mH_2O in order to indicate the boundary of the velocity profiles.
- Second panel: East projection of the mean velocity U_E measured by the ADV and friction velocity U_* obtained as established in Section 7.4.
- Third panel: Significant wave height H_S measured by the ADV both with the pressure p and velocity \vec{v} data obtained as established in Section 7.3.1. The H_S measured by the TRIAXYS sensor in the Buoy is also shown.
- Fourth panel: Temperature θ measured by the ABS at the bottom and by the ADCP buoy at the surface.
- Fifth panel: Sediment mass concentration c obtained with the STM.
- Sixth panel: ADV Probe Check raw data.
- Seventh panel: Acoustic backscatter profile of 2.5 MHz ABS transducer corrected by spreading, near field and water absorption.
- Eighth panel: Acoustic backscatter profile of 5 MHz ABS transducer corrected by spreading, near field and water absorption.
- Ninth panel: Acoustic backscatter profile of one beam of the ADCP in the buoy corrected by spreading, near field and water absorption.

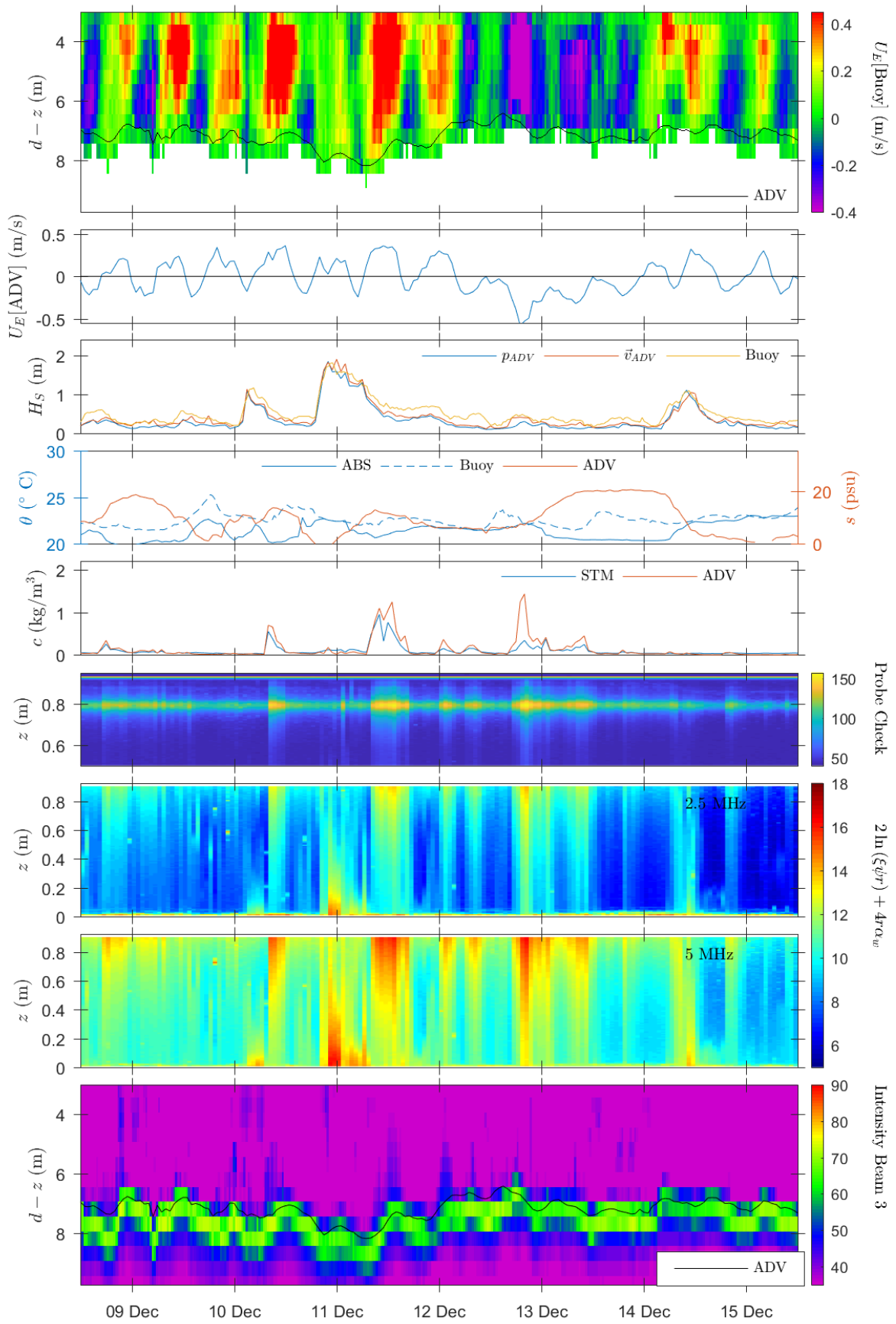


Figure 1.1: First deployment, first week.

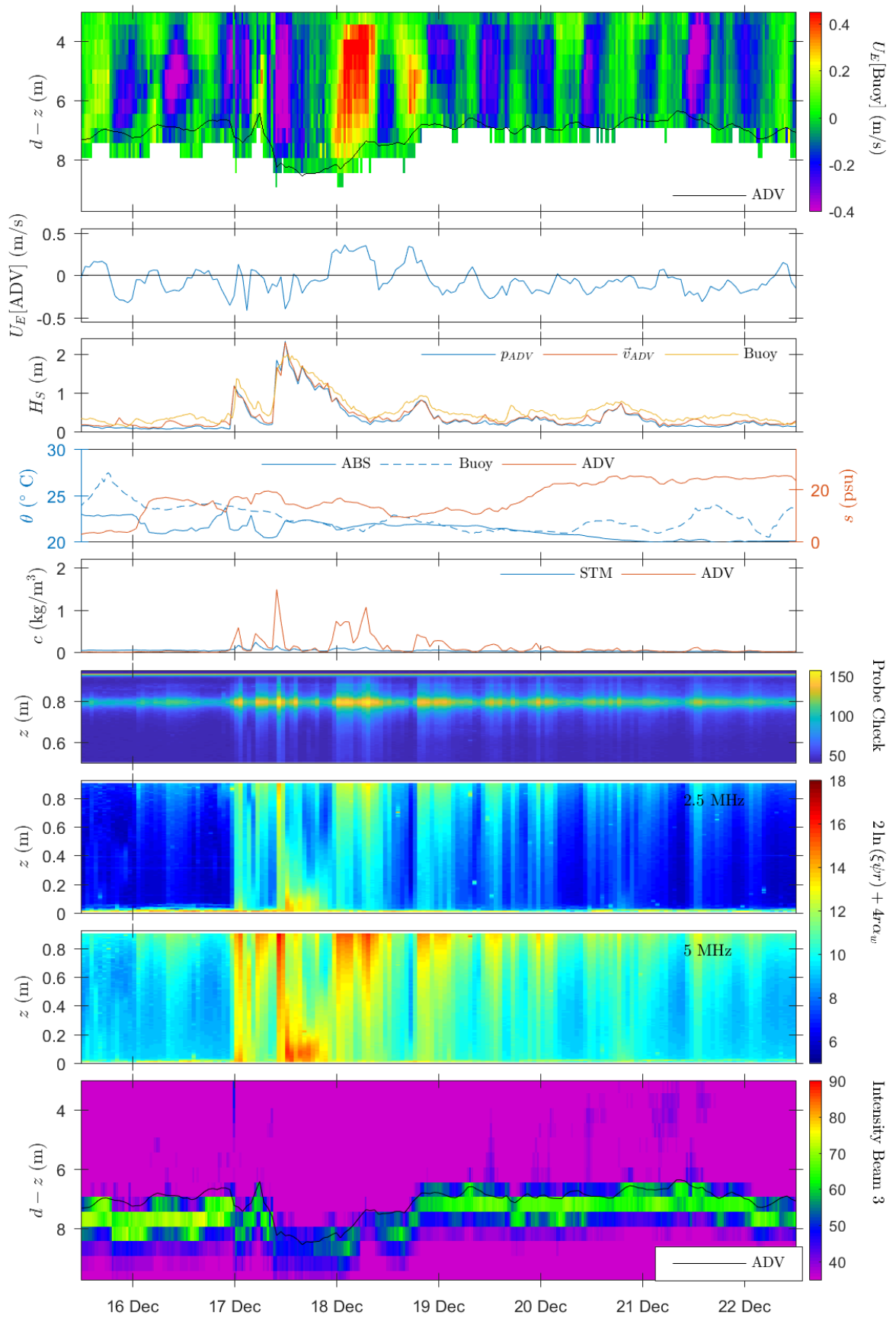


Figure 1.2: First deployment, second week.

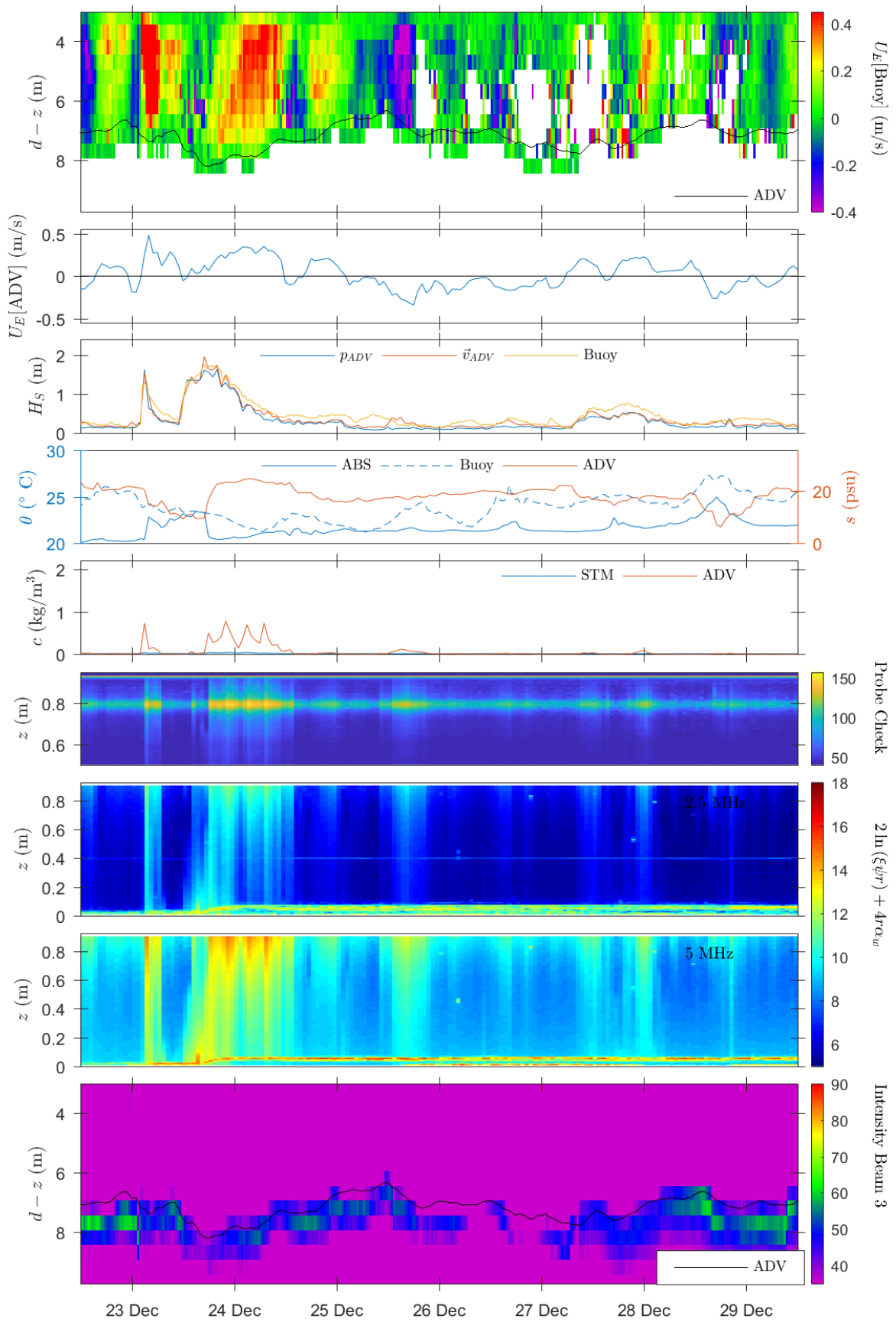


Figure 1.3: First deployment, third week.

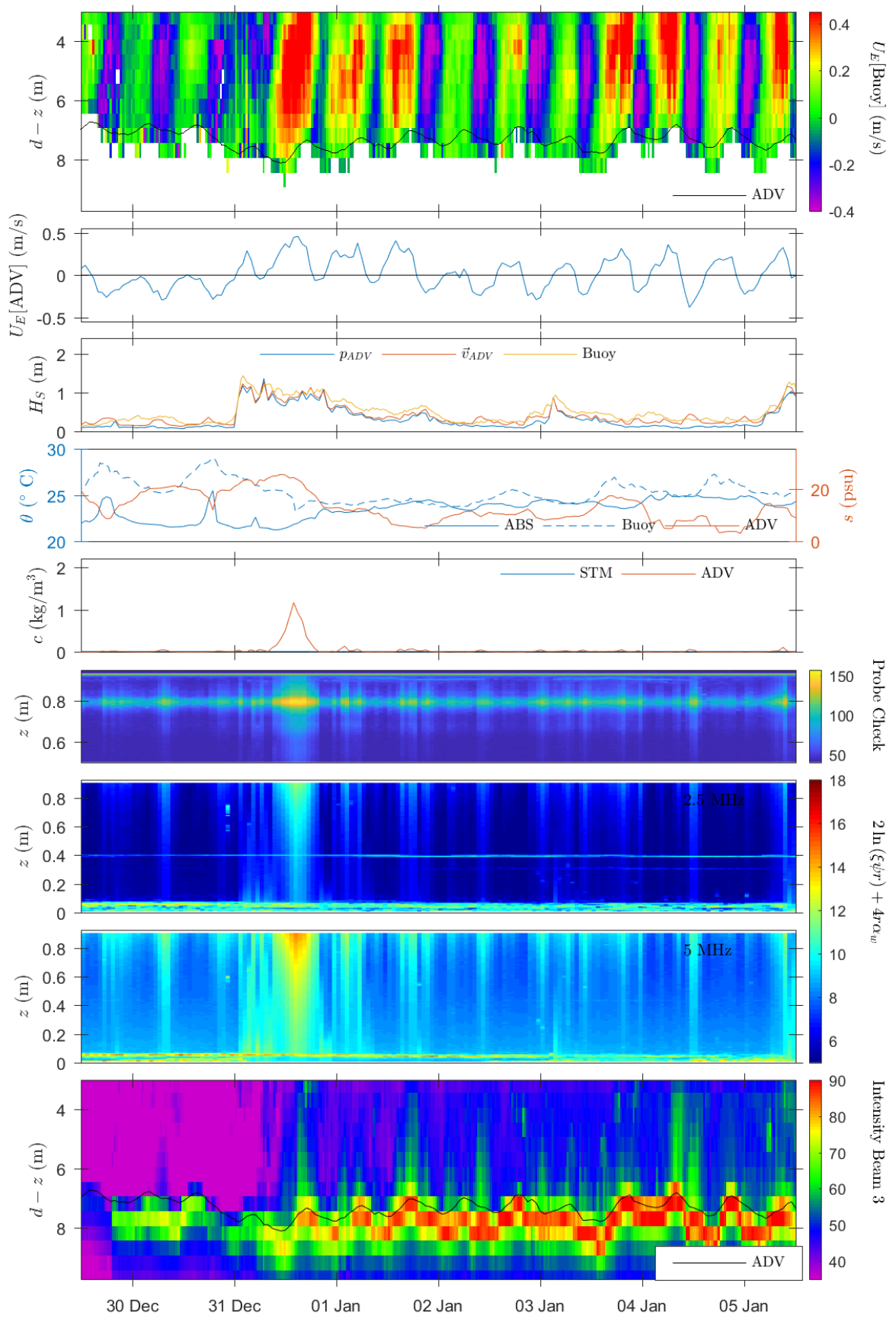


Figure 1.4: First deployment, fourth week.

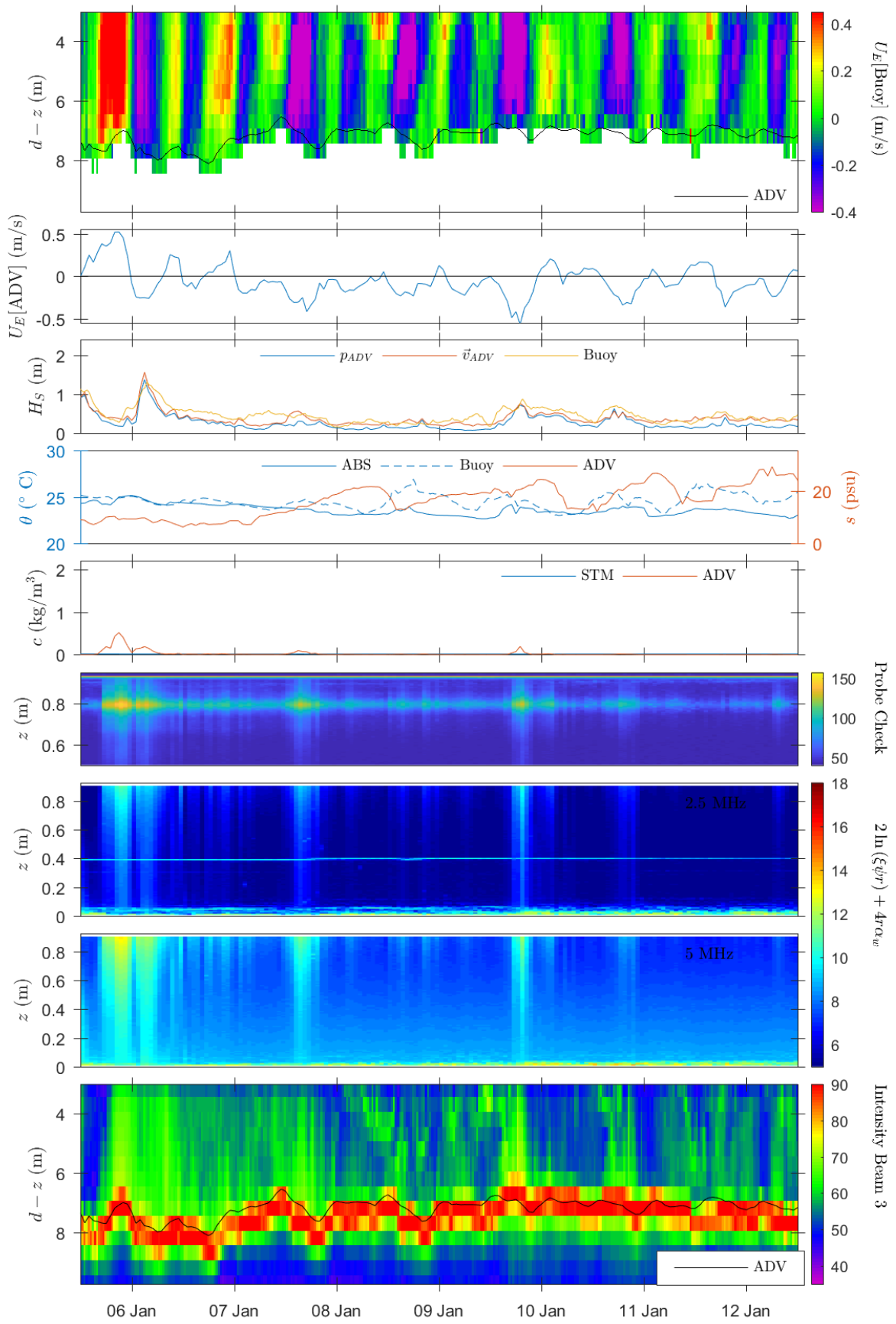


Figure 1.5: First deployment, fifth week.

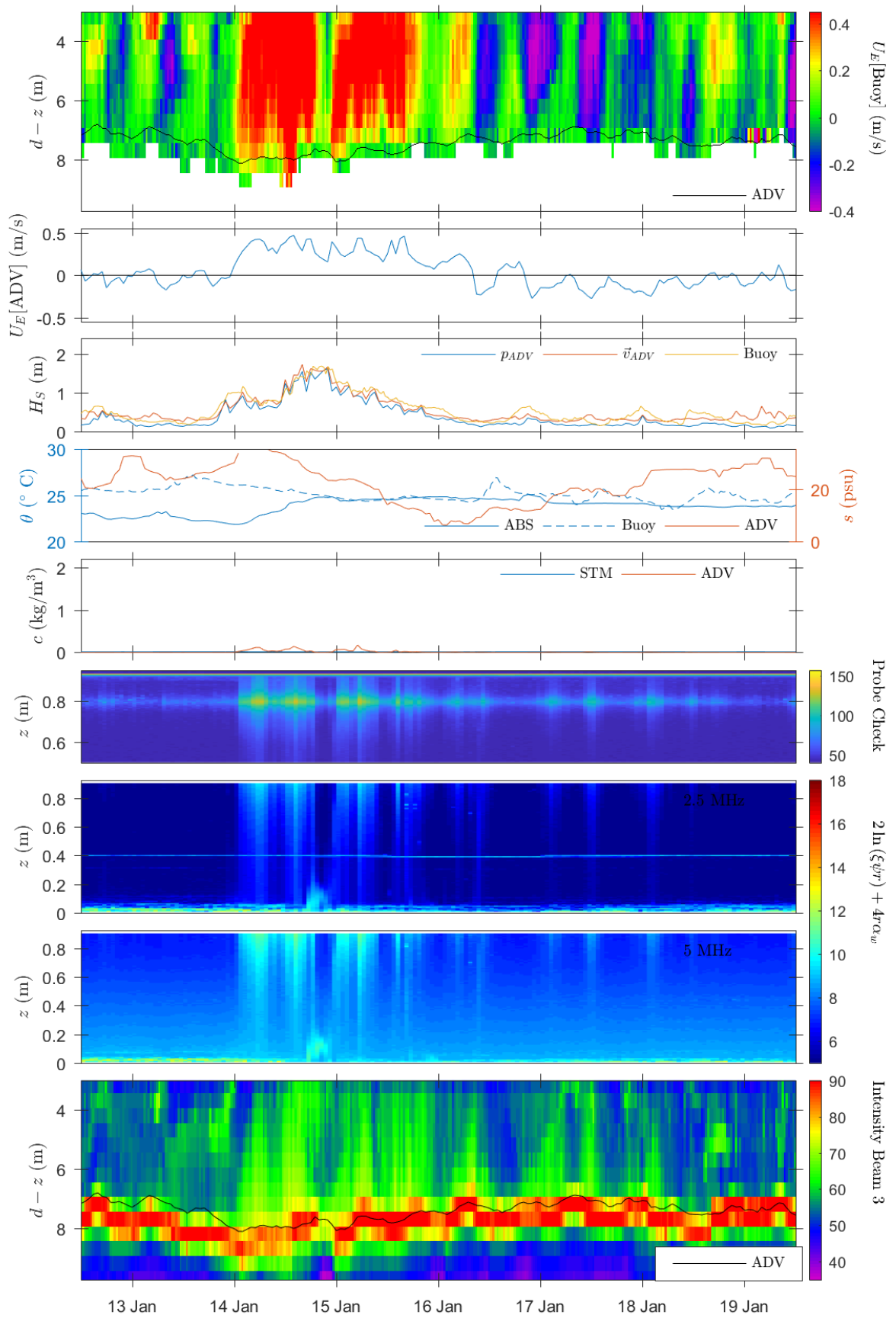


Figure 1.6: First deployment, sixth week.

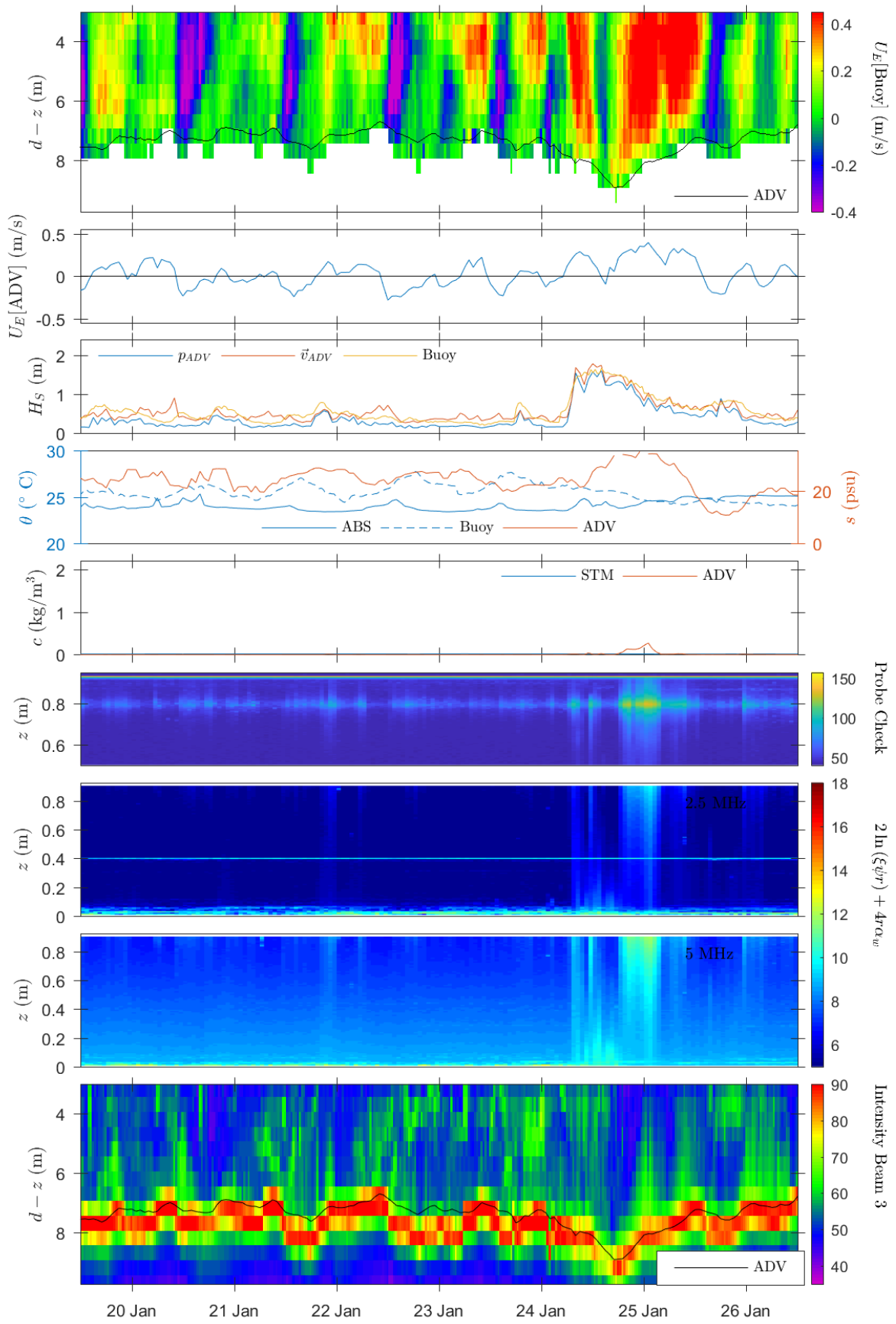


Figure 1.7: First deployment, seventh week.

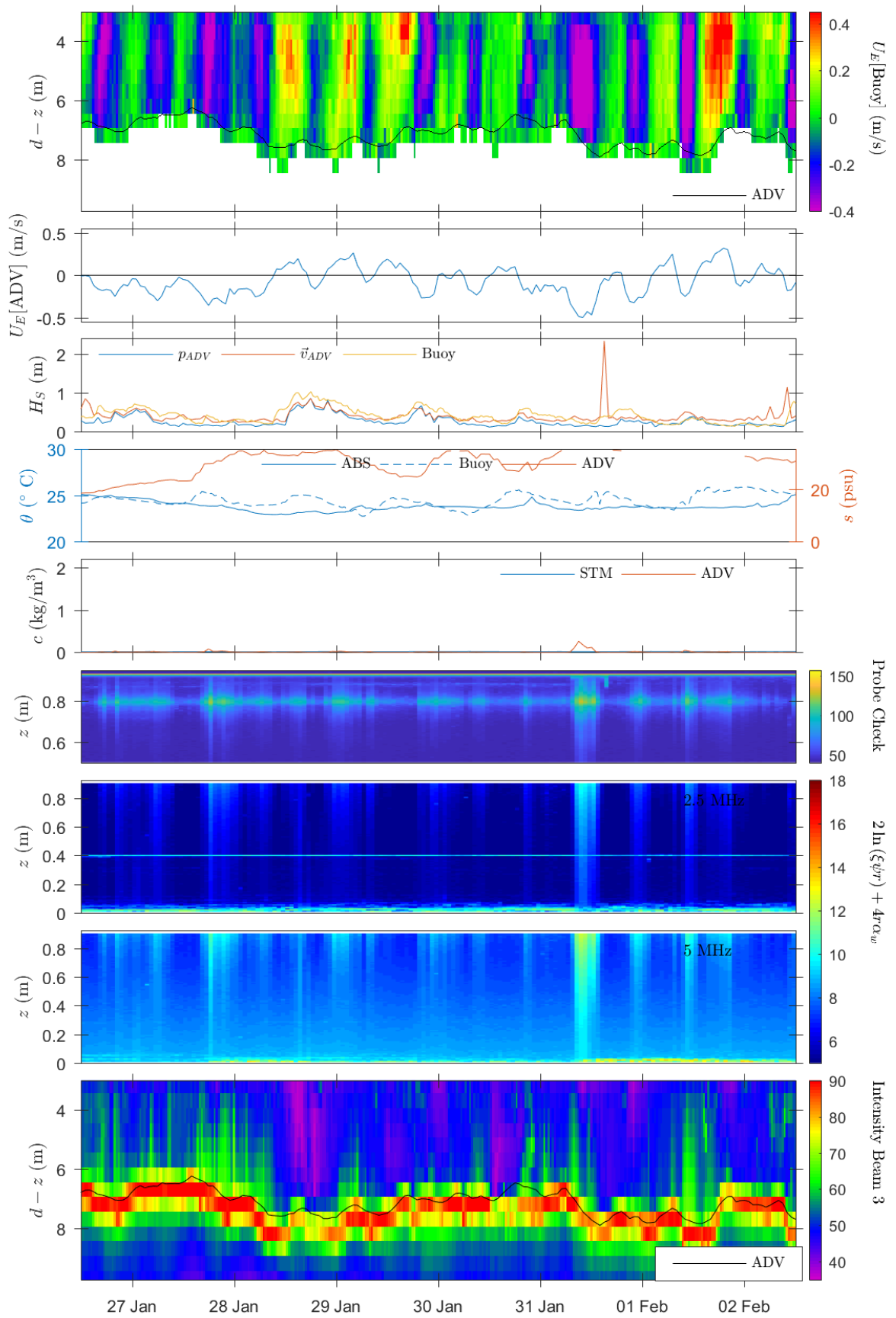


Figure 1.8: First deployment, eighth week.

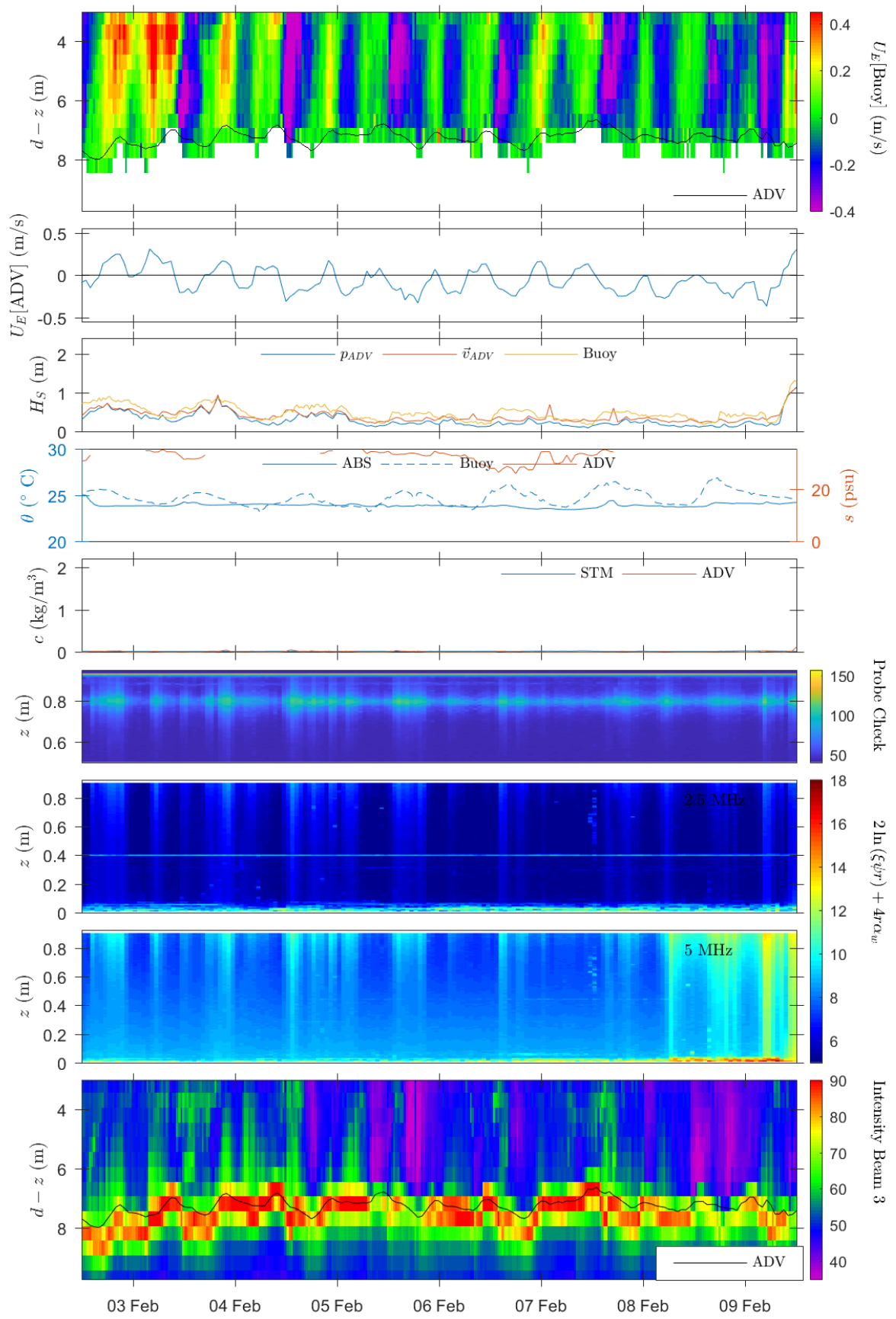


Figure 1.9: First deployment, ninth week.

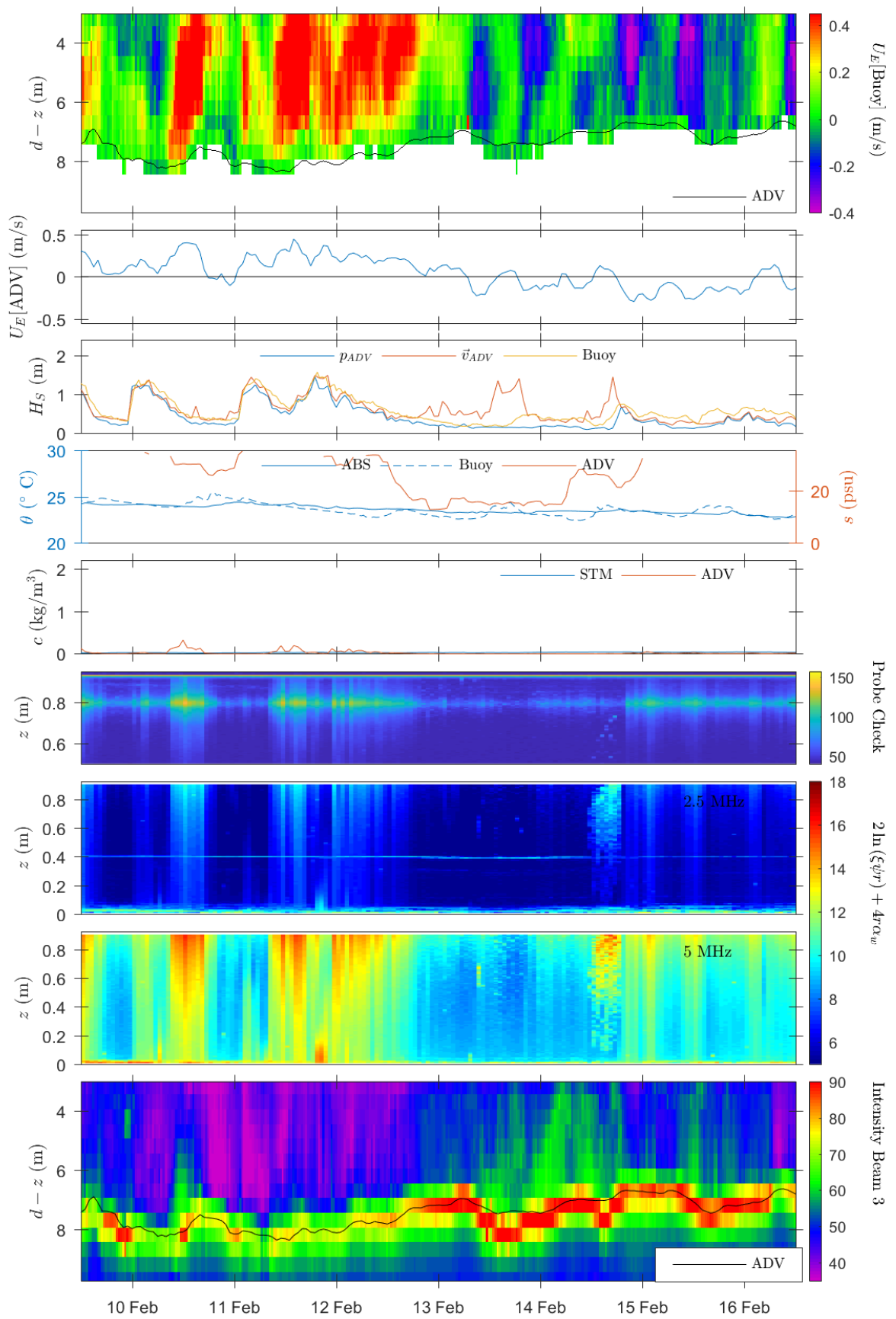


Figure 1.10: First deployment, tenth week.

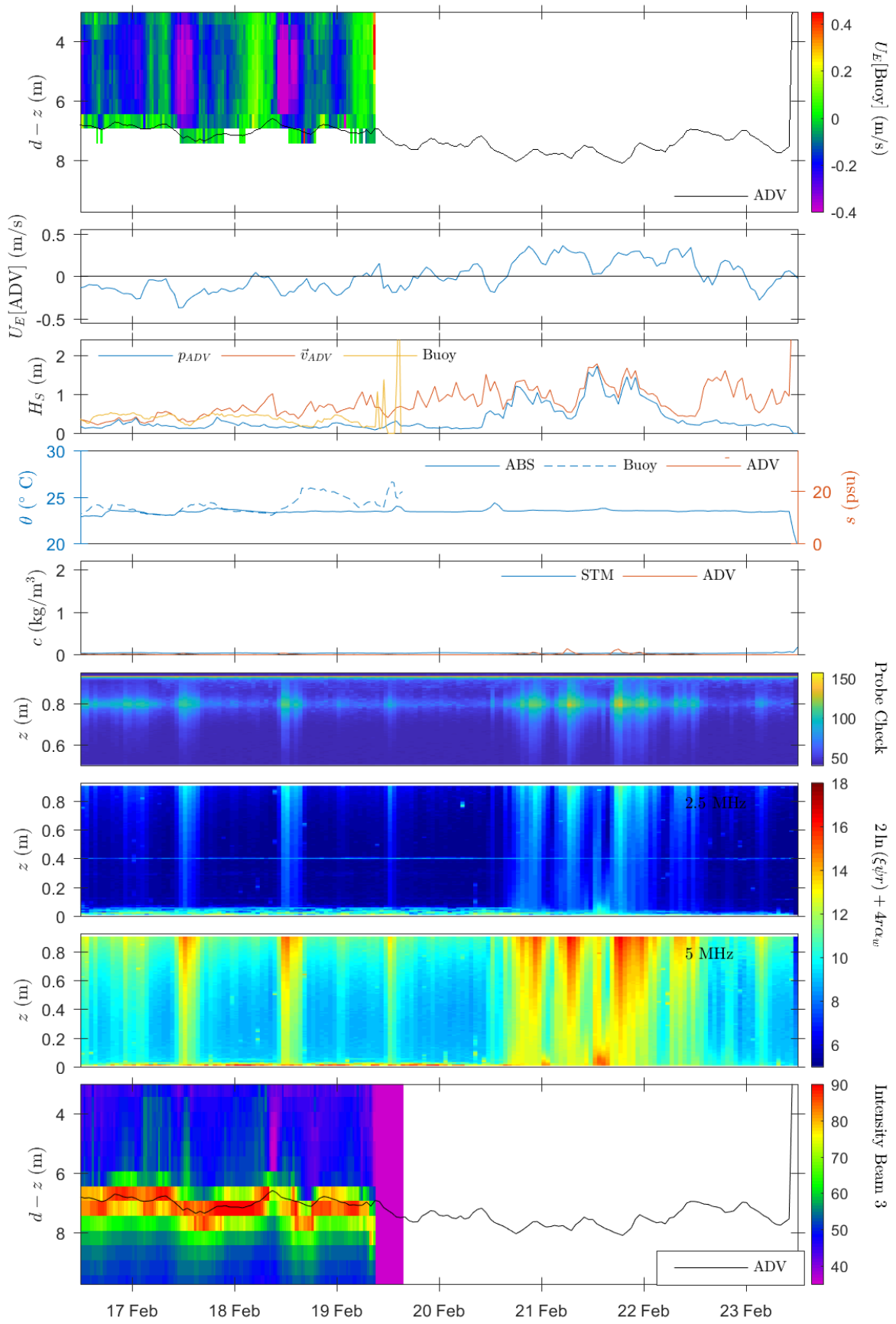


Figure 1.11: First deployment, eleventh week.

ANNEXES

Annex 1

Salinity estimation from Acoustic Doppler Velocimeter measurements



Salinity estimation from Acoustic Doppler Velocimeter measurements

Rodrigo Mosquera^{*}, Francisco Pedocchi^{**}

Instituto de Mecánica de Los Fluidos e Ingeniería Ambiental, Universidad de La República, Facultad de Ingeniería, Julio Herrera y Reissig 565, CP 11300, Montevideo, Uruguay



ARTICLE INFO

Keywords:

Acoustic Doppler Velocimeter
Salinity
Estuary

ABSTRACT

Estuarine environments tend to present significant salinity variations that can be relevant for hydrodynamics and sediment transport processes. In these environments salinity is usually estimated with high accuracy from conductivity, temperature, and pressure measurements using special instrumentation. However, there may be situations where it would be practical to use the information recorded by Acoustic Doppler Velocimeters (ADV) to estimate the salinity. In this work we present how the Probe Check information saved by the Vector ADV (Nortek, Norway), may be used to estimate the water salinity. A short theoretical explanation that justifies the proposed methodology and its practical implementation are presented. The salinity estimation obtained from the ADV Probe Check data is compared with the one computed from the conductivity, temperature and pressure records of a CTD in the Río de la Plata estuary. The results showed that the proposed methodology can be confidently used to estimate the salinity in estuarine environments.

1. Introduction

Acoustic Doppler Velocimeters (ADV) are currently used extensively to obtain detailed water velocity measurements suitable for the estimation of turbulent statistics such as turbulent kinetic energy and bottom shear stresses (Voulgaris and Trowbridge, 1998; Cartwright et al., 2013; Chanson et al., 2008; García et al., 2005; Bian et al., 2015; Kim et al., 2000). In this work we used the Vector ADV manufactured by Nortek, Norway; ADVs produced by other manufacturers are very similar, and they consist of a central piezoelectric transducer that emits an acoustic pulse and three (four in the case of the Vectrino by Nortek) transducers located on the arms that receive the acoustic return. ADVs use pulse coherent technology to measure the velocity of the targets that move in suspension in a small volume of water, called sample volume (Rusello, 2009). For this purpose, the ADV emits a pair of ultrasound acoustic pulses with known phase, and measures their returns at each receiver. Then these returns are processed using the covariance method to determine the Doppler phase shift between the two pulses. From these three (or four) phase shifts the three-dimensional velocity vector is obtained. The probe geometry and the sampling strategy allow for the determination of the “instantaneous” velocity vector at the sample volume with a frequency of several Hertz (Voulgaris and Trowbridge, 1998; Rusello, 2009).

Salinity in the field is usually estimated with high accuracy from

conductivity, temperature and pressure (depth) measurements using dedicated instrumentation, usually denominated CTDs. However, there may be situations where it would be practical to use the information recorded from an Acoustic Doppler Velocimeter (ADV) alone to estimate the salinity. In estuarine environments, for example, the salinity presents significant variations that can be relevant for hydrodynamics and sediment transport processes, and having reasonable estimations of the salinity without the need of a second instrument may be very valuable. It can also be that simultaneous salinity records are not available during the ADV deployment due to a malfunction of the dedicated CTD. Finally, in some field studies where multiple ADVs are deployed, budget limitation may restrict the possibility of deploying an equivalent number of CTDs, as CTDs and ADVs have similar price tags.

Standard ADV acquisition software allows the user to perform a check of the transducers using the Probe Check mode (Nortek-USA, 2018). The Probe Check functionality does not use the pulse coherent sampling strategy that the ADV uses for measuring the velocity; while in Probe Check mode the ADV records the amplitude of the signal received at each transducer continuously along time. Fig. 1 shows the Probe Check records obtained under two different salinities. Note that the Probe Check returns Amplitude as function of distance, and distance is computed as sound speed times recording time divided by two, using a fixed and preset sound speed. Nortek's Probe Check amplitude records usually show a first maximum close to 20 mm (not displayed in Fig. 1),

^{*} Corresponding author.

^{**} Corresponding author.

E-mail addresses: rmosquer@fing.edu.uy (R. Mosquera), kiko@fing.edu.uy (F. Pedocchi).

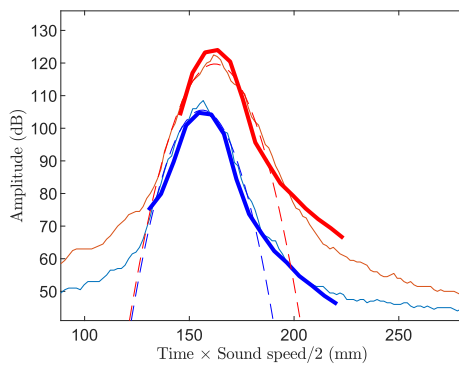


Fig. 1. Probe Check data (thin lines), theoretical curves (thick lines), and second order polynomial fit to the peak (dashed line), for 1503 m/s (blue) and 1452 m/s (red) sound speeds, computed from simultaneous CTD data. Note that the distances in the x-axis actually correspond to times, since they are computed as recording time times a constant sound speed divided by 2. (For interpretation of the references to colour in this figure legend, the reader is referred to the Web version of this article.)

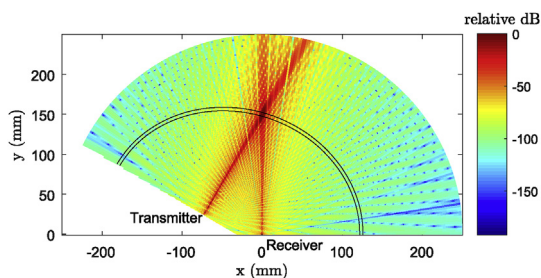


Fig. 2. Computation of the intersection pattern of the directivity of both emission and receptor transducers, along the $z = 0$ mm plane. Colors indicate the relative sound intensity in relative dB, black lines indicate an arbitrary ellipsoid shell. (For interpretation of the references to colour in this figure legend, the reader is referred to the Web version of this article.)

associated with the sound traveling directly from the emitter to the receiver; a clear second peak (displayed in Fig. 1) is observed at around 150 mm, which is associated with the return from the sample volume; and finally, a third peak (also not displayed in Fig. 1) may be observed if the ADV head is close enough to a reflecting surface. This last peak is the one the ADV uses for determining the distance to the wall. Functionalities similar to the Nortek ADV Probe Check are provided by the manufacturers for other ADV models or brands, although the approximate distances to the peaks may vary.

During field deployments, ADVs are usually configured to record few minute long bursts at several minute intervals. The sampling frequency of the variable within the burst is usually several Hertz. For example, the data presented here was obtained with an ADV configured to sample for 3 min at 32 Hz every 30 min. While in deployment mode the ADV performs and records a Probe Check at the beginning and end of each burst. In this work we present how these Probe Check records may be used to estimate the water salinity right before and after the flow velocity measurement burst.

2. Theory

The return peak from the sample volume is associated with the directivity of both emitting and receiving transducers. The directivity is the result of the three-dimensional angular distribution of acoustic energy either emitted or received by a transducer, and it is a function of the medium, the transducer size and shape, and the sound frequency (Morse and Ingard, 1986). In Fig. 2 the combination of the emitter and receiver directivities are shown to highlight how the different regions of

space may contribute to the total scattered energy that is recorded at the receiver. As the acoustic pulse leaves the emitter and travels into the water, the targets in the water scatter the sound towards the receiver. At a particular time, the signal recorded at the receiver is the integration of sound coming from a revolution ellipsoid shell with focal points located at the emitter and the receiver. Note that the time that it takes for the sound to travel from one focus of the ellipsoid to the other focus through any point on the ellipsoid surface is constant.

The numerically computed beam pattern intersection of the Vector ADV geometry is shown on Fig. 2 for illustrative purposes. The integration of the beam pattern over successive ellipsoid shells is a good approximation of the sound intensity recorded at the receiver transducer. However, small deviations due to scattering directionality may be expected. The result of the integration of this theoretical field is shown on Fig. 1 on top or the profile reported by Probe Check. This emphasizes that the maximum in the Probe Check energy profile is associated with the return from a particular ellipsoidal crust that includes the Sample Volume and corresponds to a fix region in space. Therefore, the time from the pulse emission to the maximum in the Probe Check profile must be affected by the sound speed in the water. For high sound speeds the Probe Check profile maximum will occur earlier than for low sound speeds, as shown in Fig. 1. Computations made with the beam pattern intersection of Fig. 2 and its integration (thick lines in Fig. 1) are shown for illustrative purposes only, as they are not used in the rest of this work.

The speed of sound in sea water is a function of pressure, temperature and salinity; here we will use the relation given by Del Grosso (1974). Therefore, we may use the distance to the Probe Check maximum to estimate the sound speed in water; and if pressure and temperature are recorded independently, as it is done by the Vector, the water salinity can be computed using the distance to the Probe Check maximum.

3. Materials and methods

As mentioned before we used a Vector ADV manufactured by Nortek, which has a central emitter and three receivers located on three arms. The central transducer is circular with an external diameter of 12 mm, and the three transducers located on the arms are approximately rectangular with external dimensions of 9 mm by 19 mm. The Vector emits 6 MHz ultrasound pulses, and the pulse length can be adjusted between 2 mm and 8 mm. The Sample Volume is located approximately 150 mm away from the central transducer (Nortek-USA, 2018).

For each Probe Check, the Vector records three backscatter amplitude profiles, one for each receiver; and during deployment the Vector performs and records Probe Checks twice, before and after each burst. Therefore, for each burst six sound profiles are available. When an instrument is in good condition the three Probe Check profiles look very similar, and the differences that may be observed are associated with the passage of large scatterers between the emitter and the receiver.

If a clean Probe Check profile is analyzed, it can be seen that the amplitude peak is usually defined by just two or three sampling points, one of them having the maximum value. This is due to the sampling strategy employed by Probe Check, which samples the profile at fixed intervals. As a first approximation the distance to the maximum amplitude of the profile may be computed with the distance to the maximum value of the raw profile. However, distances obtained in this way only take discrete values, which strongly limit the attainable precision of the distance to the maximum estimations. A more accurate estimation of the distance to the maximum is obtained if a fitting strategy is implemented. A fitting strategy captures the peak shape and allows to obtain the distance to the maximum with subpixel resolution (Raffel et al., 2011). Furthermore, if the subpixel distances obtained from the three transducers are averaged, the accuracy of the distance to the maximum will be further increased. If the ADV's configuration is such

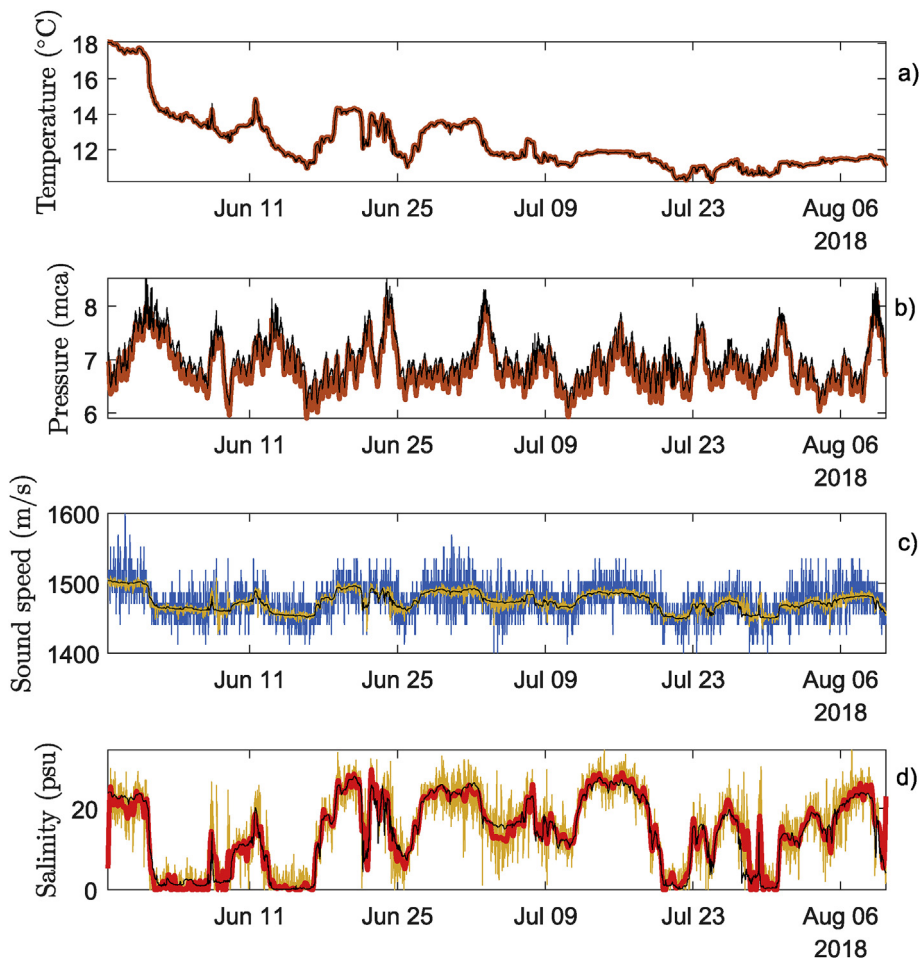


Fig. 3. Data recorded during the two month deployment at Río de la Plata. a: Temperature reported by CTD (black line) and ADV (brown line). b: Pressure recorded by CTD (black line) and ADV (brown line), note that the ADV pressure transducer was located 0.2 m above the CTD's. c: Computed sound speed by CTD (black line), computed using the Vector data and the proposed methodology with a sub-pixel estimator (yellow line), and without a sub-pixel estimator (blue line). d: Salinity computed by the CTD (black line), computed using the Vector data and the proposed methodology with a sub-pixel estimator (yellow line), and filtered using a 12 h moving average (red line). (For interpretation of the references to colour in this figure legend, the reader is referred to the Web version of this article.)

that the distances from the sampling volume to each receiver differ significantly, the procedure that follows may be applied to each transducer to obtain three estimations of the sound speed that may be later averaged.

After trying several possible fittings a simple second order polynomial fit was adopted in order to obtain the distance to the maximum amplitude with subpixel resolution

$$A = \alpha x^2 + \beta x + \gamma, \quad (1)$$

where A is the amplitude and x the distance reported by Probe Check. The second order polynomial fit allowed to capture a significant portion of the peak if a searching range for the peak location was provided (Fig. 1).

The distance to the Probe Check maximum amplitude x_{\max} can be used to estimate of the sound speed c noting that

$$c x_{\max} = K, \quad (2)$$

where K is an instrument constant ($\sim 235 \text{ m}^2/\text{s}$ for our Vector). The value of K can be obtained from the Probe Check profile in a fresh water bath with seeding particles.

Once the sound speed c is known, if the water temperature and pressure, also recorded by the ADV, are introduced in the expression given by Del Grosso (1974), the salinity can be computed. The more recent formulation of Chen and Millero (1977) for computing sound speed in natural waters, is also included with the SBE 19 plus V2 SeaCAT CTD software. However, the DelGrosso's expression has been shown to be more accurate than the one of Chen and Millero by Meinen and Watts (1997), and therefore the DelGrosso's expression is used here.

4. Deployment site

The described methodology was applied to a dataset obtained during a two month deployment in the Río de la Plata estuary 3.0 km south of the coast of Montevideo, Uruguay. Between May 25 and August 25, 2018 a Vector ADV and a Seacat 19 CTD manufactured by Seabird Inc, USA were deployed on a tripod. The measurement period covered the end of the fall and beginning of the winter season in the southern hemisphere. The geometrical configuration was such that the Vector sampling volume was located 30 cm above the bed and the Seacat water intake was located 55 cm above the bed. The average water depth at the location was 7.5 m, and it oscillated between 7 and 9 m due to both astronomical and meteorological tides, as is characteristic of the region (Fossati and Piedra-Cueva, 2008). The bed in the area is a layer of soft unconsolidated mud, several meters thick. The mud is a mix of fine cohesive sediments, mostly silt and clay (Groposo et al., 2015). The water temperature during the duration of the deployment varied between 10 and 18 °C, and the salinity between 0 and 28 PSU. The temperature, pressure and salinity, records are shown on panels (a), (b) and (d) of Fig. 3. The large variations in salinity, which are typical of the Río de la Plata in front of Montevideo, were clearly captured by the Seacat 19 CTD during the deployment. The Seacat 19 CTD and Vector temperature and pressure records show an excellent agreement.

5. Results and discussion

Fig. 3c shows the sound speed computed from the conductivity, pressure, and temperature measured by the CTD, using Del Grosso (1974) expression. Also in the same panel the sound speed estimated

using the proposed methodology with the pressure and temperature recorded by the ADV, and the distance to the maximum obtained from the Probe Check, is shown. As explained in Section 3, both the raw estimation using distance to the maximum amplitude value and the result of fitting a second order polynomial to the peak are shown.

The advantage of using a subpixel estimator can be clearly seen in Fig. 3c. If the CTD based sound speed estimation is assumed to be the target, the resulting standard deviations for the Vector sound speed estimations obtained using both methodologies during the three-month deployment were: 20.2 m/s using the raw distance to the maximum amplitude, and 5.4 m/s using the sub-pixel estimator. Considering the low computational cost of implementing a sub-pixel estimator and the appreciable improvements in the sound speed estimation, the use of a sub-pixel estimator is completely justified. In places such as the Rio de la Plata estuary, where salinity varies between 0 and 30 psu and the temperature varies between 10 and 30 °C, the sound speed is expected to vary between 1440 and 1540 m/s. Therefore, the standard deviation of the sub-pixel methodology can be estimated as 5.4 % of the measuring range.

In Fig. 3d the salinity reported by the CTD is compared with the one computed using the proposed Vector Probe Check methodology. It is clearly observed that the agreement is very good, capturing the broad salinity variations, proving that the proposed methodology may be used as trustworthy estimator of the salinity for regular studies in estuarine environments. The standard deviation of the difference between the salinity computed with the subpixel estimator (yellow line in Fig. 3d) and the one recorded by the CTD (black line in Fig. 3d) was 4.0 psu, for the recorded period. Using a 12 h moving average (M2 tide constituent), the spurious high frequency variations displayed by the salinity estimated with the Vector based methodology may be removed, allowing for a better appreciation of the results that can be achieved using the proposed method (red line in Fig. 3d).

6. Conclusions

The presented theoretical analysis, implementation and results demonstrated that it is possible to estimate water salinity for the wide range of variations that are observed in estuarine environments. The standard deviation of the instantaneous difference between the ADV and CTD salinity estimations was found to be 4 psu for the studied dataset; which may be reduced by averaging. This makes the presented methodology particularly useful for estuarine and cohesive sediment studies, where sediment transport may be strongly affected by salinity. Furthermore, the presented methodology may also be useful in the analysis of existing ADV records, where salinity measurements were not available. Finally, we believe that these results can be easily incorporated into the standard ADV post-processing software, allowing the regular user to record temperature, pressure, salinity, and water

velocity, using a single device.

Acknowledgments

The Vector ADV used in this study was acquired with support from the program Fondo María Viñas from the Agencia Nacional de Investigación e Innovación, Uruguay. The field work was performed thanks to the support of the Comisión Sectorial de Investigación Científica of the Universidad de la República, Uruguay. The authors would like to thank Matías Gonzalez, Guillermo Echavarría, Daniel Barboza, and Ricardo Zouko from the Instituto de Mecánica de los Fluidos e Ingeniería Ambiental from the Facultad de Ingeniería of the Universidad de la República, Uruguay. Thanks also to the divers from Technodive SRL, and the crew of the multicat Titón for their help during the mooring works.

References

- Bian, C., Mao, X., Jiang, W., Gu, Y., 2015. Adv-based estimates of sediment settling velocity on the shelf of the yellow and east China seas: evidence of marked seasonal and intra-tidal variations. *Geo Mar. Lett.* 35, 53–60.
- Cartwright, G.M., Friedrichs, C.T., Smith, S.J., 2013. A test of the adv-based Reynolds flux method for in situ estimation of sediment settling velocity in a muddy estuary. *Geo Mar. Lett.* 33, 477–484.
- Chanson, H., Trevethan, M., Aoki, S.I., 2008. Acoustic Doppler velocimetry (adv) in small estuary: field experience and signal post-processing. *Flow Meas. Instrum.* 19, 307–313.
- Chen, C.T., Millero, F.J., 1977. Speed of sound in seawater at high pressures. *J. Acoust. Soc. Am.* 62, 1129–1135. <https://doi.org/10.1121/1.381646>.
- Del Grosso, V.A., 1974. New equation for the speed of sound in natural waters (with comparisons to other equations). *J. Acoust. Soc. Am.* 56, 1084–1091. <https://doi.org/10.1121/1.1903388>.
- Fossati, M., Piedra-Cueva, I., 2008. Numerical modelling of residual flow and salinity in the Rio de la Plata. *Appl. Math. Model.* 32, 1066–1086.
- García, C.M., Cantero, M.I., Niño, Y., García, M.H., 2005. Turbulence measurements with Acoustic Doppler Velocimeters. *J. Hydraul. Eng.* 131, 1062–1073. [https://doi.org/10.1061/\(ASCE\)0733-9429\(2005\)131:12\(1062\)](https://doi.org/10.1061/(ASCE)0733-9429(2005)131:12(1062)).
- Groppo, V., Mosquera, R.L., Pedocchi, F., Vinzón, S.B., Gallo, M., 2015. Mud density prospection using a tuning fork. *J. Waterw. Port, Coast. Ocean Eng.* 141, 04014047. [https://doi.org/10.1061/\(ASCE\)WW.1943-5460.0000289](https://doi.org/10.1061/(ASCE)WW.1943-5460.0000289).
- Kim, S.C., Friedrichs, C.T., Maa, J.P.Y., Wright, L.D., 2000. Estimating bottom stress in tidal boundary layer from Acoustic Doppler Velocimeter data. *J. Hydraul. Eng.* 126, 399–406. [https://doi.org/10.1061/\(ASCE\)0733-9429\(2000\)126:6\(399\)](https://doi.org/10.1061/(ASCE)0733-9429(2000)126:6(399)).
- Meinen, C.S., Watts, D.R., 1997. Further evidence that the sound-speed algorithm of del grosso is more accurate than that of chen and millero. *J. Acoust. Soc. Am.* 102, 2058–2062.
- Morse, P.M., Ingard, K.U., 1986. *Theoretical Acoustics*. Princeton university press.
- Nortek-USA Vector 300 M Specifications. www.nortekgroup.com/products/vector-300-m, Accessed date: 30 November 2018.
- Raffel, M., Willert, C., Scarano, F., Kähler, C., Wereley, S., Kompenhans, J., 2011. *Particle Image Velocimetry: A Practical Guide*, vol. 30 Cambridge University Press.
- Rusello, P.J., 2009. *A Practical Primer for Pulse Coherent Instruments*. TN-027. Nortek USA.
- Voulgaris, G., Trowbridge, J.H., 1998. Evaluation of the Acoustic Doppler Velocimeter (ADV) for turbulence measurements. *J. Atmos. Ocean. Technol.* 15, 272–289.